THE UNIVERSITY OF CHICAGO

REDUCED DENSITY MATRIX APPROACHES FOR MANY-BODY SIMULATIONS ON NEAR-TERM QUANTUM COMPUTERS

A DISSERTATION SUBMITTED TO
THE FACULTY OF THE DIVISION OF THE PHYSICAL SCIENCES
IN CANDIDACY FOR THE DEGREE OF
DOCTOR OF PHILOSOPHY

DEPARTMENT OF CHEMISTRY

BY
SCOTT EVERETT SMART

CHICAGO, ILLINOIS
JUNE 2022

To Mary and Grace

TABLE OF CONTENTS

LIST OF FIGURES viii

LIST OF TABLES xvi

ACKNOWLEDGMENTS xxi

ABSTRACT xxiii

PREFACE xxiv

I PRELIMINARIES

1 INTRODUCTION TO QUANTUM CHEMISTRY 2
- 1.1 Quantum Chemistry and the Electronic Hamiltonian 2
- 1.2 First and Second Quantization and Hartree-Fock Theory 4
- 1.3 Post-Hartree Fock Methods and Electron Correlation 8
  - 1.3.1 Multi-Reference Methods 10
- 1.4 A Note on Scaling 11

2 REDUCED DENSITY MATRIX APPROACHES FOR QUANTUM CHEMISTRY 13
- 2.1 Reduced Density Matrices 13
- 2.2 N-Representability 15
- 2.3 Reconstruction of Reduced Density Matrices 18
- 2.4 Contracted Schrödinger Equations 19
  - 2.4.1 Finding a Solution of the Contracted Eigenvalue Equations 21

3 QUANTUM COMPUTING FOR MOLECULAR SIMULATION 24
- 3.1 Basics of Quantum Computation 24
  - 3.1.1 Qubits 24
  - 3.1.2 Gates and Rotations 26
  - 3.1.3 Measurement 29
- 3.2 Near-Term Quantum Devices 31
  - 3.2.1 Operator Description of Open Dynamics 32
- 3.3 Fermionic Simulation 34
  - 3.3.1 Fermionic Transformations 35
  - 3.3.2 Exponential Operators 37
- 3.4 Quantum Algorithms for Quantum Chemistry 39
  - 3.4.1 Adiabatic State Preparation 39
  - 3.4.2 Variational Quantum Eigensolver 40
  - 3.4.3 Imaginary Time Evolution 45
  - 3.4.4 Error Mitigation Techniques 45

II CHARACTERIZATION OF NOISY QUANTUM SYSTEMS FOR MANY-BODY SIMULATIONS

4 EXPERIMENTALLY DEMONSTRATING PURE N-REPRESENTABILITY CONSTRAINTS ON A QUANTUM COMPUTER . . . 53
4.1 Introduction . . . 53
4.2 Results . . . 54
4.2.1 Measurement of 1-RDM Eigenvalues . . . 54
4.2.2 Verification of Generalized Pauli Constraints . . . 58
4.3 Discussions . . . 61
4.4 Methods . . . 62
4.5 Supplemental Information . . . 69
4.5.1 Experimental Data . . . 72

5 ERROR-MITIGATING N-REPRESENTABILITY CONDITION FOR CALCULATION OF MOTT METAL-INSULATOR TRANSITION ON A QUANTUM COMPUTER . . . 85
5.1 Introduction . . . 85
5.2 Theory . . . 87
5.2.1 N-Representability . . . 87
5.2.2 Error Mitigation Scheme . . . 88
5.2.3 Hybrid Variational Algorithm . . . 89
5.3 Results and Discussion . . . 91
5.3.1 Dissociation of Linear H_3 . . . 91
5.3.2 Mott Insulator Transition for H_3 . . . 91
5.4 Conclusion . . . 93
5.5 Appendix . . . 95

6 PURE N-REPRESENTABILITY OF TWO ELECTRON ANSATZ FOR BENCHMARKING NEAR-TERM QUANTUM DEVICES . . . 109
6.1 Introduction . . . 109
6.2 Theory . . . 110
6.2.1 Structure of the Two-Electron System . . . 110
6.2.2 Variational Hybrid Algorithm . . . 112
6.2.3 Preparation of Efficient Quantum Ansatz . . . 113
6.2.4 Error Mitigation Strategies . . . 114
6.3 Results . . . 115
6.4 Discussion and Conclusion . . . 119
6.5 Appendix . . . 124

7 REDUCING TOMOGRAPHY COSTS WITH A SYMMETRY PROJECTED OPERATOR BASIS . . . 133
7.1 Introduction . . . 133
7.2 Theory . . . 135

7.3 Results and Applications . . . 137
7.3.1 Application to Reduced Density Operators . . . 137
7.3.2 Effects of Noise on Particle Count . . . 140
7.4 Conclusion . . . 143
7.5 Appendix . . . 143

8 RELAXATION OF STATIONARY STATES ON A QUANTUM COMPUTER FOR UNIQUE CHARACTERIZATION OF NOISE ON A QUANTUM COMPUTER . 159
8.1 Introduction . . . 159
8.2 Results . . . 161
8.2.1 Stationary-State Evolution with Noise . . . 161
8.2.2 Single-qubit Hamiltonians . . . 162
8.2.3 Two-qubit Hamiltonians . . . 166
8.3 Conclusions . . . 172
8.4 Supplemental Information . . . 175

III CONTRACTED QUANTUM EIGENSOLVERS

9 QUANTUM SOLVER OF CONTRACTED EIGENVALUE EQUATIONS FOR SCALABLE MOLECULAR SIMULATIONS ON QUANTUM COMPUTING DEVICES 187
9.1 Introduction . . . 187
9.2 Theory . . . 189
9.3 Results . . . 192
9.4 Discussion and Conclusions . . . 196
9.5 Methods . . . 198

10 RESOLVING CORRELATED STATES OF BENZYNE ON A QUANTUM COMPUTER WITH AN ERROR-MITIGATED QUANTUM CONTRACTED EIGENVALUE SOLVER . . . 208
10.1 Introduction . . . 208
10.2 Theory . . . 210
10.2.1 Quantum Solver of the Anti-Hermitian Contracted Schrödinger Equation 210
10.2.2 Quantum Computation . . . 213
10.2.3 Limit-Preserving Correction for an Iterative Ansatz . . . 215
10.2.4 Purification of the 2-RDM . . . 217
10.3 Benzyne Calculations . . . 219
10.4 Discussion . . . 224
10.5 Conclusions . . . 229
10.6 Appendix . . . 230
10.6.1 Electronic Structure Calculation . . . 230
10.6.2 Quantum Calculations . . . 231
10.6.3 Error Mitigation Methods . . . 243
10.6.4 Symmetry and the ACSE . . . 245

11 MANY-FERMION SIMULATION FROM THE CONTRACTED QUANTUM EIGENSOLVER WITHOUT FERMIONIC ENCODING OF THE WAVE FUNCTION . 255
11.1 Introduction . . . 255
11.2 Theory . . . 257
11.2.1 Encoded ACSE and its CQE algorithm . . . 257
11.2.2 Unencoded ACSE and its CQE algorithm . . . 259
11.2.3 Second-order Corrections to the Wave Functions and 2-RDMs . . . 261
11.2.4 Connection between the Encoded and Unencoded ACSEs . . . 262
11.2.5 Practical Considerations of the CQE Algorithm . . . 264
11.3 Applications . . . 266
11.3.1 Molecular Simulations . . . 266
11.3.2 Investigation of Resource Requirements . . . 269
11.3.3 Generation of the ${}^{2}_{Q}A$ Matrix . . . 271
11.4 Discussion . . . 274
11.5 Conclusion . . . 276
11.6 Appendix . . . 277

12 ACCELERATED CONVERGENCE OF CONTRACTED QUANTUM EIGENSOLVERS THROUGH A QUASI-SECOND-ORDER, LOCALLY PARAMETERIZED OPTIMIZATION . . . 284
12.1 Introduction . . . 284
12.2 Theory . . . 285
12.2.1 Solution of the ACSE . . . 286
12.2.2 Local Parameterization of the Contracted Quantum Eigensolver . . . 287
12.2.3 Quasi-Second-Order CQE Algorithms . . . 289
12.2.4 Resource-Optimized CQE Search Directions . . . 292
12.3 Applications and Results . . . 294
12.3.1 Implementation of Optimized CQE . . . 294
12.3.2 Encoding-Free CQE . . . 298
12.3.3 Comparison with VQE . . . 300
12.4 Discussion . . . 303
12.5 Conclusion . . . 306
12.6 Computational Details . . . 307

13 QUANTUM CONTRACTED EIGENSOLVER FOR SOLVING THE CONTRACTED SCHRÖDIGNER EQUATION . . . 312
13.1 Introduction . . . 312
13.2 Theory . . . 314
13.2.1 Contracted Schrödinger Equation . . . 314
13.2.2 Quantum Eigensolver for Solving the CSE . . . 316
13.2.3 Obtaining the Residuals of the HCSE . . . 317
13.2.4 Implementing the Exponential Hermitian Operator . . . 319
13.3 Results and Discussion . . . 320
13.4 Conclusion . . . 325

LIST OF FIGURES

1 A single-reference state used to represent the 1s orbital, representing the lowest quantum number solution to the hydrogen atom from the Schrödinger equation. Spatially, this corresponds to a normalized and integrable function depending on the electron coordinate r. xxvi
2 Describing stretched hydrogen as a pure singlet requires two states (or, multiple references) which cannot be rotated or expressed as a single-state. This is equivalent to the well known Bell state, exhibiting genuine quantum entanglement.xxvii
3 DiVincenzo's five criteria for a universal quantum device. xxix

4.1 Orbital occupations of the 1-electron reduced density matrix (1-RDM) form convex polytopes. The eigenvalues (natural occupations) of the 1-RDM, ordered from largest to smallest, form a special convex set with "flat" sides known as a polytope. Because the three smallest eigenvalues for a 3-electrons-in-6-orbitals state (n_4, n_5, n_6) determine the other eigenvalues, we can visualize the polytope in three dimensions. The figure shows two polytopes: (*i*) the Pauli polytope of eigenvalues obeying the ordinary Pauli constraints (the combination of the yellow and blue regions) as well as (*ii*) the generalized Pauli polytope of eigenvalues obeying the generalized Pauli constraints (the yellow region only). The plane separating the yellow and blue regions arises from the Borland-Dennis inequality shown in Eq. (4.3). 57
4.2 Measured orbital occupations verify generalized Pauli principle. The scatter plot of the three lowest measured 1-electron reduced density matrix (1-RDM) eigenvalues (n_4, n_5, n_6) is shown relative to the Pauli polytope, the combination of the yellow and blue regions, and the smaller generalized Pauli polytope, only the yellow region. Results show that none of the eigenvalues lie in the part (blue) of the Pauli polytope which is forbidden for pure quantum states by the Borland-Dennis constraint. 60
4.3 Orbital occupations of correlated 3-electron atoms and molecules. The lowest three eigenvalues (natural occupations) of the 1-electron reduced density matrix (1-RDM) for ground and excited states of 3-electron-in-6-orbital atoms and molecules (n_4, n_5, n_6) are shown: **a** Lithium atom (red) and the π orbitals of the Boron atom (blue). **b** Allyl radical in the cyclic form (C_3H_3, red) and linear H_3 (blue). The triplet of occupation numbers from ground and excited states tends to gravitate towards the boundaries of the polytope, reflecting the interplay between the energy optimization and the restrictions imposed on fermions from the Pauli constraints. These eigenvalues were calculated by full configuration interaction on a classical computer. 61

4.4 Each point represents the 3 largest eigenvalues of an experimental 1-RDM generated from the quantum computer. The algorithm used is the second quantum algorithm presented in the methods, equation 13, and the points represent executions of that algorithm with randomly selected parameters to achieve a total filling of the set. Note that two points did violate the generalize Pauli constraints, due to the propagation of error in the longer quantum circuit. There are a total of 59 points measured here, and so the validity of the confirmation of the generalized Pauli constraints still stands. 71
4.5 Shows the experimental (red) and ideal (blue) 3 largest eigenvalues of the 1-RDM generated by a single $C_i^j R_y$ on qubits i and j. The values are all shifted away form the vertex upon which true bipartite or separable states lie. Additionally, the shift in error in this case is to be pushed into the polytope. 72

5.1 Depicts the dissociation curve for the doublet H_3 with respect to the bond distance from the center H to the two exterior H atoms in a linear geometry. The crosses were calculated with a variational quantum algorithm on the quantum computer, while the line was generated with a full configuration interaction (FCI) calculation on a classical computer. Energies are listed in Hartrees. The inset plot depicts the error from the full-CI method also with respect to the separated distance, and is reported in milli-Hartrees, mH. The dashed line is at 1.6 mH, which corresponds with 1.0 kcal / mol, generally used as a guide for chemical accuracy. The effect of errors is discussed in the text and in Appendix 5.5. Variability from a single run is on the order of $2-0.2$ mH, and in our optimization we purposefully oversample the target region. 92
5.2 Shows the sum of squares of the off-diagonal elements, τ, of the 1-RDM of H_3 in the local Löwdin atomic orbital basis along the dissociation curve of H_3. Here, $\tau = \sum_{i \neq j} \|^1 D_j^i \|^2$ where i, j are orbital indices in the Löwdin atomic orbital basis. The Hartree-Fock result is shown as a dashed-dotted line, the FCI result is solid, and our variational quantum computation is shown as crosses. The bottom dashed line shows the dissociated limit where $\tau = 0$, and the natural orbitals approach the atomic ones. That H_3 serves as a Mott-Insulator can be seen between these distances, as $\tau \to 0$ with increasing distance, highlighting the mean field and 2-electron approaches. 94
5.3 Depicts the dissociation curve for the doublet H_3 with respect to the bond distance from the center H to the two exterior H atoms in a linear geometry across a variety of methods, including Full Configuration Interaction (FCI), second-order perturbation theory (MP2), restricted open-shell Hartree-Fock method (SCF), and our variational algorithm. Coupled-cluster with singles and doubled (CCSD) actually is equivalent to the FCI result for a 3-electron in 3-spatial-orbital system, due to the restriction of movement of the 3 electrons. For more orbitals this is not the case. With the exception of the RDM-QC method, PySCF was used for calculations[47]. 96

5.4 Depicts the (a) first and (b) second macro iteration of the Nelder-Mead simplex optimization of H_3, where the separation from the central atom is 1.34 Å. Between the two iterations an orbital rotation is performed. The vertical axis represents the energy difference between the measured energy and the full configuration interaction result in milli-Hartrees (mH), while the horizontal axis shows the number of function evaluations. For clarity we only show evaluations with an energy difference of 20 mH. The blue dashed line shows the energy of the best simplex point along the optimization, while the green line shows the "chemical accuracy" threshold of 1.6 mH. Error bars correspond with a 90% confidence interval based largely on sampling errors in the quantum computer. The variational design of the algorithm and oversampling in the target region allow for higher confidence results in the final energy. 98

6.1 Dissociation curves for the ground state of H_2 from the variational quantum algorithm on the quantum computer and the full configuration interaction are shown. Both results were run with 4 qubits, but on 5- and 14- qubit frameworks. The inset shows the difference in energy from the FCI results in mhartrees. The increased error for the shortest distance relates to the difficulty in reaching the Hartree-Fock state on a quantum computer when using entangling gates. For more experimental details, see the Appendix. 116

6.2 Measured (unordered) occupation numbers with respect to the coefficient $t_{11'}^{22'}$ of the single double excitation operator within the entangling circuit. Blue triangles represent the first qubit, and green circles represent the second qubit, unordered. Unfilled objects show the raw occupations, and filled objects the symmetry-corrected occupations. Uncertainties for the values are similar in size to the markers. 117

6.3 (Left) measured occupations of the 6-qubit system following symmetry application of N and S_z, as well as the boundaries of the ideal polytope. Note, σ refers to the use of i or i'. Because these occupations correspond with an N-representable system, the equality $n_{1\sigma} + n_{2\sigma} + n_{3\sigma} = 1$ holds, and so we show the orthographic projection along the $n_{3\sigma}$ axis. (Right) slices of the set with respect to the entangling parameters $t_{11'}^{22'}$ and $t_{22'}^{33'}$ at values of 0.00, -0.94, -1.88, and -2.83. The device was sampled over the range $t_{11'}^{22'}, t_{22'}^{33'} \in [-\pi, 0]$ in $\frac{\pi}{10}$ intervals for the entangling parameters. The ratio of areas of the experimental and theoretical convex hulls of these obtained points is 0.48 and 0.68 for $\{n_i\}$ and $\{n_{i'}\}$, respectively. 120

6.4 Dissociation curves for the ground state of H_3^+ from the variational quantum algorithm on the quantum computer and the full configuration interaction. The experiment was run on a 14- qubit framework. The inset shows the difference in energy from the FCI results in mhartrees. The increased error for the shortest distance relates to the difficulty in reaching the Hartree-Fock state on a quantum computer when using entangling gates. For more experimental details, see the Appendix 6.5. 121

6.5 The unitary coupled cluster term for two Pauli terms, here representing the exponent of $Y_0X_1Y_2Y_3$ followed by $X_0X_1X_2Y_3$. For optimal connectivity (i.e., no intermediate CNOT gates for intermediate orbitals), there are 12 CNOT operations, generally the most error prone step. 127
6.6 The unitary coupled cluster term as seen in Fig. 6.5, but in a simplified form. Note the target qubit for the rotation here is not q_3 but q_1. Importantly, the circuit require only 8 CNOT operations, and still has the same connectivity requirements. The gate H' is defined as $S^\dagger HS$ (applied left to right). 127

7.1 (Left) Ratio of the number of total required terms in the 2-RDM versus the number of required circuits following a grouping procedure, and (right) the scaling coefficient of the number of circuits with respect to the number of qubits. The color denotes the fermionic mapping (Jordan-Wigner, Parity, and Bravyi-Kitaev), and the symbol denotes the set of symmetries applied in the projection procedure. The grouping procedure involves grouping terms according to qubit-wise commutation following Ref. [54]. The black line on the right refers to total number of terms. See Appendix 7.5 for more details. 141

8.1 Frequency scan of simulated time evolution for a single qubit. Scan of population of the $|0\rangle$ state (n_0) as a function of simulated time t and frequency ω on the ibmq_armonk device. We initially prepare the state in the 1 state and then apply 100 total gate sequences of $\exp[-i\tau H]$, where the time step is $\tau = \frac{1}{3}$, the system Hamiltonian is $H = \omega\sigma_z$, and $\omega \in (0, 0.6)$. The time t is equal to the number of gates times τ multiplied by the scaling factor 0.015. The oscillatory behavior reveals non-Markovian effects with the oscillations becoming less pronounced at higher frequencies. 163
8.2 Rate of population change with respect to simulated time for a single qubit. Approximate rate of ground-state populations changes $\frac{d}{dt}n_0$ as a function of frequency ω evaluated after the first time step, which is proportional to the spectral density. The data is taken from the scan in Fig. 8.1 from ibmq_armonk. 165
8.3 Demonstration of simulated time evolution for different devices and qubits. Different device and qubit (indicated by the i^{th} qubit Qi)) simulations over simulated time t for frequencies ω with a system Hamiltonian $H = \omega\sigma_z$, with a time step $\tau = \frac{1}{3}$. **a** Q0, ibmq_armonk. **b** Q2, ibmq_belem. **c**−**e** Q0, Q2, Q4, ibmq_bogota. **f**−**h** Q0, Q2, Q4, ibmq_casablanca. Legend shows frequencies ranging from $\omega \approx 0$ (blue, shortest dashes) to $\omega = 0.5$ (green, longest dashes). 167
8.4 Single qubit state trajectories with respect to simulated time for a range of transition frequencies. Scan of several trajectories represented in the Bloch sphere for a single qubit device for a range of transition frequencies $\omega \in [0.05, 0.15]$ in increments of 0.01, from ibmq_armonk. σ_i represents the expectation with respect to that Pauli operator as a function of time. Each simulation has an equal number of gate applications and changes only the frequency ω in the propagation with time step τ, $\exp[-i\tau H] = \exp[-i\frac{\omega\sigma_z}{3}]$. ω decreases from red ($\omega = 0.05$) to green ($\omega = 0.10$) to blue ($\omega = 0.15$). 168

8.5 Simulated time evolution of a two-qubit local system which demonstrates controlled local state transitions. Populations n_{ij} where ij refers to the eigenstate (which is the computational basis) of the two-qubit system undergoing simulated evolution for time t with time step $\tau = 1/3$ prepared on ibmq_rome. The system Hamiltonian can be described with two frequencies: $H(\omega_1, \omega_2) = \omega_1\sigma_z^1 + \omega_2\sigma_z^2$. The different plots describe permutations of two different values of ω_1 and ω_2. **a** $(\frac{1}{20}, \frac{1}{20})$; **b** $(\frac{1}{20}, \frac{1}{2})$; **c** $(\frac{1}{2}, \frac{1}{20})$, and; **d** $(\frac{1}{2}, \frac{1}{2})$. Note that the bath is not symmetric with respect to the swapping of the qubits, as there is a stronger interaction of the bath with the second qubit relative to the first qubit. The populations are represented as $n_{00} : \circ$ (blue), $n_{01} : \triangle$ (green), $n_{10} : \times$ (purple), and $n_{11} : +$ (cyan). 170

8.6 Demonstration of a $|00\rangle \leftrightarrow |11\rangle$ eigenstate transition in the simulated time evolution of a correlated two-qubit system. Simulated evolution for time t on ibmq_bogota where the timestep $\tau = 1/3$, and the Hamiltonian is composed of three variable frequencies ω_i, $\hat{H} = \omega_1\sigma_z^1 + \omega_2\sigma_z^2 + \omega_3\sigma_z^1\sigma_z^2$. **a** Using $\omega_3 = 1$, and $\omega_1,\ \omega_2 = \frac{1}{2}$, the system demonstrates expected exponential decay to the thermally mixed state. **b** With $\omega_3 = 1$ and frequencies, $\omega_1 = \frac{1}{10}$ and $\omega_2 = -\frac{1}{20}$, the difference in populations (relative to the decay seen in **a**) show a *correlated* two-qubit transition between the $|00\rangle$ and $|11\rangle$ eigenstates. The populations are represented as $n_{00} : \circ$ (blue), $n_{01} : \triangle$ (green), $n_{10} : \times$ (purple), and $n_{11} : +$ (cyan). 172

8.7 Different trajectories for two frequencies, $\omega = 0.5$ (blue) and $\omega = 0.1$ (green), with three varying Hamiltonians: (a) $H_0 = \omega\sigma_x$; (b) $H_0 = \omega\sigma_y$, and; (c) $H_0 = \omega\sigma_z$. Points were taken after 5 gate applications with each gate equal to $\tau = 1/3$. . . 176

8.8 T_1 times for the simulated system (vertical axis, unitless), and the ibmqbogota device. For the simulated system, the $\exp[i\tau\hat{H}]$ operator was implemented 600 times, where $\hat{H} = \sigma_z$ ($\omega = 1$). 2^{11} measurements were taken for each experiment. 177

9.1 For a 1-qubit Hamiltonian the solution of the quantum ACSE converges to the ground state, indicated by v_-, in about 8 iterations on a 1-qubit IBM quantum computer. 194

9.2 For the H_2 molecule the figure shows (a) the energy at each iteration in the solution of the ACSE at an internuclear distance R of 2 Å and (b) the energy dissociation curve of the molecule. The error in the ACSE on the quantum computer, due to noise, is fairly uniform throughout the dissociation, indicating that the ACSE captures the spin entanglement. 194

9.3 The error in the potential energy curves from the equal-bond dissociation of the H_3 molecule are shown for the classical and quantum solutions of the ACSE where the state is simulated on a quantum computer. The quantum solution to the ACSE is more accurate by 6 orders of magnitude. Errors are relative to the exact solution (from full configuration-interaction). Dotted line indicates "chemical accuracy" (1 kcal/mol). 195

9.4 Expanded from Figure 2 in the main text, and includes the noise model as compared with the experimental results. For the H_2 molecule the figure shows (a) the energy at each iteration in the solution of the ACSE at an internuclear distance R of 2 Å and (b) the energy dissociation curve of the molecule. The error in the ACSE on the quantum computer, due to noise, is fairly uniform throughout the dissociation, indicating that the ACSE captures the spin entanglement. 200

10.1 The quantum-ACSE algorithm. After initializing the state (0), we begin an iterative process of obtaining the ${}^2A$ elements (1) using a quantum (QPU) or classical (CPU) processor, which will have errors in the series expansion ($O(\delta^2)$), a higher measurement cost ($O(r^6)$), or errors from the 3-electron reduced cumulant matrix (${}^3\Delta$). After checking for convergence against a threshold x (2), we construct the next ansatz (3), and optionally perform a classical minimization against the step size. Finally, we measure the new 2-RDM (4), and proceed to (1) until we converge or $n = n_{\max}$. 214

10.2 Error mitigation scheme to obtain corrected 2-RDMs. We first take a set of instructions, and construct the appropriate circuit design. We run these on the quantum computer to obtain a set of measurement results which are then corrected through the inversion of a state preparation matrix (SPAM, small hatched rectangle). Measurements corresponding to diagonal elements of the 2-RDM (M_i^c) will commute with the $\hat{N}$ and $\hat{S}_z$ symmetries, and so are projected onto the proper operator space. We then apply our shift correction, Γ_n, which also preserves trace but can introduce negative eigenvalues, and optionally, a purification of the 2-RDM. 215

10.3 Molecular orbital diagram and natural-orbital occupations of the highest and occupied lowest natural orbitals for ortho-, meta-, and para-benzyne. Geometries for the ortho- and meta- isomers were obtained from reference [80] and optimized with spin-flip time dependent density functional theory (SF-TDDFT), and the para- isomer was obtained from reference [81] and optimized with spin-flip coupled cluster with singles and doubles (SF-CCSD). 220

10.4 Overview of results shows active space calculations for the different configurations of benzyne across several methods, including Hartree-Fock, CASSCF, and QACSE for [2,2] and [4,4] active spaces. The 3- and 4-qubit results utilize the limit-preserving correction (L) and purification (+) schemes of error mitigation. The data corresponds with results taken in Table 10.1. 221

10.5 Comparison of the truncation used in the ${}^2K$ matrix for ortho-, meta- and para-benzyne, with respect to the resulting accuracy given in the representation against the CASSCF result. Additionally, the number of symmetries found (i.e., the nullity of the generator) is reported next to the appropriate marker. 236

10.6 Two optimization attempts for (a) ortho-, (b) meta-, and (c) para-benzyne configurations with and without the ${}^2\Gamma$ preserving correction showing the first 5 iterations. In the meta-isomer case without the ${}^2\Gamma$ correction, unfavorable steps in choosing ϵ_n are rejected and so the run plateaus after the first step. 244

11.1 Unencoded CQE algorithm. Given some initial state that we can prepare on the quantum computer, we alternate between solving the unencoded ACSE on the quantum computer, and updating the new wave function given information from the unencoded ACSE. 260
11.2 Depictions of the quantum ACSE with an unencoded ${}^2_Q A_n$ ($\times$) and an encoded ${}^2A_n$ ($\circ$) for linear H_4, H_5, H_6 and hydrogen fluoride at equilibrium bond distance (in the STO-3G basis). For most systems, nearly identical rates of convergence are obtained with similar accuracy. 267
11.3 Dissociation plots for 8 qubit simulations of H_4 and a 6-electron and 4-orbital active space of O_2 with the encoded and unencoded CQE. Convergence criteria is 0.001 for the norm of the ${}^2B$ matrix which contains a correction to the ${}^2A$ matrix from a second-order approach. A quasi-Newton quantum CQE approach which adjusts the step direction based on a limited-memory Broyden-Fletcher-Goldarb-Shanno (BFGS) approach, where 2 or 3 vectors are stored. More details regarding this method will be presented in a subsequent work. Both the encoded and unencoded CQE exhibit similar accuracy at both equilibrium and non-equilibrium geometries. 268
11.4 Comparison of total resource count (given in $\log_{10}$ number of CNOT gates required) for equilibrium (left) and non-equilibrium (right) H_4 geometries, mirroring data seen in Table 11.2. The vertical axis contains information on whether encoded or unencoded operators are used, as well as the sparsification of ${}^2A$. The horizontal axis indicates the p-depth, or the number of previous iterations in the Ansatz to which terms are added. The resource count also accounts for the number of fermionic energy and gradient evaluations. 272
11.5 (Left) Effective scaling of the tomographic complexity of the qubit-particle and fermionic ${}^2A$ matrices (under the Jordan-Wigner transformation) with symmetry projection of $\hat{N}$ and $\hat{S}_z$. The top and bottom black bars represent estimates of the complexity from the number of terms ((Right) the number of vertices per measurement group under a coloring scheme. In particular, while this number is constant for fermionic tomography, for the qubit operators this number increases at a nearly exponential rate. 273

12.1 Comparison of methods for generating $\hat{P}$ at different H $-$ H distances for H_4. Near equilibrium, similar patterns can be seen, but away from equilibrium, gradient-descent-based approaches slow down considerably. In particular, when optimizing the 1-d step size according to a quadratic fit, an oscillatory pattern can be seen in the norm of ${}^2A$, indicating a potential valley in a direction between the oscillating gradients. The conjugate gradient approach allows for slightly more flexibility but exhibits stronger oscillations in the gradient. The quasi-Newton approaches offer quick convergence across all regions of dissociation. 295

12.2 Low threshold ($||^2 A|| = 10^{-5}$) results for varying values of sparsity with different $p-$depths and acceptance criteria, utilizing the BFGS optimizer for molecular H_4 at the intermediate distance ($D = 1.5$ Å), with the DESCENT condition. In the top two plots, we use ACCEPT = True, where elements below the sparsity threshold are automatically included if they are in included in one of the previous $p-$terms. The bottom plot has ACCEPT = False. Only the first 125 iterations are shown. . 299
12.3 Simulations of molecular H_4 and H_6 for separations of 1 Å, and 2 Å utilizing the CQE, VQE, and ADAPT-VQE with a BFGS optimizer. For H_4 a minimal ansatz is reached in the ADAPT through the VQE subroutine, and for H_6 the CQE algorithm slightly outperforms the ADAPT. VQE, here using the UCCSD anastz, provides rapid convergence for near equilibrium states, but has significant errors at larger separations, which are overcome by the iterative ADAPT-VQE and CQE algorithms. 301
12.4 Simulations of molecular lithium hydride at a separation of 2 Å utilizing CQE, VQE, fermionic ADAPT-VQE and the iterative qubit-excitation based ADAPT-VQE (IQEB), essentially a unencoded APAPT-VQE algorithm. The upper-left shows the macro iterations of each scheme, which are nearly identical for the encoded and unencoded forms, and are only slightly slower for the ADAPT. The upper-right shows the total iterations, including micro iterations in the VQE procedure with a threshold of 10^{-3} in the parameter vector. The lower-left compares the energy convergence with the ansatz cost, showing that the ADAPT does produce a more compact representation of the ansatz. The lower-right shows the number of parameter evaluations (a lower bound on the number of gradients evaluated at each optimizer step), which is linear scaling with the ACSE procedure but for ADAPT becomes quadratic with respect to the number of iterations. . . 304

13.1 (Left) Energy convergence of hydrogen chains compared with Full Configuration Interaction results. (Right) Obtained values of the HCSE residual and calculated variances (from a simulation of the full density matrix) obtained during the iterations. 321
13.2 Comparison of accuracy of linear H_4 (in a minimal basis set) dissociation to the full configuration interaction energy. Comparison is at different residual cutoffs for different methods of preparing the non-unitary evolution. (Top) Exponential prepared through least-square fit to find anti-hermitian two-body operator. (Center) Method of single-ancilla infinitesimal evolution with resets occurring at each measurement. (Bottom) Method of single-ancilla infinitesimal evolution, but compacts $\hat{P}_n$ operators at each iteration until the energy no longer decreases. Resets occur less frequently. While there exist differences in the implementation, the level of accuracy is the same throughout each. 323
13.3 Simulations of square H_4 (in a minimal basis set) at different bond lengths for different CSE methods as well as the ACSE. Distances were taken at 1.5 Å, 2.0 Å, 2.5 Å, and 3 Å(ordered top to bottom, left to right). A minimal basis set was used. Notably, when not using reset options, some operators converged to excited states in several of the cases. 324

LIST OF TABLES

4.1 Calibration Data. Calibration data from the primary and secondary algorithms on IBM's quantum computer is presented. 68

5.1 Contains calibration info for the 5 transmon qubit device, denoted as IBMQX Tenerife, Raven, or ibmqx4. Included are the readout errors for the qubits and the single and multi-qubit gate errors for each date. In general, the qubits were selected so as to have minimal error on the device. Qubit connectivity is directional with the first qubit indicating the control and second qubit indicating the target. 102

6.1 Shows the area between the two occupations (V) obtained for the entangling circuit described in the text for the two different quantum devices. The V_i and $V_{i'}$ values were calculated separately. Here we have the 5- and 14-qubit devices, respectively, given in a 95% confidence interval due to sampling. The left column indicates the values of with the different applied symmetries. 119

6.2 Calibration data for the ibm-5 and ibm-14 devices during benchmarking. U_2 and U_3 represent the errors for single qubit unitaries containing one and two $X_{\pi/2}$ pulses and two and three frame changes respectively. RO represents the readout error, and we have the standard T_1 depolarization and T_2 dephasing times. $[j]$ specifies the target qubit with control qubit i, and we report the error. 125

7.1 Example procedure for finding a set of symmetry projected operators. The vector representation of $\hat{A}$ is given as $\vec{A}$. 137

7.2 Dimension of the number of nonzero elements required for tomography of the 1- and 2-RDMs in the traditional (naive) and symmetry projected (reduced) approaches for given spin and spatial configurations of the second quantized measurement operators with $\hat{N}$, and $\hat{S}_z$ symmetries under the Jordan-Wigner transformation. We also give examples of the sets of operators in the naive (N) and reduced (R) methods corresponding with operators marked with a ($*$). Note, R is not unique in any of these cases. The cases including the $\hat{S}^2$ symmetry do not greatly affect the results, but require covering the many permutations of the spatial orbitals. A bar across spins indicates an excitation or de-excitation between these orbitals, and only the unique spin configuration is shown. $\times$ indices the Cartesian product of two sets. $\vec{Z}$ indicates a tensor product of Z gates which is constant across all operations. 139

7.3 A comparison of 2-RDMs of a two-electron system under varying levels of simulated noise (simulated and experimental) through the Frobenius norm of the difference matrices at randomly sampled points. ${}^2D$ refers to the ideal 2-RDM, ${}^2\tilde{D}$ refers to standard tomography of the 2-RDM under a noise model, and ${}^2\tilde{D}^c$ refers to the 2-RDM constructed from symmetry projected tomography under a noise model. Values represent averages of the Frobenius norms of difference matrices over 25 random states of H_2 in a minimal basis where the ansatz includes 3 parameters. In general, the differences between the noisy tomography methods are consistently much smaller than the difference to the ideal state, and are almost indistinguishable from stochastic effects (seen at the $n = \infty$ limit). More details regarding these results are included in Appendix 7.5. 142
7.4 Calibration data for the ibm-bogota device taken on November 2^{nd}, 2020, from benchmarking. U_2 and U_3 represent single qubit gate errors containing one and two $X_{\pi/2}$ pulses and two and three frame changes respectively. $\text{RO}_{i|j}$ represents the probability of measuring the state i given a prepared state j. T_1 and T_2 are the given thermal relaxation times for each qubit. Frequency refers to the qubits opeartional frequency, and influences the excited state population based on the device temperature. $[j]$ specifies the target qubit with control qubit i, and the number in paranthesis after each entry in the CNOT column indicates the gate length. The gate lengths for the U_2 and U_3 gates were 35 ns and 71 ns respectively. 149

8.1 Rate of population change for different frequencies for the local two-qubit Hamiltonian. Rate of population change for eigenstates n_{ij}, where ij are indices (corresponding to the computational basis), immediately after initialization for the two qubit system depicted in Fig. 8.5, where $H = \sigma_z^1\omega_1 + \sigma_z^2\omega_2$, and time step $\tau = \frac{1}{3}$. The rate was averaged over 15 time steps. The strongest bath interaction is related to a small frequency ω_1, which when isolated or in conjunction with ω_2 has strong enough coupling to induce state transitions. The only significant increase in the n_{11} state occurs when a low transition frequency is available for both qubits. Additionally, these rates are substantially lower than what is observed in the single qubit system, which corresponds with the better gate fidelities for this system (see Section 8.4). 169
8.2 Calibration data for ibmq armonk taken over several days. Figure 8.1 and 8.2 were generated using data from 09-18-20, and Figure 8.3 and Figure 8.8 were measured between 11-12-20 and 11-13-20. 178
8.3 Calibration from IBMQ Rome on 11-17-2020, used to generate Figure 8.4 in the main text. 178
8.4 Calibration data from ibmq-bogota, taken on 09-16-2021. See Figure 6 in the main text. 179
8.5 Single-qubit calibration data from ibm devices, taken on 09-18-2021. See Figure 3 in the main text. 179

9.1 Quantum ACSE algorithm for 2-RDM optimization. A classical solution of the ACSE with a reconstruction of the 3-RDM can be substituted in Steps (1-2) yielding a hybrid quantum-classical algorithm (denoted later as the Classical ACSE). 193
9.2 Calibration data for the ibm-5 and ibm-1 devices during benchmarking. U_2 and U_3 represent the errors for single qubit unitaries containing one and two $X_{\pi/2}$ pulses and two and three frame changes respectively, as well as the duration of the pulse. RO represents the readout error, and we have the T_1 depolarization and T_2 dephasing times. $[j]$ specifies the target qubit with control qubit i, and we report the error. For the ibm-5 device, U_2 gates were 35 ns, and U_3 gates were 71 ns. For ibm-1, U_2 gates were 142 ns, and U_3 gates were 284 ns. 201

10.1 Relative energies between the configurations of benzyne with classical CASSCF and QACSE methods for differing active spaces and levels of error mitigation, in kcal/mol. [0,0] active space refers to the initial Hartree-Fock calculation. M refers to a state preparation and measurement error, P to the application of the number projection, L to the use of the ${}^2\Gamma_n$-correction, and + to the SDP corrected state. 223
10.2 Difference in energy between the QACSE methods including various error mitigation schemes and the CASSCF result in millihartrees (mhartree). 223
10.3 Largest natural-orbital occupation numbers for the CASSCF results and the purified, ${}^2\Gamma$-corrected results for the [2,2] and [4,4] active spaces on the quantum computer. In each case, the para-benzyne solution exhibits biradical character in the highest occupied and lowest unoccupied natural orbitals, though to differing degrees based on the method. 224
10.4 Energetic error results (millihartrees) for different convergence thresholds and qubit representations for the QACSE with a quantum solution of the ACSE (or measured 3-RDM) for the ortho-, meta-, and para-benzyne configurations. The number of qubits refers to the qubit-representation and related symmetries utilized, which for ortho and meta have non-zero errors. Values of $|{}^2|A||$ refers to the convergence criteria, which is the norm of the ${}^2A$ matrix. 238
10.5 Error in energy results (millihartree) for different convergence thresholds and qubit representations for the QACSE algorithm with a reconstructed 3-RDM. The number of qubits refers to the qubit-representation and related symmetries utilized. Instead of the norm of the ${}^2A$ matrix, we use a trust region and energetic increase stopping criteria. We also indicate where or not all of the elements of the ${}^2A$ matrix are implemented. 239
10.6 Calibration data for the IBMQ Rome device taken on November 11^{th}, 2020, from randomized benchmarking of the qubit gates. The gate lengths for the U_2 and U_3 gates were 35 ns and 71 ns respectively. 241
10.7 Calibration data taken for IBMQ Bogota from December 4^{th} to 7^{th}, 2020. from benchmarking. See Table 10.6 for descriptions. The gate lengths for the U_2 and U_3 gates were 35 ns and 71 ns respectively. 242

10.8 Calibration data taken for IBMQ Santiago from August 24^{th}. The gate lengths for the $\sqrt{X}$ and X gates are both 35 ns. Santiago was used to calculate the 3-qubit meta-isomer calculation. 242

11.1 Comparing the p-depth and differing values of SPARSE$[c]$ (for ${}^{2}_{F}A$ and ${}^{2}_{Q}A$ in terms of their elements relative to the largest element) for two different lengths of H_4, in terms of the maximal CNOT gate count and number of iterations (in brackets, $[\cdot]$). A stopping criteria of 0.01 is selected for the gradient, and a quadratic trust-region step is used for choosing the step length at each step. For each instance, a similar accuracy is achieved in the fermionic and qubit cases, and for the most part, the qubit results displays a constant reduction in the number of necessary CNOT gates. 270

11.2 Upper bounds on the number of CNOT gates for evaluation of the residuals of the unencoded and encoded ACSE on the quantum computer for numerous systems. The hydrogen chains ($H_2 - H_{12}$ are in a minimal basis, with the exception of H_2 (DZ), which has a double zeta basis set. *Trotter* (or Trot.) refers to a first-order trotterization, *CD* $\langle$CNOT$\rangle$ to the average number of CNOT gates per decomposed term in the Cholesky decomposition, and *Order* refers to the number of terms in the Cholesky decomposition. We use a threshold of 10^{-6} in the Cholesky decomposition, but more (or less) strict truncations can be taken. The bottom portion of the graph refers to the effective scaling in terms of total number of applied CNOT gates. 275

12.1 Quasi-Newton CQE algorithm. 290

12.2 Conjugate Gradient CQE algorithm. 292

12.3 Reported number of iterations and CNOT gates (in brackets, $\times 10^3$) for approximate implementation schemes for the CQE with BFGS optimizer with linear H_4 at a distance of 1.5 Å. We varied the inclusion of terms in the selection of P (sorted by either $|P^{ij;kl}|$, or by the descent condition), the manner of truncation of P, as well as varying the sparsity and the $p-$depth for each condition. $*$ represents a run that did not converge, and $\times$ indicates runs that reached the maximum iterations (300). 297

12.4 Comparisons of total iterations, total CNOT gate count, and average CNOT gates per iteration for unencoded and encoded CQE using the BFGS optimizer for H_5 at various bond distances from equilibrium in the minimal STO basis. The accuracy of both approaches is largely similar across the dissociation curve, though for +1.00 and +1.25 distance separation, the unencoded CQE requires more iterations. 300

12.5 Comparison of gradient element (VQE) and residual element (ACSE) evaluations for the CQE, VQE, and ADAPT-VQE methods, corresponding to simulations for molecular H_4 and H_6 at separations of 1 Å, and 2 Å. Note the ADAPT-VQE here has a symmetry adapted pool of operators, which are not implemented here in the CQE or VQE approaches. The VQE tolerance is also taken to be quite low, i.e. 10^{-3} in the norm of the parameter vector (whereas the VQE subroutine in the ADAPT procedure is generally lower). 302

13.1 CQE algorithm for solving the CSE (HCSE). 317

ACKNOWLEDGMENTS

This thesis describes research between my advisor David A. Mazziotti and myself over the last five years. Without him, I likely would not have delved into quantum simulation, and I am extremely grateful for his support, mentorship, and encouragement throughout this entire time. I also would like to thank Profs. David I. Schuster, Sabre Kais of Purdue University, and Laurie J. Butler, all of whom I had the honor of working with. I also am grateful for Prof. Guilia Galli, who along with David Schuster and David Mazziotti are committee members. The work I have done has also been in direct collaboration with fellow students Dr. Jan-Niklas Boyn, LeeAnn M. Sager, and Dr. Preston Scrape. I also have received support as well from the Mazziotti group, Dr. Shayan Himmatayan, Dr. Anthony Schlimgen, Dr. Kade Head-Marsden, Dr. Mannas Sajjan, as well as Dr. Simon Ewing, and Danny Gibney. I am also grateful to the IBM Quantum team, for providing consistent and easily accessible quantum devices over the duration of my studies.

Outside of the hours spent in research, on campus, or at home in the midst of the novel Coronavirus pandemic, I am indebted to my wife, Mary, who has been concurrently pursuing a Ph.D. in Health Policy and Economics at the University of Illinois in Chicago and who bravely charted a new course in Chicago with me. I also would like to thank Dr. Long Pan of Colgate-Palmolive Co., whose mentorship and guidance are still with me. Of course, my parents, Will and Cate, have provided unwavering support, and I am very grateful for the many mathematical-oriented conversations with my brother, Stephen. Michael and Judy, Mary's parents, have also been immensely supportive, and the thesis would not have been put together without Judy's support.

Finally, I would like to thank the many Christians I have met and have had fellowship with at the University of Chicago, particularly the Christians on Campus RSO, as well as the church in Chicago, all of whom have been of immense support to my family and our overall well-being. My thanks are to Christ Jesus, *"in whom all the treasures of wisdom and*

knowledge are hidden." To Him be the glory.

ABSTRACT

Chemical and molecular phenomena are central to understanding the composition of the physical universe. These mechanisms arise from quantum mechanical laws, which depict molecular systems as complex quantum states and can be rigorously investigated through first-principle calculations. Unfortunately, the most accurate attempts at these calculations are prohibitively costly from a computational perspective. In theory, some of these problems can be alleviated through a quantum computer, which utilizes a quantum mechanical state as its basic element. In practice, current-generation quantum computers are limited by noise, and so new algorithms and approaches have to be developed. The reduced density matrix allows us to efficiently characterize quantum states, as well as identify features of the obtained state. Additionally, these techniques provide insights into new algorithms and sources of error mitigation. In this work I explore the use of near-term (noisy, small to intermediate scale) quantum computers and the use of the two-electron reduced density matrix as a framework for tackling this problem. The importance of N-representability for error mitigation is seen from a number of perspectives. Additionally, a class of quantum contracted eigensolvers, which solve a contraction of the Schrödinger equation, are presented. These provide polynomially scaling approaches for highly accurate computations on near-term devices.

PREFACE

> The ability to reduce everything to simple fundamental laws does not imply the ability to start from those laws and reconstruct the universe...The behavior of large and complex aggregates of elementary particles, it turns out, is not to be understood in terms of a simple extrapolation of the properties of a few particles.
>
> Anderson, P. W. (1972). More Is Different.
> Science, 177(4047), 393–396.

> We can give up on our rule about what the computer was, we can say: Let the computer itself be built of quantum mechanical elements which obey quantum mechanical laws.
>
> Feynman, R. P. (1982). Simulating physics with computers.
> Int. J. Theor. Phys, 21(6–7), 467–488

Quantum chemistry emerged nearly a century ago following the advent of the theory of quantum mechanics. Prior to this, numerous theories existed which reasoned that molecules and atoms were discrete, and not infinitesimal objects; however, an exact theory of their true nature was not yet developed. Once the quantum mechanical postulates were firmly established, some thought that the generalization from fundamental particles to molecules and all of chemistry could be seen (and possibly easily solved) naturally.[1] At the same time, it was also clear that the problem was complicated, and despite optimism towards some approximate quantum mechanical treatment, actual chemical oriented calculations were limited.

In 1927, Heitler and London used the equation of Schrödinger to describe the interac-

tion present in the hydrogen molecule. The agreement with chemical reality led to its wide adoption and the formation of so called valence bond theory, and their work is recognized as the genesis of the field of quantum chemistry. Over the last century, the field has advanced steadily with increasingly powerful computational resources, allowing more and more challenging problems to be tackled. Current quantum chemistry methods are used in tandem with experimental results to help understand chemical reactions and dynamics, construct or assist in new material design, screen for viable synthetic candidates in biochemical problems, and many other applications. Methods range from near exact treatments and first principles calculations, to schemes where approximate quantum chemical calculations are used as a seed or kernel within a much larger framework.

Despite the success of conventional theoretical chemistry methods, problematic systems and environments remain. While we typically portray classical objects with their position and velocity, quantum mechanical objects are portrayed by their wavefunction or state. A key element of quantum mechanics not present in classical mechanics is that of entanglement - that is, a relation between two states such that their dependence on one another can never be separated in any frame of reference (see treatments on the double-slit experiment [2]). While the term superposition might be more widely understood, as a quantum state can exist as a quantum mechanical superposition of different states, sometimes these superpositions can be resolved trivially through a different frame of reference, and are not entangled. For molecular systems, the idea of entanglement can be related to the commonly used basis of Slater determinants states (which themselves are composed of products of orbitals). When a molecular systems is essentially described by a single state we can treat it with a single-reference (or a single state) method. Reasonable (polynomial scaling) approximations can expand upon this single-reference and create broadly successful solutions. We also describe the electrons as having a *dynamic* correlation, where we are primarily interested in finding the contributions of many states to our dominant single state. Methods such as density

$$|\psi_H\rangle = |\phi_{1s\alpha}\rangle = \frac{1}{\sqrt{\pi}} a_0^{-\frac{3}{2}} (e^{-\frac{r}{a_0}}) \tag{1}$$

Figure 1: A single-reference state used to represent the 1s orbital, representing the lowest quantum number solution to the hydrogen atom from the Schrödinger equation. Spatially, this corresponds to a normalized and integrable function depending on the electron coordinate r.

functional theory and coupled cluster serve as prime examples of successful single-reference methods. The properties and most stable state (or ground state) of many molecules are described by single-reference methods.

When the state of interest is not primarily from a single-reference, we require a class of methods called multi-reference methods. The problem then is that the states (and the electrons themselves) experience a correlation (which is in essence related to the notion of quantum entanglement), and so multiple states are needed to describe basic approximations to the state. The electrons in these circumstances are said to have a sort of static correlation - possibly implying that regardless of how electrons are excited or perturbed off of them, the correlation of these states is static. These states occur quite commonly: in dissociative processes, transition states, metal complexes (where exterior electrons in higher spin-angular momentum orbitals can interact in surprising ways), the formation of condensates, periodic or metallic systems, excited states and many other physical systems.

While the essential problem remains the same - trying to find a representation of a state closest to nature - because (single- and multi-reference) theories are generally described from a certain reference, the derivation of the problems can vary significantly. *In general*, multi-reference methods do not scale as well as single-reference problems. Additionally, the nature of quantum mechanics is such that the exact state (which we represent with a finite number of orbitals in space) scales exponentially with regards to the number of electrons and orbitals. This means that often times the exact answer can only be obtained at an exponential cost.

The challenges associated with simulating strongly-correlated molecular systems have

$$|\psi_{\mathrm{H-H}\infty}\rangle = \frac{1}{\sqrt{2}}|\phi^A_{1s\alpha}\phi^B_{1s\beta}\rangle - \frac{1}{\sqrt{2}}|\phi^A_{1s\beta}\phi^B_{1s\alpha}\rangle \tag{2}$$

Figure 2: Describing stretched hydrogen as a pure singlet requires two states (or, multiple references) which cannot be rotated or expressed as a single-state. This is equivalent to the well known Bell state, exhibiting genuine quantum entanglement.

prompted numerous new methods and techniques. One approach is built upon two observations. First, in quantum mechanics, particles are indistinguishable. This is simply to say that we cannot put a label on electron one or electron two, and then keep track of each individual electron, and simply must say that a system has two electrons. There is no distinguishing feature between electrons. Second, the electrostatic interaction in molecular systems is pairwise, meaning the force they experience can be summed in terms of individual forces from all other electrons. Thus if we can describe *any pair* of electrons in all space, we can then describe our entire system. This leads to a group of methods called reduced density matrix methods, where we integrate our state over all but two electrons to yield a two-electron reduced density matrix. As a gross simplification, because these methods do not describe states but the pair of electrons in space, they are in many ways agnostic to whether a problem needs a single state or multiple states. Regardless, in moving from a known state (or wavefunction) to a reduced density matrix, we introduce the N-representability problem (or quantum marginal problem). The question of having a method that is accurate and reliable across broad classes of molecular systems is still somewhat open. In particular, strongly correlated many-body systems remains are a challenging domain in quantum chemistry.

In 1982 the physicist Richard Feynman proposed another approach for simulating problems of physics (and thus chemistry) [3]. A classical computer, which has a determined state (i.e., a string of bits 10001010100), is well suited to describe certain classical problems where the state of the physical system is well known. However, in quantum mechanics, there are many possible states with certain probabilities that have to be accounted for. During a

lecture at Caltech, Feynman proposed a method of simulating quantum mechanical systems, which was to use a quantum mechanical object to simulate another quantum mechanical object, one of the first ideations of a quantum computer.

Outside of the problem of physical simulations, interest in the computational power of a quantum computer was also an open question. Work by Deutsch and Jzosa in 1992 provided an instance of an algorithm that a quantum computer was decidedly faster than a classical one. In 1994 Peter Shor[4] at Bell Labs provided an instance of an algorithm for prime factorization on a quantum computer that had an exponential scaling advantage over any known classical algorithm (often referred to as a quantum advantage). These results, as well as work in quantum error correction and the notion of a fault tolerant quantum device,[5–7] became driving factors in the development of quantum computers and quantum algorithms.

To affirm Feynman's hypothesis, Seth Lloyd in 1996[8] introduced a method which showed that certain classes of physical systems could in fact be simulated exponentially quicker on a quantum computer than on a classical one. The particular system is one which has a $k-$local-interaction - that is, the force which a particle experiences depends on at most k other particles. As molecular systems are described by the attractive and repulsive laws of electrodynamics, a molecular system, which has kinetic energy of the nuclei and electrons, a proton-proton repulsive force, a proton-electron attractive force, and a electron-electron repulsive interaction, can indeed *in principle* be simulated efficiently on a quantum computer. Despite that in principle this is possible, methods of preparing ground states and a general solution to the Schrödinger equation on a quantum computer were not clear. DiVincenzo in 2000[9] hypothesized a set of five criteria (see Fig. 3) which would be necessary for a fault-tolerant quantum computer. Over the last two decades several of these criteria individually or in groups have been met [10], but not all simultaneously. Because the qubit is quite a general idea, many different quantum systems can be used to construct one, such as superconducting systems, ion-traps, spin-$\frac{1}{2}$ systems, and others[7]. Certain designs are more

Figure 3: DiVincenzo's five criteria for a universal quantum device.

1. A scalable physical system with well characterized qubits
2. The ability to initialize the state to a simple fiducial state
3. Long relevant coherence times, longer than the gate operation times
4. A "universal" set of quantum gates
5. A qubit-specific measurement capability

amenable to scaling. Producing an initial state requires extremely cold systems for most architectures, and the length of time for a system to 'reset' can provide a challenge. The coherence time greatly depends on the architecture, and will always be relative to the time scale of other operations. Numerous sets of universal gates are known as well, which in general require (near) complete control over a single qubit, and then a specific type of interaction between pairs of qubits. General operations on multiple qubits can be deconstructed in terms of these smaller ones to obtain a universal set of gates. In practice, single-qubit gate errors are already quite small for many systems, and the two-qubit gate seems to be the most challenging. Physical operations that can entangle two-qubits are generally induce some of the highest errors while additionally being very critical components for constructing nontrivial entangled states. Measurement also is challenging - in current generation devices measurement errors are some of the largest. Fast measurement relative to the device timing is also important for considering large scale implementations requiring a large number of measurements. While the level of accuracy for each of these aspects might seem impossible to hold simultaneously, once a certain threshold is reached, the quantum computer (similar to a classical computer) could potentially be able to detect and correct its own errors.

In 2010, Aspuru-Guzik et al. used a photonic quantum computer to calculate the energy of molecular hydrogen using quantum phase estimation and Hamiltonian evolution[11]. However, even at that time it was clear that simpler algorithms would be needed for use in noisy devices. In 2014 the variational quantum eigensolver was introduced by Guzik et al. again, with a two-qubit system[12]. This introduced the first quantum-classical algo-

rithm - preparing a state on a quantum computer and optimizing parameters on a classical computer. Kandala et al. at IBM in 2017 demonstrated a four and six-qubit simulation using the variational quantum eigensolver with superconducting qubits[13]. Around that time, the IBM Quantum Experience launched, providing open access for the public as well as researchers to run simple commands on quantum computers. The success of these simulations on noisy quantum devices bolstered efforts to simulate quantum mechanical systems. Indeed, particularly in the era of noisy intermediate scale quantum (NISQ) devices, quantum chemistry and quantum simulation are seen as areas which could benefit from pre-fault tolerant quantum computers.

The similarities between calculations carried out on current generation quantum devices and those undertaken at the beginning of the computing era are worth noting. Access to computational resources was not universal, the computational power of devices was not well established, and algorithms and techniques had to be suited for the applications at hand. The scope of problems, however, was quite different. In the early years of quantum chemistry, most research tried to establish theoretical explanations behind experimental results, such as exploring the nature of bonding or the interactions of molecules with light (spectroscopy). The nature and choice of a suitable basis (which is now taken for granted) was not yet established. In the era of quantum computing, we instead are trying to probe the usefulness of quantum computers and ascertain ways to maximally utilize an emerging technology. A key distinction is the rate of scaling. Moore's law as applied to quantum computing is almost unfathomable, as if quantum computers were even to reliably improve by even a linear number of qubits per year, the growth in capability and the relevant problem scopes would improve exponentially. Thus, the current era of quantum simulations seems to be expanding upon already known results, but could quickly lead to a paradigm shift in physical simulations.

In this thesis I highlight the role of the reduced density matrix in quantum simulations of

molecular systems, particularly for simulations on NISQ devices. This is partially motivated by the fact that in most algorithms for near-term quantum computers, we often are interested in measuring a form of the reduced density matrix. Because it is measured directly from the state, no approximations are made. Part of this work highlights the importance of $N-$representability (as well as spin $S-$representability), and its relevance to both molecular simulations and the success or failure of different error mitigation strategies on quantum devices. These observations allow for numerous accurate simulations of small molecular systems on near-term devices. I also introduce algorithms and error mitigation techniques which are well suited for current and near-term quantum applications. Finally, the contracted quantum eigensolver provides a polynomially scaling algorithm with rigorous convergence for finding good solutions of the Schrödinger equation.

Part I introduces a brief technical background of quantum chemistry methods, reduced density matrix theory, and the theory of quantum simulation. The latter parts cover mostly published work.

Part II investigates $N-$representability in quantum systems and the role of noise in many-body simulations. In chapter 4 we used a quantum device to highlight a pure N-representability constraint for a representation of the 3-electron in 6-orbital system. These constraints are similarly explored as tools for constructing ansatz in chapters 5 and 6. In Chapter 5 we characterize a Mott insulator transition in H_3 for a 3-qubit system using the 3-electron in 6-orbital condition. We also introduce a hybrid quantum-classical algorithm rotating with an orbital rotation step based on a quantum-seeded classical step. Chapter 6 investigates a 2-electron ansatz, which has a known exact form for any amount of orbitals, as a source of error mitigation as well as a benchmark for noisy devices. In particular, we utilize it to benchmark two IBM systems and show the importance of the number and projected spin symmetry. Chapter 7 discusses an efficient tomography of fermionic operators. The application is inspired by finding a minimal set of operators needed to measure a fermionic

operator, and reduces the number of measurements needed through a process called symmetry projection. Chapter 8 is not explicitly derived in terms of reduced density matrices, but instead develops a way of studying noise and considers the effect of noise on the simulated quantum system. Because the work deals with small systems, generalizations to larger systems naturally require reduced density matrices. Chapter 10 also utilizes the ensemble N-representability conditions as a source of error correction, presenting a generalization beyond the pure $N-$representability constraints seen in earlier chapters.

Part III introduces the class of contracted quantum eigensolvers. Instead of using the variational principle with a parameterizable ansatz, we instead solve a contraction of the Schrödinger equation, which often can be aided or expressed in terms of reduced density matrices. Chapter 9 introduces a contracted quantum eigensolver of the anti-Hermitian contracted Schrödigner equation which has exponential advantages over its classical counterpart. Chapter 11 builds upon work investigating the role of fermionic encoding by introducing an unencoded (or encoding-free) variant of the quantum contracted eigensolver. Chapter 12 introduces ideas from classical optimization theory into the contracted quantum eigensolver, establishing convergence of these techniques. Work involving the anti-Hermitian contracted Schrödinger equation is particularly well-suited for near-term applications, as the CQE for solving the ACSE is easy to implement and can be adapted in a variety of ways. Chapter 10 shows an application of the ACSE method towards resolving the correlated isomers of benzyne, utilizing error mitigation strategies developed in earlier parts and showing a path forward for generalized molecular simulations on near-term quantum computers. Finally, Chapter 13 provides a look at current work, introducing a contracted quantum eigensolver for solving the complete contracted Schrödinger equation with polynomial scaling, which provides an exact condition for eigenstates of the wavefunction and associated reduced density matrices.

References

[1] K. Gavroglou, *Neither physics nor chemistry : a history of quantum chemistry*, edited by A. Simoes, Transformations (M.I.T. Press) (MIT Press, Cambridge, Mass., 2012) description based on print version record.

[2] R. P. Feynman, R. B. Leighton, and M. Sands, *The Feynman lectures on physics; New millennium ed.* (Basic Books, New York, NY, 2010) originally published 1963-1965.

[3] R. P. Feynman, International Journal of Theoretical Physics **21**, 467 (1982).

[4] P. W. Shor, SIAM Journal on Computing **26**, 1484 (1997), arXiv:9508027 [quant-ph] .

[5] S. Aaronson and D. Gottesman, Physical Review A - Atomic, Molecular, and Optical Physics **70**, 1 (2004), arXiv:0406196 [quant-ph] .

[6] D. Gottesman, **2008** (1997), arXiv:9705052 [quant-ph] .

[7] M. A. Nielsen and I. L. Chuang, *Cambridge University Press* (Cambridge University Press, Cambridge, 2010) p. 702, arXiv:arXiv:1011.1669v3 .

[8] S. Lloyd, Science **273**, 1073 (1996).

[9] D. P. DiVincenzo, Fortschritte der Physik **48**, 771 (2000), arXiv:0002077 [quant-ph] .

[10] I. Georgescu, Nature Reviews Physics **2**, 666 (2020).

[11] B. P. Lanyon, J. D. Whitfield, G. G. Gillett, M. E. Goggin, M. P. Almeida, I. Kassal, J. D. Biamonte, M. Mohseni, B. J. Powell, M. Barbieri, A. Aspuru-Guzik, and A. G. White, Nature Chemistry **2**, 106 (2010), arXiv:0905.0887 .

[12] A. Peruzzo, J. McClean, P. Shadbolt, M.-H. Yung, X.-Q. Zhou, P. J. Love, A. Aspuru-Guzik, and J. L. O'Brien, Nature Communications **5**, 4213 (2014), arXiv:1304.3061 .

[13] A. Kandala, A. Mezzacapo, K. Temme, M. Takita, M. Brink, J. M. Chow, and J. M. Gambetta, Nature **549**, 242 (2017), arXiv:1704.05018 .

Part I

Preliminaries

CHAPTER 1

INTRODUCTION TO QUANTUM CHEMISTRY

1.1 Quantum Chemistry and the Electronic Hamiltonian

Quantum chemistry involves the description of chemical processes or systems using theoretical tools, generally either to understand some phenomena or to predict and discover properties of a system. The total objective is to understand the behavior of a system (which we have not yet defined) utilizing the Schrödinger equation.[1, 2] For time dependent processes this is given by:

$$i\hbar\frac{d}{dt}|\psi(t)\rangle = \hat{H}|\psi(t)\rangle \tag{1.1}$$

where the system is described by a wavefunction (in the bra-ket notation of Dirac) $|\psi\rangle$ and a Hamiltonian $\hat{H}$. In general, $|\psi\rangle$ belongs to a Hilbert space, meaning that we can obtain properties like the norm and compare its overlap with other systems (wavefunctions). For time independent processes this leads to the time-independent Schrödigner equation:

$$\hat{H}|\Psi\rangle = E|\Psi\rangle \tag{1.2}$$

which is an eigenvalue equation, and gives stationary states of the Hamiltonian. Given a good enough set of solutions $\{|\Psi_k\rangle\}$, we can predict numerous properties of the system, depending on the scope and scale of the problem. The solutions are often used to seed further computations, whether in large scale simulations, time-dependent dynamical processes, realistic or solvent based simulations, in looking at novel properties of periodic materials, or in reaction dynamics and pathways. In quantum mechanics, the states are usually ordered by eigenvalues of the Hamiltonian. That is, in nature, systems equilibrate towards stable configurations, which are typically dominated by the lowest energy states, or ground states (unless other states are easily accessible, which is not uncommon!).

For a molecular system, we first must describe the Hamiltonian. The total energy is determined by the kinetic energy and electrostatic interactions of the nuclei and electrons. Given nuclei indexed by I and electrons indexed by i, the Hamiltonian is:

$$\hat{H} = -\sum_I \frac{1}{2M_I}\nabla_I^2 + \sum_{I<J} \frac{Z_I Z_J}{r_{IJ}} - \sum_i \frac{1}{2}\nabla_i^2 - \sum_{Ii} \frac{Z_I}{r_{Ii}} + \sum_{i<j} \frac{1}{r_{ij}}. \tag{1.3}$$

where we are in atomic units, Z_I refers to the atomic charge, M_I to the nuclear mass, and r_{ab} gives the distance between two particles. In practice this is challenging to solve, particularly because the nuclei have substantially more mass than the electrons and there are multiple scales of problems here. Additionally, we often have some experimental data on the position of the nuclei, or are seeking some insight on a given configuration or orientation of the molecule. Thus, we generally attempt to separate the nuclear and electronic degrees of freedom. [3, 4] Given a configuration $\vec{R}$ of nuclear coordinates and $\vec{r}$ electronic coordinates, we can define the electronic Hamiltonian as:

$$\hat{H}_e(\vec{R}) = -\sum_i \frac{1}{2}\nabla_i^2 - \sum_{Ii} \frac{Z_I}{r_{Ii}} + \sum_{i<j} \frac{1}{r_{ij}} \tag{1.4}$$

which will have solutions $|\phi_k\rangle$. Given a set of solutions $|\phi_k\rangle$, and a nuclear solution $|\chi_k\rangle$, we envision a potential solution to the total Hamiltonian:

$$|\psi\rangle = |\phi_k(\vec{R};\vec{r})\rangle|\chi_k(\vec{R})\rangle \tag{1.5}$$

Unfortunately however, $|\psi\rangle$ is not a eigenfunction of the total molecular Hamiltonian as a coupling term (r.h.s.) can be seen:

$$(\hat{H} - E)|\psi\rangle = -\sum_I \frac{1}{2M_I}(|\chi_k\rangle\nabla_I^2|\phi_k\rangle + 2\nabla_I|\chi_k\rangle\nabla_I|\phi_k\rangle). \tag{1.6}$$

The role of the coupling is often ignored due to the large M_i in the denominator. One can also add an adiabatic correction, which is to consider the expectation of the coupling terms for a given electronic state, and then adds this to the nuclear Schrödinger equation. The breakdown of this occurs when there is coupling in the off-diagonal elements, which can occur in situations where there is overlap between the potential energy surfaces. Despite these cases, which are critical for fields with strongly varying nuclear degrees of freedom or close-lying excited states such as reaction dynamics, the electronic Hamiltonian gives us a more reasonable problem that we can begin to tackle molecular problems with.

1.2 First and Second Quantization and Hartree-Fock Theory

To find a solution to the electronic Schrödinger equation, we first begin with a simple system. A one-electron system, such as a hydrogen atom or hydrogen-like system, has an exact analytical solution to the Schrödinger equation.[5] The resultant set of wavefunctions are called the hydrogenic atomic orbitals, and are the basis of the orbital picture of modern chemistry. For anything larger than a one-electron system, the electron-electron interaction in the Hamiltonian does not permit an analytical solution, and we are forced to approximate what a many-body wavefunction would look like.

The variational principle of quantum mechanics says that given a trial wavefunction $|\psi\rangle$, the ground state $|\Psi\rangle$ will always be lower in energy:

$$\frac{\langle\psi|\hat{H}|\psi\rangle}{\langle\psi|\psi\rangle} \leq \langle\Psi|\hat{H}|\Psi\rangle. \tag{1.7}$$

Importantly, this holds for *any* trial wavefunction, so even a poor choice of wavefunction can still give us an energy. If we are able to increase the flexibility of the wavefunction and decrease the energy, then our new state is closer in energy to the ground state.

For our molecular system composed of several atoms, we can take a subset of hydrogenic

orbitals for each atom, and simply make them orthogonal to one another. If we do this in a controlled way with specially constructed basis set types (i.e. containing larger and larger subsets of orbitals per atom), we can extrapolate our properties or result to an infinite (or complete) basis set, in principle solving the electronic Schrödinger equation exactly. Note that *any* basis set that is complete (i.e. that can span the entire Hilbert space in the infinite limit) can be used. For calculations in physics and materials, plane wave basis sets are commonly used, whereas for chemical systems the hydrogenic orbitals serve as an important basis. Despite having a representation of the problem, it is still not trivial to find an eigenfunction of the Hamiltonian, and we first need a computationally feasible trail wavefunction that we can use in a variational algorithm or in tandem with other numerical techniques.

For many-body simulations, because quantum particles are indistinguishable, the wavefunction contains a certain symmetry with respect to permutation of two particles. Electrons are spin-$\frac{1}{2}$ particles, which are part of a class of particles called fermions, which have a negative sign change in the wavefunction when any two particles are permuted. The resulting wavefunction is said to be antisymmetric:

$$|\psi(1,2)\rangle = -|\psi(2,1)\rangle. \tag{1.8}$$

The simplest way to express a N-electron functions while preserving antisymmetry from a basis of one-electron functions is the Slater determinant[4]:

$$\psi_{SD} = \frac{1}{\sqrt{N!}} \det \begin{bmatrix} \phi_1(1) & \phi_2(1) & \cdots & \phi_N(1) \\ \phi_1(2) & \phi_2(2) & \cdots & \phi_N(2) \\ \cdots & \cdots & & \cdots \\ \phi_1(N) & \phi_2(N) & \cdots & \phi_N(N) \end{bmatrix}. \tag{1.9}$$

Evaluation of the operator expressions in (1.4) against determinant wavefunctions leads to the one- and two-electron integral expressions according to the Slater-Condon rules. Explicitly, given a Slater determinant $|\psi\rangle$, a Slater determinant that differs from $|\psi\rangle$ by two orbitals i and j, $|\psi_j^i\rangle$ and a Slater determinant that differs from $|\psi\rangle$ by in four orbitals i, j, k, and l, $|\psi_{jl}^{ik}\rangle$, we have for a one-electron operator $\hat{O}$:

$$\langle\psi|\hat{O}|\psi\rangle = \sum_i \int d1\phi_i^*(1)\hat{O}(1)\phi_i(1) = \sum_i O_{ii} \tag{1.10}$$

$$\langle\psi|\hat{O}|\psi_j^i\rangle = \int d1\phi_i^*(1)\hat{O}(1)\phi_j(1) = O_{ij}. \tag{1.11}$$

$$\langle\psi|\hat{O}|\psi_{jl}^{ik}\rangle = 0 \tag{1.12}$$

We can similarly define a two electron operator:

$$\hat{T}_{jl}^{ik} = \int d1d2\phi_i^*(1)\phi_k^*(2)T(12)\phi_j(1)\phi_l(2) \tag{1.13}$$

Then the associated Slater-Condon rules are:

$$\langle\psi|\hat{T}|\psi\rangle = \sum_{a\neq b} T_{ab}^{ab} - T_{ab}^{ba} \tag{1.14}$$

$$\langle\psi|\hat{T}|\psi_j^i\rangle = \sum_a T_{ja}^{ia} - T_{ja}^{ai} \tag{1.15}$$

$$\langle\psi|\hat{T}|\psi_{jl}^{ik}\rangle = T_{jl}^{ik}. \tag{1.16}$$

For many-body systems, the Slater determinant scales exponentially, and so performing operations directly on a Slater determinant is not feasible for more than a few orbitals. The formalism of second quantization provides us with another way of constructing a Slater determinant.[6, 7] In second quantization we replace the particles themselves with a fermionic field, which can be excited or relaxed, representing different N-particle modes. We can

define a creation operator $a_i^\dagger$, and an annihilation operator a_i, which creates or annihilates a fermionic mode in an orbital i (note the dagger † refers to the conjugate transpose of the operator). These have the following anticommutation relations:

$$a_i^\dagger a_j + a_j a_i^\dagger = \delta_{ij} \tag{1.17}$$

$$a_i^\dagger a_j^\dagger + a_j^\dagger a_i^\dagger = 0 \tag{1.18}$$

where δ_{ij} is the Kronecker delta function. We can construct a Slater determinant as a product of creation operators:

$$|\psi_{SD}\rangle = a_N^\dagger \cdots a_2^\dagger a_1^\dagger |0\rangle \tag{1.19}$$

where $|0\rangle$ is the fully unoccupied vector, or null ket. Additionally, we rewrite operators in a similar way in second quantization. Notable, we have one electron operators:

$${}^1\hat{O} = \sum_{ij} O_j^i a_i^\dagger a_j \tag{1.20}$$

and two electron operators:

$${}^2\hat{T} = \frac{1}{2} \sum_{ijkl} T_{jl}^{ik} a_i^\dagger a_k^\dagger a_l a_j, \tag{1.21}$$

where O_j^i and T_{jl}^{ik} are integral expressions exactly as above. The molecular Hamiltonian can then written in second quantization as:

$$\hat{H}_e = \sum_{ij} K_j^i a_i^\dagger a_j + \frac{1}{2} \sum_{ijkl} V_{jl}^{ik} a_i^\dagger a_k^\dagger a_l a_j, \tag{1.22}$$

where K_j^i represents the one electron integrals, and V_{jl}^{ik} are elements of the two-electron integrals. Notice we have replaced operators dependent on the number of particles with a

form that is particle agnostic - seemingly removing dependence on the particles! This is one of the hallmarks of second quantization.

The Slater determinant gives us a very versatile tool for the construction of fermionic wavefunctions. If we variational minimize a Slater determinant, we arrive at the Hartree Fock method. When we evaluate the electronic Hamiltonian against the Slater determinant we get the Fock operator:

$$\hat{F}_i\phi_i(1) = \hat{h}\phi_i(1) + \sum_{j}^{N/2} \left[2\hat{J}_j(1) - \hat{K}_j(1)\right]\phi_i(1) \tag{1.23}$$

where $\hat{J}$ and $\hat{K}$ are the Coloumb and exchange integrals respectively, and i represents a spatial orbital. The Hartree-Fock method for a set of orthonormal orbitals gives the following secular equation:

$$FC = \epsilon C \tag{1.24}$$

where C is a coefficient matrix of orbital coefficients. Diagonalization of F provides an optimal set of coefficients. If we create a new Slater determinant using the new orbitals, the Fock matrix is likely not diagonal, and we can iteratively construct new sets of orbitals. This is also known as the self-consistent field theory, or Hartree-Fock method. Multiple variations depending on restricted, open-shell, or unrestricted Slater determinants are known, and have their respective theories.[4, 7]

1.3 Post-Hartree Fock Methods and Electron Correlation

It is possible to show that any $N-$particle antisymmetric wavefunction can be expressed as sums of Slater determinants. Note that for a basis of size r, there are $\binom{r}{N}$ possible configurations or Slater determinants, representing an exponentially complex problem.

The initial guess, or the solution to the Hartree-Fock procedure, is known as the reference

determinant, and provides a single-reference wavefunction to input to other methods. In general, the Hartree-Fock reference can account for the majority of the energy of the solution, providing often up to 99% of the total electronic energy. However, the remaining 1% is still quite large from the standpoint of physical processes and chemical reactions, and so often it is needed to describe chemical phenomena.

Given a Hartree-Fock initial wavefunction ψ, we can express the exact wavefunction in that basis as:

$$|\Psi\rangle = c_0|\psi_0\rangle + \sum_{ia} c_a^i a_i^\dagger a_a|\psi\rangle + \sum_{ijab} c_{ab}^{ij} a_i^\dagger a_j^\dagger a_b a_a|\psi\rangle + \cdots \tag{1.25}$$

where c_i are coefficients. This form of Ψ with second quantized operators is simply a representation of the complete basis of Slater determinants relative to the reference determinant. To determine these coefficients, we can perform a brute force diagonalization of the Hamiltonian matrix. That is, we express the operator H in the basis of all possible Slater determinants, and then we diagonalize the matrix. This method is called the Full Configuration Interaction, or FCI method, and provides an exact solutions of the Schrodinger equation relative to the given basis set.

Because FCI scales exponentially with system size, computers today can still tackle only relatively small systems, limited to between 20-24 electrons and orbitals. For situations where the Hartree-Fock provides significant overlap with true wavefunction (i.e. c_0 is large), single-reference methods which account for dynamic effects can be used with great success.

Numerous single-reference methods exist, with large differences in scaling and accuracy. For instance, one can take a truncation of CI, such as a singles and doubles truncation, which only has coefficient c_0, c_j^i, and c_{jl}^{ik}. The problem with truncated CI and similar methods is that they are not size extensive. A perturbative expansion of the energy can also be taken, leading to Møller-Plesset Perturbation Theory [4].

The other method worth noting, which has connections to later chapters, is the coupled

cluster method [7]. If we define a cluster operator $\hat{T}$, with excitations $\{T_i\}$ we can specify a coupled cluster ansatz:

$$|\psi_{CC}\rangle = e^{\hat{T}}|\psi_0\rangle. \tag{1.26}$$

The secular equations for the coupled cluster methodology are given by taking expansions around the wavefunction and energy:

$$\langle\psi_0|e^{-\hat{T}}\hat{H}e^{\hat{T}}|\psi_0\rangle = E \tag{1.27}$$

$$\langle\phi|e^{-\hat{T}}He^{\hat{T}}|\psi_0\rangle = 0 \tag{1.28}$$

where ϕ is taken to be determinant which exists from the a direct application of the $\hat{T}$ operator. This results in a series of non-linear equations which are generally solved through the Jacobi method or with a iterative procedure and attempt to reach the above condition.

The nature of $\hat{T}$ operator determines the definition of the method. The most commonly used operators are the coupled cluster singles and doubles ansatz, CCSD:

$$\hat{T}_{SD} = \hat{T}_1 + \hat{T}_2 = \sum_{ia} T_a^i a_i^\dagger a_a + \sum_{ijab} T_{ab}^{ij} a_i^\dagger a_j^\dagger a_b a_a \tag{1.29}$$

Inclusion of the complete triples (denoted as the CCSDT method), a select pool of triples, or a perturbed triples contribution (such as in CCSD(T)) into the $\hat{T}$ operator, can greatly increase the accuracy of the coupled cluster method, particularly for single reference methods.

1.3.1 Multi-Reference Methods

When the desired electronic state is not dominated by the Hartree-Fock reference, such as which commonly occurs in dissociative processes, multi-reference methods are needed. The resulting systems is often said to be strongly correlated, or to have static correlation.

For these systems, we typically perform a configuration interaction calculation in a space

of orbitals, paired with an orbital optimization. The resulting method is termed the complete active space self consistent field method, or CASSCF. Similar to how Hartree-Fock is used as a initial guess for single-reference methods, the CASSCF wavefunction is a commonly used initial wavefunction for multi-reference methods.

Methods of note for multi-reference methods are multi-reference perturbation theory (MRPT2 or NEVPT2), multi-reference coupled cluster methods (MR-CC), and reduced density matrix methods, which are detailed in the next chapter.

1.4 A Note on Scaling

In this work big-O notation is often used to refer to the effective scaling of a procedure. That it, if a method scales as $O(r^4)$ with respect to some parameter r, then a doubling of the size of r should result in the number of required calculations being approximately $(2r)^4 = 2^4 r^4$, or 2^4 times as long. While this is not always the case due to constant or lower-scaling prefactors associated with many calculations, these trends can usually be seen when r is taken to be larger than the prefactors.

References

[1] R. P. Feynman, R. B. Leighton, and M. Sands, *The Feynman lectures on physics; New millennium ed.* (Basic Books, New York, NY, 2010) originally published 1963-1965.

[2] J. S. Townsend, *A modern approach to quantum mechanics*, 2nd ed. (University Science Books, Mill Valley, California, 2012).

[3] I. Mayer, *Simple Theorems, Proofs, and Derivations in Quantum Chemistry*, edited by P. G. Mezey (Kluwer Academic / Plenum Publishers, New York, 2003).

[4] A. Szabo and N. S. Ostlund, *Modern Quantum Chemistry: Introduction to Advanced Electronic Structure Theory* (Dover Publications, New York, 1996).

[5] J. E. House, *Fundamentals of Quantum Chemistry*, 2nd ed. (Elsevier Academic Press, San Diego, CA, 2004).

[6] P. Jorgensen and J. Simans, *New York* (Academic Press, Inc., London, 1981).

[7] T. Helgaker, P. Jørgensen, and J. Olsen, *Molecular Electronic-Structure Theory* (John Wiley & Sons, Ltd, Chichester, UK, 2000) p. 908.

CHAPTER 2

REDUCED DENSITY MATRIX APPROACHES FOR QUANTUM CHEMISTRY

As discussed in previous chapters, electrons are indistinguishable, which implies that expectation values are identical for different particles or importantly, pairs of particles [1–3] :

$$\sum_{i=1}^{N}\langle\psi|\hat{h}(i)|\psi\rangle = N\langle\psi|\hat{h}(1)|\psi\rangle \tag{2.1}$$

$$\sum_{j>i=1}^{N}\langle\psi|\hat{V}(ij)|\psi\rangle = N(N-1)\langle\psi|\hat{V}(12)|\psi\rangle \tag{2.2}$$

From these, we can define a reduced Hamiltonian operator:

$${}^{2}\hat{K}(12) = \frac{N}{2}(\hat{h}(1)+\hat{h}(2)) + \frac{N(N-1)}{2}\hat{v}(12) \tag{2.3}$$

Because molecular systems involve only two-body interactions, to measure physical properties we do not need to capture all of the degrees of freedom, but only that of the electron pair. Using the reduced density matrix, or RDM, we are able to convey and calculate all two-electron properties of a system. In particular, these often allow us to directly treat instances of strong correlation, and can provide alternate criteria on the wavefunction.

2.1 Reduced Density Matrices

In work by Dirac in the 1930's, the k-electron reduced density operator was introduced as:

$$\gamma_k(12...k;1'2'...k') = \frac{N!}{N-k!}\int d(k+1)...dN\psi(1,2,.,.,k,..,N)\psi^*(1',2',...k',k+1,..,N). \tag{2.4}$$

The matrix form can be obtained by integrating against the basis. The second-quantized form, which is now more commonly used, is written as follows:

$$ {}^{k}D^{i_1 i_2 \ldots i_k}_{j_1 j_2 \ldots j_k} = \langle \psi | a^{\dagger}_{i_1} a^{\dagger}_{i_2} \cdots a^{\dagger}_{i_k} a_{j_k} \cdots a_{j_2} a_{j_1} | \psi \rangle. \tag{2.5} $$

Note, we define the eigenvalues of the associated $k-$RDM as the set of $\{{}^{k}\lambda_i\}$. Depending on the convention, different normalizations of the $k-$RDMs can be used, as the trace of the RDM will in general not be equal to 1. Additionally, the $k-$RDM is antisymmetric with respect to any of the upper and lower indices. That is, swapping any two indices will result in a sign change as follows:

$$ {}^{k}D^{i_1 i_2 \ldots i_k}_{j_1 j_2 \ldots j_k} = -{}^{k}D^{i_2 i_1 \ldots i_k}_{j_1 j_2 \ldots j_k} = -{}^{k}D^{i_1 i_2 \ldots i_k}_{j_2 j_1 \ldots j_k} = {}^{k}D^{i_2 i_1 \ldots i_k}_{j_2 j_1 \ldots j_k}. \tag{2.6} $$

While the total spin (i.e. the sum of α and β orbitals) of the creation indices and annihilation indices must be equal, unlike classical electron integrals, the spin orbital of the upper and lower indices does not necessarily need to be equivalent.

The 1-RDM and 2-RDM explicitly are then defined as:

$$ {}^{1}D^{i}_{j} = \langle \psi | a^{\dagger}_{i} a_{j} | \psi \rangle \tag{2.7} $$

$$ {}^{2}D^{ik}_{jl} = \langle \psi | a^{\dagger}_{i} a^{\dagger}_{k} a_{l} a_{j} | \psi \rangle. \tag{2.8} $$

The trace of the 1-RDM and 2-RDM are N and $N(N-1)$, respectively. Using the 2-RDM, we can obtain the energy as:

$$ E = \mathrm{Tr}\ {}^{2}K\,{}^{2}D \tag{2.9} $$

where ${}^{2}K$ is the reduced Hamiltonian matrix obtained from the reduced Hamiltonian oper-

ator above, with elements given by:

$$ {}^2K^{ik}_{jl} = \frac{1}{2(N-1)}(\delta_{ij}\,{}^1K^k_l + \delta_{kl}\,{}^1K^i_j + {}^2V^{ik}_{jl}). \tag{2.10} $$

Furthermore, there numerous properties of 2-RDMs that we can explore. For instance, the projected spin (the $\hat{S}_z$ operator) commutes with the molecular Hamiltonian. Thus, our 2-RDM we only have to consider distinct spin blocks, and the 1-RDM will have a block diagonal form

$$ {}^1D = \begin{pmatrix} \alpha\alpha & 0 \\ 0 & \beta\beta \end{pmatrix} \tag{2.11} $$

whereas the 2-RDM will have the following spin blocks:

$$ {}^2D = \begin{pmatrix} \alpha\alpha\alpha\alpha & 0 & 0 & 0 \\ 0 & \alpha\beta\alpha\beta & \alpha\beta\beta\alpha & 0 \\ 0 & \beta\alpha\alpha\beta & \beta\alpha\beta\alpha & 0 \\ 0 & 0 & 0 & \beta\beta\beta\beta \end{pmatrix}. \tag{2.12} $$

Because there is no dependence on α or β in the Hamiltonian, the two can be used interchangeably, and commonly only unique spin combinations are stored.

2.2 N-Representability

Given that a RDM can be directly obtained from a wavefunction, one question is whether or not an RDM is always associated with a wavefunction ψ? Because an RDM is a matrix, the answer is strictly no - there exist many RDMs which do not come from a physical system. A necessary (tautologically) condition for RDM to represent a physical state is that the matrix is positive semi-definite, or that it has positive eigenvalues. This implies that for all nonzero vectors v, the matrix $v^{Tk}Dv$ is is non negative [2].

Let ψ be the preimage of the reduced density matrix ${}^2D$ (i.e. integration of ψ gives ${}^2D$). When there are is at least one ψ such that 2.8 holds, we say that ${}^2D$ is pure-state N-representable. If ${}^2D$ is composed from multiple pure states, i.e.

$$ {}^2D = \sum_i c_i {}^2D_i \tag{2.13} $$

then the state is simply N-representable. The manifold of N-representable 2-RDMs is convex (i.e., any combination of any RDMs is itself an RDM), which implies that there are certain criteria or constraints we can use to ascertain whether or not a given RDM is N-representable or not. An ensemble N-representability condition is a criteria such that when satisfied, the corresponding 2-RDM is N-representable. A pure state N-representability condition is a criteria such that when satisfied, the corresponding 2-RDM is pure-state N-representable. Because states have a variety of degrees of freedom in their basis set representation, these criteria will typically be manifest as conditions on the eigenvalues or a subset of eigenvalues of the RDM.

Constraints on the 1-RDM

From the Pauli exclusion principle, we know that the occupations of an orbital that an electron is in are between 0 and 1. This leads to a very simple necessary constraint on the 1-RDM:

$$ {}^1D \succcurlyeq 0. \tag{2.14} $$

Additionally, we know holes can be viewed in tandem with particles. Thus, the 1-hole matrix, defined as:

$$ {}^1Q^i_j = \langle \psi | a_i a^\dagger_j | \psi \rangle \tag{2.15} $$

also must be positive semidefinite:

$$ {}^1Q \succcurlyeq 0 \tag{2.16} $$

. While these were known constraints for $N-$representability, the pure state case is more challenging.

As an example, The 3-electron and 6-orbital approach, first noted by Borland and Dennis[4], has a set of inequalities on the ordered occupations of the 1-RDM:

$$^1\lambda_1 + {}^1\lambda_6 = 1 \tag{2.17}$$

$$^1\lambda_2 + {}^1\lambda_5 = 1 \tag{2.18}$$

$$^1\lambda_3 + {}^1\lambda_4 = 1 \tag{2.19}$$

$$^1\lambda_5 + {}^1\lambda_6 \geq {}^1\lambda_4. \tag{2.20}$$

These provide necessary conditions for a pure $N-$representable state of 3-electrons and 6-orbitals. Importantly, in 2008, Klaychko and Atalunbuk derived a set of generalized Pauli constraints, which provide necessary constraints for pure states [5, 6]. Other instances of these are covered in chapters 4, 5, and 6.

Constraints on the 2-RDM

In addition to the 2-particle reduced density matrix, we can construct a particle-hole, and hole-hole reduced density matrix:

$$^2G^{ij}_{kl} = \langle\psi|a^\dagger_i a_k a^\dagger_j a_l|\psi\rangle \tag{2.21}$$

$$^2Q^{ij}_{kl} = \langle\psi|a_i a_k a^\dagger_l a^\dagger_j|\psi\rangle \tag{2.22}$$

which also must be positive semidefinite:

$$^2D \succcurlyeq 0 \tag{2.23}$$

$$^2G \succcurlyeq 0 \tag{2.24}$$

$$^2Q \succcurlyeq 0. \tag{2.25}$$

Similar to the 1-RDM case, these serve as a set of necessary Additionally, further constraints can be derived from higher order positivity conditions. For instance, the 3-RDM is known to induce certain constraints on the 2-RDM. Pure constraints on 2-RDM in isolation from the 1-RDM have not yet been derived, but the 1-RDM can be used to provide a set of pure 2-RDM constraints.

The minimization of the energy of a 2-RDM subject to these constraints forms a semidefinite program, which can be solved using techniques of semidefinite programming and convex optimization. This leads to the so called variational 2-RDM approach.

2.3 Reconstruction of Reduced Density Matrices

In general, the problem of the constructing a reduced density matrix without a wavefunction can be quite challenging. We can quite easily produce a lower RDM from a higher RDM, but this process involves integration, and thus we often necessarily lose information on the state. While it is possible to work with larger RDMs (which originate from a wavefunction), say the 3-RDM or 4-RDM (which scale as $O(r^6)$ and $O(r^8)$ respectively), typically these lead to prohibitively costly algorithms, and so are not practical in many instances. A method of approximating higher RDMs in terms of lower ones through the use of Schwinger probes was introduced by Mazziotti in 1998[7], using the cumulant reduced density matrix.

We begin by defining the Grassmanian wedge product of two RDMs. In particular, given

k RDM and $N-k$ RDM B and C, the wedge product gives elements according to:

$$B^{i_1 i_2 \cdots i_k}_{j_1 j_2 \cdots j_k} \wedge C^{i_{k+1} \cdots i_N}_{j_{k+1} \cdots j_N} = \frac{k!(N-k)!}{(N!)^2} \sum_{\pi,\sigma} \epsilon(\sigma)\epsilon(\pi)\hat{\pi}\hat{\sigma} B^{i_1 i_2 \cdots i_k}_{j_1 j_2 \cdots j_k} C^{i_{k+1} \cdots i_N}_{j_{k+1} \cdots j_N} \tag{2.26}$$

where $\hat{\sigma}$ and $\hat{\pi}$ are permutation operators, ϵ returns the sign of the permutation, and σ and π are taken over the $N!$ permutations of the upper and lower indices, respectively.

From this, we can introduce a cumulant $p-$RDM ${}^p\Delta$, such that:

$$\frac{1}{1!}{}^1D = {}^1\Delta \tag{2.27}$$

$$\frac{1}{2!}{}^2D = {}^1 2! {}^1\Delta \wedge {}^1\Delta + 2! {}^2\Delta \tag{2.28}$$

$$\frac{1}{3!}{}^3D = {}^3\Delta + {}^1\Delta^3 + 3{}^2\Delta \wedge {}^1\Delta \tag{2.29}$$

$$\frac{1}{4!}{}^4D = {}^4\Delta + {}^1\Delta^4 + 6{}^2\Delta \wedge {}^1\Delta^2 + 4{}^3\Delta \wedge {}^1\Delta = 3{}^2\Delta^2. \tag{2.30}$$

The cumulant RDM allows us to express a given $k-$RDM in terms of lower RDMs and their cumulants. A common approximation to obtain a $k-$RDM given a $k-1$RDM is to set ${}^k\Delta = 0$, and apply the wedge product, although numerous cumulant approximations have been made as well.[2, 3]

2.4 Contracted Schrödinger Equations

The contracted Schrödinger equation (CSE) was introduced by Nakatsuji in 1972 as the density equation, and later shown in second quantization by Mazziotti [2, 3, 8–10]. In particular, we can contract or project the Schrödinger equation onto a two-particle space to yield the CSE:

$$\langle \psi | a^\dagger_i a^\dagger_k a_l a_j \hat{H} | \psi \rangle = {}^2D^{ik}_{jl} E \tag{2.31}$$

When ψ is an eigenstate of H, the above equation is clearly satisfied. Multiplication by ${}^2K^{ik}_{jl}$ yields the dispersion relation,

$$\langle\psi|\hat{H}^2|\psi\rangle - E^2 = 0 \tag{2.32}$$

which is the variance in the energy. If the CSE is satisfied, then the variance of the energy is 0 and we are at an eigenstate. Thus, the CSE or density equation is a necessary and sufficient condition to satisfy the Schrödinger equation.

We can separate the CSE into hermitian and anti-hermitian components, yielding the hermitian CSE (HCSE) and anti-hermitian CSE (ACSE)[10, 11]:

$$\langle\psi|\{a_i^\dagger a_k^\dagger a_l a_j, \hat{H} - E\}|\psi\rangle = 0 \tag{2.33}$$

$$\langle\psi|[a_i^\dagger a_k^\dagger a_l a_j, \hat{H}]|\psi\rangle = 0 \tag{2.34}$$

Note we have removed the factor of $\frac{1}{2}$, for reasons that will become clear later. The HCSE can be expressed explicitly in terms of reduced density matrices. Defining a matrix ${}^2W$:

$${}^2W^{pr}_{qs} = {}^2K^{pr}_{qs} - {}^2K^{rp}_{qs} \tag{2.35}$$

we can express the HCSE as:

$$\begin{aligned} 0 = &\sum_{prqs} 2^2K^{pr4}_{qs} D^{prik}_{jlqs} \\ &+ \sum_{prq} {}^2W^{pr3}_{kq} D^{pri}_{jlq} + {}^2W^{pr3}_{qi} D^{prk}_{jlq} + {}^2W^{pj3}_{qr} D^{ikp}_{qrl} + {}^2W^{lp3}_{qr} D^{ikp}_{qrj} \\ &+ \sum_{pq} {}^2W^{pq2}_{ik} D^{pq}_{jl} + {}^2W^{jl2}_{pq} D^{ik}_{pq} - {}^2E D^{ik}_{jl} \end{aligned} \tag{2.36}$$

The ACSE on the other hand, can be expressed similarly:

$$\begin{aligned} 0 = &\sum_{prq} {}^2W_{qr}^{pj3}D_{qrl}^{ikp} + {}^2W_{qr}^{lp3}D_{qrj}^{ikp} - {}^2W_{kq}^{pr3}D_{jlq}^{pri} - {}^2W_{qi}^{pr3}D_{jlq}^{prk} \\ &+ \sum_{pq} {}^2W_{pq}^{jl2}D_{pq}^{ik} - {}^2W_{ik}^{pq2}D_{jl}^{pq} \end{aligned} \tag{2.37}$$

Notably, the HCSE depends on at most the 4-RDM, whereas the ACSE depends only on the 3-RDM.

2.4.1 Finding a Solution of the Contracted Eigenvalue Equations

We can find a solution to these equations through an iterative procedure treating the residuals and the reduced density matrices as a pair of differential equations. Consider a generic two-body operator:

$$\hat{M} = \sum_{ijkl} M_{kl}^{ij} a_i^\dagger a_k^\dagger a_l a_j \tag{2.38}$$

which will be antisymmetric from the nature of the fermionic operators. If we consider a wavefunction $|\psi\rangle$ we can look at the energy of an infinitesimal expansions around it by our operator $\hat{M}$:

$$E(\epsilon) = \frac{\langle\psi|e^{\epsilon M\dagger}\hat{H}e^{\epsilon M}|\psi\rangle}{\langle\psi|e^{\epsilon M + M^\dagger}|\psi\rangle}. \tag{2.39}$$

We can transform M and $M^\dagger$ into hermitian and anti-hermitian operators:

$$\hat{S} = \frac{\hat{M} + \hat{M}^\dagger}{2} \tag{2.40}$$

$$\hat{A} = \frac{\hat{M} - \hat{M}^\dagger}{2} \tag{2.41}$$

Which yields a total energy expression:

$$E(\epsilon) = E(0) + \epsilon\frac{\langle\psi|\{\hat{S},\hat{H}\}|\psi\rangle - \langle\psi|[\hat{A},\hat{H}]|\psi\rangle}{1 + 2\epsilon\langle\psi|\hat{S}|\psi\rangle}. \tag{2.42}$$

The derivative with respect to elements of S and A are given by their respective equations:

$$\frac{1}{\epsilon}\frac{dE(\epsilon)}{dA^{ik}_{jl}} = -\langle\psi|[a^\dagger_i a^\dagger_j a_l a_j, \hat{H}]|\psi\rangle \tag{2.43}$$

$$\frac{1}{\epsilon}\frac{dE(\epsilon)}{dS^{ik}_{jl}} = \langle\psi|\{a^\dagger_i a^\dagger_j a_l a_j, \hat{H}\}|\psi\rangle - 2E^2 D^{ik}_{jl} \tag{2.44}$$

which are the ACSE and HCSE, respectively. Classically, we can choose to obtain a maximal increase in energy. Given that, we obtain the update formula for the 2-RDM as:

$${}^2D^{pr}_{qs}(\epsilon) = \langle\psi|e^{S-A}a^\dagger_p a^\dagger_r a_s a_q e^{S+A}|\psi\rangle \tag{2.45}$$

$$= {}^2D^{pr}_{qs}(0) + \frac{\epsilon\langle\psi|\{S, a^\dagger_p a^\dagger_j a_l a_j\}|\psi\rangle - \epsilon\langle\psi|[A, a^\dagger_i a^\dagger_j a_l a_j]|\psi\rangle}{1 + 2\epsilon\langle\psi|\hat{S}|\psi\rangle}. \tag{2.46}$$

This provides an update formula for the 2-RDM. We can treat these as a system of differential equations and iteratively update them given small ϵ. Though a general algorithm is shown, in practice we do not need to optimize with respect to both hermitian and antihermitian operators. When $M = A$, we have the ACSE method, and when $M = S$, we have the HCSE method. The method for solving the ACSE is more commonly used, as it can be applied more easily given that it only requires a 3-RDM. Currently there have been numerous applications to many different systems, including the treatment of strongly correlated system. The method scales as approximately $O(r^6)$, and is competitive with coupled cluster CCSD(T) techniques.

References

[1] A. Coleman and V. Yukalov, *Reduced Density Matrices: Coulson's Challenge* (Springer, Berlin Heidelberg New York, 2000).

[2] J. Cioslowski, *Many-Electron Densities and Reduced Density Matrices*, edited by J. Cioslowski, Mathematical and Computational Chemistry, Vol. 91 (Springer US, Boston, MA, 2000) pp. 399–404.

[3] D. A. Mazziotti, ed., *Advances in Chemical Physics*, Advances in Chemical Physics, Vol. 134 (John Wiley & Sons, Inc., Hoboken, NJ, USA, 2007) p. 574.

[4] R. E. Borland and K. Dennis, Journal of Physics B: Atomic and Molecular Physics **5**, 7 (1972).

[5] M. Altunbulak, Ph.D. Thesis (2008).

[6] A. A. Klyachko, arXiv **quant-ph**, 4 (2009), arXiv:0904.2009 .

[7] D. a. Mazziotti, Chemical Physics Letters **289**, 419 (1998).

[8] H. Nakatsuji, Physical Review A **14**, 41 (1976).

[9] D. A. Mazziotti, Physical Review A **57**, 4219 (1998).

[10] D. A. Mazziotti, Physical Review A **69**, 012507 (2004).

[11] D. A. Mazziotti, Physical Review A - Atomic, Molecular, and Optical Physics **75**, 1 (2007).

CHAPTER 3

QUANTUM COMPUTING FOR MOLECULAR SIMULATION

The goal of quantum simulation on a quantum computer (as can be attributed to Feynman in the preface) is to use one quantum mechanical object to simulate another. If we try to model our molecular system using the direct controls of a similar quantum system, this is referred to as analog quantum simulation. If instead we use a logical computational set of operations, which are used extensively in quantum computation, then we have digital quantum simulation. Because analog quantum simulation is significantly more limited in practice, and requires device specific constraints, the focus here is on digital quantum simulation.

As the basics of quantum simulation are less well documented than quantum computation, which has several excellent introductory materials[1], the following chapter gives a brief overview of quantum simulation for many-body physical systems. The field of quantum simulation has developed rapidly during the time of this thesis, and thus several of the topics are the current state-of-the-art, relevant for the current generation of quantum computers.

3.1 Basics of Quantum Computation

In this section we introduce qubits, quantum gate operations, which are necessarily unitary, and measurement.

3.1.1 Qubits

The basic computing element of the quantum computer is the qubit, or quantum bit. A qubit is a two-level system, the state of which can be represent as two-dimensional complex vector:

$$|\psi\rangle = \begin{pmatrix} \alpha \\ \beta \end{pmatrix}, \quad |\alpha|^2 + |\beta|^2 = 1 \tag{3.1}$$

where α refers to the $|0\rangle$ state coefficient, and β to $|1\rangle$ state coefficient. This basis set is referred to as the computational basis, akin to classical bits populating 0 and 1. If we consider the density matrix ρ, we have a matrix representation of the state:

$$\rho = \begin{pmatrix} \alpha\alpha^* & \alpha\beta^* \\ \beta\alpha^* & \beta\beta^* \end{pmatrix}. \tag{3.2}$$

There are an important set of matrices for the characterization of two-level systems, called the Pauli spin matrices. These are defined as:

$$\sigma_x = \begin{pmatrix} 0 & 1 \\ 1 & 0 \end{pmatrix}, \quad \sigma_y = \begin{pmatrix} 0 & -i \\ i & 0 \end{pmatrix}, \quad \sigma_z = \begin{pmatrix} 1 & 0 \\ 0 & -1 \end{pmatrix}, \tag{3.3}$$

and have the following important commutation and anticommutation relations:

$$[\sigma_l, \sigma_j] = 2\epsilon_{ljk}\sigma_k \tag{3.4}$$

$$\{\sigma_l, \sigma_j\} = 2\delta_{lj}I \tag{3.5}$$

where ϵ_{ljk} is the Levi-Civita symbols. The Pauli matrices are unitary, have Tr $= 0$, $|\det \sigma_i|=1$ and have eigenvalues of $+1$ and -1. For the sake of completion the eigenvec-

tors are given as:

$$|+z\rangle = |0\rangle \tag{3.6}$$

$$|-z\rangle = |1\rangle \tag{3.7}$$

$$|+x\rangle = \frac{1}{\sqrt{2}}(|0\rangle + |1\rangle) \tag{3.8}$$

$$|-x\rangle = \frac{1}{\sqrt{2}}(|0\rangle - |1\rangle) \tag{3.9}$$

$$|+y\rangle = \frac{1}{\sqrt{2}}(|0\rangle + i|1\rangle) \tag{3.10}$$

$$|-y\rangle = \frac{1}{\sqrt{2}}(|0\rangle - i|1\rangle) \tag{3.11}$$

$$\tag{3.12}$$

The Pauli matrices form a complete basis of the special unitary group $SU(2)$. We can thus represent a single qubit density matrix in the basis of Pauli operators as:

$$\rho = \frac{1}{2}(I + \vec{d} \cdot \vec{\sigma}) \tag{3.13}$$

where $\vec{\sigma} = (\sigma_x, \sigma_y, \sigma_z)$ and $\vec{d}$ is a unit vector defined with components by:

$$d_i = \text{Tr } \sigma_i \rho. \tag{3.14}$$

3.1.2 Gates and Rotations

Multiple connections can be made between the Pauli set, the group of 3-dimensional rotations ($SO(3)$), and Lie algebras. First, we can represent $\vec{d_i}$ as a vector along the unit sphere, with axis given by the positive and negative eigenstates of each Pauli matrix. From the theory of Lie groups one can see that exponentiation of the axis operator times i induces a rotation

around that axis [2, 3]:

$$R_j(\theta) = e^{-i\frac{\theta}{2}\sigma_j} \tag{3.15}$$

where $R_j(\theta)$ is a rotation around the j-axis by angle θ. Given that our single-qubit can be represented by a sphere (with axes given by the Pauli matrix contributions), called the Bloch sphere, we can naturally relate these rotation operators with rotations on the unit sphere. Thus, with only two different rotations, we can prepare any single qubit state.

In going beyond a single qubit, many-qubit states are typically described by tensor products of single qubit states. Given a state $|0\rangle$ on qubit 1 and $|1$ on qubit 2, the resultant state is $|\psi_{01}\rangle = |0\rangle \otimes |1\rangle = |01\rangle$. The size of the state space doubles, and in general for $n-$qubits the state space will have 2^n elements. The example of $|\psi_{01}\rangle$ is an example of a separable state - a measurement (see proceeding sections) of qubit 1 will always produce the 0 state, and a measurement of qubit 2 will always produce the 1 state. These states are independent statistically, and the state is said to be separable. If we take a different state, for instance the Bell state,

$$|\psi_{\text{Bell}}\rangle = \frac{1}{\sqrt{2}}(|00\rangle + |11\rangle), \tag{3.16}$$

then we are said to have an entangled state. Measurement (see next section) of qubit 1 will result in the $|0\rangle$ and $|1\rangle$ state being measured with equal probability, but will always lead to the same state being measured on qubit 2. There is no local basis that results in the two results being separable, and the state is said to be entangled. A natural connection with the idea of a weakly or strongly correlated molecular state can be made, as inherently it depends on the entangled nature of the system.

We can also consider tensor products of operators to form matrices. If we use tensor products of Pauli matrices, we can extend our notion of a complete operator basis to an arbitrary number of qubits. A Pauli string $p_1 p_2 \cdots p_k$ is defined as a tensor product of

single-qubit Pauli operators:

$$p_1 p_2 \cdots p_k = \sigma_{p_1}^1 \otimes \sigma_{p_2}^2 \otimes \cdots \otimes \sigma_{p_k}^k \tag{3.17}$$

where σ_j^q refers to the Pauli j operator acting on qubit q. There are many different notations, but as an example, XYIYZ is a 5-qubit Pauli string equivalent to $\sigma_x^1 \otimes \sigma_y^2 \otimes I^3 \sigma_y^4 \otimes \sigma_z^5$.

While a simple operator like XX does not generate an entangled quantum state, the exponential of such an operator does. In particular, if we consider the gate $U = e^{i\frac{\theta}{2}XX}$, this is equivalent to $U = II\cos\frac{\theta}{2} + iXX\sin(\frac{\theta}{2})$, which produces a 'rotation'-like effect between II and XX. Although the idea of a more than 3-dimensional rotation is not generally defined, if we are in an eigenstate of the XX operator, the rotation gate will only introduces a complex valued phase.

To carry out this gate we need the conditional-NOT gate, or CNOT gate, which acts on qubits j and k:

$$CX_j^k = |0\rangle\langle 0|^j \otimes I^k + |1\rangle\langle 1|^j \otimes X^k, \tag{3.18}$$

and applies a NOT gate to qubit k conditioned on the state in qubit i. We see how this state can produce entangled states we note that the Bell state can be quickly prepared as:

$$|\psi_{\text{Bell}}\rangle = CX_1^2 H_1 |0\rangle. \tag{3.19}$$

Using a CNOT gate, we can prepare a multi-qubit Pauli string of solely Z operations using techniques from quantum computation by applying forward sequence of CNOT gates to condition the target qubit with every other qubit, a $R_z(\theta)$ gate, and then a reversal of the CNOT sequence.

Example 1. *Exponential ZZ Gate If we have a $k-$length string of Z operations, we can use*

the following sequence to apply $e^{i\frac{\theta}{2}Z^k}$ *in the computational basis.*

$$|n_1 n_2 n_3 \cdots n_k\rangle \rightarrow^{CX_1^2} |n_1(n_1+n_2)n_3 \cdots n_k\rangle \tag{3.20}$$

$$\rightarrow^{CX_2^3} |n_1 m_2(n_1+n_2+n_3)\cdots n_k\rangle \tag{3.21}$$

$$\rightarrow^{CX_{k-1}^k} |m_1 m_2 \cdots \sum_{j=1}^{k} n_j\rangle \tag{3.22}$$

$$\rightarrow^{Rz_k(\theta)} e^{i\frac{\theta}{2}(-1)^{m_k+1}} |m_1 m_2 \cdots m_k\rangle \tag{3.23}$$

$$\rightarrow^{CX_{k-1}^k} e^{i\frac{\theta}{2}(-1)^{m_k+1}} |m_1 m_2 \cdots n_k\rangle \tag{3.24}$$

$$\rightarrow^{CX_1^2} e^{i\frac{\theta}{2}(-1)^{m_k+1}} |n_1 n_2 \cdot \cdot n_k\rangle \tag{3.25}$$

$$= e^{iZZ\cdots Z} |n_1 n_2 \cdot \cdot n_k\rangle \tag{3.26}$$

showing that this sequence of CNOT gates and local Rz gate is equivalent to the exponential of the Pauli Z^k *string.*

Because of the exponential basis change identity

$$U e^V U^\dagger = e^{UVU^\dagger} \tag{3.27}$$

we can rotate from the Z^k Pauli string to arbitrary Pauli strings of length k by using single-qubit basis rotations as discussed above. This is a very powerful tool for digital quantum simulation, as the Pauli string operators are the native language of current generation quantum computers. It is often the case that we have non-unitary operators, or simply operators in a different basis, which have to be expressed in the Pauli basis for practical computation.

3.1.3 Measurement

Measurement in quantum mechanics is a non-unitary process, which projects the quantum state into the basis of measurement [1]. There is substantial work related to frames of

reference and different types of quantum measurement (such as positive operator valued measurement), but for our purposes, common measurements are performed in the computational basis. That is, given a state $|\psi\rangle$, a measurement on qubit k of the $|z+\rangle$ state is the following non-unitary matrix:

$$M_{|z+\rangle} = \begin{pmatrix} 1 & 0 \\ 0 & 0 \end{pmatrix} \tag{3.28}$$

Similar to Pauli operators, we can change our basis of measurement using single-qubit basis rotations. For many multi-qubit systems, these measurements are applied to every qubit, meaning that for an $n-$qubit local measurement, every measurement outcome will be a n-length string of 0s and 1s. From this, we actually can measure up to $2^n - 1$ different measurement outcomes. In the computational basis, we can obtain the expectation for all permutations of $k = 1$ to $k = n$, Z^k strings (i.e. $Z_1, Z_1Z_2, Z_1Z_2Z_4$, etc.). Besides the Hadamard transformation and S gates, which allow us to rotate the state to the X and Y Pauli bases, if we utilize the CNOT gate (i.e. the Clifford group) we can transform our set of Z measurements to any other Pauli string.

An aspect which is likely not emphasized enough, relates to probabilistic nature of quantum computing and the nature of quantum measurement. While quantum computers could be considered deterministic devices in given the same instructions, the same state is prepared, the process of measurement means that the result will always be probabilistic.

When we are attempting to measure a $k-$qubit Pauli string P, M times, we change to the basis of measurement from the computational basis, and then prepare and measure the state M independent times. The expectation is calculated directly from the resultant counts:

$$\langle P \rangle = \frac{1}{M} \sum_{i=1}^{M} \langle \psi | P | \psi \rangle |_i \tag{3.29}$$

where $|_i$ indicates the value obtained following the $i - th$ measurement, and the associated

variance of this is:

$$\text{Var } P = \frac{1}{M}\sum_{n=1}^{M}(\langle P^2\rangle - \langle P\rangle^2) = \frac{1}{M}\sum_{n=1}^{M}(1 - \langle P\rangle^2). \tag{3.30}$$

Given an observable $\hat{H} = \sum_i h_i \hat{P}_i$, and assuming that the terms are statistically independent, we have that:

$$\text{Var } H = \sum_{i=1} \frac{h_i^2}{M}(1 - \langle P_i\rangle^2) \tag{3.31}$$

which leads to a natural relation between the number of measurements and the required error estimate.

However, unfortunately it is not always the case that two strings are statistically independent, and thus we have to consider the covariance of all related terms. Because this is generally not feasible to do, we can use other variance estimation techniques, such as estimating the standard deviation from the sampled mean statistics and the central limit theorem.

3.2 Near-Term Quantum Devices

Near-term quantum devices include all of the components listed in the above section: qubits, single- and two-qubit gate control, and measurement capabilities. However, there are numerous limitations in each of these regards which in the aggregate lend to the description of the modern generation of quantum computers as noisy intermediate-scale quantum devices, or NISQ device[4]. The phrase 'near-term,' refers to the limitations of current devices and devices in the near-future, before the advent of devices with quantum error correction capabilities necessary for a fault-tolerant device. Despite that logical qubits have been demonstrated, the complexity of these systems and requirements for arbitrary connectivity between logical qubits remains an significant challenge, and instead quantum systems composed of multiple, minimally mitigated qubits are used.

The reason for these limitations is beyond the scope of the present work, but there are several takeaways for near-term devices. An closed quantum system is one which exists completely isolated from any environmental or external interactions. A open quantum system is one which has an interaction with a bath, or an environment, allowing for the exchange of energy or information. Quantum mechanical theory and the Schrödinger equation is strictly defined for closed quantum systems, and more complex techniques are needed to describe an open quantum system.

While qubit design is important, and constructing reliable qubits is challenging, the more relevant challenges for near-term simulations are related to two-qubit gate fidelity and measurement, as these are significant sources of errors. Additionally, sometimes the performance of a qubit is viewed through the lens of the single qubit gate error and measurement errors, but these are distinct factors, especially from a design perspective. Because quantum gates are complex and have a variety of error (not just bit-flip), modelling the success or failure of even a simple gate is not straightforward.

If we describe a gate or measurement (instances of a quantum process) as having a certain success fidelity $p \in [0, 1]$, then repeated applications of that gate $m-$times result in a total success probability of p^m, implying an exponentially fast decay. Because the p associated with two-qubit gates (often 0.1 to 0.01) is about an order of magnitude higher than single qubit gates (0.01 to 0.001), it tends to dominate errors rate. Measurement also has a substantial error, but only occurs once versus the m instances of a two-qubit gate.

3.2.1 Operator Description of Open Dynamics

Given a system in a Hilbert space $\mathcal{H}_A$ and a bath in a space $\mathcal{B}$, the total system is described as $\mathcal{A} \otimes \mathcal{H}_B$[5]. The joint evolution of the total system is governed by the Schrodinger equation, where

$$H = \sum_{ij} h_{ij} \hat{P}_i^a \otimes \hat{P}_j^b \tag{3.32}$$

where $\hat{P}_i^a$ is a Pauli string acting on system a. When we trace over the bath degrees of freedom, we obtain a reduced density matrix, not to be confused with the $k-$particle RDM of the previous chapter. Given a basis of states of the bath ϕ_i^b, the partial trace of a state ρ is defined as:

$$\mathrm{Tr_B}\ \rho = \sum_k \langle \phi_k^b | \rho | \phi_k^B \rangle = \rho_A. \tag{3.33}$$

Unless the state is separable with regards to the subspaces A and B, the resulting state cannot be represented by a single wavefunction. Generally, for a time dependent process, we do consider the state to be separable initially, and then we observe the dynamics of the open quantum system.

Given an initial state

$$\rho(0) = |\psi\rangle\langle\psi| \otimes (\sum_i \lambda_i |\phi_i\rangle\langle\phi_i|) \tag{3.34}$$

, we can apply the time evolution operator U, and then trace over the bath. The resultant state of system at time t is given in a Kraus operator representation:

$$\rho(t) = \sum_{IJ} K_{IJ}(t)\rho(0)K_{IJ}^\dagger(t), \tag{3.35}$$

where K_{IJ} is a Kraus operator and is defined by:

$$K_{IJ} = \sqrt{\lambda_J}\langle\phi_I|e^{i\hat{H}t}|\phi_J\rangle. \tag{3.36}$$

There are several important properties of Kraus operators. Notably $\sum_{IJ} K_{IJ}K_{IJ}^\dagger = 1$, which preserves normalization.

The depolarizing map is an important noise channel, and which is used in generating common noise models. The depolarizing channel returns the mixed state with probability p,

or leaves the state unchanged with probability $1-p$:

$$f_{\text{depol}}[\rho] = p\frac{I}{2^n} + (1-p)\rho. \tag{3.37}$$

and has associated Kraus operators:

$$K_I = \sqrt{1-\frac{3}{4}pI}, \quad K_{j=X,Y,Z} = \sqrt{p}4\sigma_j. \tag{3.38}$$

The effect of this channel is to contract the state, as the probability of the state remaining intact decays as $(1-p)^n$, indicating that with probability $1-(1-p^n$, we are in the maximally mixed state which bears no information. Other important channels include dephasing channels, amplitude damping channels, as well the effect of thermal distributions on the prepared state. These are discussed in more detail in chapter 7.

While it is important to understand the mechanics of how the operators work, often times one is unable to causally associated a noise source or channel with an experiment. Certain types of noise, such as rotating frames of refernce or mild dephasing noise, can be offset by the algorithm (such as when the degrees of freedom of the algorithm can account for a changer in frame) as well as by certain types of error correction. Other sources of noise can be mitigated fairly well in a number of instances. Indeed, often a simulation can be run against a certain single- or two-qubit noise channel to test the predicted performance. Other types of noise, such as depolarizing noise, are more challenging to overcome, as they deteriorate the amount of information in a state in a way that is somewhat unrecoverable.

3.3 Fermionic Simulation

To simulate chemical systems, we first need to understand how to represent fermionic systems. Work by Abrams and Lloyd in 1997 showed that either a first quantized or second quantized approach could be performed for fermionic simulation. Given a input ψ, an an-

tisymmetrization procedure can be carried out with register qubits involving carried out $O(n^2(lnm)^2)$ steps, where n is the number of particles and m the number of states.

Second quantization provides a more natural mapping, and is used almost exclusively in near-term algorithms. As mentioned previously, we can work with representation of Slater determinants, and carry out antisymmetric operations and measurement using anticommuting operators. In general, given a fermionic operator, we use a fermionic transformation which strictly is a mapping from the fermionic operator basis to the Pauli operator basis.

3.3.1 Fermionic Transformations

The Jordan-Wigner transformation is defined as follows for the fermionic creation and annihilation operators:

$$a_k^\dagger \mapsto \frac{1}{2}(\sigma_x^k - i\sigma_y^k)\bigotimes_{l=1}^{k-1}\sigma_z^l \tag{3.39}$$

$$a_k \mapsto \frac{1}{2}(\sigma_x^k + i\sigma_y^k)\bigotimes_{l=1}^{k-1}\sigma_z^l \tag{3.40}$$

These operators are strictly non-local, as if $k-$operators are used, the operators in general act on more than k qubits. The Jordan-Wigner transformation encodes the occupations locally and the fermionic sign nonlocally. From these we can also clearly see the composite particle and hole operators:

$$a_k^\dagger a_k = \frac{1}{2}(I^k - \sigma_z^k), \tag{3.41}$$

$$a_k a_k^\dagger = \frac{1}{2}(I^k + \sigma_z^k), \tag{3.42}$$

which do not affect the sign of the wavefunction and are thus local operators.

There also exists a the parity mapping[6], which is another valid fermionic mapping for n qubits. The parity mapping stores in qubit j the parity (mod 2) of the occupations of

all orbitals up to orbital j ($p_j = \sum_{i \leq j} n_i$). To represent a creation or annihilation operator involves checking to see if the current $j-$th orbital is occupied or unoccupied by looking at the $j-1$ orbital, and then if applicable flipping the $j+1$ to n sites, which included the occupation of the $j-$th site.

$$a_k^\dagger \mapsto \frac{1}{2}(\sigma_z^{k-1}\sigma_x^k - i\sigma_y^k) \bigotimes_{l=k+1}^{n} \sigma_x^l \tag{3.43}$$

$$a_k^\dagger \mapsto \frac{1}{2}(\sigma_z^{k-1}\sigma_x^k + i\sigma_y^k) \bigotimes_{l=k+1}^{n} \sigma_x^l. \tag{3.44}$$

The particle and hole operators are thus given as:

$$a_k^\dagger a_k = \frac{1}{2}(I^{k-1}I^k - \sigma_z^{k-1}\sigma_z^k) \tag{3.45}$$

$$a_k a_k^\dagger = \frac{1}{2}(I^{k-1}I^k - \sigma_z^{k-1}\sigma_z^k), \tag{3.46}$$

which are nonlocal, in that the occupation of a particular site depends on the present site and the site under it. Thus, we say that the parity mapping stores the occupations nonlocally, but the fermionic sign locally. Both the Jordan-Wigner and the Parity mapping incur an additional linear scaling cost with respect to system size, but just with regards to different mappings.

A noteworthy mapping is the Bravyi-Kitaev mapping[7], which is commonly used in simulations (but not necessarily in practice), and stores information on both the occupation and parity nonlocally. Thus, the linear scaling problem is actually reduced to a logarithmic one. For near-term computing the usefulness of the Bravyi-Kitaev mapping is somewhat unclear. The benefit in scaling does not seem to outweigh the somewhat disconnected CNOT gate structures that is required, although this should be less of a concern for high-performance quantum computers.

There are also a variety of compact mappings, which are broadly defined, but generally

map a set of states directly to the quantum computer based on the dimensionality of the ideal and encoded Hilbert spaces. The main question in these instances is how to preserve fermionic operations, and the exact nature of the mapping.

Example 2. *Compact Two-Qubit Mapping of H_2 in a minimal basis set.*

$$|1010\rangle \mapsto |00\rangle$$

$$|1001\rangle \mapsto |01\rangle$$

$$|0110\rangle \mapsto |10\rangle$$

$$|0101\rangle \mapsto |11\rangle$$

In all of these mappings, we can see that mappings are generally made from a fermionic set of creation and annihilation operators, to a set of operators that is more amenable to the quantum computer. However, fermionic operators are generally non-unitary, and so must either be used in measurement, in non-unitary simulation, or put into a unitary form.

3.3.2 Exponential Operators

The most simply way to generate a unitary operator from a non-unitary one is to put the operator in an anti-Hermitian form. That is, given A, if we can derive A' such that $A'^{\dagger} = -A'$, then the matrix is said to be antihermitian. Given an antihermitian operator, the following matrix is unitary:

$$U = e^{-A}. \tag{3.47}$$

which can be seen by applying $U^{\dagger}$. Thus, an operator such as:

$$A = a_i^{\dagger} a_j - a_j^{\dagger} a_i \tag{3.48}$$

can be exponentiated to become a unitary operator. Let us try to simulate the unitary

$$U = e^{A^f}. \tag{3.49}$$

Given an anti-Hermitian fermionic operator, we first transform it to the qubit basis, which in general will be expressed as a sum of Pauli strings:

$$A^f \mapsto A^q = \sum_j a_j \hat{P}_j \tag{3.50}$$

The simple reason for this is the Pauli operator basis is not number-conserving. Additionally, it is generally only reasonable to implement the exponent of one Pauli string at a time, leading to an expression like:

$$V = e^{a_1 \hat{P}_1} e^{a_2 \hat{P}_2} \cdots e^{a_k \hat{P}_k} = \prod_{j=1^k} e^{a_j P_j} \tag{3.51}$$

If all P_j commute with each other, then indeed we have that

$$\forall\ j, k, \quad e^{a_j P_j} e^{a_k P_k} = e^{a_j P_j + a_k P_k} \tag{3.52}$$

and so $V = U$. Generally, some elements will commute, and others will not, requiring us to use approximations. We can still use this form, but according to the Trotter-Suzuki formula it has an associated error:

$$U - V = O(k^2 ||a||_\infty^2). \tag{3.53}$$

A first order trotterization of U has the form of V, and typically, is used only for small $||a||_\infty$If $||a||_\infty^2$ is replaced with a stepsize τ, when the first order trotterization is applied $1/\tau$ times, the error approaches zero as τ goes to 0. Of course, this requires longer and longer approximate circuits, and so is not desirable compared to other methods. Higher order trotterization schemes exist, which are discussed in several places.

When $A = iHt$, the problem of efficiently and accurately simulating e^A is referred to as Hamiltonian simulation, which has been studied extensively (and perhaps first introduced again by Lloyd in 1996). While the first-order trotterization is perhaps the most straightforward manner of Hamiltonian simulation, numerous efficient techniques have been developed with more favorable scaling, such as qubitization. As many of these require either deep circuits or extensive anciliary registers, their suitability for near-term quantum computation is more in question.

3.4 Quantum Algorithms for Quantum Chemistry

Once we have an eigenstate, there are many direct measurement schemes, such as the quantum phase estimation technique, that allow us to measure observables very efficiently using only a tool such as the quantum Fourier transform. However, preparing an eigenstate for a molecular system is still quite challenging.

A number of algorithms have emerged as potential candidates for preparing molecular eigenstates. We discuss a limited number here, focusing on the ground state preparation via the adiabatic algorithm, the variational quantum eigensolver, and imaginary time evolution. Numerous excited state methods have emerged as well, but more significant efforts have been made towards the ground state problem. A review of many of these methods can be found in Ref. [8].

3.4.1 Adiabatic State Preparation

The adiabatic algorithm was introduced by Farhi in 2000[9], and provides a means of state preparation via evolution of a slowly varying Hamiltonian. Specifically, given a Hamiltonian with a parameter $s \in [0, 1]$ that has eigenstates $|\psi(s)\rangle$ for each point s:

$$H(s) = H_0(1 - s) + sV \tag{3.54}$$

we prepare a state $|\phi(s)\rangle$ as an eigenstate of H_0, $|\psi_0(0)\rangle$. Let us define a timestep parameter τ, $s = t\tau$. From the adiabatic theorem we can show that if there is a nonzero energy gap between the $|\psi_0(s)\rangle$ and $|\psi_1\rangle$, then the

$$\lim_{\tau \to 0} |\langle \psi_0(1) | \phi(1) \rangle| = 1 \tag{3.55}$$

That is, if we vary the Hamiltonian with a small enough time step, we will remain in an instantaneous eigenstate, and we eventually we will reach a target eigenstate of the Hamiltonian up to a controllable error in τ. Specifically, given a minimum energy gap

$$g_{\min} = \min_s E_1(s) - E_0(s), \tag{3.56}$$

and derivative term:

$$\epsilon = \max_s |\langle \psi_1(s) | \frac{dH}{ds} | \psi_0(s) \rangle, \tag{3.57}$$

then we simply need to take $\tau << \frac{g^2}{\epsilon}$ in order to obtain the target ground state.

The adiabatic theorem has many benefits, namely that it is robust and easy to implement, requiring few measurements and a almost black-box means of state preparation. In practice however, the small step size is too costly for near-term devices. Also, a hallmark of strongly correlated systems is that there often exist degenerate energy states, making the adiabatic approach unsuitable for strongly correlated systems. Despite these limitations, the adiabatic approach has served as an inspiration for numerous algorithms and continues to be an area of active research.

3.4.2 Variational Quantum Eigensolver

The variational quantum eigensolver, or VQE, was introduced by Peruzzo et al. in 2014 [10]. The general idea of the variational quantum eigensolver is quite straightforward, and

provides a means to perform a hybrid quantum-classical algorithm, utilizing both quantum and classical resources. Additionally, it has proved to be well suited for imperfect and noisy-quantum devices. Though it was originally intended for physical simulations, it has led to several new avenues of research and adaptions for various applications, which broadly are called variational quantum algorithms (VQAs).

As originally introduced for the ground state problem, the variational quantum eigensolver begins with a state with a set of parameters $\{\theta_i\}$:

$$|\psi\rangle = |\psi(\theta)\rangle = U(\theta)|\psi_0\rangle \tag{3.58}$$

the variational quantum eigensolver then solves the problem:

$$E_{\text{VQE}} = \min_{\theta} \langle\psi(\theta)|\hat{H}|\psi(\theta)\rangle. \tag{3.59}$$

This is achieved iteratively through evaluations of the energy

$$E(\theta) = \langle\psi(\theta)|\hat{H}|\psi(\theta)\rangle, \tag{3.60}$$

on the quantum computer, and an optimization of the parameters θ with a classical optimization. For gradient-free optimization, only energy evaluations are needed, though for gradient-based techniques one requires separate circuits for each θ_i:

$$\frac{dE}{d\theta_i} = \langle\frac{d}{d\theta_i}\psi(\theta)|\hat{H}|\psi(\theta)\rangle + \langle\psi(\theta)|\hat{H}|\frac{d}{d\theta_i}\psi(\theta)\rangle. \tag{3.61}$$

Hessian-based approaches are possible, but in general, statistical fluctuations in the measured quantities lead to more robust approaches being needed. For small systems, derivative free approaches have been quite successful - though for larger systems the size of the parameter space can be quite challenging.

As mentioned above, the idea of using a variational ansatz is not specific to quantum simulation, and can be generalized in a number of different ways. The use of VQE applied to other target observables, or the inclusion of additional constraints in the optimization problem have led to numerous variational quantum algorithms.

The form of the ansatz also plays a critical role in the success of the VQE algorithm. Over the last few years, a number of ansatz for use in the variational quantum eigensolver have emerged. These can roughly be categorized as chemical-inspired ansatz, hardware-efficient heuristic ansatz, or application-inspired ansatz.

Chemical Inspired Ansatz

The unitary coupled cluster ansatz was one of the first proposed variational ansatz, and was indeed used in the seminal paper by Peruzzo. The unitary coupled cluster ansatz is defined essentially similar to the coupled cluster anstaz, but requires the cluster amplitude t to be antihermitian, so that the resulting form is unitary. As mentioned earlier, this allows for an actual implementation on a quantum device.

The singles and doubles UCC ansatz is defined as follows:

$$|\psi_{\text{UCCSD}}\rangle = \exp\left[\sum_{ia} t_a^i (a_i^\dagger a_a - a_a^\dagger a_i) + \sum_{i<j,a<b} t_{ab}^{ij} (a_i^\dagger a_j^\dagger a_b a_a - a_a^\dagger a_b^\dagger a_j a_i)\right] |\psi_{\text{HF}}\rangle \quad (3.62)$$

where like the coupled cluster ansatz, i, j are unoccupied orbitals and a, b are occupied orbitals, and t_a^i and t_{ab}^{ij} correspond with real variational parameters. To implement this, we usually separate the terms according to a first order trotterization.[11]

Work in the early 2000's studying the exponential form of the ansatz lead to the inclusion of a generalized ansatz, which is sometimes referred to as the generalized coupled cluster. A discussion of the relations between these ansatz forms and the contracted quantum eigensolver is seen in chapter. While an iterative UCCSD ansatz would be rather cumbersome and

scale quite poorly with respect to the number of parameters, a pair coupled cluster ansatz was introduced which had an iterative design and could increase the depth of the circuits by adding another generalized pair ansatz to the VQE ansatz. [12]

The adaptive derivative-based pseudo-trotterized ansatz (ADAPT-VQE) also is some what related to the idea of a unitary coupled cluster ansatz, as it choose the pool of operators from a generalized pool of single and double excitations [13].

Another family of ansatz that are physically inspired attempt to match the variational ansatz to a target evolution. In particular, simulated time evolution, and imaginary time evolution, both can be the targets of a variational optimization in the VQE. Note, the variational formulation of the imaginary time evolution operator requires some modifications to the normal procedure. Jastrow-factor inspired ansatz[14], which have some non-unitary contributions and require normalization via post processing, also have been seen to increase the flexibility of the VQE.

Hardware-Efficient Ansatz

While the ansatz forms are reasonable from the above discussion, in practice available hardware can have numerous limitations. This has resulted in the development of so called hardware-efficient, or heuristic ansatz designs. These range from using gates that are native to the device, to minimal sets of entanglers.

One such instance can be seen in the work of Kandala et al. in 2017, where molecular states were represented with single-qubit rotation gates intertwined with entangling CNOT gates [15]. Each rotation was paramterized, and additional flexiblity could be provided to the ansatz through increasing the depth or adding an additional 'layer' of the paramterized ansatz. Because a gate sequence like e^{iXX} does not commute with the number or projected spin operator, additional constraints are imposed as Lagrangian multipliers in the optimization.

For high quality simulations, care is usually taken to optimize the gate structure, particularly in the CNOT gates to optimally match the layout configuration of the available devices. These efforts can be seen in numerous quantum simulations.

Similar work also looks at minimally preserving basic physical properties, such as the projected spin and particle number.[16] An instance of a two-qubit number preserving gate is:

$$U_N = \begin{pmatrix} 1 & 0 & 0 & 0 \\ 0 & c & -s & 0 \\ 0 & s & c & 0 \\ 0 & 0 & 0 & 1 \end{pmatrix}. \tag{3.63}$$

While this does not always result in a gate that has a corresponding fermionic operator - number preserving operations end up being an important aspect of simulation that works for a different reason - the isomorphism of the set of fermionic wavefunction and the so-called qubit particle-wavefunctions, or wavefunctions prepared without fermionic antisymmetry considerations. This is explored in more detail in Chapter 11.

Application Inspired Ansatz

In some instances, the problem at hands requires a particular ansatz form. The generalized Pauli constraint inspired ansatz of chapters 5 and 6 are instances of implementing the above operator.

In other instances, the ansatz attempts to prepare not a chemical state, but is used as a tool to yield some underlying parameters of the system. There also are ansatz based on efficient product formulas of Pauli strings or other factors that are efficient in from the perspective of quantum computation.

3.4.3 Imaginary Time Evolution

If we consider time evolution, and then let $\tau = it$, τ represents evolution with respect to imaginary time. We can apply the imaginary time evolution operator:

$$|\psi\rangle \rightarrow e^{-\tau \hat{H}}|\psi\rangle \tag{3.64}$$

which carries out the evolution in imaginary time. The reason why this method is preferred over standard time evolution can be seen in the coefficients of the eigenstates $|\psi_k\rangle$:

$$e^{-\tau \hat{H}}|\psi\rangle = \sum_k e^{-\tau \hat{H}} c_k |\psi_k\rangle \tag{3.65}$$

$$= \sum_k e^{-\tau E_k} c_k |\psi_k\rangle. \tag{3.66}$$

As τ goes to infinity, the wavefunction coefficients will be dominated by the largest eigenvalue, and will converge exponentially quickly. However, the exponential operator here is non-unitary, and so cannot be natively employed on a quantum computer. Recent work has explored two methods of tackling this problem. The first finds the least-squares fit of the imaginary time evolution operator onto a local-set of unitaries [17]. This however requires significant tomography, and is only exact when the $N-$body unitary space is utilized. Another method involves using McLachlan's variational principle to find an ansatz that minimize the unitary evolution [18].

3.4.4 Error Mitigation Techniques

Error mitigation techniques include a heuristic and theoretical approaches for counteracting the effect of errors on a quantum computer. Error correction refers to the explicit quantum error correction codes and stabilizer formalism introduces for quantum computing, although in some instances one might argue that an error mitigation techniques does 'correct' a certain

type of error. We cover few here, noting that this is an extremely active and important area of research.

Post-Processing

As alluded to above, preserving the particle symmetry in a quantum simulation can greatly affect the performance. Unfortunately, it is rather common for higher or lower particle states to enter into a simulation. If $\langle N \rangle$ is included as a constraint in the optimization, it is likely that a larger variance will still remain, even if $\langle \hat{N} \rangle - N_{\text{target}}$ is close to 0.

We can first consider a projective error mitigation. Given the $j-$th result of $\langle \psi | M_i | \psi \rangle |_j$ of a measurement M_i for an N particle state, if M_i commutes with the number operator, such as with diagonal elements, then we can measure the number operator for that given result. This also applies to the projected spin operator $\hat{S}_z$.

Despite that all of the 2-RDM operators do commute with the number and projected spin operator, the transformed Pauli operators used generally do not commute, and so only the diagonal elements affecting the trace of the 2-RDM are corrected. While it would be desirable to correct the off-diagonal elements, an efficient way that does not introduce more errors into these measurements has not yet been developed. An instance of a diagonal and off-diagonal correction to the 1-RDM can be seen in Arute et al. [19]

A more general approach utilizes symmetries of the Hamiltonian [20], along with an additional measurement set, to project the measured quantum state into a proper symmetry state. These are generally taken to be symmetries of the Hamiltonian in the Pauli basis, and so do not include the number of and projected spin symmetries. Interestingly, a way of tapering symmetries of the Hamiltonian was later introduced, so that the Hamiltonian could be transformed prior to a run. An example of qubit tapering can be seen in 10. Because this restricts the state to the proper symmetry subspace prior to the quantum calculation, it could potentially be a more successful techniques. However, in the case that multiple symmetry

states are needed, one would use the more general approach, as tapering off qubits allows for only a single symmetry state to be utilized.

Another techniques which potentially requires only an additional set of measurements, is referred to as a quantum subspace expansion.[21] Given a reference state $|\psi\rangle$, one obtains the linear or quadratic response around $|\psi\rangle$, and then solves the generalized eigenvalue equation. That is, given a set of linear operators acting on the state:

$$\{a_i^\dagger a_j \rangle\} \tag{3.67}$$

we solve the generalized eigenvalue problem:

$$H_{LR}C = S_{LR}CE \tag{3.68}$$

where S_{LR} is the overlap matrix, and C is a coefficient matrix of eigenvectors. We can formulate this problem in terms of reduced density matrices, in which we can associated this with solving the associated configuration interaction singles problem. This leads to a set of eigenstates along the single excitation manifold, which is thought to dominate in some physical processes. Additionally, the resultant ground state is expanded around the linear subspace, and in so approaches the true solution. In practice, the linear expansion requires the 4-RDM (although this can be approximated using reconstruction based techniques). The methods was further expanded to include virtual contributions from inactive orbitals as well, allowing for higher accuracy calculations.

Extrapolative Techniques

Temme et al. in 2017 proposed the idea of extrapolating a noise source to the 0 noise limit[22, 23]. That is, given an observable O subject to a noise source paramterized by λ,

we can expand O in terms of λ:

$$O(\lambda) = O(0) + c_1\lambda + c_2\lambda^2 + ... \tag{3.69}$$

The above formulation is used commonly in Richardson extrapolation, where we are attempting to determine $O(0)$ given information on c_1, c_2, etc. One of the concerns is in the nature of noise source and simulating a truly controllable noise source. Because noise can be associated simply through the addition of more gates, one method is to insert a sequence of gates which is the identity in principle, but practically results in more noise, such as a pair of CNOT gates.

More recent work has explored using phase estimation to apply a phase to the quantum state, and then fit the phase to determine the coefficients of an eigenstate. Extrapolative techniques can also be used to determine other quantities, and were recently demonstrated for the simulation of open quantum systems. Several other techniques exist, though the general success or failure of many has not yet been demonstrated [24, 25].

References

[1] M. A. Nielsen and I. L. Chuang, *Cambridge University Press* (Cambridge University Press, Cambridge, 2010) p. 702, arXiv:arXiv:1011.1669v3 .

[2] J. S. Townsend, *A modern approach to quantum mechanics*, 2nd ed. (University Science Books, Mill Valley, California, 2012).

[3] B. C. Hall, (2000), arXiv:0005032 [math-ph] .

[4] J. Preskill, Quantum **2**, 79 (2018), arXiv:arXiv:1801.00862v3 .

[5] D. A. Lidar, (2019), arXiv:1902.00967 .

[6] J. T. Seeley, M. J. Richard, and P. J. Love, The Journal of Chemical Physics **137**, 224109 (2012), arXiv:1208.5986 .

[7] S. B. Bravyi and A. Y. Kitaev, Journal of Chemical Physics **298**, 210 (2000), arXiv:0003137 [quant-ph] .

[8] S. McArdle, S. Endo, A. Aspuru-Guzik, S. C. Benjamin, and X. Yuan, Reviews of Modern Physics **92**, 015003 (2020), arXiv:1808.10402 .

[9] E. Farhi, J. Goldstone, S. Gutmann, and M. Sipser, (2000), quant-ph/0001106, arXiv:0001106 [quant-ph] .

[10] A. Peruzzo, J. McClean, P. Shadbolt, M.-H. Yung, X.-Q. Zhou, P. J. Love, A. Aspuru-Guzik, and J. L. O'Brien, Nature Communications **5**, 4213 (2014), arXiv:1304.3061 .

[11] J. Romero, R. Babbush, J. R. McClean, C. Hempel, P. J. Love, and A. Aspuru-Guzik, Quantum Science and Technology **4**, 1168 (2019), arXiv:1701.02691 .

[12] J. Lee, W. J. Huggins, M. Head-Gordon, and K. B. Whaley, Journal of Chemical Theory and Computation **15**, 311 (2018), arXiv:1810.02327 .

[13] H. R. Grimsley, S. E. Economou, E. Barnes, and N. J. Mayhall, Nature Communications **10**, 3007 (2018), arXiv:1812.11173 .

[14] F. Benfenati, G. Mazzola, C. Capecci, P. K. Barkoutsos, P. J. Ollitrault, I. Tavernelli, and L. Guidoni, Journal of Chemical Theory and Computation **17**, 3946 (2021), arXiv:2101.09316 .

[15] A. Kandala, A. Mezzacapo, K. Temme, M. Takita, M. Brink, J. M. Chow, and J. M. Gambetta, Nature **549**, 242 (2017), arXiv:1704.05018 .

[16] B. T. Gard, L. Zhu, G. S. Barron, N. J. Mayhall, S. E. Economou, and E. Barnes, npj Quantum Information **6** (2020), 10.1038/s41534-019-0240-1, arXiv:1904.10910 .

[17] M. Motta, C. Sun, A. T. Tan, M. J. O'Rourke, E. Ye, A. J. Minnich, F. G. Brandão, and G. K. L. Chan, Nature Physics **16**, 205 (2020), arXiv:1901.07653 .

[18] S. McArdle, T. Jones, S. Endo, Y. Li, S. C. Benjamin, and X. Yuan, npj Quantum Information **5**, 75 (2019), arXiv:1804.03023 .

[19] F. Arute, K. Arya, R. Babbush, D. Bacon, J. C. Bardin, R. Barends, S. Boixo, M. Broughton, B. B. Buckley, D. A. Buell, B. Burkett, N. Bushnell, Y. Chen, Z. Chen, B. Chiaro, R. Collins, W. Courtney, S. Demura, A. Dunsworth, E. Farhi, A. Fowler, B. Foxen, C. Gidney, M. Giustina, R. Graff, S. Habegger, M. P. Harrigan, A. Ho, S. Hong, T. Huang, W. J. Huggins, L. Ioffe, S. V. Isakov, E. Jeffrey, Z. Jiang, C. Jones, D. Kafri, K. Kechedzhi, J. Kelly, S. Kim, P. V. Klimov, A. Korotkov, F. Kostritsa, D. Landhuis, P. Laptev, M. Lindmark, E. Lucero, O. Martin, J. M. Martinis, J. R. McClean, M. McEwen, A. Megrant, X. Mi, M. Mohseni, W. Mruczkiewicz, J. Mutus, O. Naaman, M. Neeley, C. Neill, H. Neven, M. Y. Niu, T. E. O'Brien, E. Ostby, A. Petukhov, H. Putterman, C. Quintana, P. Roushan, N. C. Rubin, D. Sank, K. J. Satzinger, V. Smelyanskiy, D. Strain, K. J. Sung, M. Szalay, T. Y. Takeshita, A. Vainsencher, T. White, N. Wiebe, Z. J. Yao, P. Yeh, and A. Zalcman, Science **369**, 1084 (2020), arXiv:2004.04174 .

[20] X. Bonet-Monroig, R. Sagastizabal, M. Singh, and T. E. O'Brien, Physical Review A **98**, 062339 (2018).

[21] J. R. McClean, M. E. Kimchi-Schwartz, J. Carter, and W. A. de Jong, Physical Review A **95**, 042308 (2017), arXiv:1603.05681 .

[22] K. Temme, S. Bravyi, and J. M. Gambetta, Physical Review Letters **119**, 1 (2017), arXiv:1612.02058 .

[23] A. Kandala, K. Temme, A. D. Córcoles, A. Mezzacapo, J. M. Chow, and J. M. Gambetta, Nature **567**, 491 (2019), arXiv:1805.04492 .

[24] T. E. O'Brien, S. Polla, N. C. Rubin, W. J. Huggins, S. McArdle, S. Boixo, J. R. McClean, and R. Babbush, , 1 (2020), arXiv:2010.02538 .

[25] N. C. Rubin, R. Babbush, and J. McClean, New Journal of Physics **20**, 053020 (2018), arXiv:1801.03524 .

Part II

Characterization of Noisy Quantum Systems for Many-Body Simulations

CHAPTER 4

EXPERIMENTALLY DEMONSTRATING PURE N-REPRESENTABILITY CONSTRAINTS ON A QUANTUM COMPUTER

4.1 Introduction

While performing calculations with classical computers at IBM, Borland and Dennis discovered something unexpected and surprising about the electronic structure of atoms and molecules[1]. In 1926 Pauli had observed that no more than a single electron can occupy a given one-electron quantum state known as a spin orbital[2]. Formally, the Pauli exclusion principle implies that the spin-orbital occupations are rigorously bounded by zero and one. In their calculations Borland and Dennis discovered, however, that even in three-electron atoms and molecules there are additional constraints beyond the well-known exclusion principle. In 2006 Klyachko (and in 2008 with Altunbulak) presented a systematic mathematical procedure for generating these constraints for potentially arbitrary numbers of electrons and orbitals[3, 4]. These inequalities, which have become known as generalized Pauli constraints[5–8], provide new insights into the electron structure of many-electron atoms and molecules[7, 9–12], the limitations of entanglement as a resource for quantum control[13, 14], as well as the fundamental distinctions between open and closed quantum systems[15].

In this work we use quantum states prepared on a quantum computer to provide experimental verification of the generalized Pauli constraints. Quantum computers differ from

classical computers in that quantum states can be prepared on the quantum computer. Algorithms which utilize these quantum states promise a large computational advantage over known classical algorithms for solving critically important problems such as integer factorization, eigenvalues estimation, and fermionic simulation[16–19]. Rapid advances in quantum hardware and hybrid classical-quantum algorithms have led to multi-qubit experimental implementations[20–22]. We first randomly prepare the quantum state of a 3-electron system and second measure the occupations of the natural orbitals. The natural orbitals are the eigenfunctions of the 1-electron reduced density matrix (1-RDM) that is defined by integrating the many-electron density matrix over the coordinates of all electrons except one

$$^1D(1;\bar{1}) = \int \Psi(123)\Psi^*(\bar{1}23)d2d3 \tag{4.1}$$

in which $\Psi(123)$ is the 3-electron wave function. The two-step process is repeated many times on the quantum computer to explore all possible physically realizable orbital occupations. Because of the generalized Pauli constraints a large convex set of orbital occupations should be experimentally forbidden. In contrast to the classical computations of Borland and Dennis, we are not representing the quantum states by matrices but rather preparing quantum states directly, which allows us to measure the orbital occupations experimentally.

4.2 Results

4.2.1 Measurement of 1-RDM Eigenvalues

Pauli observed in 1926 that for quantum systems of fermion particles such as electrons the occupation n_i of each spin orbital must obey the following inequalities:

$$0 \leq n_i \leq 1, \tag{4.2}$$

known as the Pauli exclusion principle or Pauli constraints. In 1963 Coleman proved mathematically that these constraints plus a normalization constraint in which the occupation numbers sum to N are necessary and sufficient for the occupation numbers n_i to represent at least one ensemble state of N electrons[23]. Borland and Dennis in 1972, however, discovered that there exist additional conditions on the occupation numbers for the representation of at least one pure state of N electrons, which are presently known as the generalized Pauli constraints[1]. A pure state is a quantum state that is describable by a single wave function. Borland and Dennis found the following generalized Pauli constraints for three electrons in six orbitals:

$$n_5 + n_6 - n_4 \geq 0 \tag{4.3}$$

where

$$n_1 + n_6 = 1 \tag{4.4}$$

$$n_2 + n_5 = 1 \tag{4.5}$$

$$n_3 + n_4 = 1, \tag{4.6}$$

where n_i are the natural-orbital occupations ordered from largest to smallest.

To test the generalized Pauli constraints on a quantum computer, we prepare an initial pure state $|\Psi_0(123)\rangle$ of 3 fermions in 6 orbitals and perform arbitrary unitary transformations $\hat{U}_i$ of the initial state to generate a set of random pure states $|\Psi_i(123)\rangle$ of 3 fermions in 6 orbitals

$$|\Psi_i(123)\rangle = \hat{U}_i|\Psi_0(123)\rangle. \tag{4.7}$$

We measure the matrix elements of the 1-RDM of each state $|\Psi_i(123)\rangle$ generated on the quantum computer and check each 1-RDM to verify satisfaction of the generalized Pauli constraints for 3 fermions in 6 orbitals. The 1-RDM is diagonalized on a classical computer and the eigenvalues (natural occupation numbers) are inserted into the generalized Pauli

constraints to check for satisfaction. The eigenvalues of the 1-RDM, ordered from highest to lowest, form a special type of convex set with "flat" sides known as a polytope. The boundaries or "flat" sides of the polytope are determined by the Pauli and generalized Pauli constraints. Suppose the experimental data satisfies the Pauli constraints but not the generalized Pauli constraints, then the smallest 3 eigenvalues of each measured 1-RDM will describe the Pauli polytope which is shown as the combined yellow and blue regions in Fig. 4.1. On the other hand, suppose the experimental data obeys not only the Pauli constraints but also the generalized Pauli constraints, then the smallest 3 eigenvalues of each measured 1-RDM will only describe the smaller generalized Pauli polytope, pictured as just the yellow region in Fig. 4.1. Comparison of the measured scatter plot of 1-RDM eigenvalues with these two polytopes provides an experimental means of observing the generalized Pauli constraints and thereby verifying their validity in a quantum system.

The system of 3 fermions in 6 orbitals can be expressed as a system of 3 qubits, allowing the above procedure to be simplified. Because the occupations of each pair, $\{n_1, n_6\}$, $\{n_2, n_5\}$, and $\{n_3, n_4\}$, must sum to one, the three electron systems has a one-to-one mapping to a system of three qubits. The occupation numbers n_4, n_5, and n_6, which are eigenvalues of the 1-RDM, can be viewed as the eigenvalues p_1, p_2, and p_3 of the 1-qubit reduced density matrix of a three-qubits system. Hence, for the three-qubits system the generalized Pauli constraints in Eqs. 4.3-4.6 can be written as the single inequality

$$p_2 + p_3 - p_1 \geq 0, \tag{4.8}$$

which was first obtained by Higuchi in 2002[24]. The Higuchi inequalities for N qubits are a subset of the generalized Pauli constraints for N electrons in $2N$ orbitals. In the case of three electrons in six orbitals the Higuchi inequality is equivalent to the generalized Pauli constraint in Eq. (4.3) under the assumption that Eqs. 4.4-4.6 hold. In the quantum computation we exploit this relationship to represent the 3 electron in 6 orbital quantum

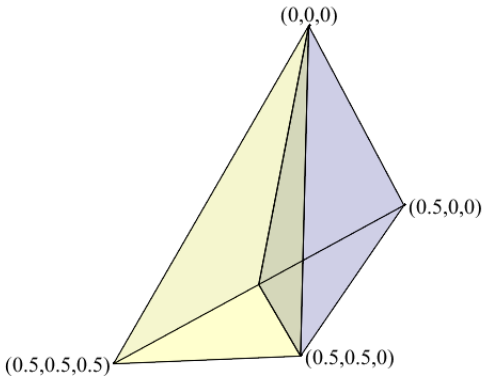

Figure 4.1: Orbital occupations of the 1-electron reduced density matrix (1-RDM) form convex polytopes. The eigenvalues (natural occupations) of the 1-RDM, ordered from largest to smallest, form a special convex set with "flat" sides known as a polytope. Because the three smallest eigenvalues for a 3-electrons-in-6-orbitals state (n_4, n_5, n_6) determine the other eigenvalues, we can visualize the polytope in three dimensions. The figure shows two polytopes: (*i*) the Pauli polytope of eigenvalues obeying the ordinary Pauli constraints (the combination of the yellow and blue regions) as well as (*ii*) the generalized Pauli polytope of eigenvalues obeying the generalized Pauli constraints (the yellow region only). The plane separating the yellow and blue regions arises from the Borland-Dennis inequality shown in Eq. (4.3).

system efficiently as a 3 qubit system with a compact fermionic mapping, described in the Methods section. In this representation the violation of the Higuchi inequality in Eq. (4.8) is equivalent to the violation of the generalized Pauli inequality in Eq. (4.3).

The initial 3-qubit state is chosen to be the non-interacting state in which all 3 qubits are in their lower-energy (off) state. The arbitrary unitary transformations are generated on the quantum computer from

$$\mathbb{U}_a^1 = C_3^2 R_{y,3}(\theta_3) C_1^2 R_{y,1}(\theta_2) C_1^3 R_{y,1}(\theta_1), \tag{4.9}$$

where the parameters α, β, and γ in the Pauli rotation matrices $R_y(\alpha)$ are chosen randomly and the C_i^j are controlled NOT (CNOT) gates. The rotation matrices are applied to the control qubit of the ensuing CNOT gate. It is known that any 3-qubit state can be prepared from the non-interacting state by a unitary transformation built from only 3 CNOT gates plus universal single-qubit gates[25]. The above transformation generates states that span the most general entanglement class for the system and whose 1-qubit RDMs cover all possible real 1-qubit occupation numbers[14, 26, 27]. Computations were also performed with a slightly more general transformation, discussed in the Methods and Figure 4.4, albeit without a significant change in the results. Because of the mapping between the 3-qubit and the 3-fermion-in-6-orbitals system, the measured occupations p_1, p_2, and p_3 are equivalent to the natural occupations (eigenvalues) n_4, n_5, and n_6 of the 1-RDM. For the remainder of this work we primarily discuss the results in terms of the 3-fermion system.

4.2.2 Verification of Generalized Pauli Constraints

The scatter plot of the measured 1-RDM natural occupations is shown in Fig. 4.2 relative to the Pauli polytope, the combination of the yellow and blue regions, and the smaller generalized Pauli polytope, only the yellow region. Results show that the physical system only

accesses the generalized Pauli polytope (yellow), defined by the generalized Pauli constraints. None of the natural occupation numbers lie in the part (blue) of the Pauli polytope which is forbidden by the Borland-Dennis constraint. Therefore, the experimental data from the quantum computer verifies the generalization of the Pauli exclusion principle for pure states. Figure 4.4 visualizes the effect of error on the occupation numbers. We observe that the errors consistently push the triplet of occupations into the generalized Pauli polytope, which reflects upon the nature of the quantum noise. Despite the presence of quantum noise the fundamental result is statistically robust[14]. The Pauli polytope is twice the size of the generalized Pauli polytope. Consequently, without further restrictions beyond the ordinary Pauli constraints the probability of a randomly prepared state being in the yellow region would be one out of two. The probability of n random states being on the yellow side, therefore, would be $1/2^n$. With n being approximately 60, we observe that the probability of measuring all 60 points within the yellow region would be $1/2^{60}$ or a highly improbable one in one quintillion. Hence, we have verified the generalized Pauli exclusion principle by quantum computer to a high degree of confidence.

Despite the restrictions on the pure-state observables from the generalized Pauli constraints, the set of realizable 1-RDMs exhibits all limits of quantum behavior including the mean-field limit as well as the strong-electron-correlation limit including phenomena like superconductivity. Figure 4.3 shows examples of chemical systems which widely vary in the degree of correlation present. As observed in previous work, for 3-electron-in-6-orbital systems the ground-state triplet of occupation numbers (n_4, n_5, n_6) lies on the Borland-Dennis generalized Pauli constraint, separating pure and ensemble states in the set of 1-RDMs. Excited-state natural occupation numbers of these systems, in contrast, can lie on the generalized Pauli constraint like the ground states or elsewhere in the polytope, reflecting substantial variations in the one-electron properties of excited states[7]. The 3 lowest occupation numbers (n_4, n_5, n_6) can be readily expressed in the natural-orbital basis set in terms of

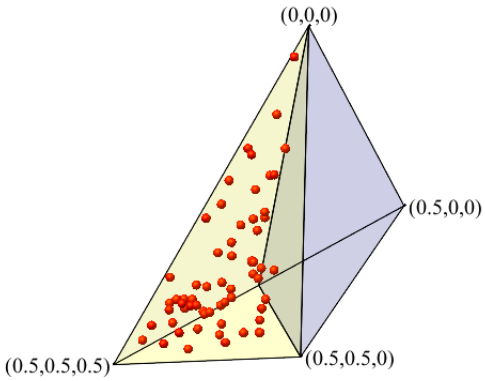

Figure 4.2: Measured orbital occupations verify generalized Pauli principle. The scatter plot of the three lowest measured 1-electron reduced density matrix (1-RDM) eigenvalues (n_4, n_5, n_6) is shown relative to the Pauli polytope, the combination of the yellow and blue regions, and the smaller generalized Pauli polytope, only the yellow region. Results show that none of the eigenvalues lie in the part (blue) of the Pauli polytope which is forbidden for pure quantum states by the Borland-Dennis constraint.

single, double, and triple excitations from the single determinant $|\phi_1\phi_2\phi_3\rangle$, composed of the 3 most occupied natural orbitals; for n_u where u indicates the index of one of the unoccupied orbitals of the reference determinant we have

$$n_u = \sum_i |c_i^u|^2 + \sum_{ija} |c_{ij}^{au}|^2 + \sum_{ijkab} |c_{ijk}^{abu}|^2 \tag{4.10}$$

in which i, j, and k denote indices of natural orbitals in the reference determinant and a and b denote indices of natural orbitals not in the reference determinant and c_i^u, c_{ij}^{au}, c_{ijk}^{abu} are the single-, double-, and triple-excitation coefficients. From the formula we observe that when (n_4, n_5, n_6) equals $(0, 0, 0)$, all of the excitation coefficients vanish, and the quantum state is the reference determinant $|\phi_1\phi_2\phi_3\rangle$. All other points in the polytope have contributions from one or more of the excitation coefficients. The triple excitations vanish when the natural occupation numbers (n_4, n_5, n_6) are pinned to the Borland-Dennis inequality[3, 4, 11]. The triplet of occupation numbers from ground and excited states tends to gravitate towards the

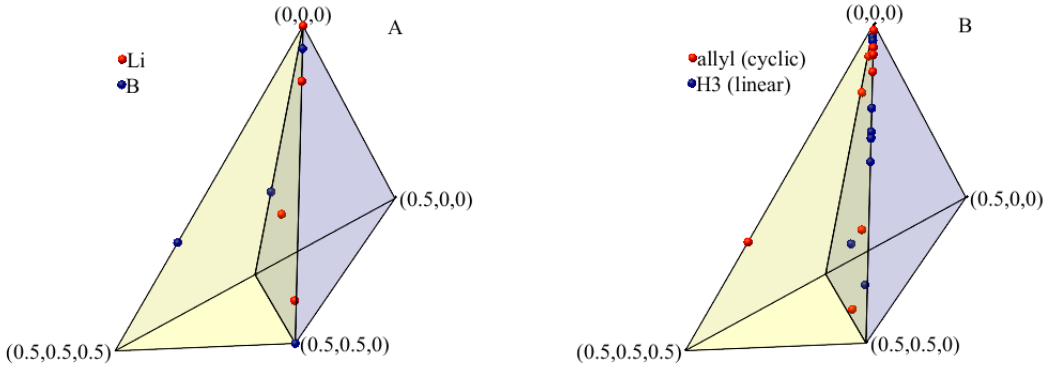

Figure 4.3: Orbital occupations of correlated 3-electron atoms and molecules. The lowest three eigenvalues (natural occupations) of the 1-electron reduced density matrix (1-RDM) for ground and excited states of 3-electron-in-6-orbital atoms and molecules (n_4, n_5, n_6) are shown: **a** Lithium atom (red) and the π orbitals of the Boron atom (blue). **b** Allyl radical in the cyclic form (C_3H_3, red) and linear H_3 (blue). The triplet of occupation numbers from ground and excited states tends to gravitate towards the boundaries of the polytope, reflecting the interplay between the energy optimization and the restrictions imposed on fermions from the Pauli constraints. These eigenvalues were calculated by full configuration interaction on a classical computer.

boundaries of the polytope, reflecting the interplay between the energy optimization and the restrictions imposed on fermions from the Pauli constraints.

4.3 Discussions

The generalized Pauli constraints, discovered by Borland and Dennis on a classical computer, have been verified through calculations with a quantum computer. While a quantum state is represented by vectors and matrices on a classical computer, it is actually prepared and manipulated on a quantum computer. Consequently, the presented computations can be interpreted as experiments that are measuring the generalized Pauli constraints' satisfaction by the correlated quantum states generated on the computer. Using random unitary transformations to generate a statistical sample of the possible states, we observe that all of the states satisfy the generalized Pauli constraint, experimentally verifying the validity of the

constraint to a high degree of confidence. The generalized Pauli constraints have profound consequences for quantum phenomena. First, their existence proves fundamental limitations on quantum entanglement's ability to emulate one-electron occupations and properties of ensemble quantum states. Second, they imply the Higuchi inequalities and thereby place significant restrictions on many-qubit systems in pure states. These restrictions may provide an exploitable resource for efficient error correction. Finally, their recent extension to the two-electron reduced density matrix (2-RDM) provides new conditions for the 2-RDM to represent at least one many-electron pure-state quantum system[10]. Such conditions can potentially be used to enhance the direct variational calculation of the 2-RDM[28], which is applicable to treating strongly correlated atomic and molecular quantum systems at a polynomial-scaling computational cost[29–31].

4.4 Methods

We include details on the quantum algorithm used in the article and its variants, the method for generating the parameters, the quantum tomography of the one-electron reduced density matrix, and relevant details on the experimental quantum device used.

Quantum Algorithms

Two algorithms were used in this work. Both utilize 3 CNOT gates, which allow for the whole set of 3-qubit occupation numbers to be spanned with suitable single qubit rotations. A single CNOT can form a biseperable system, while two CNOT gates can reach the GHZ state and spread a far range of the polytope, but three CNOT gates are required to saturate the Higuchi inequality[24–27]. Complex unitary transformations can be used, increasing the set of all possible quantum states, but these transformations span the same set of occupations as real rotations.

The first algorithm takes a minimalistic approach, and spans the polytope by parame-

terizing only three rotations. The algorithm (applied right to left) is as follows:

$$\mathbb{U}_a^1 = C_3^2 R_{y,3}(\theta_3) C_1^2 R_{y,1}(\theta_2) C_1^3 R_{y,1}(\theta_1), \tag{4.11}$$

where $R_{y,i}$ refers to a qubit rotation around the y-axis of the Bloch Sphere onto the ith qubit (later we drop the y, as we only use R_y rotations), defined as:

$$R_{y,i}(\theta) = \begin{pmatrix} \cos(\frac{\theta}{2}) & -\sin(\frac{\theta}{2}) \\ \sin(\frac{\theta}{2}) & \cos(\frac{\theta}{2}) \end{pmatrix}. \tag{4.12}$$

C_i^j is the standard CNOT gate with i control and j target qubits. The control qubit is rotated prior to a CNOT transformation. The sequence of transformations produce a wave function of the form:

$$|\Psi_f\rangle = \alpha|000\rangle + \beta|011\rangle + \gamma|101\rangle + \delta|110\rangle, \tag{4.13}$$

where α, β, γ, and δ are all functions of θ_1, θ_2, and θ_3, and the wave function has no diagonal elements in the 1-RDM.

The second algorithm provides a over-redundant representation of the system, including some local degrees of freedom[27], and involves rotations on both the target and control qubit prior to the rotation, and is as follows:

$$\mathbb{U}_a^2 = C_3^1 R_3(\theta_6) R_1(\theta_5) C_2^3 R_2(\theta_4) R_3(\theta_3) C_2^1 R_2(\theta_2) R_1(\theta_1), \tag{4.14}$$

Note that the CNOT identity

$$C_1^2 = H_1 H_2 C_2^1 H_1 H_2 \tag{4.15}$$

implies that by performing certain single-qubit rotations on both qubits, we somewhat eliminate the dependence of the qubit orderings with a generic rotation. Of course the wave function is of a more general form, involving all 8 qubit states, and so the off-diagonal elements need to be determined.

Parameter Generation

The parameters for each run were obtained by classically simulating the circuit over a range of parameters (from 0° to 45° in 0.1° intervals), calculating the theoretical eigenvalues after applying a given algorithm, and then either: 1) adding the point to a set if a point was further from all other points by a set distance, or; 2) discarding the point. Thus for the first algorithm we sampled 90 million points, and for the second, 8 quadrillion. The minimum distance for inclusion was 0.075. Only 62 and 59 points were selected for the first and second respectively. More points could have been used, but this would not have provided additional clarity, due to the scale of the shifts from errors. In general, unbiased random sampling did not yield 'graphically' uniform sets, as the occupation numbers are not a uniform distribution, leading to the occurence of clustering in certain areas of the polytope.

Quantum Tomography of the 1-RDM

The quantum tomography of the 3-electrons-in-6-orbitals system is simplified by its mapping to a system of 3 qubits. We derive the unitary transformations required to perform quantum tomography of the 1-RDM for a completely general many-electron state and outline the simplified application of this tomography for the 3-electrons-in-6-orbitals system.

Consider the unitary transformation in terms of the rotation angle ϕ

$$U = e^{\phi\hat{\alpha}} \tag{4.16}$$

where

$$\hat{\alpha} = (\hat{a}_i^\dagger \hat{a}_j - \hat{a}_j^\dagger \hat{a}_i) \tag{4.17}$$

where $\hat{a}_i^\dagger$ and $\hat{a}_i$ are second-quantized operators that create and annihilate an electron in orbital i. We can express this unitary transformation U in the following closed form:

$$e^{\phi\hat{\alpha}} = \hat{\beta}\cos\phi + \hat{\alpha}\sin\phi + (1-\hat{\beta}), \tag{4.18}$$

where

$$\hat{\beta} = \hat{a}_i^\dagger \hat{a}_i + \hat{a}_j^\dagger \hat{a}_j + \hat{a}_i^\dagger \hat{a}_j^\dagger \hat{a}_i \hat{a}_j + \hat{a}_j^\dagger \hat{a}_i^\dagger \hat{a}_j \hat{a}_i. \tag{4.19}$$

Using the Baker-Campbell-Hausdorff expansion, we evaluate the unitary transformation of the projection operator $\hat{M}$ for measuring the occupation of the i^{th} orbital

$$e^{-\phi\hat{\alpha}} \hat{M} e^{\phi\hat{\alpha}} = i^\dagger i + \frac{\hat{\zeta}}{2}\sin 2\phi - \hat{\eta}\sin^2\phi \tag{4.20}$$

where

$$\hat{M} = \hat{a}_i^\dagger \hat{a}_i \tag{4.21}$$

and

$$\hat{\zeta} = \hat{a}_i^\dagger \hat{a}_j + \hat{a}_j^\dagger \hat{a}_i \tag{4.22}$$

$$\hat{\eta} = \hat{a}_i^\dagger \hat{a}_i - \hat{a}_j^\dagger \hat{a}_j. \tag{4.23}$$

If we set the angle ϕ to $\pi/4$ and take the expectation value with respect to the quantum state $|\Psi\rangle$, we obtain

$$\langle\Psi| e^{-\frac{\pi}{4}\hat{\alpha}} \hat{M} e^{\frac{\pi}{4}\hat{\alpha}} |\Psi\rangle = \frac{1}{2}\left({}^1D_i^i + {}^1D_j^j + {}^1D_j^i + {}^1D_i^j\right) \tag{4.24}$$

in which ${}^1D^i_j$ denotes an element of the 1-RDM. Therefore, by taking expectation values for the diagonal elements of the family of 1-RDMs from these unitary transformations, we obtain information about all of the elements of the 1-RDM from which we can obtain its off-diagonal elements. While these transformations are sufficient to determine the real part of the 1-RDM, in the case that the 1-RDM has a non-vanishing imaginary component, we must also consider the unitary transformations where $\hat{\alpha}$ is defined as

$$\hat{\alpha} = i(\hat{a}^\dagger_i \hat{a}_j + \hat{a}^\dagger_j \hat{a}_i). \tag{4.25}$$

By an analogous procedure we obtain

$$\langle \Psi | e^{-\frac{\pi}{4}\hat{\alpha}} \hat{M} e^{\frac{\pi}{4}\hat{\alpha}} | \Psi \rangle = \frac{1}{2}\left({}^1D^i_i + {}^1D^j_j + i({}^1D^i_j - {}^1D^j_i) \right). \tag{4.26}$$

from which we can extract the imaginary off-diagonal elements of the 1-RDM.

Because of Eqs. (4.4-4.6) of the Borland-Dennis constraints the 6 natural orbitals of the 3-electrons-in-6-orbitals system can be paired to form 3 qubits where each qubit is a two-level system sharing an electron. We can restrict the one-body unitary transformation in Eq. (4.16) to indices i and j representing orbitals of the same qubit because other choices violate the restriction of one electron per qubit. Hence, the one-body fermionic unitary transformation can be represented as a unitary transformation of a single qubit

$$U = \begin{pmatrix} \cos\phi & -\Gamma \sin\phi \\ \Gamma \sin\phi & \cos\phi, \end{pmatrix} \tag{4.27}$$

where Γ is a global phase from the antisymmetry of electrons. This mapping to qubits can be viewed as a member of the family of compact mappings [32]. Practically, this transformation is implemented in this study for $\phi = \pi/4$ as a product of the Hadamard gate H and a Pauli-Z gate Z. If $\Gamma = 1$ and $\phi = \pi/4$, then $U = HZ$, and if $\Gamma = 1$ and $\phi = \pi/4$, then $U = ZH$.

Quantum Computation

In this work we used the IBM Quantum Experience devices (ibmqx4 and ibmqx2), available online, in particular the 5-transmon quantum computing device[33]. These cloud accessible quantum devices are fixed-frequency transmon qubits with co-planer waveguide resonators[33, 34]. Experimental calibration for these devices is included below, and connectivity is specified there. Additionally, results are included in the Section

For our purpose, we tested varying number of iterations, and found that no significant decrease in the error of a run occurred by using more than 2048 repetitions, and so the primary and secondary experiments spanning the polytope utilized 2048 repetitions of the quantum algorithm. Additionally, for showing how error shifts the occupation of a pure state, we only utilized 1024 repetitions, as in 4.

Our target variable is the distance of the measured occupation to the ideal point. Let the mean of a run with 8192 iterations be the population mean, then define a random variable χ representing the distance from the ideal point after 32 iterations (which is 2^2 times the number of possible qubit states, could be larger but should at least be the size of the number of possible outcomes). For a point lying within the GPC polytope, generated with equation 4.11, where $\theta_1 = 43.0°$, $\theta_2 = 3.0°$, and $\theta_3 = 39.0°$, we find $\mu_\chi = 0.059$ and $\sigma_\chi = 0.056$. For 2048 and 1024 iterations, this yields a standard error of 0.007, and 0.010, respectively, and a 95% confidence interval would then be ± 0.014, and ± 0.020, respectively. For other points similar values were seen, typically with higher average μ_χ. Considering the scale of our problem, where shifts from the ideal occupation are typically closer to 0.1, and direction plays a significant role, one would not expect a significant difference in results upon increased iterations.

The three qubits with the lowest two-qubit gate error and the ordering of the qubit algorithm was specified for the device connectivity. The tomography utilized the transformations $U = HZ$ and $U = ZH$, and so only involves two circuits (diagonal and off-diagonal).

Table 4.1: Calibration Data. Calibration data from the primary and secondary algorithms on IBM's quantum computer is presented.

Device:	ibmqx2 ("Sparrow")					
Calibration Date:	2-23-2018					
Temperature (° K) :	0.0164					
Version:	3.0					
Buffer (ns):	6.7					
Gate time (ns):	83.3					
Qubit:	0	1	2	3	4	
T2 (μs) :	41.5	55.3	67.1	69.8	44.2	
f (GHz):	5.27603	5.21224	5.01541	5.28059	5.07117	
T1 (μs):	59.4	67.8	68.9	48.9	66.0	
Gate Error (10^{-3}):	1.98	1.29	1.98	1.63	0.94	
Readout Error (10^{-3}):	45	36	20	16	25	
Multi-Qubit:	01	02	12	32	34	42
Error (10^{-3})	34.6	40.7	32.6	27.6	22.3	26.6

Quantum Computer Calibration

Calibration data from the primary and secondary algorithms as provided by IBM's quantum computer is presented in Table 4.1[35].

Electronic Structure Calculations

Molecular geometries for C_3H_3 were taken from the Computational Chemistry Comparison and Benchmark Database[36], and for H_3 were calculated with Gaussian 09 with the coupled cluster singles and doubles method (CCSD)[37]. The basis set used Slater-type orbitals with three Gaussians (STO-3G). Electron integrals were obtained from General Atomic and Molecular Electronic Structure System (GAMESS)[38]. Maple [39] was used to perform a full configuration interaction (FCI) calculation with a QR method[40] for ground and excited states including their 1-RDMs.

4.5 Supplemental Information

Error Considerations If we consider a simple approach to the error, we can see how the polytope is preserved upon minimal errors. Define κ_i as:

$$\kappa_i = \lambda_i + \epsilon_i \tag{4.28}$$

Where κ is the experimental eigenvalue, λ_i is the pure state value, and ϵ is the shift in the eigenvalue from errors. Note this can be from a variety of errors[41]. Based on extremum ideal cases, we can get a picture of when the GPC will be violated.

Case 1: $\lambda_2 = \lambda_3$ The GPC's are satisfied when $\lambda_1 + \lambda_2 \leq \lambda_3 + 1$. So, if the GPC are satisfied experimentally, then:

$$\kappa_1 + \kappa_2 - \kappa_3 - 1 \leq 0 \tag{4.29}$$

$$\lambda_1 + \lambda_2 - \lambda_3 + \epsilon_1 + \epsilon_2 - \epsilon_3 - 1 = \tag{4.30}$$

$$\epsilon_1 + \epsilon_2 - \epsilon_3 \leq 1 - \lambda_1 \tag{4.31}$$

In this case, if λ_1 is far from 1, then errors are less likely to cause a violation of the GPC. For instance, if $\lambda_1 = 0.5$, then $\lambda_2 = \lambda_3 = 0.5$, and the system likely will satisfy the GPC.

Case 2: $\lambda_1 + \lambda_2 = \lambda_3 + 1$ If the Borland-Dennis constraints are saturated, then the system is on the verge of violating a pure state[1]. For the GPC to hold:

$$\epsilon_1 + \epsilon_2 - \epsilon_3 \leq 0. \tag{4.32}$$

This result is regardless of the ordering constraints. We note that shifts in the error have a tendency to push towards the inside of the polytope. For instance, if a λ_i is close to 1, then likely $\epsilon_i \leq 0$, and for points closer to 0.5, then $\epsilon_i \geq 0$. **Case 3: 4-Qubit Higuchi** For a 4 qubit case, the Higuchi inequality (which results from the generalized Pauli constraints

when qubit pairing is enforced) as an equality is [24]

$$\lambda_1 + \lambda_2 + \lambda_3 = 2 + \lambda_4 \tag{4.33}$$

If this point is violated, then the state is clearly not pure. So, if Eq. 4.33 is satisfied, we find:

$$\kappa_1 + \kappa_2 + \kappa_3 - \kappa_4 - 2 \leq 0 \tag{4.34}$$

$$\lambda_1 + \lambda_2 + \lambda_3 - \lambda_4 - 2 + \epsilon_1 + \epsilon_2 + \epsilon_3 - \epsilon_4 = \tag{4.35}$$

$$\epsilon_1 + \epsilon_2 + \epsilon_3 - \epsilon_4 \leq 0 \tag{4.36}$$

and,

$$\epsilon_4 \geq \epsilon_1 + \epsilon_2 + \epsilon_3. \tag{4.37}$$

Remarks For non-entangled points, such as (1,1,1) in the 3-qubit system, where $\epsilon_i \leq 0$ for evenly distributed qubit errors, the GPC's are likely to hold, as most of the terms will contribute negatively. For points further away, then the GPC's are not as likely to hold as error terms accumulate. Points such as the GHZ state, lie somewhat into the GPC polytope, and so are not as likely to openly violate these GPC. In the compact mapping the qubit structure is preserved.

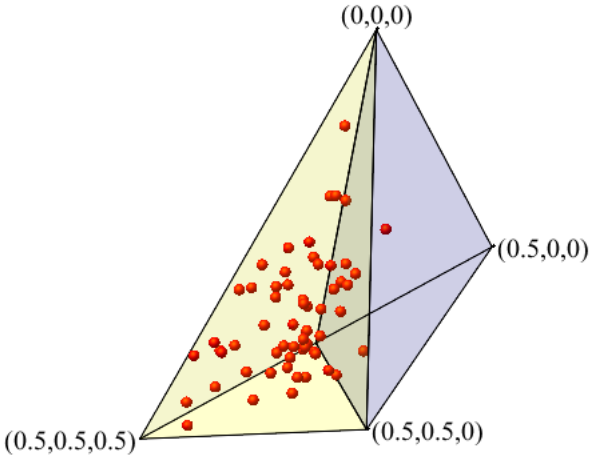

Figure 4.4: Each point represents the 3 largest eigenvalues of an experimental 1-RDM generated from the quantum computer. The algorithm used is the second quantum algorithm presented in the methods, equation 13, and the points represent executions of that algorithm with randomly selected parameters to achieve a total filling of the set. Note that two points did violate the generalize Pauli constraints, due to the propagation of error in the longer quantum circuit. There are a total of 59 points measured here, and so the validity of the confirmation of the generalized Pauli constraints still stands.

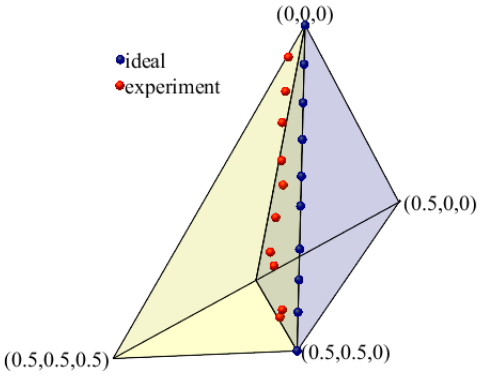

Figure 4.5: Shows the experimental (red) and ideal (blue) 3 largest eigenvalues of the 1-RDM generated by a single $C_i^j R_y$ on qubits i and j. The values are all shifted away form the vertex upon which true bipartite or separable states lie. Additionally, the shift in error in this case is to be pushed into the polytope.

4.5.1 Experimental Data

Parameters for First Algorithm (Equation 4.11)

Run	Parameters (radians)			Run	Parameters (radians)		
	λ_6	λ_5	λ_4		λ_6	λ_5	λ_4
01	0.000000	0.000000	0.000000	32	0.258309	0.827286	0.921534
02	0.558505	0.792379	0.387463	33	0.733038	1.462586	1.305506
03	1.476549	1.361357	0.136136	34	0.387463	1.103048	1.378810
04	1.172861	0.359538	1.134464	35	0.150098	1.368338	1.089085
05	1.050688	0.694641	0.516617	36	1.200787	0.219911	1.392773
06	1.322960	0.157080	0.474730	37	0.596903	1.305506	1.315978
07	1.403245	1.130973	0.561996	38	0.230383	1.064651	0.945968
08	1.284562	1.176352	0.191986	39	0.537561	1.005310	1.507964
09	0.272271	0.848230	0.467748	40	0.160570	1.246165	1.336922
10	0.534071	1.256637	0.150098	41	1.333432	1.445133	0.048869
11	1.361357	1.528908	0.568977	42	0.216421	1.204277	1.225221
12	0.879646	0.823795	0.373500	43	0.429351	1.249656	0.551524
13	0.551524	1.326450	0.680678	44	0.279253	0.073304	1.019272
14	0.855211	0.987856	1.528908	45	0.090757	0.781908	1.235693
15	0.879646	0.097738	0.970403	46	0.115192	1.036726	1.183333
16	0.031416	0.617847	0.104720	47	0.488692	1.249656	0.900590
17	0.094248	0.607375	0.492183	48	0.254818	0.788889	0.753982
18	1.434661	1.487021	1.120501	49	1.071632	1.490511	0.980875
19	1.354375	1.455605	0.342085	50	0.230383	1.022763	0.687660
20	0.914553	0.143117	0.101229	51	1.148427	0.691150	0.673697
21	0.680678	0.935496	0.394444	52	0.275762	1.134464	1.123992
22	0.767945	0.006981	0.080285	53	0.254818	0.649262	0.673697
23	1.029744	1.549852	0.017453	54	0.185005	1.406735	1.378810
24	1.434661	0.020944	0.254818	55	0.952950	1.570796	0.425860
25	0.952950	0.568977	1.392773	56	0.066323	1.459095	1.054179
26	1.567306	1.197296	0.411898	57	0.293215	0.443314	0.436332
27	0.139626	1.518436	1.542871	58	0.834267	1.036726	0.502655
28	0.090757	1.092576	0.600393	59	1.560324	1.570796	0.000000
29	0.013963	1.308997	0.652753	60	0.366519	1.424189	1.427679
30	0.638791	1.001819	1.078613	61	0.261799	1.473058	1.281072
31	0.164061	0.108210	0.408407	62	0.045379	1.504474	0.897099

Parameters for Second Algorithm (4.14)

Run	Parameters (radians)					
	θ_6	θ_5	θ_4	θ_3	θ_2	θ_1
01	0.000000	0.000000	0.000000	0.000000	0.000000	0.000000
02	1.123992	1.155408	0.565487	1.089085	0.586431	1.497492
03	1.452114	0.383972	0.603884	0.467748	0.258309	0.544543
04	1.200787	1.514946	0.024435	1.214749	1.403245	0.987856
05	0.921534	0.705113	1.075123	0.952950	0.722566	0.024435
06	0.760964	0.272271	0.066323	1.567306	0.104720	0.328122
07	1.459095	1.288053	0.457276	1.249656	1.158899	0.376991
08	0.397935	1.110029	1.043707	0.352557	0.083776	0.139626
09	0.321141	0.513127	0.027925	1.298525	0.851721	0.561996
10	0.942478	1.099557	0.181514	0.150098	0.020944	0.376991
11	0.247837	0.904081	1.165880	0.897099	1.521927	1.462586
12	1.068142	1.542871	0.125664	1.036726	0.216421	0.244346
13	0.167552	1.350885	0.139626	0.994838	0.317650	0.013963
14	0.544543	1.340413	0.356047	0.244346	1.036726	0.373500
15	1.064651	1.462586	0.010472	1.207768	1.078613	1.560324
16	0.335103	0.020944	0.792379	1.162389	0.411898	0.150098
17	1.151917	1.172861	0.589921	0.247837	0.925025	1.434661
18	0.226893	0.027925	0.394444	1.211259	0.760964	0.541052
19	0.443314	1.497492	0.380482	0.530580	0.492183	0.694641
20	0.157080	1.525418	0.136136	1.347394	0.705113	0.460767
21	0.338594	0.390954	0.474730	0.443314	1.085595	0.443314
22	0.555015	1.110029	0.383972	0.275762	1.385791	0.024435
23	0.000000	1.445133	1.452114	0.010472	0.024435	1.096067
24	0.006981	1.410226	0.038397	1.305506	0.897099	0.219911
25	0.041888	1.553343	0.027925	0.621337	0.370010	1.071632
26	0.006981	0.520108	0.247837	1.434661	0.188496	0.380482
27	1.308997	1.434661	0.132645	0.300197	1.127483	1.448623
28	0.108210	0.240855	1.560324	1.403245	0.139626	1.340413
29	1.040216	1.214749	0.115192	0.904081	0.740020	0.331613
30	0.324631	1.033235	0.502655	0.555015	1.392773	1.057670

Parameters for Second Algorithm (4.14)

Run	Parameters (radians)					
	λ_6	λ_5	λ_4	λ_3	λ_2	λ_1
31	0.324631	1.141445	0.052360	0.258309	0.621337	0.254818
32	0.610865	0.265290	1.427679	0.593412	0.555015	0.198968
33	0.146608	0.774926	0.638791	0.830777	1.075123	1.480039
34	0.293215	1.521927	0.003491	1.560324	0.991347	0.820305
35	0.352557	1.148427	0.715585	0.740020	0.527089	0.000000
36	0.010472	0.471239	1.567306	1.075123	0.289725	1.504474
37	0.474730	0.760964	1.549852	0.949459	0.181514	1.521927
38	0.160570	0.066323	0.048869	1.385791	0.816814	0.188496
39	0.034907	0.432842	1.497492	1.158899	0.984366	1.235693
40	0.781908	1.057670	0.157080	0.719076	0.897099	0.911062
41	1.497492	1.497492	0.090757	1.148427	0.041888	0.471239
42	0.125664	0.373500	1.385791	1.448623	0.858702	0.108210
43	0.289725	0.471239	0.205949	1.494002	0.558505	0.020944
44	1.291544	0.370010	0.855211	1.270600	0.010472	1.518436
45	0.628319	1.329941	0.841249	0.446804	1.183333	1.057670
46	0.076794	1.120501	0.205949	1.232202	0.254818	0.446804
47	0.764454	1.071632	1.473058	0.628319	0.429351	1.179843
48	0.198968	1.410226	0.876155	1.228712	0.181514	0.048869
49	0.219911	0.883137	0.314159	1.047198	1.242674	0.733038
50	1.452114	1.033235	0.223402	1.455605	0.188496	1.396263
51	1.539380	0.617847	0.122173	1.403245	0.136136	1.556834
52	0.132645	0.502655	0.474730	0.719076	0.893609	0.307178
53	0.373500	0.387463	0.013963	1.466077	0.310669	0.349066
54	0.045379	1.068142	0.247837	1.197296	0.663225	0.080285
55	0.069813	0.729548	1.190315	1.563815	1.302016	0.911062
56	0.415388	0.303687	1.406735	1.260128	0.240855	1.322960
57	0.010472	0.020944	0.108210	1.567306	1.448623	0.136136
58	0.286234	1.242674	0.167552	0.890118	0.013963	1.424189
59	0.635300	1.431170	0.174533	1.085595	1.350885	1.288053

Results for First Algorithm (4.11)

Run	Ideal Occupation Numbers						Experimental Occupation Numbers					
	λ_6	λ_5	λ_4	λ_3	λ_2	λ_1	λ_6	λ_5	λ_4	λ_3	λ_2	λ_1
01	0.000000	0.000000	0.000000	1.000000	1.000000	1.000000	0.039226	0.042805	0.048070	0.951930	0.957195	0.960774
02	0.103666	0.107409	0.202271	0.797729	0.892591	0.896334	0.142815	0.171985	0.264524	0.735476	0.828015	0.857185
03	0.330926	0.453381	0.490217	0.509783	0.546619	0.669074	0.360998	0.422781	0.454477	0.545523	0.577219	0.639002
04	0.155221	0.318631	0.418114	0.581886	0.681369	0.844779	0.213472	0.368537	0.412302	0.587698	0.631463	0.786528
05	0.028807	0.283942	0.309091	0.690909	0.716058	0.971193	0.118396	0.323277	0.402069	0.597931	0.676723	0.881604
06	0.026106	0.378856	0.390910	0.609090	0.621144	0.973894	0.111018	0.396069	0.422190	0.577810	0.603931	0.888982
07	0.082150	0.429441	0.464497	0.535503	0.570559	0.917850	0.149040	0.422178	0.491197	0.508803	0.577822	0.850960
08	0.226888	0.361423	0.445749	0.554251	0.638577	0.773112	0.239581	0.377324	0.440578	0.559422	0.622676	0.760419
09	0.070147	0.159385	0.181524	0.818476	0.840615	0.929853	0.160462	0.213392	0.268486	0.731514	0.786608	0.839538
10	0.074468	0.311032	0.367008	0.632992	0.688968	0.925532	0.130611	0.342262	0.379911	0.620089	0.657738	0.869389
11	0.219093	0.412422	0.495647	0.504353	0.587578	0.780907	0.270010	0.401232	0.446930	0.553070	0.598768	0.729990
12	0.080560	0.203262	0.283454	0.716546	0.796738	0.919440	0.161982	0.227369	0.334648	0.665352	0.772631	0.838018
13	0.169042	0.246016	0.396974	0.603026	0.753984	0.830958	0.202822	0.284957	0.408051	0.591949	0.715043	0.797178
14	0.173717	0.319426	0.486263	0.513737	0.680574	0.826283	0.207205	0.386298	0.421381	0.578619	0.613702	0.792795
15	0.182809	0.187845	0.319938	0.680062	0.812155	0.817191	0.227857	0.234617	0.345949	0.654051	0.765383	0.772143
16	0.002985	0.092637	0.093718	0.906282	0.907363	0.997015	0.064065	0.173661	0.191931	0.808069	0.826339	0.935935
17	0.061304	0.091247	0.125469	0.874531	0.908753	0.938696	0.146833	0.187845	0.193038	0.806962	0.812155	0.853167
18	0.037360	0.470466	0.494322	0.505678	0.529534	0.962640	0.118134	0.452276	0.467773	0.532227	0.547724	0.881866
19	0.283134	0.398854	0.487660	0.512340	0.601146	0.716866	0.289524	0.438042	0.461802	0.538198	0.561958	0.710476
20	0.001935	0.196489	0.198046	0.801954	0.803511	0.998065	0.115279	0.268338	0.286740	0.713260	0.731662	0.884721
21	0.128746	0.141266	0.269414	0.730586	0.858734	0.871254	0.197218	0.223855	0.339909	0.660091	0.776145	0.802782
22	0.001428	0.140339	0.141489	0.858511	0.859661	0.998572	0.085035	0.220149	0.225024	0.774976	0.779851	0.914965
23	0.242520	0.482052	0.494606	0.505394	0.517948	0.757480	0.299350	0.413123	0.417757	0.582243	0.586877	0.700650
24	0.013636	0.432157	0.434333	0.565667	0.567843	0.986364	0.116998	0.435517	0.446824	0.553176	0.564483	0.883002
25	0.209294	0.255991	0.448709	0.551291	0.744009	0.790706	0.276032	0.355805	0.465789	0.534211	0.644195	0.723968
26	0.146448	0.498401	0.499363	0.500637	0.501599	0.853552	0.206289	0.468853	0.477280	0.522720	0.531147	0.793711
27	0.429805	0.474086	0.486175	0.513825	0.525914	0.570195	0.403176	0.439546	0.445398	0.554602	0.560454	0.596824
28	0.089141	0.270847	0.287412	0.712588	0.729153	0.910859	0.142018	0.342894	0.362646	0.637354	0.657106	0.857982
29	0.102831	0.370603	0.393100	0.606900	0.629397	0.897169	0.134512	0.361751	0.392268	0.607732	0.638249	0.865488
30	0.151367	0.283733	0.310314	0.689686	0.716267	0.848633	0.214534	0.317372	0.362894	0.637106	0.682628	0.785466
31	0.009599	0.040304	0.047285	0.952715	0.959696	0.990401	0.089871	0.120461	0.140598	0.859402	0.879539	0.910129

Results for First Algorithm (4.11)

Run	Ideal Occupation Numbers						Experimental Occupation Numbers					
	λ_6	λ_5	λ_4	λ_3	λ_2	λ_1	λ_6	λ_5	λ_4	λ_3	λ_2	λ_1
32	0.172790	0.207730	0.220494	0.779506	0.792270	0.827210	0.265751	0.279746	0.287422	0.712578	0.720254	0.734249
33	0.164869	0.402577	0.459870	0.540130	0.597423	0.835131	0.221842	0.436499	0.452213	0.547787	0.563501	0.778158
34	0.291273	0.291455	0.411668	0.588332	0.708545	0.708727	0.321680	0.410045	0.413394	0.586606	0.589955	0.678320
35	0.270957	0.388515	0.400592	0.599408	0.611485	0.729043	0.284673	0.403027	0.450136	0.549864	0.596973	0.715327
36	0.313507	0.323542	0.467981	0.532019	0.676458	0.686493	0.360241	0.370191	0.458419	0.541581	0.629809	0.639759
37	0.204503	0.391574	0.395759	0.604241	0.608426	0.795497	0.249603	0.428764	0.487990	0.512010	0.571236	0.750397
38	0.215249	0.264000	0.277211	0.722789	0.736000	0.784751	0.248703	0.314914	0.354721	0.645279	0.685086	0.751297
39	0.267438	0.269873	0.473033	0.526967	0.730127	0.732562	0.294148	0.392426	0.450836	0.549164	0.607574	0.705852
40	0.342572	0.385617	0.389339	0.610661	0.614383	0.657428	0.376866	0.386204	0.429381	0.570619	0.613796	0.623134
41	0.382569	0.413855	0.485264	0.514736	0.586145	0.617431	0.359820	0.414965	0.424881	0.575119	0.585035	0.640180
42	0.324996	0.334582	0.344994	0.655006	0.665418	0.675004	0.355994	0.362831	0.438770	0.561230	0.637169	0.644006
43	0.112789	0.262089	0.356500	0.643500	0.737911	0.887211	0.175564	0.310471	0.384153	0.615847	0.689529	0.824436
44	0.020660	0.230114	0.248156	0.751844	0.769886	0.979340	0.141410	0.288038	0.320565	0.679435	0.711962	0.858590
45	0.146675	0.336243	0.353168	0.646832	0.663757	0.853325	0.282895	0.358960	0.410858	0.589142	0.641040	0.717105
46	0.247166	0.312331	0.358033	0.641967	0.687669	0.752834	0.360707	0.364623	0.376387	0.623613	0.635377	0.639293
47	0.225780	0.227412	0.360650	0.639350	0.772588	0.774220	0.264616	0.330907	0.423545	0.576455	0.669093	0.735384
48	0.147285	0.159059	0.181952	0.818048	0.840941	0.852715	0.239695	0.245027	0.278932	0.721068	0.754973	0.760305
49	0.114072	0.366852	0.480804	0.519196	0.633148	0.885928	0.183038	0.429483	0.484103	0.515897	0.570517	0.816962
50	0.123842	0.236842	0.246378	0.753622	0.763158	0.876158	0.219272	0.293998	0.345027	0.654973	0.706002	0.780728
51	0.017550	0.339818	0.342074	0.657926	0.660182	0.982450	0.112681	0.418504	0.429415	0.570585	0.581496	0.887319
52	0.292119	0.296674	0.297423	0.702577	0.703326	0.707881	0.317226	0.381252	0.426031	0.573969	0.618748	0.682774
53	0.114596	0.121858	0.141208	0.858792	0.878142	0.885404	0.209758	0.221236	0.234184	0.765816	0.778764	0.790242
54	0.395345	0.406224	0.419731	0.580269	0.593776	0.604655	0.368352	0.469881	0.472849	0.527151	0.530119	0.631648
55	0.236229	0.331633	0.500000	0.500000	0.668367	0.763771	0.328794	0.337507	0.422116	0.577884	0.662493	0.671206
56	0.253572	0.443838	0.444388	0.555612	0.556162	0.746428	0.344103	0.396047	0.412213	0.587787	0.603953	0.655897
57	0.064453	0.066187	0.067610	0.932390	0.933813	0.935547	0.159067	0.176161	0.185379	0.814621	0.823839	0.840933
58	0.123368	0.205683	0.329033	0.670967	0.794317	0.876632	0.181197	0.320269	0.412500	0.587500	0.679731	0.818803
59	0.494764	0.500000	0.500000	0.500000	0.500000	0.505236	0.442669	0.445291	0.480561	0.519439	0.554709	0.557331
60	0.314133	0.431810	0.433423	0.566577	0.568190	0.685867	0.314887	0.466136	0.492611	0.507389	0.533864	0.685113
61	0.362023	0.362636	0.452871	0.547129	0.637364	0.637977	0.327875	0.453837	0.457293	0.542707	0.546163	0.672125
62	0.188382	0.461640	0.466898	0.533102	0.538360	0.811618	0.286137	0.410971	0.419101	0.580899	0.589029	0.713863

Results for Figure 4

Run	Ideal Occupation Numbers			Experimental Occupation Numbers		
	λ_4	λ_5	λ_6	λ_4	λ_5	λ_6
1	0.000000	0.000000	0.000000	0.04949022	0.04636596	0.04492188
2	0.500000	0.500000	0.000000	0.45105483	0.44232491	0.05336489
3	0.17594	0.17594	0.000000	0.20804211	0.20492941	0.05612038
4	0.390928	0.390928	0.000000	0.36842836	0.367227	0.06869865
5	0.277682	0.277682	0.000000	0.29563694	0.29098368	0.06938023
6	0.060176	0.060176	0.000000	0.10236155	0.09833948	0.05071332
7	0.119231	0.119231	0.000000	0.14881748	0.14760163	0.05644493
8	0.440798	0.440798	0.000000	0.4378366	0.43333575	0.04527722
9	0.343833	0.343833	0.000000	0.34827726	0.34486482	0.08102623
10	0.232087	0.232087	0.000000	0.24951219	0.23755348	0.05553423

Results for Second Algorithm (4.14)

Run	Ideal Occupation Numbers						Experimental Occupation Numbers					
	λ_6	λ_5	λ_4	λ_3	λ_2	λ_1	λ_6	λ_5	λ_4	λ_3	λ_2	λ_1
01	0.000000	0.000000	0.000000	1.000000	1.000000	1.000000	0.078918	0.103023	0.131014	0.868986	0.896977	0.921082
02	0.153752	0.178404	0.208726	0.791274	0.821596	0.846248	0.240566	0.281498	0.343991	0.656009	0.718502	0.759434
03	0.025727	0.059079	0.059165	0.940835	0.940921	0.974273	0.123507	0.144244	0.266019	0.733981	0.855756	0.876493
04	0.038914	0.461198	0.471595	0.528405	0.538802	0.961086	0.064995	0.345330	0.446503	0.553497	0.654670	0.935005
05	0.055095	0.121064	0.140590	0.859410	0.878936	0.944905	0.073973	0.140226	0.338111	0.661889	0.859774	0.926027
06	0.167793	0.313775	0.374869	0.625131	0.686225	0.832207	0.187331	0.263089	0.272831	0.727169	0.736911	0.812669
07	0.033269	0.247206	0.247961	0.752039	0.752794	0.966731	0.096152	0.248068	0.325796	0.674204	0.751932	0.903848
08	0.009385	0.313721	0.316522	0.683478	0.686279	0.990615	0.091431	0.289006	0.296026	0.703974	0.710994	0.908569
09	0.248148	0.327048	0.436849	0.563151	0.672952	0.751852	0.171985	0.359896	0.368431	0.631569	0.640104	0.828015
10	0.184375	0.268598	0.320818	0.679182	0.731402	0.815625	0.285247	0.291111	0.336145	0.663855	0.708889	0.714753
11	0.293896	0.334283	0.354728	0.645272	0.665717	0.706104	0.302153	0.303650	0.329716	0.670284	0.696350	0.697847
12	0.323457	0.382480	0.439406	0.560594	0.617520	0.676543	0.341624	0.378933	0.405459	0.594541	0.621067	0.658376
13	0.237938	0.386440	0.478436	0.521564	0.613560	0.762062	0.185962	0.380418	0.471692	0.528308	0.619582	0.814038
14	0.229383	0.272568	0.378417	0.621583	0.727432	0.770617	0.222411	0.255855	0.397135	0.602865	0.744145	0.777589
15	0.105973	0.377052	0.452047	0.547953	0.622948	0.894027	0.126462	0.371115	0.477491	0.522509	0.628885	0.873538
16	0.090537	0.255454	0.294904	0.705096	0.744546	0.909463	0.056796	0.279712	0.324183	0.675817	0.720288	0.943204
17	0.089874	0.202033	0.218673	0.781327	0.797967	0.910126	0.137379	0.261174	0.263192	0.736808	0.738826	0.862621
18	0.096342	0.299131	0.340936	0.659064	0.700869	0.903658	0.065250	0.302003	0.331250	0.668750	0.697997	0.934750
19	0.080144	0.323003	0.401482	0.598518	0.676997	0.919856	0.166959	0.284433	0.396663	0.603337	0.715567	0.833041
20	0.242000	0.252059	0.438646	0.561354	0.747941	0.758000	0.223434	0.253290	0.413447	0.586553	0.746710	0.776566
21	0.108800	0.112709	0.213934	0.786066	0.887291	0.891200	0.120789	0.177183	0.228617	0.771383	0.822817	0.879211
22	0.267209	0.295098	0.304648	0.695352	0.704902	0.732791	0.213359	0.281179	0.341171	0.658829	0.718821	0.786641
23	0.265265	0.442480	0.442495	0.557505	0.557520	0.734735	0.371460	0.402289	0.467888	0.532112	0.597711	0.628540
24	0.159837	0.351466	0.497264	0.502736	0.648534	0.840163	0.241584	0.295702	0.477004	0.522996	0.704298	0.758416
25	0.080576	0.420363	0.498761	0.501239	0.579637	0.919424	0.190154	0.394846	0.460341	0.539659	0.605154	0.809846
26	0.193884	0.466044	0.496590	0.503410	0.533956	0.806116	0.092236	0.418655	0.428171	0.571829	0.581345	0.907764
27	0.047548	0.396358	0.408133	0.591867	0.603642	0.952452	0.124018	0.394527	0.408970	0.591030	0.605473	0.875982
28	0.373493	0.434878	0.454897	0.545103	0.565122	0.626507	0.324202	0.395647	0.395970	0.604030	0.604353	0.675798
29	0.233465	0.339212	0.370342	0.629658	0.660788	0.766535	0.244771	0.330616	0.439020	0.560980	0.669384	0.755229
30	0.176315	0.201138	0.352996	0.647004	0.798862	0.823685	0.218504	0.303902	0.457869	0.542131	0.696098	0.781496

Results for Second Algorithm (4.14)

Run	Ideal Occupation Numbers						Experimental Occupation Numbers					
	λ_6	λ_5	λ_4	λ_3	λ_2	λ_1	λ_6	λ_5	λ_4	λ_3	λ_2	λ_1
31	0.146941	0.303335	0.434666	0.565334	0.696665	0.853059	0.226388	0.411901	0.434399	0.565601	0.588099	0.773612
32	0.001246	0.107464	0.107722	0.892278	0.892536	0.998754	0.138326	0.266476	0.309763	0.690237	0.733524	0.861674
33	0.171730	0.251651	0.394950	0.605050	0.748349	0.828270	0.268670	0.330075	0.454461	0.545539	0.669925	0.731330
34	0.206812	0.309447	0.492781	0.507219	0.690553	0.793188	0.216635	0.264843	0.398720	0.601280	0.735157	0.783365
35	0.116246	0.366136	0.372274	0.627726	0.633864	0.883754	0.086600	0.327322	0.369614	0.630386	0.672678	0.913400
36	0.463862	0.486709	0.489756	0.510244	0.513291	0.536138	0.284285	0.404775	0.435434	0.564566	0.595225	0.715715
37	0.263257	0.392842	0.396853	0.603147	0.607158	0.736743	0.238765	0.297279	0.355256	0.644744	0.702721	0.761235
38	0.380470	0.382360	0.493998	0.506002	0.617640	0.619530	0.194689	0.420481	0.474902	0.525098	0.579519	0.805311
39	0.303408	0.476487	0.479921	0.520079	0.523513	0.696592	0.340724	0.382721	0.383292	0.616708	0.617279	0.659276
40	0.220524	0.220913	0.294919	0.705081	0.779087	0.779476	0.231396	0.283722	0.493359	0.506641	0.716278	0.768604
41	0.436609	0.439744	0.441957	0.558043	0.560256	0.563391	0.400117	0.480684	0.489734	0.510266	0.519316	0.599883
42	0.001990	0.363695	0.364423	0.635577	0.636305	0.998010	0.107581	0.293300	0.345993	0.654007	0.706700	0.892419
43	0.371511	0.380129	0.384290	0.615710	0.619871	0.628489	0.220629	0.334427	0.438848	0.561152	0.665573	0.779371
44	0.033087	0.173960	0.187170	0.812830	0.826040	0.966913	0.409690	0.445214	0.465246	0.534754	0.554786	0.590310
45	0.147571	0.155183	0.272524	0.727476	0.844817	0.852429	0.186937	0.218045	0.331956	0.668044	0.781955	0.813063
46	0.139847	0.434040	0.476786	0.523214	0.565960	0.860153	0.122467	0.364806	0.393065	0.606935	0.635194	0.877533
47	0.152199	0.222812	0.269730	0.730270	0.777188	0.847801	0.282675	0.310433	0.406442	0.593558	0.689567	0.717325
48	0.094651	0.163577	0.167172	0.832828	0.836423	0.905349	0.088010	0.197020	0.212054	0.787946	0.802980	0.911990
49	0.170485	0.408445	0.410048	0.589952	0.591555	0.829515	0.220707	0.355858	0.445915	0.554085	0.644142	0.779293
50	0.222912	0.227862	0.228681	0.771319	0.772138	0.777088	0.385862	0.396879	0.399569	0.600431	0.603121	0.614138
51	0.091112	0.092760	0.094342	0.905658	0.907240	0.908888	0.251955	0.274392	0.299091	0.700909	0.725608	0.748045
52	0.124431	0.238200	0.352610	0.647390	0.761800	0.875569	0.114666	0.260593	0.355927	0.644073	0.739407	0.885334
53	0.325790	0.327103	0.480450	0.519550	0.672897	0.674210	0.172065	0.355264	0.406289	0.593711	0.644736	0.827935
54	0.275652	0.289028	0.482934	0.517066	0.710972	0.724348	0.203269	0.327830	0.446083	0.553917	0.672170	0.796731
55	0.096284	0.192065	0.280743	0.719257	0.807935	0.903716	0.231994	0.252630	0.335351	0.664649	0.747370	0.768006
56	0.297597	0.298408	0.406909	0.593091	0.701592	0.702403	0.328527	0.353424	0.415444	0.584556	0.646576	0.671473
57	0.378964	0.489011	0.494729	0.505271	0.510989	0.621036	0.209195	0.385359	0.444718	0.555282	0.614641	0.790805
58	0.086966	0.436412	0.437119	0.562881	0.563588	0.913034	0.261557	0.446724	0.465678	0.534322	0.553276	0.738443
59	0.189415	0.348889	0.425569	0.574431	0.651111	0.810585	0.176874	0.331931	0.406250	0.593750	0.668069	0.823126

References

[1] R. E. Borland and K. Dennis, J. Phys. B At. Mol. Opt. **5**, 7 (1972).

[2] W. Pauli, Z. Phys. **31**, 765 (1925).

[3] A. A. Klyachko, J. Phys. Conf. Ser. **36**, 72 (2006), arXiv:0511102 [quant-ph] .

[4] M. Altunbulak and A. Klyachko, Commun. Math. Phys. **282**, 287 (2008), arXiv:0802.0918 .

[5] C. Schilling, D. Gross, and M. Christandl, Phys. Rev. Lett. **110**, 040404 (2013), arXiv:1210.5531 .

[6] C. L. Benavides-Riveros and M. Springborg, Phys. Rev. A **92**, 012512 (2015), arXiv:1409.6953 .

[7] R. Chakraborty and D. A. Mazziotti, Phys. Rev. A **89**, 042505 (2014), arXiv:arXiv:1404.5223v1 .

[8] C. Schilling, M. Altunbulak, S. Knecht, A. Lopes, J. D. Whitfield, M. Christandl, D. Gross, and M. Reiher, Phys. Rev. A , 052503 (2018), arXiv:1710.03074 .

[9] I. Theophilou, N. N. Lathiotakis, M. A. Marques, and N. Helbig, J. Chem. Phys. **142** (2015), 10.1063/1.4918346, arXiv:1503.0074 .

[10] D. A. Mazziotti, Phys. Rev. A **94**, 032516 (2016).

[11] C. L. Benavides-Riveros and C. Schilling, Z. Phys. Chem. **230**, 703 (2016), arXiv:1711.09129 .

[12] R. M. Erdahl, "The lower bound method for density matrices and semidefinite programming," in *Reduced-Density-Matrix Mechanics: With Application to Many-*

Electron Atoms and Molecules (John Wiley & Sons, Ltd, 2007) Chap. 4, pp. 61–91, https://onlinelibrary.wiley.com/doi/pdf/10.1002/9780470106600.ch4 .

[13] H. A. Rabitz, M. M. Hsieh, and C. M. Rosenthal, Science **303**, 1998 (2004), http://science.sciencemag.org/content/303/5666/1998.full.pdf .

[14] M. Walter, B. Doran, D. Gross, and M. Christandl, Science **340**, 1205 (2012), arXiv:1208.0365 .

[15] R. Chakraborty and D. A. Mazziotti, Phys. Rev. A **91**, 010101 (2015).

[16] P. W. Shor, SIAM. J. Comput. **26**, 1484 (1997), arXiv:9508027 [quant-ph] .

[17] D. S. Abrams and S. Lloyd, Phys. Rev. Lett. **79**, 2586 (1997), arXiv:9703054 [quant-ph] .

[18] S. B. Bravyi and A. Y. Kitaev, Ann. Phys. (N.Y.) **298**, 210 (2002), arXiv:0003137 [quant-ph] .

[19] T. Bian, D. Murphy, R. Xia, A. Daskin, and S. Kais, Preprint at arXiv:1804.05453, , 1 (2018), arXiv:1804.05453 .

[20] A. Kandala, A. Mezzacapo, K. Temme, M. Takita, M. Brink, J. M. Chow, and J. M. Gambetta, Nature **549**, 242 (2017), arXiv:1704.05018 .

[21] R. K. Naik, N. Leung, S. Chakram, P. Groszkowski, Y. Lu, N. Earnest, D. C. McKay, J. Koch, and D. I. Schuster, Nat. Commun. , 1 (2017), arXiv:1705.00579 .

[22] J. M. Gambetta, J. M. Chow, and M. Steffen, npj Quant. Inform. **3**, 2 (2017), arXiv:1510.04375 .

[23] A. J. Coleman, Rev. Mod. Phys. **35**, 668 (1963).

[24] A. Higuchi, A. Sudbery, and J. Szulc, Phys. Rev. Lett. **90**, 107902 (2003), arXiv:0209085 [quant-ph] .

[25] M. Žnidarič, O. Giraud, and B. Georgeot, Phys. Rev. A **77**, 032330 (2008).

[26] A. Acín, A. Andrianov, L. Costa, E. Jané, J. I. Latorre, and R. Tarrach, Phys. Rev. Lett. **85**, 1560 (2000), arXiv:0003050 [quant-ph] .

[27] A. Sudbery, J. Phys. A Math. Gen. **34**, 643 (2001), arXiv:0001116 [quant-ph] .

[28] D. A. Mazziotti, Phys. Rev. Lett. **117**, 153001 (2016).

[29] J. M. Montgomery and D. A. Mazziotti, J. Phys. Chem. A **122**, 4988 (2018), pMID: 29771514, https://doi.org/10.1021/acs.jpca.8b00941 .

[30] M. Sajjan and D. A. Mazziotti, Commun. Chem. **1**, 31 (2018).

[31] S. Safaei and D. A. Mazziotti, Phys. Rev. B **98**, 045122 (2018).

[32] A. Aspuru-Guzik, Science **309**, 1704 (2005), arXiv:0905.0887 .

[33] J. Koch, T. M. Yu, J. Gambetta, A. A. Houck, D. I. Schuster, J. Majer, A. Blais, M. H. Devoret, S. M. Girvin, and R. J. Schoelkopf, Phys. Rev. A **76**, 042319 (2007), arXiv:0703002 [cond-mat] .

[34] J. M. Chow, A. D. Córcoles, J. M. Gambetta, C. Rigetti, B. R. Johnson, J. A. Smolin, J. R. Rozen, G. A. Keefe, M. B. Rothwell, M. B. Ketchen, and M. Steffen, Phys. Rev. Lett. **107**, 080502 (2011), arXiv:1106.0553 .

[35] IBM-Q-Team., "IBM-Q-5 Yorktown backend specification v3.0," (2018).

[36] R. D. Johnson III, "NIST 101, Computational chemistry comparison and benchmark database," (2018).

[37] M. J. Frisch, G. W. Trucks, H. B. Schlegel, G. E. Scuseria, M. A. Robb, J. R. Cheeseman, G. Scalmani, V. Barone, B. Mennucci, G. A. Petersson, H. Nakatsuji, M. Caricato, X. Li, H. P. Hratchian, A. F. Izmaylov, J. Bloino, G. Zheng, J. L. Sonnenberg, M. Hada, M. Ehara, K. Toyota, R. Fukuda, J. Hasegawa, M. Ishida, T. Nakajima, Y. Honda, O. Kitao, H. Nakai, T. Vreven, J. A. J. Montgomery, J. E. Peralta, F. Ogliaro, M. Bearpark, J. J. Heyd, E. Brothers, K. N. Kudin, V. N. Staroverov, T. Keith, R. Kobayash, J. Normand, K. Raghavachari, A. Rendell, J. C. Burant, S. S. Iyengar, J. Tomasi, M. Cossi, N. Rega, J. M. Millam, M. Klene, J. E. Knox, J. B. Cross, V. Bakken, C. Adamo, J. Jaramillo, R. Gomperts, R. E. Stratmann, O. Yazyev, A. J. Austin, R. Cammi, C. Pomelli, J. W. Ochterski, R. L. Martin, K. Morokuma, V. G. Zakrzewski, G. A. Voth, P. Salvador, J. J. Dannenberg, S. Dapprich, A. D. Daniels, O. Farkas, J. B. Foresman, J. V. Ortiz, J. Cioslowski, and D. J. Fox, "Gaussian 09, Rev. B.01," (2010).

[38] M. W. Schmidt, K. K. Baldridge, J. A. Boatz, S. T. Elbert, M. S. Gordon, J. H. Jensen, S. Koseki, N. Matsunaga, K. A. Nguyen, S. Su, T. L. Windus, M. Dupuis, and J. A. Montgomery, J. Comput. Chem. **14**, 1347 (1993).

[39] "Maple 2018 (Maplesoft, Waterloo, 2018)," .

[40] G. Golub and C. F. V. Loan, *Matrix Computations* (Johns Hopkins University Press, Baltimore, MD, 1996).

[41] M. A. Nielsen and I. L. Chuang, *Cambridge University Press* (2010) arXiv:arXiv:1011.1669v3 .

CHAPTER 5

ERROR-MITIGATING N-REPRESENTABILITY CONDITION FOR CALCULATION OF MOTT METAL-INSULATOR TRANSITION ON A QUANTUM COMPUTER

Material from: Smart, S. E., & Mazziotti, D. A. (2019). Quantum-classical hybrid algorithm using an error-mitigating N-representability condition to compute the Mott metal-insulator transition. Physical Review A, 100(2), 022517.

5.1 Introduction

Quantum computers hold the promise of tackling some of the most challenging simulations of many-electron quantum systems [1, 2]. A number of quantum algorithms have been developed which exhibit lower scaling than their classical counterparts [3–5], but emerging quantum hardware is far from being capable of long coherence times, arbitrary connectivity and low gate error, which are requirements for most of these algorithms. As a consequence, efforts to maximally utilize the available devices have taken inspiration from quantum and classical regimes alike [6–10]. In particular, hybrid quantum-classical algorithms have been developed, which attempt to separate efficiently quantum and classical components of a problem [11–13]. Quantum hardware is used to prepare and measure a quantum state, or encode information, with the remaining tasks distributed to a conventional computer for classical execution [11, 14].

While recent hybrid quantum-classical algorithms like the quantum eigensolver method compute the two-electron reduced density matrix (2-RDM) to determine the energy, they are developed with the wave function's variational principle and hence, they do not consider the 2-RDM's variational principle. The key distinction between these two variational approaches is that the variational principle of the 2-RDM contains additional constraints that

are necessary for the 2-RDM to represent at least one N-electron density matrix or wave function, known as N-representability conditions [15–22]. While a perfect quantum computer would be able to operate with the variational principle of the wave function, near-term quantum computers operate with substantial noise that disrupts the N-representability of the measured 2-RDM. Error mitigation schemes based on extrapolative procedures or inherent stabilizer codes have been recently prepared and implemented highlighting the success of such schemes [23–26]. The 2-RDM principle provides a physical resource for error correction in the form of the N-representability conditions. Previous work has considered the use of these conditions to perform quantum tomography of 1-electron RDMs (1-RDMs) and 2-RDMs from noisqy experimental data, and more recent work has proposed the extension of these ideas to measurements from a quantum computer [27–29].

In this paper we propose and implement a quantum-classical hybrid algorithm for molecular electronic structure that uses a 2-RDM variational principle in which the 2-RDM is constrained by N-representability conditions. Previous electronic structure calculations on quantum computers have largely treated 2- or 4-electron atoms or molecules in closed-shell states without significant electron correlation [9, 12, 30–32]. We implement an algorithm for 3-electron molecules in open-shell, doublet states with significant strong electron correlation. A pure-state N-representability condition, known as a generalized Pauli constraint, which was originally discovered by Borland and Dennis at IBM in a series of computations on a classical computer [33], allows us to express the N-representable 2-RDM for three-electron systems as a functional of only the 1-RDM [34, 35]. We optimize the eigenvalues of the 1-RDM on the quantum computer and its eigenfunctions, which are not restricted by N-representability, on the classical computer. Computation of the strongly correlated dissociation of molecular H_3 yields its potential energy surface and an accurate prediction of its Mott metal-to-insulator transition [36]. Energies are computed with errors of about 0.0001 atomic units (or less than 0.1 kcal/mol).

5.2 Theory

5.2.1 N-Representability

For an N-electron system ($N \geq 2$), we can write the two-electron reduced density matrix (2-RDM) as:

$$^2D(12,\bar{1}\bar{2}) = \int \psi(123...N)\psi^*(\bar{1}\bar{2}3...N)d(3...N). \tag{5.1}$$

The 2-RDM of a system has all the information necessary for calculating energy and other molecular properties. For instance, the energy of a molecular system is obtained as:

$$E = \mathrm{Tr}(^2K\ ^2D), \tag{5.2}$$

where ^2K is the reduced Hamiltonian. Although the energy is expressible as a linear functional of the 2-RDM, the 2-RDM must be constrained by N-representability conditions for it to be representable by at least one N-electron density matrix or wave function [15, 21, 37]. Necessary ensemble-state and pure-state N-representability conditions are known [21, 38]. The pure-state N-representability conditions of the 1-RDM, also known as the generalized Pauli constraints, are in the form of linear inequalities on the set of 1-RDM eigenvalues (occupation numbers) for a given number of electrons and orbitals.

In this work we focus on the 3-electron in 6-orbital system, which has occupation numbers $\{n_i\}$ (and $1 \leq i \leq 6, i \in \mathbb{N}$), where $n_i \geq n_{i+1}$. The constraints on $\{n_i\}$ for a pure system, known as the Borland-Dennis constraints [33] are as follows:

$$n_5 + n_6 - \quad n_4 \geq 0 \tag{5.3}$$

$$n_1 + n_6 \quad = 1 \tag{5.4}$$

$$n_2 + n_5 \quad = 1 \tag{5.5}$$

$$n_3 + n_4 \quad = 1 \tag{5.6}$$

When a wave function saturates the inequality, then its expansion contains only Slater determinants that also saturate the inequality, which is known as a selection rule, and hence, in this case only 3 determinants contribute to its expansion [39]:

$$|\psi\rangle = \alpha|111000\rangle + \beta|100110\rangle + \gamma|010101\rangle \tag{5.7}$$

where $|\gamma|^2 = (1 - |\alpha|^2 - |\beta|^2)$, $1 \geq |\alpha|^2 \geq |\beta|^2$, and $|\alpha|^2 \geq |\beta|^2 + |\gamma|^2$. Any two n_i, n_j of the 1-RDM where $i + j \neq 7$, are linearly dependent basis vectors of the wavefunction $|\psi\rangle$ up to phases. Using this, we are able to carefully reconstruct the 2-RDM from the 1-RDM (see Appendix 5.5).

5.2.2 Error Mitigation Scheme

While the N-representability condition itself acts like a form of error correction by constraining the 1- and 2-RDMs to be representable by a wave function, in obtaining 1-RDM's from a quantum computer an additional error mitigation scheme can be implemented to ensure that all permissible 1-RDM eigenvalues are explored. The set of occupation numbers that satisfy the pure constraints on a system forms a multi-dimensional convex set with "flat" sides known as a polytope. For instance, in the case of 3-electrons in 6-orbitals, the Pauli exclusion principle defines 4 "planes" in the space spanned by $\{n_4, n_5, n_6\}$:

$$n_6 - n_5 = 0 \tag{5.8}$$

$$n_5 - n_4 = 0 \tag{5.9}$$

$$n_6 = 0 \tag{5.10}$$

$$n_4 - \frac{1}{2} = 0, \tag{5.11}$$

where (5.8) and (5.9) are from the ordering constraints, and (5.10) and (5.11) are from fermionic limits on occupations. The generalized Pauli constraints provides a another plane, defined as (5.3) (which actually is stronger than (5.10)). The intersection of these planes provides the relevant polytope. The Hartree-Fock (or initialized qubit) state is one extrema of the polytope with the constraints defining the facets of the polytope, given as $v_{HF} = (0, 0, 0)$.

The basic principle of the error mitigation is to remap the extrema of the polytope to adjust for errors detected through an initial set of measurements. In other words, let the set of all points in the polytope under the pure constraints be A, and the set of measurable points under error be A'. Then, we introduce a mapping T:

$$T : A' \to A. \tag{5.12}$$

and A includes the desired region. In the present work we employ this as a simple affine transformation.

5.2.3 Hybrid Variational Algorithm

The optimization of the 1-RDM is carried out in the natural-orbital basis set on the quantum computer. Orbital rotations, which are necessary to determine the energetically optimal natural orbitals, scale polynomially with the number of orbitals and hence, are treated on the classical computer. This partitioning of tasks between the quantum and classical computers, physically motivated by the structure of the N-representability conditions, reduces the complexity of the optimization.

To stay in the natural orbital basis, we use the following 3-qubit gate sequence:

$$\hat{U}(\theta_1, \theta_2) = C_2^1 R_2^y(\theta_2) C_1^3 R_1^y(\theta_1) \tag{5.13}$$

where C_i^j and $R_j^y(\theta_i)$ are the controlled-NOT and Y-rotation gates. This series of trans-

formation was derived form the specific knowledge of the 3-qubit system, and the resulting state spans one of the planes in (5.9) ($n_5 = n_4$). The quantum state has a diagonal 1-qubit RDM, and a standard qubit measurement in the computational basis is sufficient to obtain the 1-RDM.

The set of possible occupation numbers of a 1-RDM generated by (5.13) forms a curved two-dimensional surface within the polytope. A transformation T_i from the qubit space to the molecular space of (5.7) is given by

$$\begin{aligned} T_i &= G_i Q_i^{-1} \\ T_i &: \mathbb{C}^{2^3} \rightarrow \wedge^3 \mathcal{H}_6, \end{aligned} \tag{5.14}$$

where G_i are vertices of the space spanned by (5.7) subject to ordering constraints, and Q_i are vertices of the measured set of our algorithm (5.13). The i indices correspond with the triangulation of the curved surface. Note that when compared with (5.12), we use a composition to map directly to the desired 3-electron-6-orbital Hilbert space.

During the optimization, the 1-qubit RDM is measured on the quantum computer, the error mitigating transformation T_i is applied, and the 2-RDM is constructed classically from the corrected 1-RDM elements. Following the convergence with respect to ${}^2D$, Givens rotations are carried out classically on the ${}^2K$ matrix to minimize the energy according to (5.2). The process is carried out iteratively until both methods converge. The Nelder-Mead simplex or steepest descent algorithms were used for both optimizations. See Appendix 5.5 for more details.

5.3 Results and Discussion

5.3.1 Dissociation of Linear H_3

Figure 5.3.1 presents the dissociation of the linear H_3 molecule in its ground doublet state into three hydrogen atoms from equal stretching of the two bonds. Calculations were performed in the Slater-type-orbital minimal basis set (STO-3G) with results compared to those from classical full configuration interaction (FCI). Using the RDM method on the quantum computer (RDM-QC), we obtain a highly accurate potential energy curve for the H_3 dissociation even for values of the internuclear distance greater than 2 Å where strong electron correlation is present due to the spin entanglement among the energetically degenerate H-atom 1s orbitals. Traditional single-reference methods like second-order many-body perturbation theory or the coupled cluster singles-double method either diverge or fail to converge as the bond is stretched beyond 2 Å. Throughout the dissociation curve energy errors from RDM-QC are consistently less than 0.0001 a.u. (or less than 0.1 kcal/mol) relative to FCI. While uncertainty from sampling does lead to larger error margins for each particular evaluation (on the order of $0.002 - 0.0002$ a.u.), the optimization threshold allows for oversampling in the target region. Because our reconstruction ensures we construct a physical RDM, the energy obtained will correspond with a real system. To the best of our knowledge, these are some of the most accurate energies obtained to date with a generalized quantum architecture. The tolerances of the algorithm are well suited for low iterations on the IBM device, but can be tightened to accomplish lower error rates.

5.3.2 Mott Insulator Transition for H_3

Using the computed 1-RDM, we can also calculate one-electron properties of the system. Upon dissociation molecular H_3 undergoes a Mott transition from a metal to an insulator. The transition can be observed from sum of the squares of the off-diagonal elements of the

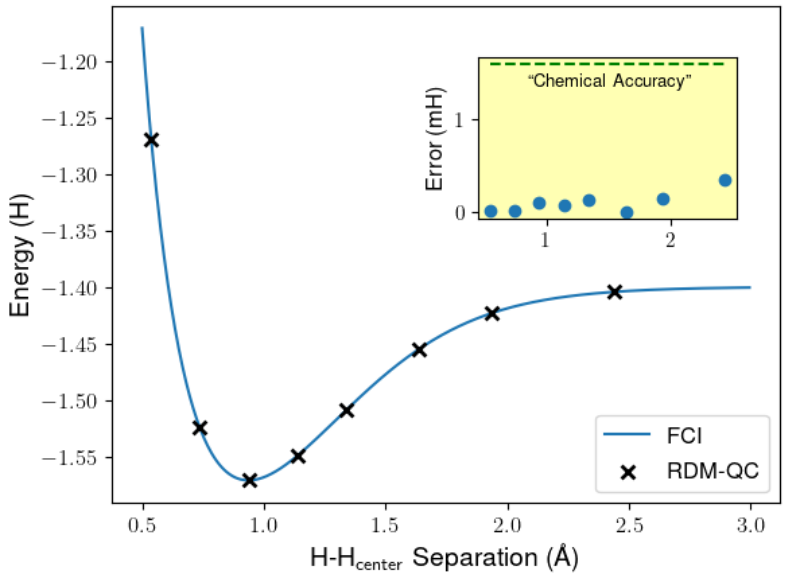

Figure 5.1: Depicts the dissociation curve for the doublet H_3 with respect to the bond distance from the center H to the two exterior H atoms in a linear geometry. The crosses were calculated with a variational quantum algorithm on the quantum computer, while the line was generated with a full configuration interaction (FCI) calculation on a classical computer. Energies are listed in Hartrees. The inset plot depicts the error from the full-CI method also with respect to the separated distance, and is reported in milli-Hartrees, mH. The dashed line is at 1.6 mH, which corresponds with 1.0 kcal / mol, generally used as a guide for chemical accuracy. The effect of errors is discussed in the text and in Appendix 5.5. Variability from a single run is on the order of $2 - 0.2$ mH, and in our optimization we purposefully oversample the target region.

1-RDM in the local atomic-orbital basis set. Figure 5.3.2 compares the sum of squares from the RDM calculation on the quantum computer (RDM-QC) with the corresponding results from Hartree-Fock (HF) and FCI. We observe that HF theory fails to capture the metal-to-insulator transition, remaining metallic throughout the dissociation but the RDM-QC correctly predicts the transition in close agreement with FCI. RDM-QC captures this transition because its parameterization captures the requisite strong electron correlation. Figure 5.5 also shows the curve from second-order many-body perturbation theory which, unlike the algorithm on the quantum computer, breaks down in the region of the bond dissociation.

The expression of the pure N-representability condition in terms of the natural orbitals, it suggests a natural partition of the electronic structure calculation between the quantum and classical computers. Minimization of the energy as a functional of the 2-RDM in the natural-orbital basis set is performed on the quantum computer while optimization of the natural orbitals is performed by inexpensive, polynomially scaling orbital rotations on the classical computer. In the language of quantum information non-local degrees of freedom, responsible for multi-particle entanglement, are optimized on the quantum computer, and local degrees of freedom are optimized on the classical computer [40, 41]. In classical electronic structure the separation of the orbital optimization has precedent in methods like self-consistent-field methods, Brueckner-orbital coupled cluster theory, and natural-orbital functional theories [21, 42–46].

5.4 Conclusion

A quantum-classical hybrid algorithm for molecular electronic structure is implemented that uses a 2-RDM-based energy variational principle in which the energy is minimized with the 2-RDM constrained by N-representability conditions. Computations are performed for the strongly correlated dissociation of the H_3 molecule. The QC-RDM calculation accurately

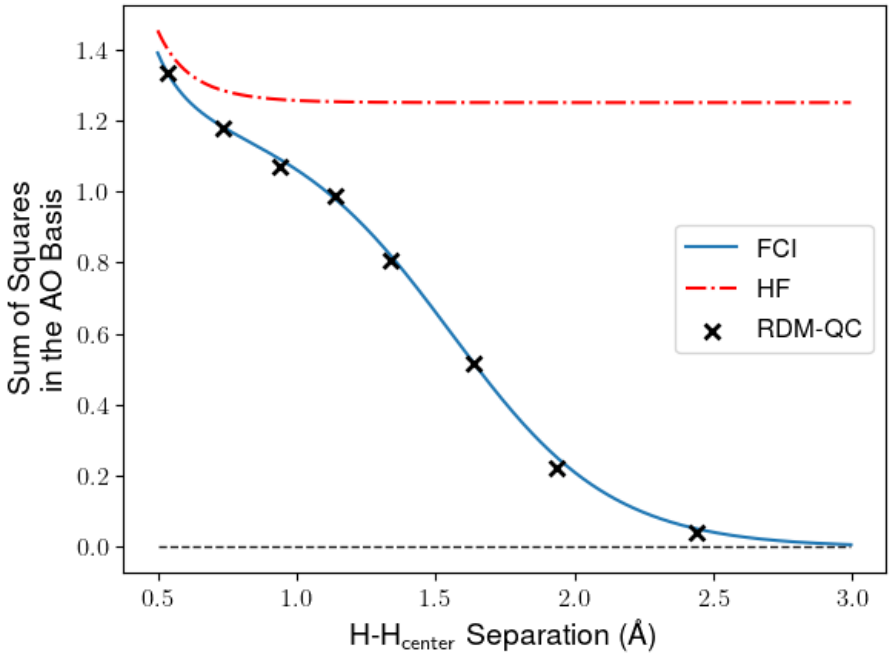

Figure 5.2: Shows the sum of squares of the off-diagonal elements, τ, of the 1-RDM of H_3 in the local Löwdin atomic orbital basis along the dissociation curve of H_3. Here, $\tau = \sum_{i \neq j} \|^1 D^i_j\|^2$ where i, j are orbital indices in the Löwdin atomic orbital basis. The Hartree-Fock result is shown as a dashed-dotted line, the FCI result is solid, and our variational quantum computation is shown as crosses. The bottom dashed line shows the dissociated limit where $\tau = 0$, and the natural orbitals approach the atomic ones. That H_3 serves as a Mott-Insulator can be seen between these distances, as $\tau \to 0$ with increasing distance, highlighting the mean field and 2-electron approaches.

captures the potential energy curve within an error of about 0.1 kcal/mol even in the dissociation region where classical single-reference methods fail. It also yields the 1- and 2-RDMs with the 1-RDM revealing the Mott transition from a metal to an insulator.

While previously employed hybrid algorithms like the variational quantum eigensolver also compute the 2-RDM en route to the energy, the present work uses a 2-RDM-based variational principle in that we explicitly constrain the 1- and 2-RDMs to be pure N-representable. The N-representability conditions provide a physically motivated error mitigation scheme which is critical to achieving accurate results on near-term quantum computers which are noisy and prone to errors. While the present work employs an N-representability condition for 3-electron systems due to Borland and Dennis, the 2-RDM-based variational principle on a quantum computer is applicable to systems with arbitrary N through the use of more general N-representability conditions. The present work provides an important step towards harnessing two-electron reduced density matrix theory within the context of quantum computing for accurate computations of many-electron molecules and materials.

5.5 Appendix

The following appendices contain information on: computational details, both classical and quantum; the the wavefunction used in the above ansatz; information on the reconstruction of the 2-RDM as a function of the eigenvalues of the 1-RDM; the mapping of the wavefunction to the quantum computer, and; details on the quantum device used.

Appendix A: Computational Details

The electronic structure package PySCF [47] was used to obtain electron integrals and to perform restricted open-shell Hartree-Fock and full configuration interaction calculations.

For the quantum computation we used the IBM Quantum Experience devices (ibmqx4), available online, with a 5-transmon quantum computing device [48]. These cloud acces-

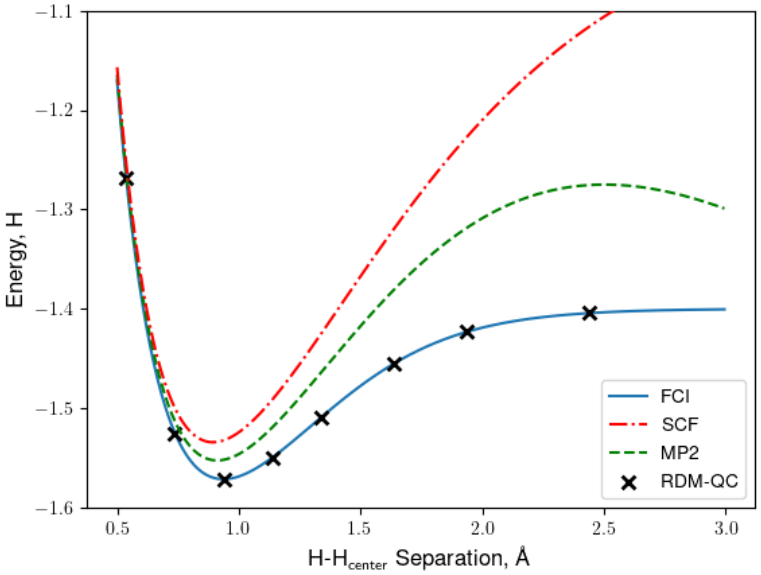

Figure 5.3: Depicts the dissociation curve for the doublet H_3 with respect to the bond distance from the center H to the two exterior H atoms in a linear geometry across a variety of methods, including Full Configuration Interaction (FCI), second-order perturbation theory (MP2), restricted open-shell Hartree-Fock method (SCF), and our variational algorithm. Coupled-cluster with singles and doubled (CCSD) actually is equivalent to the FCI result for a 3-electron in 3-spatial-orbital system, due to the restriction of movement of the 3 electrons. For more orbitals this is not the case. With the exception of the RDM-QC method, PySCF was used for calculations[47].

sible quantum devices are fixed-frequency transmon qubits with co-planer waveguide resonators [48, 49]. Experimental calibration and connectivity of these devices is included in Appendix 5.5. The quantum information package Qiskit was used for interfacing with the device [50].

A compact qubit mapping was utilized, similar to previous work with a 3-electron in 6-orbital system [51], although adapted for the current work. Each evaluation of the quantum computer had 2048 measurements on the 3-qubit populations, with no additional tomography required. About 2 macro iterations were required for most distances (with only one taking 5 iterations). The stopping criteria on the quantum computer was a distance of 0.1° of the simplex vertices to the centroid (although repeatability errors for set parameters were on a larger scale than this). A threshold of 0.1 mH between the quantum computation and the orbital rotations was required for the macro iterations to terminate. We illustrate the optimization with data taken from the point $d = 1.34$ in Figure 5.5.

Despite the relatively high sampling error which occurs, the algorithm itself is able to find much higher accuracy answers due to repeated sampling across the valley of the energy surface, as well as the N-representability constraints ensuring that a physical system is represented. We find that sampling even within a distance of 2° could lead to highly variable results, and so the criteria of convergence for the simplex implies that the region is well sampled.

Appendix B: Mapping the GPC Wavefunction

Here we explicitly describe the mapping of the wavefunction. We first map the computational qubit states (q_{ik}, where i is qubit number, k is the qubit state, 0 or 1) to the GPC orbitals (n_i). Then, we use an additional mapping from the GPC orbitals to the molecular spin

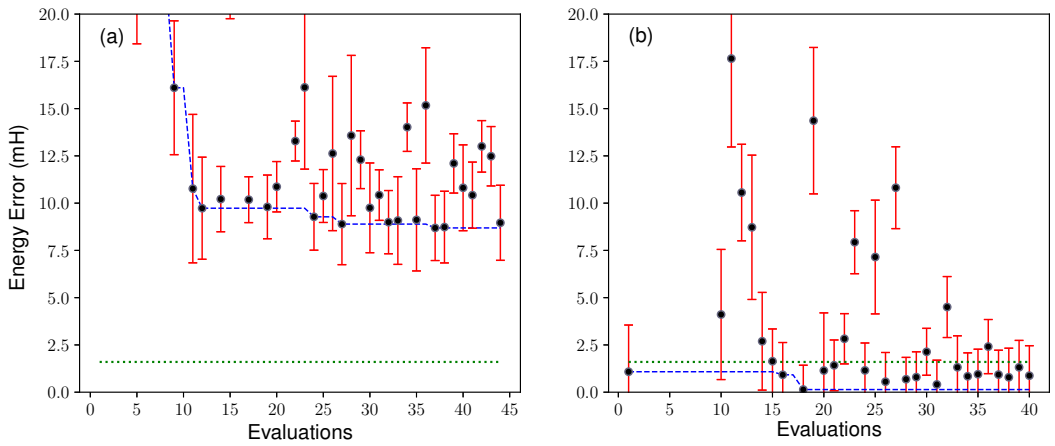

Figure 5.4: Depicts the (a) first and (b) second macro iteration of the Nelder-Mead simplex optimization of H_3, where the separation from the central atom is 1.34 Å. Between the two iterations an orbital rotation is performed. The vertical axis represents the energy difference between the measured energy and the full configuration interaction result in milli-Hartrees (mH), while the horizontal axis shows the number of function evaluations. For clarity we only show evaluations with an energy difference of 20 mH. The blue dashed line shows the energy of the best simplex point along the optimization, while the green line shows the "chemical accuracy" threshold of 1.6 mH. Error bars correspond with a 90% confidence interval based largely on sampling errors in the quantum computer. The variational design of the algorithm and oversampling in the target region allow for higher confidence results in the final energy.

orbitals (ψ_i). The mappings are as follows:

$$q_{1,0} \leftrightarrow n_1 \leftrightarrow \phi_{1\alpha} \tag{5.15}$$

$$q_{2,0} \leftrightarrow n_2 \leftrightarrow \phi_{2\alpha} \tag{5.16}$$

$$q_{3,0} \leftrightarrow n_3 \leftrightarrow \phi_{1\beta} \tag{5.17}$$

$$q_{3,1} \leftrightarrow n_4 \leftrightarrow \phi_{3\alpha} \tag{5.18}$$

$$q_{2,1} \leftrightarrow n_5 \leftrightarrow \phi_{2\beta} \tag{5.19}$$

$$q_{1,1} \leftrightarrow n_6 \leftrightarrow \phi_{3\beta} \tag{5.20}$$

These are by no means unique mappings, but are useful for our implementation. For instance, the GPC's are ordered, but qubits or spin orbitals need not be, and so we choose the parameters in Appendix 5.5 and the preparing gates in (5.13) to account for this.

Appendix C: Reconstruction of the 2-Electron Reduced-Density-Matrix (2-RDM)

The wavefunction which is pinned to the Borland-Dennis constraint is given in (5.7). We can also parameterize this in terms of the eigenvalues (occupations) of the 1-electron reduced-density-matrix (1-RDM) n_i, and a coefficient phase p_i.

$$\begin{aligned} |\psi\rangle = p_\alpha \sqrt{1 - n_5 - n_6}|111000\rangle \\ + p_\beta \sqrt{n_5}|100110\rangle \\ + p_\gamma \sqrt{n_6}|010101\rangle. \end{aligned} \tag{5.21}$$

Our choice of n_5, n_6 is somewhat arbitrary, but shows that having only two non-matching n_i is sufficient to represent the wavefunction. From this, the 2-RDM *in the GPC basis* can be constructed as follows. We choose a $S_z = +1/2$ spin state with the following α/β orbital

$$
{}^2D^{\alpha,\beta}_{\alpha,\beta} = \begin{pmatrix}
1-n_5-n_6 & * & * & * & * & * \\
0 & n_5 & * & * & * & * \\
0 & 0 & 1-n_5-n_6 & * & * & * \\
0 & p_\beta\sqrt{n_5 n_6} & 0 & n_6 & * & * \\
0 & 0 & p_\alpha p_\beta\sqrt{(1-n_5-n_6)(n_5)} & 0 & n_5 & * \\
-p_\alpha\sqrt{(1-n_5-n_6)(n_6)} & 0 & 0 & 0 & 0 & n_6
\end{pmatrix}, \tag{5.24}
$$

assignment: $\alpha \in \{1,2,4\}, \beta \in \{3,5,6\}$. An element of the 2-RDM is given by:

$$
{}^2D^{i,k}_{j,l} = \langle\psi|\hat{a}^\dagger_i\hat{a}^\dagger_k\hat{a}_l\hat{a}_j|\psi\rangle \tag{5.22}
$$

where $\hat{a}^\dagger_i$,$\hat{a}_i$ are the second-quantized creation and annihilation operators, respectively. The $\alpha\alpha$ and $\alpha\beta$ blocks of the 2-RDM are given by (see next page for $\alpha\beta$ block):

$$
{}^2D^{\alpha,\alpha}_{\alpha,\alpha} = \begin{pmatrix}
1-n_5-n_6 & 0 & 0 \\
0 & n_5 & 0 \\
0 & 0 & n_6
\end{pmatrix}, \tag{5.23}
$$

with the column basis $\{\hat{a}_2\hat{a}_1, \hat{a}_4\hat{a}_1, \hat{a}_4\hat{a}_2\}$, used in the $\alpha\alpha$ block, and the column basis $\{\hat{a}_3\hat{a}_1, \hat{a}_5\hat{a}_1, \hat{a}_3\hat{a}_2, \hat{a}_6\hat{a}_2, \hat{a}_5\hat{a}_4, \hat{a}_6\hat{a}_5\}$ for the $\alpha\beta$ block (note that $\hat{a}^\dagger_i\hat{a}^\dagger_j(\hat{a}_6\hat{a}_1/\hat{a}_5\hat{a}_2/\hat{a}_3\hat{a}_4)$ are all equal to 0 for any i,j). The non-zero elements which require the flexibility of the sign are: $\hat{a}^\dagger_4\hat{a}^\dagger_6\hat{a}_3\hat{a}_1$, $\hat{a}^\dagger_2\hat{a}^\dagger_6\hat{a}_5\hat{a}_1$, and $\hat{a}^\dagger_4\hat{a}^\dagger_5\hat{a}_3\hat{a}_2$ and their Hermitian conjugates ($*$ terms). Additionally, we have set $p_\gamma = 1$, but still have equivalent degrees of freedom in the sign of the two remaining terms. Our treatment of these sign terms is included in the next section.

Appendix D: Wavefunction Parity Mapping for the Quantum Device

In constructing our terms p_i, the main requirement is that they do not break the continuity of the potential surface, and that all degrees of freedom are still reachable. Because of the symmetry of the n_i and their repeating structure with respect to the input parameters θ_i, we

are able to link p_i with these parameters. We also bound the input θ_i to the minimal region required to create any point in the plane. Define a new variable ϕ which maps $(-\infty, \infty)$ to $[-\pi/4, \pi/4]$:

$$\phi(\theta) = (-1)^{x(\theta)}\Big[(\theta + \frac{\pi}{4}) \bmod \frac{\pi}{2}\Big] \tag{5.25}$$

where

$$x(\theta) = \frac{\theta - \frac{\pi}{4} - (\theta + \frac{\pi}{4}) \bmod \frac{\pi}{2}}{\frac{\pi}{2}}. \tag{5.26}$$

While we never will have switching between the ordering of n_1 with n_3 or n_2 with n_3, it is possible to switch between n_1 and n_2, and our sign mapping should be invariant to this switch. We achieve this by requiring that if $\phi_1 < 0$, then:

$$\text{if } \phi_2 \geq -\phi_1 \text{ and } \phi_2 \geq 0 \rightarrow \gamma < 0, \text{ else } \rightarrow \beta < 0 \tag{5.27}$$

And if $\phi_2 < 0$:

$$\text{if } \phi_2 \geq -\phi_1 \text{ and } \phi_2 \geq 0 \rightarrow \gamma < 0, \text{ else } \rightarrow \beta < 0. \tag{5.28}$$

Combined, these conditions produce a mapping of the set of θ_1, θ_2 to a $\pm$ sign, which is symmetric across the line $\theta_1 = \theta_2$. This gives the required mapping of signs. While the surface is not smooth because of the boundary around $\frac{n\pi}{4}$, it still is continuous.

Appendix E: Quantum Computer Errors

Calibration data used in obtaining the H_3 calculations on the IBM device is included in Table 5.1 [52].

References

[1] S. Lloyd, Science **273**, 1073 (1996).

Table 5.1: Contains calibration info for the 5 transmon qubit device, denoted as IBMQX Tenerife, Raven, or ibmqx4. Included are the readout errors for the qubits and the single and multi-qubit gate errors for each date. In general, the qubits were selected so as to have minimal error on the device. Qubit connectivity is directional with the first qubit indicating the control and second qubit indicating the target.

Calibration Date:	1	2	3	4	5	6
Readout Error (10^{-3})						
Q0:	64	74	66	56	66	87
Q1:	65	75	52	43	43	75
Q2:	16	19	18	18	25	19
Q3:	38	13	24	33	30	81
Q4:	45	37	208	219	323	309
Gate Error (10^{-3})						
Q0:	0.77	1.03	1.20	0.86	0.69	0.86
Q1:	1.80	2.32	1.63	1.72	1.29	1.20
Q2:	1.03	1.20	0.94	1.03	1.46	0.86
Q3:	1.46	1.63	1.29	1.63	1.80	1.72
Q4:	1.37	1.29	1.63	1.20	3.35	3.35
Q1−Q0:	29.2	37.5	32.9	24.6	27.9	32.5
Q2−Q0:	30.5	27.5	28.6	24.9	31.2	32.6
Q2−Q1:	29.9	42.7	34.5	32.7	41.4	34.5
Q3−Q2:	43.3	69.6	50.8	65.7	60.6	59.3
Q3−Q4:	36.9	45.1	40.8	36.6	69.9	79.5
Q4−Q2:	43.8	46.3	55.5	47.8	91.0	72.2

[2] A. Aspuru-Guzik, A. D. Dutoi, P. J. Love, and M. Head-Gordon, Science **309**, 1704 (2005), arXiv:0905.0887 .

[3] D. S. Abrams and S. Lloyd, Phys. Rev. Lett. **79**, 2586 (1997), arXiv:9703054 [quant-ph] .

[4] D. S. Abrams and S. Lloyd, Phys. Rev. Lett. **83**, 5162 (1999), arXiv:9807070 [quant-ph] .

[5] E. Farhi, J. Goldstone, S. Gutmann, and M. Sipser, arXiv:quant-ph/0001106 (2000), quant-ph/0001106, arXiv:0001106 [quant-ph] .

[6] H. Wang, S. Kais, A. Aspuru-Guzik, and M. R. Hoffmann, Phys. Chem. Chem. Phys. **10**, 5388 (2008), arXiv:0907.0854 .

[7] M. H. Devoret and R. J. Schoelkopf, Science **339**, 1169 (2013), arXiv:0402594v3 [arXiv:cond-mat] .

[8] N. Moll, P. Barkoutsos, L. S. Bishop, J. M. Chow, A. Cross, D. J. Egger, S. Filipp, A. Fuhrer, J. M. Gambetta, M. Ganzhorn, A. Kandala, A. Mezzacapo, P. Müller, W. Riess, G. Salis, J. Smolin, I. Tavernelli, and K. Temme, Quantum Sci. Tech. **3**, 030503 (2018), arXiv:1710.01022 .

[9] A. Kandala, K. Temme, A. D. Corcoles, A. Mezzacapo, J. M. Chow, and J. M. Gambetta, arXiv:1805.04492 (2018), arXiv:1805.04492 .

[10] T. Bian, D. Murphy, R. Xia, A. Daskin, and S. Kais, , 1 (2018), arXiv:1804.05453 .

[11] A. Peruzzo, J. McClean, P. Shadbolt, M.-H. Yung, X.-Q. Zhou, P. J. Love, A. Aspuru-Guzik, and J. L. O'Brien, Nature Communications **5**, 4213 (2014), arXiv:1304.3061 .

[12] A. Kandala, A. Mezzacapo, K. Temme, M. Takita, M. Brink, J. M. Chow, and J. M. Gambetta, Nature **549**, 242 (2017), arXiv:1704.05018 .

[13] R. Santagati, J. Wang, A. A. Gentile, S. Paesani, N. Wiebe, J. R. McClean, S. Morley-Short, P. J. Shadbolt, D. Bonneau, J. W. Silverstone, D. P. Tew, X. Zhou, J. L. O'Brien, and M. G. Thompson, Science Advances **4**, 1 (2018), arXiv:1611.03511 .

[14] J. R. McClean, J. Romero, R. Babbush, and A. Aspuru-Guzik, New J. Phys. **18**, 023023 (2016), arXiv:1509.04279 .

[15] A. J. Coleman, Int. J. Quantum Chem. **XIII**, 67 (1978).

[16] A. J. Coleman, Rev. Mod. Phys. **35**, 668 (1963), arXiv:0310359v1 [arXiv:cond-mat] .

[17] R. Erdahl and B. Jin, "On calculating approximate and exact density matrices," in *Many-Electron Densities and Reduced Density Matrices*, edited by J. Cioslowski (Springer US, Boston, MA, 2000) pp. 57–84.

[18] D. A. Mazziotti and R. M. Erdahl, Phys. Rev. A **63**, 042113 (2001).

[19] M. Nakata, H. Nakatsuji, M. Ehara, M. Fukuda, K. Nakata, and K. Fujisawa, J. Chem. Phys. **114**, 8282 (2001).

[20] Z. Zhao, B. J. Braams, M. Fukuda, M. L. Overton, and J. K. Percus, J. Chem. Phys. **120**, 2095 (2004).

[21] D. A. Mazziotti, ed., *Advances in Chemical Physics*, Advances in Chemical Physics, Vol. 134 (John Wiley & Sons, Inc., Hoboken, NJ, USA, 2007) p. 574.

[22] D. A. Mazziotti, Phys. Rev. Lett. **108**, 263002 (2012), arXiv:1112.5866 .

[23] Y. Li and S. C. Benjamin, Phys. Rev. X **7**, 021050 (2017), arXiv:1611.09301 .

[24] K. Temme, S. Bravyi, and J. M. Gambetta, Phys. Rev. Lett. **119**, 1 (2017), arXiv:1612.02058 .

[25] A. Kandala, K. Temme, A. D. Córcoles, A. Mezzacapo, J. M. Chow, and J. M. Gambetta, Nature **567**, 491 (2019), arXiv:1805.04492 .

[26] X. Bonet-Monroig, R. Sagastizabal, M. Singh, and T. E. O'Brien, Phys. Rev. A **98**, 1 (2018).

[27] J. J. Foley and D. A. Mazziotti, Phys. Rev. A **86**, 012512 (2012).

[28] N. C. Rubin, R. Babbush, and J. McClean, New J. Phys. **20**, 053020 (2018), arXiv:1801.03524 .

[29] R. Sagastizabal, X. Bonet-Monroig, M. Singh, M. A. Rol, C. C. Bultink, X. Fu, C. H. Price, V. P. Ostroukh, N. Muthusubramanian, A. Bruno, M. Beekman, N. Haider, T. E. O'Brien, and L. DiCarlo, , 1 (2019), arXiv:1902.11258 .

[30] Y. Shen, X. Zhang, S. Zhang, J.-N. Zhang, M.-H. Yung, and K. Kim, Phys. Rev. A **95**, 020501 (2017), arXiv:1506.00443 .

[31] J. R. Mcclean, M. E. Kimchi-Schwartz, J. Carter, W. A. de Jong, M. E. Schwartz, J. Carter, and W. A. D. Jong, Phys. Rev. A **95**, 042308 (2017), arXiv:1603.05681 .

[32] J. I. Colless, V. V. Ramasesh, D. Dahlen, M. S. Blok, M. E. Kimchi-Schwartz, J. R. McClean, J. Carter, W. A. De Jong, and I. Siddiqi, Phys. Rev. X **8**, 11021 (2018), arXiv:1707.06408 .

[33] R. E. Borland and K. Dennis, J. Phys. B - At. Mol. Opt. **5**, 7 (1972).

[34] R. Chakraborty and D. A. Mazziotti, Phys. Rev. A **89**, 042505 (2014), arXiv:arXiv:1404.5223v1 .

[35] C. Schilling, M. Altunbulak, S. Knecht, A. Lopes, J. D. Whitfield, M. Christandl, D. Gross, and M. Reiher, Phys. Rev. A **97**, 052503 (2018), arXiv:1710.03074 .

[36] R. Ma, B. Saxberg, C. Owens, N. Leung, Y. Lu, J. Simon, and D. I. Schuster, Nature **566**, 51–57 (2019).

[37] D. A. Mazziotti, Phys. Rev. A **94**, 032516 (2016).

[38] M. Altunbulak and A. Klyachko, Commun. Math. Phys. **282**, 287 (2008), arXiv:0802.0918 .

[39] C. L. Benavides-Riveros and C. Schilling, Z. Phys. Chem. **230**, 703 (2016), arXiv:1711.09129 .

[40] N. Linden, S. Popescu, and S. Popescu, Fortschr. Phys. **46**, 567 (1998), arXiv:9711016 [quant-ph] .

[41] A. Acín, A. Andrianov, E. Jané, and R. Tarrach, J. Phys. A-Math. Gen. **34** (2001), 10.1088/0305-4470/34/35/301, arXiv:0009107 [quant-ph] .

[42] R. A. Chiles and C. E. Dykstra, J. Chem. Phys. **74**, 4544 (1981).

[43] N. C. Handy, J. A. Pople, M. Head-gordon, K. Raghavachari, and G. W. Trucks, Chem. Phys. Lett. **164**, 185 (1989).

[44] M. W. Schmidt and M. S. Gordon, Ann. Rev. Phys. Chem. **49**, 233 (1998).

[45] T. Helgaker, P. Jørgensen, and J. Olsen, *John Wiley & Sons, LTD. - Chichester.* (John Wiley & Sons, Ltd, Chichester, UK, 2000) p. 908.

[46] M. Piris, in *Advances in Chemical Physics*, Vol. 134 (2007) pp. 385–427.

[47] Q. Sun, T. C. Berkelbach, N. S. Blunt, G. H. Booth, S. Guo, Z. Li, J. Liu, J. McClain, E. R. Sayfutyarova, S. Sharma, S. Wouters, and G. K.-L. Chan, arXiv:1701.08223 , 1 (2017), arXiv:1701.08223 .

[48] J. Koch, T. M. Yu, J. Gambetta, A. A. Houck, D. I. Schuster, J. Majer, A. Blais, M. H. Devoret, S. M. Girvin, and R. J. Schoelkopf, Phys. Rev. A **76**, 042319 (2007), arXiv:0703002 [cond-mat] .

[49] J. M. Chow, A. D. Córcoles, J. M. Gambetta, C. Rigetti, B. R. Johnson, J. A. Smolin, J. R. Rozen, G. A. Keefe, M. B. Rothwell, M. B. Ketchen, and M. Steffen, Phys. Rev. Lett. **107**, 080502 (2011), arXiv:1106.0553 .

[50] G. Aleksandrowicz, T. Alexander, P. Barkoutsos, L. Bello, Y. Ben-Haim, D. Bucher, F. J. Cabrera-Hernádez, J. Carballo-Franquis, A. Chen, C.-F. Chen, J. M. Chow, A. D. Córcoles-Gonzales, A. J. Cross, A. Cross, J. Cruz-Benito, C. Culver, S. D. L. P. González, E. D. L. Torre, D. Ding, E. Dumitrescu, I. Duran, P. Eendebak, M. Everitt, I. F. Sertage, A. Frisch, A. Fuhrer, J. Gambetta, B. G. Gago, J. Gomez-Mosquera, D. Greenberg, I. Hamamura, V. Havlicek, J. Hellmers, Ł. Herok, H. Horii, S. Hu, T. Imamichi, T. Itoko, A. Javadi-Abhari, N. Kanazawa, A. Karazeev, K. Krsulich, P. Liu, Y. Luh, Y. Maeng, M. Marques, F. J. Martín-Fernández, D. T. McClure, D. McKay, S. Meesala, A. Mezzacapo, N. Moll, D. M. Rodríguez, G. Nannicini, P. Nation, P. Ollitrault, L. J. O'Riordan, H. Paik, J. Pérez, A. Phan, M. Pistoia, V. Prutyanov, M. Reuter, J. Rice, A. R. Davila, R. H. P. Rudy, M. Ryu, N. Sathaye, C. Schnabel, E. Schoute, K. Setia, Y. Shi, A. Silva, Y. Siraichi, S. Sivarajah, J. A. Smolin, M. Soeken, H. Takahashi, I. Tavernelli, C. Taylor, P. Taylour, K. Trabing, M. Treinish, W. Turner, D. Vogt-Lee, C. Vuillot, J. A. Wildstrom, J. Wilson, E. Winston, C. Wood, S. Wood, S. Wörner, I. Y. Akhalwaya, and C. Zoufal, "Qiskit: An open-source framework for quantum computing," (2019).

[51] S. E. Smart, D. I. Schuster, and D. A. Mazziotti, Commun. Phys. **2** (2019), 10.1038/s42005-019-0110-3.

[52] C. Sparrow, E. Martín-López, N. Maraviglia, A. Neville, C. Harrold, J. Carolan, Y. N. Joglekar, T. Hashimoto, N. Matsuda, J. L. O'Brien, D. P. Tew, and A. Laing, Nature **557**, 660 (2018).

CHAPTER 6

PURE N-REPRESENTABILITY OF TWO ELECTRON ANSATZ FOR BENCHMARKING NEAR-TERM QUANTUM DEVICES

Material from: Smart, S. E., & Mazziotti, D. A. (2020). Efficient two-electron ansatz for benchmarking quantum chemistry on a quantum computer. Physical Review Research, 2 (2), 023048.

6.1 Introduction

Quantum computers possess a natural affinity for quantum simulation and can transform exponentially scaling problems into polynomial ones [1–3]. Quantum supremacy, the ability of a quantum computer to surpass its classical counterpart on a designated task with lower asymptotic scaling, is potentially realizable for the simulation of quantum many-electron systems [4, 5]. Work over the previous decade has been towards this goal with a focus on calculating the energy of small molecules and exploring strategies to leverage emerging quantum technologies, especially those designed to correct or mitigate quantum errors [6–8]. In this paper we introduce an efficient ansatz for a two-electron quantum-mechanical system that can be employed as a benchmark for assessing the capabilities and accuracy of quantum computers.

The two-electron density matrix (2-DM) of any two-electron system can be expressed as a functional of its one-electron reduced density matrix (1-RDM) and a set of phase factors. This representation of the 2-DM has important connections to natural-orbital functional theories and geminal-based theories in quantum chemistry [9–12]. It offers a natural separation between the nonlocal and local fermionic degrees of freedom in the system [13], scaling linearly and polynomially respectively, and can be leveraged in a variational hybrid

quantum-classical algorithm. The entangled, nonlocal degrees are treated on the quantum computer while the local degrees are treated on the classical computer, leading to an efficient simulation of the system.

For a quantum algorithm to exhibit quantum supremacy, obtaining the solution classically will be impractical except for cases that are close to the classical limits of feasibility [4, 5]. For some problems such as prime factorization, the solution can be quickly verified, but for many-body quantum systems this is not the case [14–18]. Possessing 'easy', classically solvable problems to implement and verify will be crucial to evaluate the performance of quantum devices and error mitigation schemes [19]. Our proposed quantum-classical hybrid algorithm targets only the necessary entanglement needed on the quantum computer, scales linearly with respect to basis size, and has $\mathcal{O}(1)$ circuit preparations, making it an ideal benchmark for molecular simulation. We highlight this by evaluating this ansatz through the computation of H_2 and H_3^+ on two generations of publicly available quantum devices.

6.2 Theory

Because the representation of the 2-DM in terms of the 1-RDM and phase factors has been well studied elsewhere [10, 20–22], we present in section IIA only the aspects of the theory that are relevant to the quantum-classical hybrid algorithm in section IIB. We also discuss the preparation of the linear-scaling ansatz in section IIC and practical error mitigation techniques in section IID that are employed in the benchmarks in section III.

6.2.1 Structure of the Two-Electron System

For a two-electron system the energy is given as the trace of the Hamiltonian and the density matrix:

$$E = \text{Tr}\ (HD) \tag{6.1}$$

where H and D are $2r \times 2r$ with $2r$ being the rank of the one-electron basis set and

$$D^{ij}_{kl} = g_{ij} g^*_{kl} \tag{6.2}$$

in which the wavefunction expansion coefficients g_{ij} are elements of the coefficient matrix G. From the antisymmetric nature of fermions, G must be a skew-symmetric matrix, and from a theorem by Zumino [22], G must have a block-diagonal form $\tilde{G}$ with 2×2 matrices $\mathcal{G}_i$:

$$\tilde{G} = \text{diag } (\mathcal{G}_0, \mathcal{G}_1 ... \mathcal{G}_r), \tag{6.3}$$

$$\mathcal{G}_i = \begin{pmatrix} 0 & \tilde{g}_{ii'} \\ \tilde{g}_{i'i} & 0 \end{pmatrix} = \begin{pmatrix} 0 & \tilde{g}_{ii'} \\ -\tilde{g}_{ii'} & 0 \end{pmatrix} \tag{6.4}$$

The block-diagonal form of G in Zumino's theorem defines an orbital basis set with a natural pairing of the orbitals where we denote the indices of an orbital and its pair by i and i', respectively.

The 2-DM in Zumino's basis has only nonzero elements of the form:

$$\tilde{D}^{ii'}_{kk'} = \tilde{g}_{ii'} \tilde{g}^*_{kk'}. \tag{6.5}$$

The 1-RDM, containing the one-body information, can be obtained from the 2-DM by contraction:

$${}^1\tilde{D}^i_i = \sum_k \tilde{D}^{ik}_{ik} = \tilde{D}^{ii'}_{ii'} = \tilde{g}_{ii'} \tilde{g}^*_{ii'} = n_i = n_{i'}, \tag{6.6}$$

$${}^1\tilde{D}^i_j = 0, \tag{6.7}$$

where in the second step becauase the first electron is constrained to orbital i, the second is zero except when in orbital i'. Because the 1-RDM is diagonal in Zumino's basis set, we find

that Zumino's basis set is identically the natural-orbital basis set and that the occupations n_i are the natural orbital occupations. The paired orbitals i and i', we observe, have equal occupations n_i and $n_{i'}$. For a system of two electrons with $S_z = 0$, these paired orbitals share the same spatial component with different spin components, denoted by convention as α and β. This decomposition can be viewed as a particular case ($N = 2$) of a more general result by Schmidt [23], and later by Carlson and Keller [24]. The importance of this decomposition as a quantum computing ansatz for two electrons will be manifest below.

6.2.2 Variational Hybrid Algorithm

Hybrid quantum-classical algorithms with a variational approach using the variational quantum eigensolver are among the most promising algorithms for near term applications [6, 25–27]. For our approach we utilize a variational eigensolver on the quantum device but apply it only to the optimization of the 2-DM in the natural-orbital basis. Optimization of the natural orbitals by orbital rotations is performed with polynomial scaling on the classical computer. We are able to partition the nonlocal and local degrees of freedom between the quantum and classical calculations respectively.

Using the structure given in Eqs. (6.3)-(6.7), we see that to evaluate the $\tilde{D}$ matrix, we need only: (1) the natural orbital occupations, measured as the orbital populations on the quantum computer, and (2) the phase corresponding to the natural orbital coefficients, which for a real wavefunction, is simply the parity of the term and which can easily be measured on the quantum computer. That is, we need the phase $\xi_{ii'}$ where

$$\tilde{g}_{ii'} = \sqrt{n_i}\xi_{ii'}. \tag{6.8}$$

In general, the phases can be measured through tomography on the quantum computer of certain terms of $\tilde{D}$ requiring only $\mathcal{O}(1)$ additional circuit preparations (see below). The

specific ansatz that we use to implement $\tilde{D}$ is discussed in the next section.

After convergence criteria in the optimization of $\tilde{D}$ on the quantum computer is satisfied through gradient-free optimization (see Appendix 6.5), we optimize the energy on the classical computer through one-body unitary transformations of the Hamiltonian. Specifically, we optimize the orbitals through a series of Givens rotations. The optimization continues until the energy converges to a given threshold. The algorithm can be visualized with the following variational equations for energy from the quantum computer (E_Q) and the classical computer (E_C):

$$E_Q[\mathbf{t}] = \text{Tr } \langle \tilde{D}(\mathbf{t}) \rangle H \tag{6.9}$$

$$E_C[\theta] = \text{Tr } \tilde{D} H(\theta) \tag{6.10}$$

where $\mathbf{t}$ and θ collectively represent the parameters in the ansatz and in the orbital rotations respectively. Alternating these quantum and classical calculations thus leads to convergence of the entire system.

6.2.3 Preparation of Efficient Quantum Ansatz

To create a state of the form in Eq. (6.3) on the quantum computer, we need to implement double excitations from orbitals ii' to kk'. If we consider an initial wavefunction $\tilde{G}_0$ from a standard Hartree-Fock calculation, the ansatz to generate a generic $\tilde{G}$ is:

$$\tilde{G} = \prod_{i=1}^{r-1} \left(\exp \; t_{ii'}^{\bar{i}\bar{i}'} \right) \tilde{G}_0, \tag{6.11}$$

where $\bar{i} = i + 1$, and $t_{ii'}^{\bar{i}\bar{i}'}$ is an antihermitian, antisymmetric two-body matrix with nonzero elements corresponding to an excitation between i, i' and $(i+1), (i+1)'$. The operators acting on $\tilde{G}_0$ can be easily expressed in second quantization as shown in the Appendix 6.5.

The ansatz is a subset of the unitary coupled cluster (UCC)[28] or antihermitian contracted Schrödinger equation (ACSE) ansatz [29]. From there we perform a Jordan-Wigner transformation (though others may be utilized) which yields an exponential of Pauli strings that are implementable on a quantum device as strings of CNOT gates [30]. Additionally, the implementation naturally requires only a nearest neighbor connectivity among qubits.

Finally, the tomography of the state involves only the measurement of the orbital occupations for a given qubit, which are obtained in the computational basis, as well as the sign. Because there are only $r-1$ phase terms (last phase is equivalent to a global phase), we can perform tomography of a linear amount of sequential terms in $\tilde{D}$. These terms have the form $\tilde{D}_{ii'}^{jj'}$, where $j = i+1$. Because terms like $\tilde{D}_{ii'}^{jj'}$ and $\tilde{D}_{(i+2)(i+2)'}^{(j+2)(j+2)'}$ are qubit-wise commuting, we can measure $r/2$ terms simultaneously, leading to a constant number of circuit preparations. In this work we evaluated H_2 and H_3+ using the Jordan-Wigner transformation in 4- and 6- qubit cases. There is only one phase term in the 4-qubit calculations of H_2, which we measured by direct tomography on the quantum computer, whereas the two phases of the 6-qubit calculation of H_3^+ were computed by optimization on the classical computer due to significant corruption of the phase.

6.2.4 Error Mitigation Strategies

Even if we model a two-electron system on a quantum computer and construct the state through the above tomography, we may find that our occupations n_i and $n_{i'}$ do not match for a given i, which implies a violation of the fermion statistics. Because the two-electron ansatz in Section IIB formally guarantees a two-electron wavefunction, any deviation in pure-state N-representability (up to sampling errors) is due to errors on the quantum computer [10, 31, 32].

The effect of errors on current quantum computers can easily influence the N-representability of a system with the extent somewhat depending on the fermionic mapping. For a compact

mapping, S_z and N will typically remain constant, but for more general mappings, this is not the case. Other errors can also accumulate, making it difficult to reach certain extrema of the set of density matrices. To address this, we use a projective technique where we map the set of accessible points onto the ideal set of points (see the Appendix). We achieve this by finding an affine transformation A that maps from the accessible but error-prone set S' to the ideal set S.

For a general mapping, it is easy for the quantum system to violate N and S_z. By utilizing a symmetry verification technique [16, 17], along with the structure of our tomography requiring only measurements of diagonal terms, we can filter out results which do not obey the correct N and S_z values which effectively projects the resulting state into an eigenstate of the chosen operator. This can be extended to other operators S which commute with the Hamiltonian:

$$[S, H] = 0. \tag{6.12}$$

As will be seen in the results, the symmetry verification is useful in bringing the results back to the set of all two-electron states, and then the projection restores the equality of the two pairing-related sets of occupations, n_i and $n_{i'}$.

6.3 Results

Using the two-electron ansatz, we first treat the molecular dissociation of H_2 in a minimal basis set (STO-3G) of two electrons in four orbitals. The quantum algorithm is implemented on both the 5- and 14- qubit devices, denoted as ibm-5 and ibm-14, representing two generations of superconducting quantum devices by IBM. With the Jordan-Wigner transformation [33] the system can be represented with 4-qubits though more compact mappings are certainly possible. Note in this basis only a single excitation is possible. Figure 6.3 shows the potential energy curve of the H_2 molecule, computed with full error mitigation.

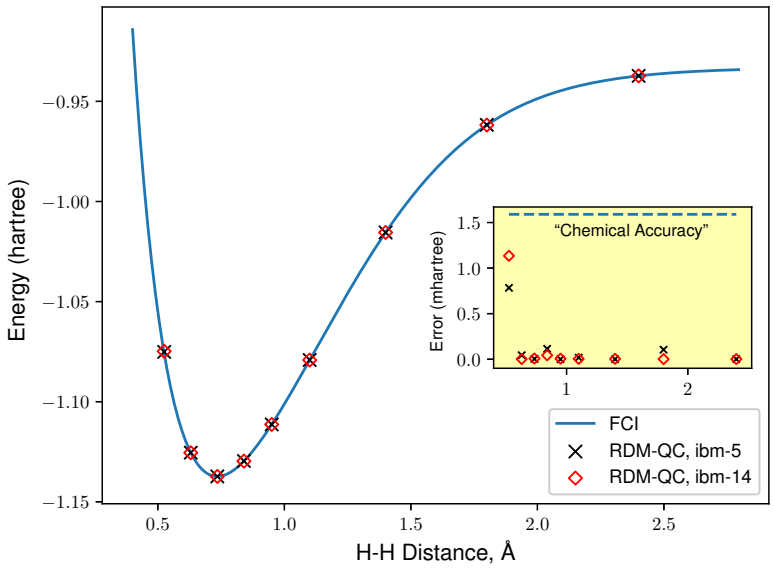

Figure 6.1: Dissociation curves for the ground state of H_2 from the variational quantum algorithm on the quantum computer and the full configuration interaction are shown. Both results were run with 4 qubits, but on 5- and 14- qubit frameworks. The inset shows the difference in energy from the FCI results in mhartrees. The increased error for the shortest distance relates to the difficulty in reaching the Hartree-Fock state on a quantum computer when using entangling gates. For more experimental details, see the Appendix.

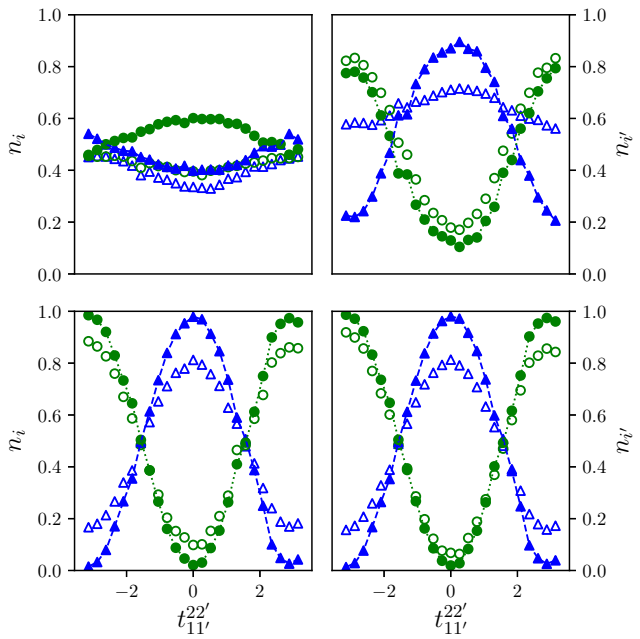

Figure 6.2: Measured (unordered) occupation numbers with respect to the coefficient $t_{11'}^{22'}$ of the single double excitation operator within the entangling circuit. Blue triangles represent the first qubit, and green circles represent the second qubit, unordered. Unfilled objects show the raw occupations, and filled objects the symmetry-corrected occupations. Uncertainties for the values are similar in size to the markers.

With the help of error mitigation techniques, both quantum devices are able to capture the dissociation of the molecule, achieving mhartree accuracy across the spectrum of states, leaving differences in the devices somewhat unclear. Inspection of the device calibration (Appendix A, Table II) indicate that large measurement errors likely occur on ibm-5 with superior performance expected from ibm-14. Scans of the 1-RDMs with respect to the $t_{11'}^{22'}$ parameter controlling the single double excitation are shown in Figure 6.3. The ibm-5 device is seen on the top row, and the ibm-14 on the lower row, and we also show the effect of the symmetry verification in correcting the occupations.

While the ibm-5 device maintains continuity with respect to $t_{11'}^{22'}$, it has distinct problems. First, we observe (see top left insert) correlated measurement error in the set of qubit occupation $\{n_i\}$ which cause an inversion in the expected relationship between n_1 and n_2

among the i (α) occupations. Second, we find that symmetry verification is effective in increasing the differentiability of the two states (note for a decohered system, n_1 and n_2 would be identically 0.5), yet it was not able to correct for the reversal in ordering seen on the qubits, and somewhat reinforces it for n_2.

On ibm-14, while there is still a contraction of the occupation numbers across the range of $t_{11'}^{22'}$, the obtained curve is continuous, and the two sets of occupations correspond to expected values. With symmetry verification, we obtain nearly the ideal occupations, which otherwise are far from spanning the full spectrum of occupations. The effect of our further correction is to stretch the sinusoidal curves in Fig. 6.3 so that their maxima and minima are 1.0 and 0.0 respectively, hence it is not shown here.

To quantify the effects of symmetry verification, we calculate the area between the two changing orbital occupations for both $\{n_i\}$ and $\{n_{i'}\}$ (denoted as V_i and $V_{i'}$, where $V_i = n_2 - n_1$, and $V_{i'} = n_{2'} - n_{1'}$,) subject to different symmetries, as well as the uncertainty in measurement after each symmetry is applied, and show these in Table 1. The maximum and minimum values for this metric would be 2 and 0, representing fully error-free and fully decohered states respectively. In each case, application of multiple symmetries serves to increase the resulting 'reach' of the state, without increasing variance with respect to decreased measurement counts.

Computations with 6 orbitals are performed only on the ibm-14 device since more than 5 qubits are required. Using simplifications seen in Nam et al. [34], we are able to construct a gate with 8 CNOT gates which still requires only neighboring connections (see Appendix 6.5). Due to the longer depth of the circuit, the effects of noise are more pronounced and we find it difficult to reliably measure the phase of the 2-DM terms required in Eq. (6.8) and note that these are not always continuous. To show the overall effect of errors on the 6-qubit system on the local occupations, we present a scan of possible symmetry verified 1-RDMs over a range of the parametrized entangling gates in Fig. 6.4. Additional details

Table 6.1: Shows the area between the two occupations (V) obtained for the entangling circuit described in the text for the two different quantum devices. The V_i and $V_{i'}$ values were calculated separately. Here we have the 5- and 14-qubit devices, respectively, given in a 95% confidence interval due to sampling. The left column indicates the values of with the different applied symmetries.

Device	5-qubit		14-qubit	
	V_i	$V_{i'}$	V_i	$V_{i'}$
None	0.096±0.005	0.861±0.007	1.405±0.007	1.476±0.007
N	0.18±0.01	0.75±0.01	1.89±0.01	1.907±0.009
S_z	0.25±0.01	1.06±0.02	1.723±0.009	1.736±0.009
N, S_z	0.33±0.02	1.43±0.02	1.93±0.01	1.94±0.01

regarding the computation are seen in Appendix 6.5. While we do not show the occupations in terms of the parameters, the effect of the aggregate errors for this case is again to shrink the portion of the hyperplane accessible to the quantum device.

Expectedly, the obtained results differ greatly depending on the qubits and available connectivity of the quantum device, though in general we still observe a degree of continuity in the local 1-RDM properties. By dealing with the phases classically, we are able to calculate the dissociation curve for triangular H_3^+ in Fig. 6.4. Again, we are able to obtain chemically accurate energies across the dissociation curve, although there was difficulty in sampling the uncorrelated Hartree-Fock state which is a vertex of the polytope. The error mitigation techniques we use also extend the capabilities of noise-limited quantum computers, which otherwise do not span the ideal N-representability of the state[35].

6.4 Discussion and Conclusion

In this work we present an ansatz for two-electron quantum systems which can be implemented on near-term and future quantum computers. Applying this on two public-access quantum computers highlights the successes and differences of two generations of quantum computers, as well as the difficulties which must be overcome in approaching more compli-

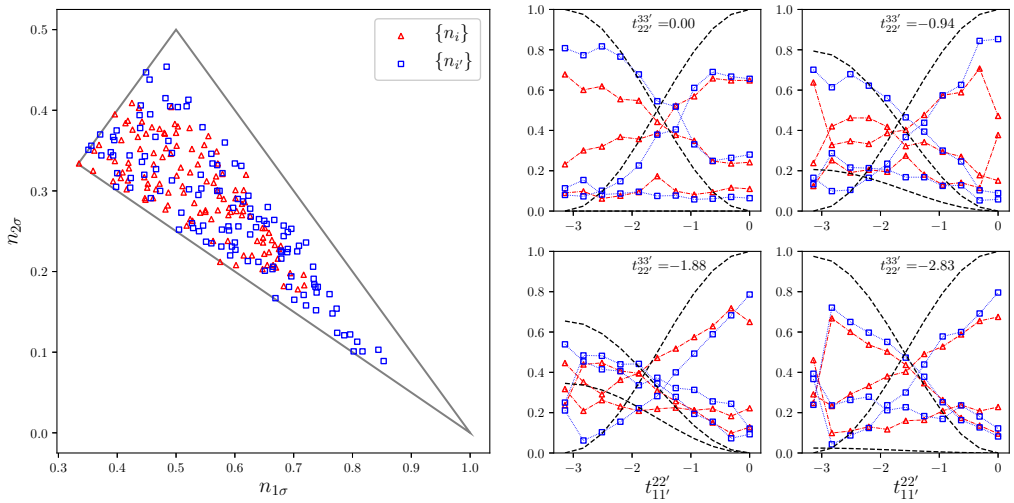

Figure 6.3: (Left) measured occupations of the 6-qubit system following symmetry application of N and S_z, as well as the boundaries of the ideal polytope. Note, σ refers to the use of i or i'. Because these occupations correspond with an N-representable system, the equality $n_{1\sigma} + n_{2\sigma} + n_{3\sigma} = 1$ holds, and so we show the orthographic projection along the $n_{3\sigma}$ axis. (Right) slices of the set with respect to the entangling parameters $t_{11'}^{22'}$ and $t_{22'}^{33'}$ at values of 0.00, -0.94, -1.88, and -2.83. The device was sampled over the range $t_{11'}^{22'}, t_{22'}^{33'} \in [-\pi, 0]$ in $\frac{\pi}{10}$ intervals for the entangling parameters. The ratio of areas of the experimental and theoretical convex hulls of these obtained points is 0.48 and 0.68 for $\{n_i\}$ and $\{n_{i'}\}$, respectively.

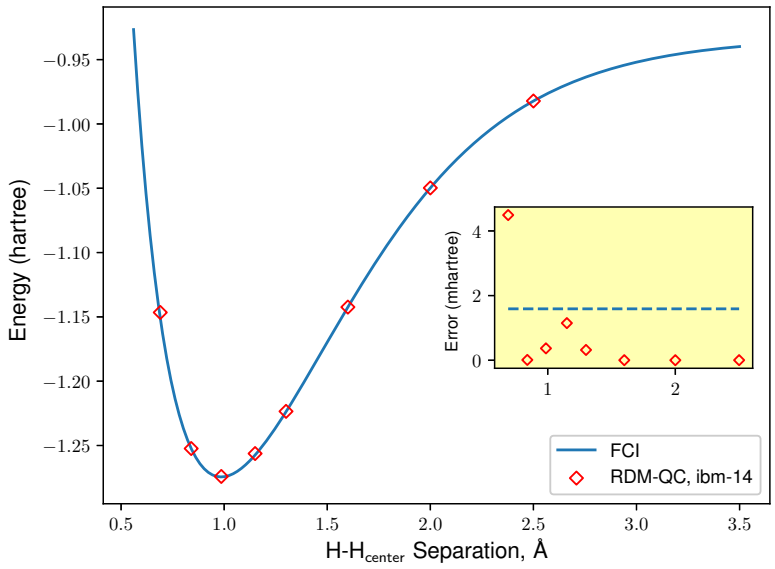

Figure 6.4: Dissociation curves for the ground state of H_3^+ from the variational quantum algorithm on the quantum computer and the full configuration interaction. The experiment was run on a 14- qubit framework. The inset shows the difference in energy from the FCI results in mhartrees. The increased error for the shortest distance relates to the difficulty in reaching the Hartree-Fock state on a quantum computer when using entangling gates. For more experimental details, see the Appendix 6.5.

cated systems. We also show that using error mitigation strategies we are able to simulate both H_2 and H_3^+ to high accuracy. The proposed ansatz can be readily applied to two-electron atoms and molecules in larger basis sets with similar types of error mitigation. The gate sequence proposed here can be applied as a generic ansatz, removing the need for long expansions of the required exponential operators.

The ansatz is efficient mainly in regards to its scalabiltiy with respect to other methods of state preparation. Unitary coupled cluster, which for a two-electron system only needs to be expressed with single and double excitations (i.e., UCCSD), and which additionally has only one occupied orbital for the α and β excitaitons, still will have $\mathcal{O}(r^2)$ terms in the ansatz. Further Tomography additionally would require measurement of the $\alpha\beta$ block of the 2-DM, which naively has $\mathcal{O}(r^4)$ terms, and does not benefit from having only one occupied orbital like UCCSD, and so the method would scale as $\mathcal{O}(d^2M^4)$ where d refers to depth and M to number of measurements. Other methods based on the propagation of the Hamiltonian could be implemented, but also have large costs, and would not necessarily lead to the same advantages that result from the structure of the 2-DM.

From the results, it is clear one cannot rely solely on the energy or other external molecular properties to investigate the integrity of the quantum device, particularly in comparing the performance of the two-qubit devices on the 4-qubit calculation. While averaged or localized metrics related to qubit depolarization, dephasing, or bit-flip errors are often used as indicators of performance of the quantum device, they may not translate directly to the fidelity of a simulated fermionic system, particularly with multi-qubit or environmental effects. Looking at these metrics in conjunction with the physical properties of benchmark problems like the ground state energy of two-electron atoms and molecules will yield greater insights into the fidelity of a quantum device and its needs for error mitigation or correction.

The method of symmetry verification for error mitigation is useful in that its different forms are low cost and can easily correct flagrant faults in the output, such as particle

count (or more generally, parity) and the projected spin symmetries. Others forms of error mitigation related to the RDMs can be implemented as constraints on the tomography from N-representability, or in a form of post-correction of the 2-RDM (two-electron reduced density matrix) where the measured 2-RDM is purified through semidefinite programming, which can be applied to arbitrary N-systems [35]. The mapping we use can have difficulties when errors begin to change the ordering of occupations for larger and larger systems.

The electron pair itself plays a key role in such phenomena as superconductivity and bonding, and yet the exact energy of a two-electron system itself cannot be solved exactly with known methods. Such a problem shows the essence of the electron-electron interaction as well as some of the complexities of electron correlation and quantum mechanics. The theory in this work could also be seen as a subset of more complex geminal-based wave-function methods, which appear in classical electronic structure theory where the electron pair is treated as the fundamental unit to improve the accuracy beyond the mean-field approximation[10]. As suggested by a reviewer, an optimal extension to pair theories or natural orbital functional theories which have favorable reduced scaling on the quantum computer could be implemented as potential benchmarks, likely at quadratic cost in the ansatz.

Here we show that the properties of the two-electron system lead to an ansatz which is well suited for use in a hybrid quantum-classical approach, where degrees of freedom that would increase exponentially with N are treated on the quantum computer, while non-exponentially increasing degrees of freedom are treated on the classical computer. Generally, these algorithms could assist in achieving quantum supremacy by further lowering resource requirements on the quantum computer as well as tomography and measurement costs. The system also is useful as a benchmark for molecular simulation on a quantum computer, where it serves as a simple yet effective way to assess the performance of an arbitrary quantum device. This work is clearly applicable for the current state of noisy quantum computers, but

will continue to be relevant as improving generations of quantum computers are developed. The two-electron ansatz, albeit polynomially scaling even on a classical computer, can serve as a powerful benchmark for quantum computers due to the availability of accurate results from classical computers and the requirements shared by its solution and the solution of exponentially scaling many-electron problems.

6.5 Appendix

Appendix A: Computational Details

The electronic structure package PySCF [36] was used to obtain the one- and two- electron integrals and to perform restricted Hartree-Fock and full configuration interaction (FCI) calculations.

For the quantum computation we used the IBM Quantum Experience devices Yorktown (Sparrow, 5-qubits) and Melbourne (Albatross, 14-qubits), available online. The former has triangular-type coupling between qubits, and the latter has square-type coupling between qubits. These cloud accessible quantum devices are fixed-frequency transmon qubits with co-planer waveguide resonators [37, 38]. The quantum information software development kit QISKIT was used to interface with the device. We include the calibration data in Table II.

For the 6-qubit case, 2^{11} measurements were obtained, and we used a simple Nelder-Mead simplex method with the Han initial simplex for the 6-qubit case on the quantum computer. Classically orbital rotations were performed with Givens rotations, with the Broyden-Fletcher-Goldfarb-Shanno (BFGS) algorithm being utilized. Convergence criteria were more strict for the 4-qubit case, with convergence between the ${}^2D$ and ${}^2K$ steps being 1 mH. In the 4- and 6-qubit cases, we chose the best of 2 runs as the optimal results. While this did not make a difference for most points, for those it did, the difference in energies for the 2 runs were usually significant, indicating that noise had led the optimization into some

Table 6.2: Calibration data for the ibm-5 and ibm-14 devices during benchmarking. U_2 and U_3 represent the errors for single qubit unitaries containing one and two $X_{\pi/2}$ pulses and two and three frame changes respectively. RO represents the readout error, and we have the standard T_1 depolarization and T_2 dephasing times. $[j]$ specifies the target qubit with control qubit i, and we report the error.

Qubit i	$\mathbf{U}_2$ (10^{-3})	$\mathbf{U}_3$ (10^{-3})	**RO** (10^{-2})	$\mathbf{T}_1$ (μs)	$\mathbf{T}_2$ (μs)	$[j]$ $\mathbf{CX}_i^j$ (10^{-2})		
ibm-5								
0	2.7	5.5	5	46	53	[1] 5.1	[2] 4.2	
1	2.9	5.8	25	62	53	[2] 6.8		
2	6.4	12.9	1	85	74			
3	3.8	7.6	17	61	28	[2] 7.9	[4] 4.0	
4	2.8	5.7	36	68	62	[2] 4.2		
ibm-14								
0	2.3	4.7	3	62	22			
1	5.1	10.1	10	54	101	[0] 3.7	[2] 6.4	
2	3.9	7.8	5	75	168	[3] 6.7		
3	1.5	3.0	27	63	51			
4	2.4	4.8	6	56	34	[3] 5.6	[10] 5.4	
5	2.3	4.6	4	24	46	[4] 6.1	[6] 7.5	[9] 5.9
6	2.3	4.6	4	77	53	[8] 2.9		
7	1.3	2.7	16	50	82	[8] 2.3		
8	1.5	3.0	4	125	183			
9	2.8	5.6	4	44	65	[8] 7.0	[10] 4.0	
10	2.5	5.0	4	51	55			
11	181	362	34	63	102	[3] 14	[10] 10	[12] 11
12	3.7	7.3	9	89	177	[2] 7.3		
13	5.1	10.3	4	26	59	[1] 13	[12] 3.9	

local minima.

Appendix B: Error Mitigation with N-Representability of $\wedge^2\mathcal{H}_n$

The error correction is similar to previous work where we look for a transformation A to map the experimental polytope S' to the correct polytope S. The structure of the N-representability conditions is such that the ordering inequalities applied to each of the half-sets ($\{n_i\}$ and $\{n_{i'}\}$) describe a hyperplane. The vertices V^r can be described as a set with

elements v_j^r (r spatial orbitals):

$$v_j^r = [\frac{H(j-1)}{j}, \frac{H(j-2)}{j}, ..., \frac{H(j-r)}{j}] \tag{6.13}$$

where $1 \leq j \leq r$ and $H(x)$ is the Heaviside step function. The vertices for $\wedge^2\mathcal{H}_4$ are given as $v_1^2 = (1,0)$, $v_2^2 = (\frac{1}{2}, \frac{1}{2})$. The vertices for $\wedge^2\mathcal{H}_6$ are then: $v_1^3 = (1,0,0)$, $v_2^3 = (\frac{1}{2}, \frac{1}{2}, 0)$, $v_3^3 = (\frac{1}{3}, \frac{1}{3}, \frac{1}{3})$. These form a $r-1$ dimensional hyperplane in the r dimensional subspace for the two half sets, respectively. The practical effect of symmetry verification here (mostly from the S_z application) is to project noisy points onto the plane. The effect of the N-representability application then is to map the measured points to the extreme points of $V^{n'}$. This can be visualized in Fig. (6.4) by mapping the accessible triangular plane to the black outlined plane.

For points close to the edges, one can imagine that with significant non-coherent error the projected points might lie outside of the space. We account for this by re-projecting these points into the polytope according to the closest edge. A simple semi-definite program would also suffice, though we take a more geometric approach. For mild errors we find that this method is satisfactory.

Appendix C: Second-Quantization Treatment of Entangling Gates and Phase

The exponential operator in (6.11) has a readily recognizable form in second quantization. Utilizing creation and annihilation operators in the natural orbital basis the operator:

$$\hat{T}_j^i = t_{jj'}^{ii'} \hat{a}_i^\dagger \hat{a}_{i'}^\dagger \hat{a}_{j'} \hat{a}_j \tag{6.14}$$

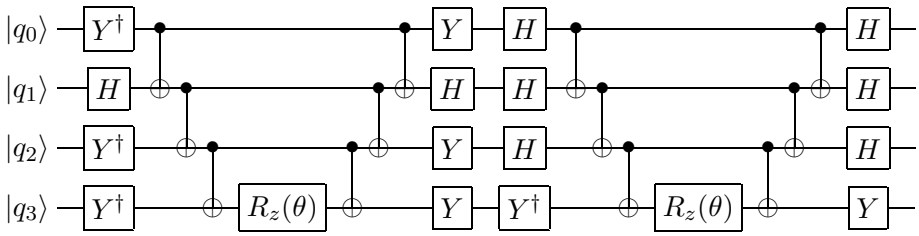

Figure 6.5: The unitary coupled cluster term for two Pauli terms, here representing the exponent of $Y_0X_1Y_2Y_3$ followed by $X_0X_1X_2Y_3$. For optimal connectivity (i.e., no intermediate CNOT gates for intermediate orbitals), there are 12 CNOT operations, generally the most error prone step.

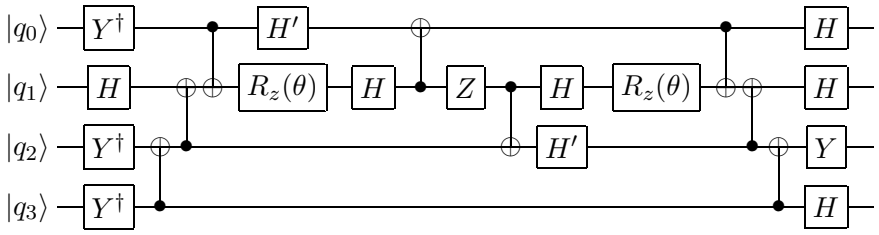

Figure 6.6: The unitary coupled cluster term as seen in Fig. 6.5, but in a simplified form. Note the target qubit for the rotation here is not q_3 but q_1. Importantly, the circuit require only 8 CNOT operations, and still has the same connectivity requirements. The gate H' is defined as $S^\dagger HS$ (applied left to right).

where $t^{ii'}_{jj'}$ is a scalar, and anti symmetric with respect to swapping lower or upper indices, can be used to construct a two-body unitary operator U:

$$U = \exp(\hat{T}^i_j - \hat{T}^{i\dagger}_j). \tag{6.15}$$

Only one exponential Pauli term is needed to excite the initial double excitation. After that, a simplification was performed akin to that of Nam et al.[34]. For a system of two electrons, because do not consider number or spin changing operations, using the inverse Jordan-Wigner mapping we can simplify the total number of Pauli terms needed in the exponential to two.

To measure the phase of the terms in Eq. (6.8), we are interested in tomography of the

2-DM elements. Using the Jordan-Wigner transformation we can approximate the total operator as:

$$\langle M_{ij} \rangle = \langle \hat{a}_i^\dagger \hat{a}_{i'}^\dagger \hat{a}_{j'} \hat{a}_j + \hat{a}_j^\dagger \hat{a}_{j'}^\dagger \hat{a}_{i'} \hat{a}_i \rangle \tag{6.16}$$

$$\approx \frac{1}{4} \langle X_i X_j X_{i'} X_{j'} \rangle + \frac{1}{4} \langle X_i X_j Y_{i'} Y_{j'} \rangle \tag{6.17}$$

$$\approx \frac{1}{4} \langle X_i X_j X_{i'} X_{j'} \rangle + \frac{1}{4} \langle Y_i Y_j X_{i'} X_{j'} \rangle. \tag{6.18}$$

Where we utilize the fact that any non-number conserving elements will be contribute 0. Due to the limited amount of sign terms we need to measure, and the fact every other excitation in the linear sequence will be completely commuting, we can prepare one circuit with only X_i terms, and another with alternating X and Y pairs which with give sign terms of either (6.16) or (6.18), yielding only 2 circuit preparations and a $\mathcal{O}(1)$ complexity. Note, obtaining all of the proper terms also scales as $\mathcal{O}(1)$, taking no more than 8 additional circuits. This method however did not yield significant increases in the accuracy in our computations, and so for our optimizations we used the approximate circuit.

One issue with a direct measurement of the sign is that while the diagonal elements we measure can be symmetry verified, the N and S_z operators do not necessarily commute with the Pauli terms (despite commuting with the operator as a whole). $[\hat{N}, X_1 X_2 Y_3 Y_4] \neq 0$. To partially address this we attempted to use in-line symmetry measurements, where we cast the Pauli measurement onto an ancilla qubit, allowing by propagating through the circuit to the corresponding entangling gate. This requires explicit connectivity requirements and attention to the layout, as a change in Pauli basis between the applied entangler and the required Pauli term. One issue we found was that while the sign information obtained in this manner was coherent and exhibited the proper behavior and change in sign with respect to $t_{11'}^{22'}$, there was a phase difference on the ancilla which resulted in the sign information being shifted from the magnitude of the occupations. A direct measurement of the Pauli

terms, while not allowing for symmetry verification, still contained the correct qualitative information, and so was utilized for the 4-qubit case. For the 6-qubit case, obtaining reliable information throughout the longer optimization requirements was more difficult, and so to ease the demands on the quantum computer we mapped the sign of the elements to the sign of the ideal function generated by our entanglers (a simple product of sine and cosine functions).

References

[1] D. S. Abrams and S. Lloyd, Phys. Rev. Lett. **83**, 5162 (1999).

[2] R. Santagati, J. Wang, A. A. Gentile, S. Paesani, N. Wiebe, J. R. McClean, S. Morley-Short, P. J. Shadbolt, D. Bonneau, J. W. Silverstone, D. P. Tew, X. Zhou, J. L. O'Brien, and M. G. Thompson, Science Advances **4**, 1 (2018).

[3] R. Babbush, P. J. Love, and A. Aspuru-Guzik, Scientific Reports **4**, 6603 (2015).

[4] S. McArdle, S. Endo, A. Aspuru-Guzik, S. Benjamin, and X. Yuan, arXiv: 1808.10402 , 1 (2018).

[5] I. Kassal, J. D. Whitfield, A. Perdomo-Ortiz, M.-h. Yung, and A. Aspuru-Guzik, Annu. Rev. Phys. Chem. **62**, 185 (2011).

[6] A. Kandala, A. Mezzacapo, K. Temme, M. Takita, M. Brink, J. M. Chow, and J. M. Gambetta, Nature **549**, 242 (2017).

[7] A. Kandala, K. Temme, A. D. Córcoles, A. Mezzacapo, J. M. Chow, and J. M. Gambetta, Nature **567**, 491 (2019).

[8] N. Moll, P. Barkoutsos, L. S. Bishop, J. M. Chow, A. Cross, D. J. Egger, S. Filipp, A. Fuhrer, J. M. Gambetta, M. Ganzhorn, A. Kandala, A. Mezzacapo, P. Müller,

W. Riess, G. Salis, J. Smolin, I. Tavernelli, and K. Temme, Quantum Sci. Tech. **3**, 030503 (2018).

[9] M. Piris, in *Adv. Chem. Phys.*, Vol. 134 (2007) pp. 385–427.

[10] A. Coleman and V. Yukalov, *Reduced Density Matrices: Coulson's Challenge* (Springer, Berlin Heidelberg New York, 2000).

[11] D. A. Mazziotti, J. Chem. Phys. **112**, 10125 (2000).

[12] P. A. Johnson, P. W. Ayers, P. A. Limacher, S. D. Baerdemacker, D. V. Neck, and P. Bultinck, Comput. Theor. Chem. **1003**, 101 (2013).

[13] M. Walter, D. Gross, and J. Eisert, arXiv: 1612.02437 , 1 (2016).

[14] J. R. McClean, M. E. Kimchi-Schwartz, J. Carter, and W. A. de Jong, Phys. Rev. A **95**, 042308 (2017).

[15] K. Temme, S. Bravyi, and J. M. Gambetta, Phys. Rev. Lett. **119**, 1 (2017).

[16] X. Bonet-Monroig, R. Sagastizabal, M. Singh, and T. E. O'Brien, Phys. Rev. A **98**, 1 (2018).

[17] R. Sagastizabal, X. Bonet-Monroig, M. Singh, M. A. Rol, C. C. Bultink, X. Fu, C. H. Price, V. P. Ostroukh, N. Muthusubramanian, A. Bruno, M. Beekman, N. Haider, T. E. O'Brien, and L. DiCarlo, Phys. Rev. A **100**, 010302 (2019).

[18] J. Preskill, Quantum **2**, 79 (2018).

[19] D. Wecker, M. B. Hastings, and M. Troyer, Phys. Rev. A **92**, 042303 (2015).

[20] P.-O. Löwdin and H. Shull, Phys. Rev. **101**, 1730 (1956).

[21] P.-O. Löwdin, Rev. Mod. Phys. **32**, 328 (1960).

[22] B. Zumino, J. Math. Phys. **3**, 1055 (1962).

[23] E. Schmidt, Math. Ann. **63**, 433 (1907).

[24] B. C. Carlson and J. M. Keller, Phys. Rev. **121**, 659 (1961).

[25] A. Peruzzo, J. McClean, P. Shadbolt, M.-H. Yung, X.-Q. Zhou, P. J. Love, A. Aspuru-Guzik, and J. L. O'Brien, Nat. Commun. **5**, 4213 (2014).

[26] J. R. McClean, J. Romero, R. Babbush, and A. Aspuru-Guzik, New J. Phys. **18**, 023023 (2016).

[27] H. R. Grimsley, S. E. Economou, E. Barnes, and N. J. Mayhall, Nat. Commun. (2018).

[28] J. Romero, R. Babbush, J. R. McClean, C. Hempel, P. J. Love, and A. Aspuru-Guzik, Quantum Sci. Tech. **4**, 014008 (2018).

[29] D. A. Mazziotti, Phys. Rev. A **75**, 1 (2007).

[30] M. A. Nielsen and I. L. Chuang, *Cambridge University Press* (2010) p. 702, arXiv:1011.1669v3 .

[31] M. Altunbulak and A. Klyachko, Commun. Math. Phys. **282**, 287 (2008).

[32] D. A. Mazziotti, Phys. Rev. A **94**, 032516 (2016).

[33] P. Jordan and E. Wigner, Z. Phys. **47**, 631 (1928).

[34] Y. Nam, J.-s. Chen, N. C. Pisenti, K. Wright, C. Delaney, D. Maslov, K. R. Brown, S. Allen, J. M. Amini, J. Apisdorf, K. M. Beck, A. Blinov, V. Chaplin, M. Chmielewski, C. Collins, S. Debnath, A. M. Ducore, K. M. Hudek, M. Keesan, S. M. Kreikemeier, J. Mizrahi, P. Solomon, M. Williams, J. D. Wong-Campos, C. Monroe, and J. Kim, arXiv: 1902.10171 , 1 (2019).

[35] S. E. Smart and D. A. Mazziotti, Phys. Rev. A **100**, 022517 (2019).

[36] Q. Sun, T. C. Berkelbach, N. S. Blunt, G. H. Booth, S. Guo, Z. Li, J. Liu, J. McClain, E. R. Sayfutyarova, S. Sharma, S. Wouters, and G. K.-L. Chan, arXiv: 1701.08223 , 1 (2017).

[37] J. Koch, T. M. Yu, J. Gambetta, A. A. Houck, D. I. Schuster, J. Majer, A. Blais, M. H. Devoret, S. M. Girvin, and R. J. Schoelkopf, Phys. Rev. A **76**, 042319 (2007).

[38] J. M. Chow, A. D. Córcoles, J. M. Gambetta, C. Rigetti, B. R. Johnson, J. A. Smolin, J. R. Rozen, G. A. Keefe, M. B. Rothwell, M. B. Ketchen, and M. Steffen, Phys. Rev. Lett. **107**, 080502 (2011).

CHAPTER 7

REDUCING TOMOGRAPHY COSTS WITH A SYMMETRY PROJECTED OPERATOR BASIS

Material from: Smart, S. E., & Mazziotti, D. A. (2021). Lowering tomography costs in quantum simulation with a symmetry projected operator basis. Physical Review A, 103 (1), 012420.

7.1 Introduction

One of the fundamental challenges in quantum simulation is the storage and propagation of exponentially scaling many-body quantum states. Many classical computational methods treat these states approximately, using perturbative and truncated approaches or local approximations, and result in polynomial algorithms which potentially sacrifice key characteristics of the quantum state [1, 2]. Reduced density matrix (RDM) methods focus on reducing the required state information to the $k-$body interaction inherent in the system (such as the 2-RDM for fermionic simulations) [3–15]. In these cases, the 2-RDM then is subject to its own set of criteria, such as $N-$representability, but can deal with many-body phenomena in an easier manner [3, 16–18].

An easy way to reduce the required amount of information to describe the state is through utilizing symmetries. Symmetries are conserved quantities, preserved through the preparation and propagation of a state [2, 19, 20]. For molecular systems, particle number, total and projected spin, invariance under time-reversal, and often molecular point groups are examples of symmetries. These can be used in classical electronic structure calculations to substantially reduce the number of resources necessary to simulate a system [2, 21, 22]. On a quantum computer, the exponentially scaling state can be prepared efficiently for many applications. For systems with a $k-$body interaction, tomography of the $k-$RDM is suf-

ficient to describe the system's physical properties. Storage of the state (which is critical for near-term applications) can be reduced to the tomography of the k-RDM based on the $k-$body interaction [15, 23–26]. In contrast to classical RDMs method, a pure quantum state would automatically satisfy the $N-$representability problem.

In quantum computing, symmetries are utilized in a wide range of settings. There is ongoing work to utilize number-preserving gate sequences [27, 28], design algorithms for preparing symmetry preserving ansatz [29–35], reduce symmetry violations through variational constraints [36–38], reduce the simulated Hilbert space through varied applications of symmetries [39–41], and to utilize symmetries as a form of error mitigation [42–44].

Despite potential reductions in the state complexity using symmetries or other methods, tomography still can require a large set of measurements. For molecular systems, the Hamiltonian and 2-RDM scale as $O(r^4)$, where r is the number of basis functions, and many heuristic and systematic ways involving graph-theoretic or combinatorial approaches have been introduced to lower this number, which in some cases can render an apparent scaling of $O(r^3)$ or $O(r^2)$ with swap networks [24, 45–47]. Within quantum simulation as a whole, fermionic tomography is particularly challenging due to the nonlocal characteristics of fermionic operators and prevents a logarithmic reduction in complexity seen with other qubit systems [24].

In this work we present a method of lowering measurement and tomography costs for quantum states and RDMs by exploiting the quantum state's symmetries. By finding the symmetry projected form of our measurement operators, we can re-express our operators in a minimal basis on the quantum computer. The method leads to a constant scaling improvement in the number of terms which has to be measured, and can be combined with other measurement techniques to reduce circuit preparation costs for near-term calculations.

7.2 Theory

A symmetry for a quantum system can be defined mathematically as a non-zero operator $\hat{S}$ which commutes with the system Hamiltonian $\hat{H}$,

$$[\hat{H}, \hat{S}] = 0. \tag{7.1}$$

Consider a set of n symmetries $\mathcal{S} = \{S_1, S_2, ..., S_n\}$ where each symmetry commutes with all other symmetries (note that the most common set in fermionic simulation of $\hat{N}, \hat{S}_z$, and $\hat{S}^2$ obeys this). We can find a basis which is a mutual eigenbasis of each element of $\mathcal{S}$, and then we denote a wavefunction which obeys each of these symmetries:

$$|\psi\rangle = \sum_{\alpha} c_\alpha |\alpha, s_1, s_2, ..., s_n\rangle, \tag{7.2}$$

where each s_i represents the eigenvalues of the i-th symmetry. Now, let $\hat{A}$ be an operator acting on this state in this symmetry basis:

$$\hat{A} = \sum a^{\alpha, t_1, t_2, ...t_n}_{\beta, u_1, u_2, ...u_n} |\alpha, t_1, t_2, ..., t_n\rangle\langle\beta, u_1, u_2, ..., u_n|. \tag{7.3}$$

Then, if we are interested in the expectation of $\hat{A}$, we can evaluate it as:

$$\langle\hat{A}\rangle = \sum_{i,j} c_i^* c_j a^{i, s_1, s_2, ..., s_n}_{j, s_1, s_2, ..., s_n} \tag{7.4}$$

and so we have projected $\hat{A}$ into the specific subspace of each symmetry, despite that $\hat{A}$ does not necessarily commute with $\hat{S}$. Note that if each symmetry did not commute, our eigenvectors would not be simultaneous eigenstates, and we could instead apply the operators in terms of increasing restrictions as relevant to the quantum state.

In quantum simulation, often we measure operators which likely do not violate these sym-

metries individually but often cannot be directly measured on the quantum computer.Instead, we map these operators to a set of measurable operators on the quantum device, which commonly today are projective measurements onto eigenvectors of the Pauli matrices. The basis of operators will not always commute with the state's symmetries, and so will be projected by the wavefunction.

To find the projected form, we could explicitly calculate the operator form in Eq. (7.4) for small systems, but this quickly becomes unfeasible with increasing system size. By noting that most operators we are interested in act non-trivially on a few local sites, we can find a projected form acting on the local space. The form of this operator can be found relatively easily for particular symmetries, and we derive our approach in Appendix 7.5. Instead of focusing on one symmetry state s, we project our operator onto a symmetry *conserving* subspace:

$$\langle \tilde{A} \rangle = \sum_s \langle \hat{P}_s \hat{A} \hat{P}_s \rangle = \sum_s \sum_{i,j} c_i^* c_j a_{j,s}^{i,s}, \tag{7.5}$$

where $\hat{P}_s$ is a projection onto a single symmetry s. The projected form can be viewed as a mixed operator resulting from projecting onto different pure symmetry states. Notably, both $\tilde{A}$ and the projected $\hat{A}$ will generally contain significantly less terms than the native qubit operators.

With these points in view, our approach is as follows. Given an operator $\hat{M}$, we express it in the Pauli basis using some transformation:

$$\hat{M} = \sum_i a_i \hat{A}_i \tag{7.6}$$

where $\hat{A}_i$ are typically Pauli strings. Then, we apply our symmetry projection to the individual $\hat{A}_i^c = \sum_s \hat{P}_s \hat{A}_i \hat{P}_s$. We represent both the operator and the Pauli strings in a vector form ($\vec{m}$, and $\vec{A}_i^c$) and then using $\vec{A}_i^c$ as columns, form a matrix of linearly independent vectors, U.

Table 7.1: Example procedure for finding a set of symmetry projected operators. The vector representation of $\hat{A}$ is given as $\vec{A}$.

Given operators sets for measurement (M), symmetries ($\mathcal{S}$) and the computational basis (A);
(0) Find a set of projection operators $\hat{P}_s$;
(1) For each measurement operator $\hat{m} \in M$:
(a) Transform $\hat{m}$ in A, $\hat{m} = \sum_i a_i \hat{A}_i$
(b) For each $\hat{A}_i$, find symmetry projected computational operators $\hat{A}_i^c$
(c) Choose linearly independent $\vec{A}_j$ as columns of U and solve for $U\vec{x}_m = \vec{m}$
(2) Apply further processing with new set of operators $\{\vec{x}_m\}$

Finally, we solve the linear system of equations for a vector $\vec{x}$:

$$U\vec{x} = \vec{m} \tag{7.7}$$

to obtain a new basis of measurement for $\hat{M}$ which is equal to or lower in dimension. In general, this will not be unique, and we can order our selection process or bias it to affect the set of terms. The process here is summarized in Table 7.1 and an example is included in Appendix 7.5.

7.3 Results and Applications

7.3.1 Application to Reduced Density Operators

This work's inspiration is centered on molecular and fermionic systems, which only need characterization of the particles pairwise interactions. These are completely captured in the two-electron reduced density matrix, or 2-RDM, which represents a partial tomography of the quantum state. Elements of the 2-RDM are measured according to:

$${}^2D^{i,k}_{j,l} = \langle\psi|a_i^\dagger a_k^\dagger a_j a_l|\psi\rangle \tag{7.8}$$

where i, j, k, and l are spin orbital indices. On the quantum computer, the most basic mapping from fermions to qubits is the Jordan-Wigner transformation. This transforms the creation and annihilation operators as [48]:

$$a_j^\dagger = \frac{1}{2}(X_j - iY_j)\bigotimes_{k=1}^{j-1} Z_k, \tag{7.9}$$

$$a_j = \frac{1}{2}(X_j + iY_j)\bigotimes_{k=1}^{j-1} Z_k, \tag{7.10}$$

where X_j, Y_j, and Z_j indicate a Pauli operator acting on qubit j. The local aspect of the operation on a qubit is defined by the X and Y gates, whereas the Z portion generates parity-conserving gates. The parity mapping [49, 50] exchanges the storage of orbital occupations and parity, and the Bravyi-Kitaev mapping stores both in a tree-like diagram [51]. Both of these schemes form linear combinations of operators which act differently on local sites and identically on nonlocal sites, and thus can be symmetry projected with our technique.

For higher order RDMs (which can be used for exploring states in a linear- or quadratic-expansive subspace or in other methods [52]), similar advantages can be seen. We show the effect of our symmetry projection technique in reducing the number of measurements for 1, 2, and 3-RDMs in Table 7.2. We specify cases with different number of excitations because particle and hole operators commute with the given molecular symmetries, whereas excitations (or de-excitations) will transform to operators in the computational basis that *individually* may not conserve a given symmetry. The set of measurements in performing tomography of the 2-RDM contains the set required for molecular Hamiltonians, and thus can be used in Hamiltonian based measurement. An advantage of focusing on the 2-RDM is that it enables systematic approaches in the tomography and that the 2-RDM itself can be used as a tool in error-mitigation [24, 25, 35, 52, 53].

One technique to lower measurement costs involves using the qubit-wise commutation

Table 7.2: Dimension of the number of nonzero elements required for tomography of the 1- and 2-RDMs in the traditional (naive) and symmetry projected (reduced) approaches for given spin and spatial configurations of the second quantized measurement operators with $\hat{N}$, and $\hat{S}_z$ symmetries under the Jordan-Wigner transformation. We also give examples of the sets of operators in the naive (N) and reduced (R) methods corresponding with operators marked with a ($*$). Note, R is not unique in any of these cases. The cases including the $\hat{S}^2$ symmetry do not greatly affect the results, but require covering the many permutations of the spatial orbitals. A bar across spins indicates an excitation or de-excitation between these orbitals, and only the unique spin configuration is shown. $\times$ indices the Cartesian product of two sets. $\vec{Z}$ indicates a tensor product of Z gates which is constant across all operations.

$k-$RDM	Spin	$q-$Sites	Naive	Reduced	Example Operator and Sets of Measurement Operators
1	$\alpha\alpha$	1	2	2	$a_i^\dagger a_j, \quad \{i,j\} \in \alpha$
	$\alpha\bar{\alpha}^*$	2	4	2	
	$\alpha\beta$	-	-	0	$\mathrm{N} = \{X_i, Y_i\} \times \{X_j, Y_j\}\vec{Z}, \ \mathrm{R} = \{X_i X_j \vec{Z}, X_i Y_j \vec{Z}\}$
2	$\alpha\alpha\alpha\alpha$	2	4	4	
	$\alpha\alpha\alpha\bar{\alpha}$	3	8	4	$a_i^\dagger a_k^\dagger a_l a_j + a_j^\dagger a_l^\dagger a_k a_i$
	$\alpha\bar{\alpha}\alpha\bar{\alpha}$	4	16	6	$\{i,j\} \in \alpha, \{k,l\} \in \beta$
	$\alpha\alpha\alpha\beta$	-	-	0	$\mathrm{N} = \{X_i X_k, Y_i Y_k\} \times \{X_l X_j, Y_l Y_j\}\vec{Z} \cup$
	$\alpha\alpha\beta\beta$	2	4	4	$\{X_i Y_k, Y_i X_k\} \times \{X_l Y_j, Y_l X_j\}\vec{Z},$
	$\alpha\alpha\bar{\beta}\beta$	3	8	4	$\mathrm{R} = \{X_i X_k X_l X_j \vec{Z}, X_i Y_k Y_l X_\mathrm{J} \vec{Z}\}$
	$\alpha\bar{\alpha}\beta\bar{\beta}^*$	4	16	4	
3	$\alpha\alpha\alpha\alpha\alpha\alpha$	3	8	8	
	$\alpha\alpha\alpha\alpha\alpha\bar{\alpha}$	4	16	8	$a_i^\dagger a_k^\dagger a_m^\dagger a_n a_l a_j + a_j^\dagger a_l^\dagger a_n^\dagger a_m a_k a_i$
	$\alpha\alpha\alpha\bar{\alpha}\alpha\bar{\alpha}$	5	32	12	$\{i,j,k,l\} \in \alpha, \ \{m,n\} \in \beta$
	$\alpha\alpha\alpha\alpha\alpha\alpha$	6	64	20	$\mathrm{N} =$
	$\alpha\alpha\alpha\alpha\alpha\beta$	-	-	0	$\{X_i X_k, Y_i Y_k\}\vec{Z} \times (\{X_m X_n, Y_m Y_n\} \times \{X_l X_j, Y_l Y_j\} \cup$
	$\alpha\alpha\alpha\alpha\beta\beta$	3	8	8	$\{X_m Y_n, Y_m X_n\} \times \{X_l Y_j, Y_l X_j\}) \cup$
	$\alpha\alpha\bar{\alpha}\alpha\beta\beta$	4	16	8	$\{X_i Y_k, Y_i X_k\}\vec{Z} \times (\{X_m Y_k, Y_m X_n\} \times \{X_l X_j, Y_l Y_j\} \cup$
	$\alpha\alpha\alpha\bar{\alpha}\beta\bar{\beta}$	4	16	8	$\{X_m X_n, Y_m Y_n\} \times \{X_l Y_j, Y_l X_j\}),$
	$\alpha\alpha\bar{\alpha}\alpha\bar{\beta}\beta$	5	32	8	$\mathrm{R} =$
	$\alpha\bar{\alpha}\alpha\bar{\alpha}\beta\beta$	5	32	12	$\{\{(X_i X_k Y_l X_j, Y_i X_k X_l X_j, X_i Y_k X_l X_j\} \times Y_m X_n \vec{Z} \cup$
	$\alpha\bar{\alpha}\alpha\bar{\alpha}\beta\bar{\beta}^*$	6	64	12	$\{X_i X_k X_l X_j, Y_i Y_k X_l X_j, Y_i X_k Y_l X_j\} \times X_m X_n \vec{Z}\}$
	$\alpha\alpha\alpha\beta\beta\beta$	-	-	0	

relation, which relates Pauli strings which can be concatenated and thus simultaneously measured through local measurement schemes. Finding the optimal grouping is a NP hard problem, but by characterizing the set of measurements as a graph problem connected by this relation, we can use coloring algorithms to reduce the number of colors (or cliques) needed [47, 54]. To consider the advantage in using our projected technique, we can compare the number of cliques obtained with the default tomography to number obtained with our method. We explore this for obtaining 2-RDMs of differing sizes in Figure 7.1. Additionally, the worst-case scaling of the number of tomography terms is $\mathcal{O}(r^4)$, and we look at overall scaling coefficient (r^n) under the grouping technique with both measurement schemes. If one used the maximally commuting method [46, 47], which for the most part finds larger groups of operators that can be simultaneously measured, the circuit depth scales polynomially with the number of terms in a group, and so our scheme would lead to reductions in the transformation required.

7.3.2 Effects of Noise on Particle Count

One implicit assumption in the above work is that the quantum state is of decent quality and that it preserves the proper symmetries throughout the simulation. Due to noise, this will almost certainly never be the case, so we are interested in how noise can affect our symmetry projected scheme's quality.

From a theoretical perspective, we can envision two broad cases. In the first, we have a mixed state which is a sum of weighted states:

$$\rho = \sum_s \sum_i \alpha_{si} |i, s\rangle\langle i, s|. \tag{7.11}$$

In this case the symmetry projection is still exact, as the states are orthogonal to each other, and our method will not be affected by errors. The second case involves a state

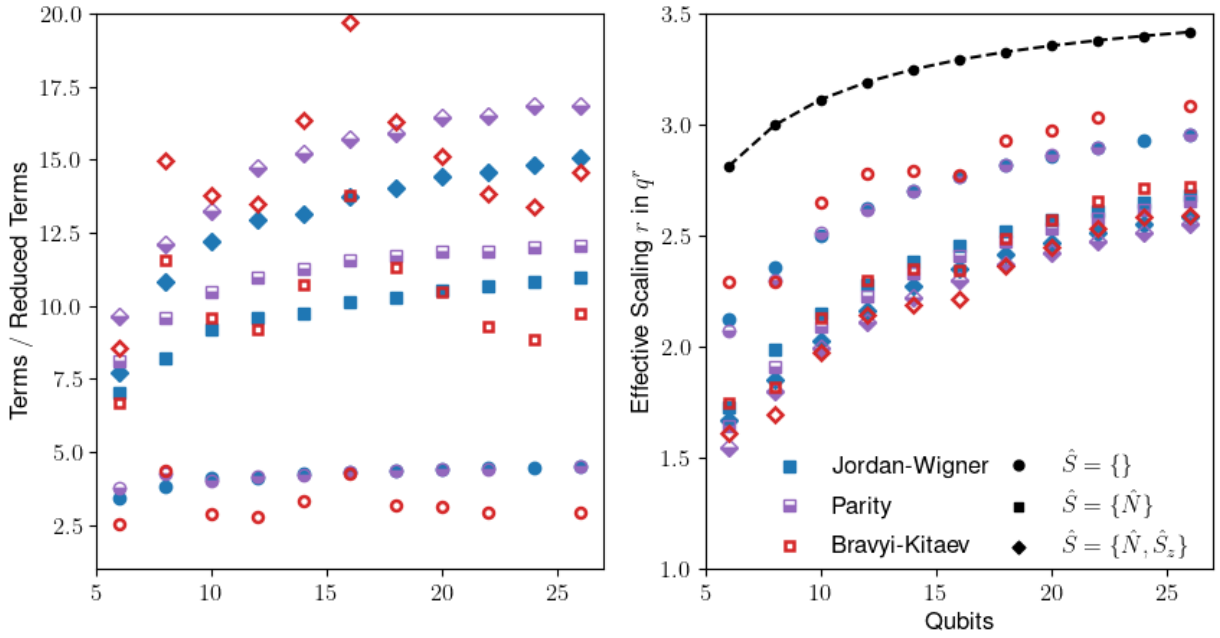

Figure 7.1: (Left) Ratio of the number of total required terms in the 2-RDM versus the number of required circuits following a grouping procedure, and (right) the scaling coefficient of the number of circuits with respect to the number of qubits. The color denotes the fermionic mapping (Jordan-Wigner, Parity, and Bravyi-Kitaev), and the symbol denotes the set of symmetries applied in the projection procedure. The grouping procedure involves grouping terms according to qubit-wise commutation following Ref. [54]. The black line on the right refers to total number of terms. See Appendix 7.5 for more details.

Table 7.3: A comparison of 2-RDMs of a two-electron system under varying levels of simulated noise (simulated and experimental) through the Frobenius norm of the difference matrices at randomly sampled points. ${}^2D$ refers to the ideal 2-RDM, ${}^2\tilde{D}$ refers to standard tomography of the 2-RDM under a noise model, and ${}^2\tilde{D}^c$ refers to the 2-RDM constructed from symmetry projected tomography under a noise model. Values represent averages of the Frobenius norms of difference matrices over 25 random states of H_2 in a minimal basis where the ansatz includes 3 parameters. In general, the differences between the noisy tomography methods are consistently much smaller than the difference to the ideal state, and are almost indistinguishable from stochastic effects (seen at the $n = \infty$ limit). More details regarding these results are included in Appendix 7.5.

$\Delta =$	${}^2D - {}^2\tilde{D}$	${}^2D - {}^2\tilde{D}^c$	${}^2\tilde{D} - {}^2\tilde{D}^c$
Noise Strength, $(\frac{1}{2})^n$	$\|\|\Delta\|\|_F$	$\|\|\Delta\|\|_F$	$\|\|\Delta\|\|_F$
$n = 0$	0.68(6)	0.69(5)	0.05(1)
$n = 1$	0.39(4)	0.39(4)	0.049(9)
$n = 2$	0.22(2)	0.23(3)	0.05(1)
$n = 3$	0.17(1)	0.17(2)	0.046(9)
$n = 4$	0.13(1)	0.14(1)	0.05(1)
$n = \infty$	0.027(5)	0.036(8)	0.05(1)
Experimental	0.87(5)	0.87(4)	0.05(1)

that is a mixture of different symmetry states, in which case our reduced tomography no longer represents the true tomography. Yet, whether or not standard tomography would offer significant advantages in this case is unclear, as significant errors still corrupt the system in a variety of ways.

To investigate the effects of noise, we simulated a minimal two-fermion in four-spin orbital system on a quantum device and with an accompanying noise model. The results are seen in Table 7.3. Importantly, the distance between the RDMs produced by the tomography methods is comparable to statistical noise, and is always less than then the distance from the true 2-RDM, when noise is present. In the case of the noise-free result, the larger variance between the two tomography methods is likely a result of propagation of sampling error, which is absent with the ideal 2-RDM.

7.4 Conclusion

Modern quantum computing has advanced drastically in the past decade, with a surge of incremental improvements in experimental and algorithmic improvements. Circuit optimization, qubit reduction, reducing the required parameter space in the classical optimization, or lowering tomography and measurement costs all have attempted to capitalize on the available quantum resources maximally. Work in utilizing system symmetries explores a fascinating aspect of quantum mechanics, and we hope that future work will continue to apply these ideas in lowering costs.

Our approach in utilizing symmetry projected operators provides a simple way to reduce the number of measurements needed, and when combined with other techniques can lead to large reductions in the effective scaling of the system. The routine can be performed in one step before the calculation, and adds no additional cost to the quantum or classical algorithm.

7.5 Appendix

Appendix A: Derivation of Local Symmetry Operators

In Section II we noted we would like to use a symmetry which exists on the local subspace of the system instead of the entire system for our method. While in general this will not hold for every symmetry, we discuss ways to identify and utilize these symmetries here.

If we consider a state as being in an eigenstate s of a symmetry $\hat{S}$, as seen in Eq. (5) the projection of the state of s onto an operator A is:

$$\langle P_s \hat{A} P_s \rangle = \sum_{i,j} c_{i,s} c^*_{j,s} a^{i,s}_{j,s}. \tag{7.12}$$

Let the state exist in the Fock space of M orbitals, $\mathcal{F}(M)$. Assume that we have symmetry

operators $\hat{T}_1$ and $\hat{T}_2$ which act on subspaces $F_1 = \mathcal{F}(N)$ and $F_2 = \mathcal{F}(M-N)$ respectively, and that we can express an eigenstate of $\hat{S}$ as:

$$|i,s\rangle = \sum_{\alpha,\beta} \sum_{t} R^{i\,\alpha\beta}_{st\;\;t'} |\alpha,t\rangle \otimes |\beta,t'\rangle \tag{7.13}$$

where t is an eigenstate of $\hat{T}_1$, t' is an eigenstate on $\hat{T}_2$ such that the direct product of vectors will be eigenvectors of the symmetry value s, and R is a rank-three tensor providing an index between the total space and the two smaller subspaces. We can also imagine a reduced representation, where we omit some of the exact state information, considering only blocks in different symmetries (as the orthogonality of the states is not used here):

$$|s\rangle = \sum_{t} R^{s}_{t,t'.} |t\rangle \otimes |t'\rangle \tag{7.14}$$

. Now, let $\hat{A}$ be an operator which acts primarily on F_1 and only adds a phase onto elements of F_2, which in denoted as:

$$\hat{A} = \sum_{a,b,c} A_{a,b,c} |a\rangle\langle b| \otimes |c\rangle\langle c| \tag{7.15}$$

where A is also a rank-three tensor, indicating the phase for a given state in F_2. For non-fermionic operators this would is unity across all states, whereas for fermionic operators there will be some phase changes depending on the states γ. Using this to evaluate the

expectation of $\hat{A}$ we find:

$$\begin{aligned}
\text{Tr } \hat{A}\rho =& \text{Tr} \sum_{i,j} \sum_{\alpha,\beta,\gamma,\delta,\epsilon,\zeta,\eta} \sum_{a,b,c,d,e} c_{i,s} c^*_{j,s} A^{\alpha,\beta,\gamma}_{a,b,c} R^{i,\delta,\epsilon}_{s,d,d'} R^{*j,\zeta,\eta}_{s,e,e'} |\alpha, a\rangle\langle\beta, b|\delta, d\rangle\langle\zeta, e| \qquad (7.16)\\
& \otimes |\gamma, c\rangle\langle\gamma, c|\epsilon, d'\rangle\langle\eta, e'|\\
=& \text{Tr}_1 \sum_{i,j} \sum_{\alpha,\beta,\gamma,\delta,\zeta} \sum_{a,b,c} c_{i,s} c^*_{j,s} A^{\alpha\,\beta\,\gamma}_{a\,b\,c} R^{i\,\delta\,\gamma}_{s\,c'\,c} R^{*j\,\zeta\,\gamma}_{s\,c'\,c} |\alpha, a\rangle\langle\beta, b|\delta, c'\rangle\langle\zeta, c'| \qquad (7.17)\\
=& \sum_k \text{Tr}_1 \sum_{i,j} \sum_{\alpha,\beta,\gamma,\delta,\zeta} c_{i,s} c^*_{j,s} A^{\alpha\,\beta\,\gamma}_{k\,k\,k'} R^{i\,\delta\,\gamma}_{s\,k\,k'} R^{*j\,\zeta\,\gamma}_{s\,k\,k'} |\alpha, k\rangle\langle\beta, k|\delta, k\rangle\langle\zeta, k|. \qquad (7.18)
\end{aligned}$$

In the last two steps we used the fact that following the partial trace over F_2 the total symmetry of the system must still give s, yielding a mixed state of pure symmetry states of $\hat{T}_1$. Through linearity we can extract a projection operator and apply it to elements of $\hat{A}$, which leads to a greatly simplified form of the operator. This is equivalent to Eq. (5) in the main text, and this projected form can be found for our set of transformed measurement operators.

The symmetries discussed in the text relating to molecular systems, $\hat{N}$, $\hat{S}_z$, and $\hat{S}^2$, all can be described in this way, and thus can be applied using this method. Symmetries which are elements of the Pauli group (i.e. tensored products of Pauli matrices) also satisfy these conditions.

Appendix B: Examples of Symmetry Projection

To illustrate our method, let $|\psi\rangle$ be a two-electron system in four $\alpha-$spin orbitals and $\hat{M}$ be defined as:

$$\hat{M} = c_1 a_1^\dagger a_2 + c_2 a_2^\dagger a_1. \qquad (7.19)$$

$\hat{M}$ here is a linear combination of 1-RDM operators. The system as a whole will obey the number symmetry $\hat{N} = \sum_{i=1}^{4} a_i^\dagger a_i$, but we can apply a reduced symmetry $\hat{N}_1 = \sum_{i=1}^{2} a_i^\dagger a_i$ to our operator. The reduced symmetry operator will have projections operators onto the $N = 0$, $N = 1$, and $N = 2$ subspaces, which can be written as:

$$P_0 = |00\rangle\langle 00|,\ P_1 = |01\rangle\langle 01| + |10\rangle\langle 10|,\ P_2 = |11\rangle\langle 11|. \tag{7.20}$$

Using the Jordan-Wigner transformation we can express $\hat{M}$ in terms of Pauli matrices yielding:

$$\hat{M} = \frac{1}{4}(c_1 + c_2)(X_1X_2 + Y_1Y_2) + \frac{i}{4}(c_1 - c_2)(X_1Y_2 - Y_1X_2) = \begin{pmatrix} 0 & 0 & 0 & 0 \\ 0 & 0 & c_2 & 0 \\ 0 & c_1 & 0 & 0 \\ 0 & 0 & 0 & 0 \end{pmatrix}. \tag{7.21}$$

One of the operators in the Pauli basis, A_{XX}, can be projected as follows:

$$\hat{A}^c_{XX} = \sum_i P_i(X_1X_2)P_i = \begin{pmatrix} 0 & 0 & 0 & 0 \\ 0 & 0 & 1 & 0 \\ 0 & 1 & 0 & 0 \\ 0 & 0 & 0 & 0 \end{pmatrix}. \tag{7.22}$$

To express this as a vector in the computational basis in the operator space, let $e_{i,j}$ denote a basis element where i, j denote the row and column index, which gives:

$$\vec{A}_{XX} = e_{10,01} + e_{01,10}. \tag{7.23}$$

Similar vector forms can be found for the other Pauli matrices:

$$\vec{A}^c_{XY} = -ie_{10,01} + ie_{01,10} \tag{7.24}$$

$$\vec{A}^c_{YX} = ie_{10,01} - ie_{01,10} \tag{7.25}$$

$$\vec{A}^c_{YY} = e_{10,01} + e_{01,10}. \tag{7.26}$$

Clearly, we are limited by the dimension of the span of these vectors, leaving us to choose two vectors. Using $\vec{A}^c_{XX}$ and $\vec{A}^c_{XY}$ as the column vectors of U, and $\vec{m}$ as the target vector, we can find the solution to the system of linear equations $U\vec{x} = \vec{m}$:

$$\begin{pmatrix} 1 & -i \\ 1 & i \end{pmatrix} \begin{pmatrix} x_1 \\ x_2 \end{pmatrix} = \begin{pmatrix} c_1 \\ c_2 \end{pmatrix} \rightarrow \vec{x} = \frac{1}{2} \begin{pmatrix} c_1 + c_2 \\ ic_1 - ic_2 \end{pmatrix}. \tag{7.27}$$

Thus a measurement of the form:

$$\hat{X} = \frac{c_1 + c_2}{2} X_1 X_2 + \frac{i(c_1 - c_2)}{2} X_1 Y_2 \tag{7.28}$$

yields equivalent information as the traditional measurement due to symmetries of the system.

Appendix C: Computational Details

Figure 7.1 was created by first generating the set of 2-RDM operators for a given molecular system and transforming them into a set of Pauli operators using fermionic-to-qubit transformations followed by our symmetry projection technique. To efficiently group terms, we expressed the set of operators as a graph utilizing the qubit-wise commuting relationship, and used an algorithm to attempt to find the minimimum clique cover [54]. The graphs were stored using the graph-tools (v 2.29) Python package [55]. A sequential coloring algorithm was used where we selected the vertices with the largest number of edges first, as this proved

to be a reliable approach which was scalable to larger qubit systems which did not yield significantly worse results than the related recursive method [54].

Table 7.3 was generated with the help of Qiskit (v 0.15.0) [56], and simulates a two-electron system in a minimal basis (STO-3G) under the Jordan-Wigner transformation on four qubits. We prepared 25 random states parameterized by a double excitation and two single excitations. The experimental results were obtained on the IBMQ Bogota device. The noise model was based on the backend-centered model in the Aer module of Qiskit, which approximates the noise channels mainly as a product of depolarizing and thermal relaxation channels acting locally on single- and two-qubit gates. The parameters were based on averages of the experimental devices, and were scaled down according to τ to model a decrease in the strength of the noise.

Appendix D: Further Computational Details

For the quantum computation and noise simulation in Table 7.3, we used the quantum computer IBMQ Bogota (5-qubits) provided through the IBM Quantum Experience, as well as a noise model based on the device. The quantum device has fixed-frequency transmon qubits with co-planer waveguide resonators [57, 58]. The Python package Qiskit (v 0.15.0) [56] was used to interface with the device. Device properties can be found in Table 7.4.

The circuit used is based on the Jordan-Wigner transformation and uses exponentials of anti-Hermitian operators. Because of the size of the system and the indistinguishablity of the action of the different Pauli operators on the state, we can use a single term to describe each of the relevant excitations [35, 43]. The target circuit can be written as:

$$U = \left[\exp\theta_1(a^\dagger_{\alpha 0}a_{\alpha 1}a^\dagger_{\beta 0}a_{\beta 1} - a^\dagger_{\beta 1}a_{\beta 0}a^\dagger_{\alpha 1}a_{\alpha 0})\right]\left[\exp\theta_2(a^\dagger_{\alpha 0}a_{\alpha 1} - a^\dagger_{\alpha 1}a_{\alpha 0})\right]\left[\exp(\theta_3 a^\dagger_{\alpha 0}a_{\alpha 1} - a^\dagger_{\alpha 1}a_{\alpha 0})\right] \tag{7.29}$$

Table 7.4: Calibration data for the ibm-bogota device taken on November 2$^{\text{nd}}$, 2020, from benchmarking. U_2 and U_3 represent single qubit gate errors containing one and two $X_{\pi/2}$ pulses and two and three frame changes respectively. $RO_{i|j}$ represents the probability of measuring the state i given a prepared state j. T_1 and T_2 are the given thermal relaxation times for each qubit. Frequency refers to the qubits opeartional frequency, and influences the excited state population based on the device temperature. $[j]$ specifies the target qubit with control qubit i, and the number in paranthesis after each entry in the CNOT column indicates the gate length. The gate lengths for the U_2 and U_3 gates were 35 ns and 71 ns respectively.

Qubit	**Frequency**	$\mathbf{U}_2$	$\mathbf{U}_3$	$\mathbf{RO}_{0\|1}$	$\mathbf{RO}_{1\|0}$	$\mathbf{T}_1$	$\mathbf{T}_2$	$[j]$ $\mathbf{CNOT}_i^j$	
i	GHz	(10^{-4})	(10^{-4})	(10^{-2})	(10^{-2})	(μs)	(μs)	(10^{-2})	
0	5.000	3.7	4.5	3.6	8.0	93.6	133.3	[1] 2.0 (690)	
1	4.845	3.2	6.5	17.3	15.1	59.9	58.5	[0] 2.0 (654)	[2] 1.0 (498)
2	4.783	1.7	3.3	5.7	3.6	77.7	120.6	[1] 1.0 (533)	[3] 1.0 (626)
3	4.858	2.4	4.8	3.0	0.9	131.1	187.1	[2] 1.0 (590)	[4] 4.8 (370)
4	4.978	13.8	27.5	5.2	2.6	101.7		[3] 4.8 (334)	

which can be simulated with limited Pauli terms as:

$$U' = [\exp i\theta_1 Y_1 X_2 X_3 X_4][\exp i\theta_2 Y_1 X_2][\exp i\theta_3 Y_3 X_4], \tag{7.30}$$

and then simplified according to normal procedures. Our resulting circuit had 8 CNOT gates and 9 single qubit gates prior to measurement. We performed tomography of both the real and imaginary elements of the 2-RDM despite having only a real wavefunction. The list of measurement circuits generated for the normal circuit (following the grouping procedure) is:

$$\begin{aligned} N = \{\ & Y_1X_2Z_3Z_4, X_1X_2Z_3Z_4, Y_1Y_2Z_3Z_4, X_1Y_2Z_3Z_4, Z_1Z_2Y_3X_4, \\ & Z_1Z_2X_3X_4, Z_1Z_2Y_3Y_4, Z_1Z_2X_3Y_4, Y_1X_2Y_3X_4, X_1X_2Y_3X_4, \\ & Y_1Y_2Y_3X_4, X_1Y_2Y_3X_4, Y_1X_2X_3X_4, X_1X_2X_3X_4, Y_1Y_2X_3X_4, \\ & X_1Y_2X_3X_4, Y_1X_2Y_3Y_4, X_1X_2Y_3Y_4, Y_1Y_2Y_3Y_4, X_1Y_2Y_3Y_4, \\ & Y_1X_2X_3Y_4, X_1X_2X_3Y_4, Y_1Y_2X_3Y_4, X_1Y_2X_3Y_4, Z_1Z_2Z_3Z_4\}, \end{aligned}$$

whereas the set of reduced circuits (with the same grouping procedure) is given by:

$$R = \{\ X_1X_2Z_3Z_4, Y_1X_2Z_3Z_4, Z_1Z_2X_3X_4, Z_1Z_2Y_3X_4, X_1X_2X_3X_4,$$
$$X_1X_2Y_3X_4, Y_1X_2X_3X_4, Y_1X_2Y_3X_4, Z_1Z_2Z_3Z_4\}.$$

Appendix E: Noise Model

The noise model used in generating the results in Table 7.3 is adapted from the provided noise model in Qiskit [56], and consists of a depolarizing channel followed by a thermal relaxation channel on each gate, with a readout error applied at measurement. Information on the model is adapted from the documentation provided in Qiskit [56]. Wood et al. is also referenced in the documentation and contains useful information regarding error channel representations and transformations [59]. A useful online discussion of the benefits (applicability to short T_1 processes such as on single qubit gates) and limitations (non-T_1 dominated behavior of CNOT gates, does not treat cross-talk errors, etc.) of the noise model is included in the references [60].

In our adaptation of the model, we averaged over all qubits for many of the parameters to reduce inconsistencies across the simulated device, and then scaled these parameters to simulate a consistently decreasing noise. We found that using either our model, the given model, or a model based solely on depolarizing noise did not result in signficant differences in the Frobenius norms of the difference matrices between the obtained 2-RDMs.

Thermal Relaxation Channel

The T_1 time describes the thermal relaxation of the qubit from the excited state to the ground state and the T_2 time describes the coherence time of the qubit. Their respective relaxation rates for a given gate length T_g are given as $r_{T_1} = \exp\frac{-T_g}{T_1}$ and $r_{T_2} = \exp\frac{-T_g}{T_2}$. For $T_2 < T_1$, T_1 relaxation becomes the main consideration and the channel is expressed

as a mixture of reset operations (proejctive measurements to $|0\rangle$ or $|1\rangle$) and unitary errors. Consider a ground state population n_0 and an excited state population:

$$n_1 = (1 + \exp \frac{2hf}{k_B T})^{-1} \tag{7.31}$$

where h is Planck's constant, k_B is the Boltzmann constant, T and f are the qubit temperature and frequency, and $n_0 + n_1 = 1$. The probability of a reset error occuring is defined as:

$$p_{reset} = 1 - r_{T_1}. \tag{7.32}$$

Using the populations we can obtain the probability to reset to the $|0\rangle$ state p_{r0}, the probability to reset to the $|1\rangle$ state p_{r1}, and the probability to apply a Z gate p_z as:

$$p_{r0} = n_0 p_{reset}, \quad p_{r1} = n_1 p_{reset}, \quad p_z = \frac{1}{2}(1 - p_{reset})(1 - \frac{r_{T_2}}{r_{T_1}}). \tag{7.33}$$

For the case where $T_2 > T_1$, the Choi-matrix representation is used. For a nosie channel $\mathcal{E}$, the Choi-matrix in the column representation $\mathcal{C}$ is defined by:

$$\mathcal{C} = \sum_{i,j} |i\rangle\langle j| \otimes \mathcal{E}(|i\rangle\langle j|), \tag{7.34}$$

and the resulting action on the state can be determined as

$$\mathcal{E}(\rho) = \mathrm{Tr}_1 \mathcal{C}(\rho^T \otimes \mathbb{I}) \tag{7.35}$$

where we trace over the first system. The Choi matrix used in the model is:

$$\mathcal{C} = \begin{pmatrix} 1 - n_1 p_{reset} & 0 & 0 & r_{T_2} \\ 0 & p_e p_{reset} & 0 & 0 \\ 0 & 0 & n_0 p_{reset} & 0 \\ r_{T_2} & 0 & 0 & 1 - n_0 p_{reset} \end{pmatrix}. \tag{7.36}$$

The Choi matrix is then converted to Kraus operators and then to Pauli gates to be implemented in the simulation.

Depolarizing Channel

The depolarizing channel acting on n qubits is given as [61]:

$$\mathcal{E}_{depol} = (1 - \lambda)I + \lambda D. \tag{7.37}$$

where I is the identity channel, D is the completely depolarizing channel, and $0 \leq \lambda \leq \frac{4^n}{4^n - 1}$ (for n qubits) indicates the relative strength.

If we consider the total fidelity as a function of the thermal relaxation and depolarizing channels, we have that:

$$F = F(\mathcal{E}_{depol} \circ \mathcal{E}_{relax}) \tag{7.38}$$

$$= (1 - \lambda)F(\mathcal{E}_{relax}) + \lambda F(D \circ \mathcal{E}_{relax}) \tag{7.39}$$

$$= (1 - \lambda)F(\mathcal{E}_{relax}) + \lambda F(D) \tag{7.40}$$

$$= F(\mathcal{E}_{relax}) - \lambda \frac{F(\mathcal{E}_{relax})d - 1}{d} \tag{7.41}$$

where d is the dimension of the system and the average fidelity of the depolarizing channel

is $1/d$. From this we can solve for λ:

$$\lambda = d\frac{F(\mathcal{E}_{relax}) - F}{F(\mathcal{E}_{relax})d - 1}. \tag{7.42}$$

The gate fidelity of these channels is given by:

$$F_{avg}(\mathcal{E}, U) = \int d\psi \langle\psi|U^\dagger \mathcal{E}(|\psi\rangle\langle\psi|)U|\psi\rangle \tag{7.43}$$

$$= \frac{F_{\text{pro}}(\mathcal{E}, U)d + 1}{d + 1} \tag{7.44}$$

$$= \frac{\text{Tr}(S_U^\dagger S_\mathcal{E}^\dagger) + d}{d(d + 1)} \tag{7.45}$$

where F_{pro} indicates the process fidelity and S represents the superator representation of a quantum channel. With all of these components, the model applies the depolarizing channel onto the one- or two-qubit gate followed by the thermal relaxation channel applied to each individual qubit.

Readout Error

Finally, the readout errors on the devices are treated as single qubit errors. These modify the output based on the probability of reading one output given another. For instance, measuring the state for the qubit q $|0\rangle$ will give $|1\rangle$ with a probability $p = \mathbf{RO}_{1|0}(q)$, and will give $|0\rangle$ with a probability $1 - p$.

References

[1] A. Szabo and N. S. Ostlund, *Modern Quantum Chemistry: Introduction to Advanced Electronic Structure Theory* (Dover Publications, New York, 1996).

[2] T. Helgaker, P. Jørgensen, and J. Olsen, *Molecular Electronic-Structure Theory* (John Wiley & Sons, Ltd, Chichester, UK, 2000) p. 908.

[3] A. Coleman and V. Yukalov, *Reduced Density Matrices: Coulson's Challenge* (Springer, Berlin Heidelberg New York, 2000).

[4] D. A. Mazziotti, ed., *Advances in Chemical Physics*, Advances in Chemical Physics, Vol. 134 (John Wiley & Sons, Inc., Hoboken, NJ, USA, 2007) p. 574.

[5] Z. Zhao, B. J. Braams, M. Fukuda, M. L. Overton, and J. K. Percus, J. Chem. Phys. **120**, 2095 (2004).

[6] D. A. Mazziotti, Phys. Rev. Lett. **93**, 213001 (2004).

[7] N. Shenvi and A. F. Izmaylov, Phys. Rev. Lett. **105**, 213003 (2010).

[8] D. A. Mazziotti, Phys. Rev. Lett. **106**, 083001 (2011).

[9] B. Verstichel, H. van Aggelen, W. Poelmans, and D. Van Neck, Phys. Rev. Lett. **108**, 213001 (2012).

[10] C. Schilling, D. Gross, and M. Christandl, Phys. Rev. Lett. **110**, 040404 (2013).

[11] D. A. Mazziotti, Phys. Rev. Lett. **117**, 153001 (2016).

[12] M. Piris, Phys. Rev. Lett. **119**, 063002 (2017).

[13] A. Rubio-García, J. Dukelsky, D. R. Alcoba, P. Capuzzi, O. B. Oña, E. Ríos, A. Torre, and L. Lain, J. Chem. Phys. **151**, 154104 (2019).

[14] D. A. Mazziotti, Phys. Rev. Lett. **97**, 143002 (2006).

[15] S. E. Smart and D. A. Mazziotti, http://arxiv.org/abs/2004.11416v1 .

[16] A. J. Coleman, Rev. Mod. Phys. **35**, 668 (1963).

[17] D. A. Mazziotti, Phys. Rev. Lett. **108**, 263002 (2012), arXiv:1112.5866 .

[18] J.-N. Boyn, J. Xie, J. S. Anderson, and D. A. Mazziotti, J. Phys. Chem. Lett. , 4584 (2020).

[19] R. P. R. P. Feynman, R. B. Leighton, and M. L. M. L. Sands, *The Feynman lectures on physics* (1963–1965) pp. xii + 513, three volumes.

[20] D. M. Bishop, *Group Theory and Chemistry* (Dover Publications, Mineola, N.Y., 1993).

[21] G. Gidofalvi and D. A. Mazziotti, Phys. Rev. A **72**, 052505 (2005).

[22] H. Nakatsuji, Chemical Physics Letters **67**, 329 (1979).

[23] N. C. Rubin, R. Babbush, and J. McClean, New J. Phys. **20**, 053020 (2018), arXiv:1801.03524 .

[24] X. Bonet-Monroig, R. Babbush, and T. E. O'Brien, , 1 (2019), arXiv:1908.05628 .

[25] S. E. Smart and D. A. Mazziotti, Phys. Rev. A **100**, 022517 (2019).

[26] L. M. Sager, S. E. Smart, and D. A. Mazziotti, http://arxiv.org/abs/2004.13868v1 .

[27] M. Roth, M. Ganzhorn, N. Moll, S. Filipp, G. Salis, and S. Schmidt, Physical Review A **96**, 1 (2017), arXiv:arXiv:1708.02090v1 .

[28] M. Ganzhorn, P. Egger, D. J. an d Barkoutsos, P. Ollitrault, G. Salis, N. Moll, M. Roth, A. Fuhrer, P. Mueller, S. Woerner, I. Tavernelli, and S. Filipp, Physical Review Applied **11**, 1 (2019), arXiv:1809.05057 .

[29] H. Wang, S. Ashhab, and F. Nori, Physical Review A - Atomic, Molecular, and Optical Physics **79** (2009), 10.1103/PhysRevA.79.042335, arXiv:0902.1419 .

[30] J. D. Whitfield, Journal of Chemical Physics **139** (2013), 10.1063/1.4812566.

[31] P. K. Barkoutsos, J. F. Gonthier, I. Sokolov, N. Moll, G. Salis, A. Fuhrer, M. Ganzhorn, D. J. Egger, M. Troyer, A. Mezzacapo, S. Filipp, and I. Tavernelli, Physical Review A **98**, 022322 (2018), arXiv:1805.04340 .

[32] S. A. Fischer and D. Gunlycke, (2019), arXiv:1907.01493 .

[33] G. S. Barron, B. T. Gard, O. J. Altman, N. J. Mayhall, E. Barnes, S. E. Economou, and V. Tech, , 1 (2020), arXiv:arXiv:2003.00171v1 .

[34] B. T. Gard, L. Zhu, G. S. Barron, N. J. Mayhall, S. E. Economou, and E. Barnes, npj Quantum Inf. **6** (2020), 10.1038/s41534-019-0240-1, arXiv:1904.10910 .

[35] S. E. Smart and D. A. Mazziotti, Phys. Rev. Res. **2**, 023048 (2020).

[36] J. R. McClean, J. Romero, R. Babbush, and A. Aspuru-Guzik, New Journal of Physics **18**, 023023 (2016), arXiv:1509.04279 .

[37] A. Kandala, A. Mezzacapo, K. Temme, M. Takita, M. Brink, J. M. Chow, and J. M. Gambetta, Nature **549**, 242 (2017), arXiv:1704.05018 .

[38] I. G. Ryabinkin, S. N. Genin, and A. F. Izmaylov, Journal of Chemical Theory and Computation **15**, 249 (2019), arXiv:1806.00461 .

[39] N. Moll, A. Fuhrer, P. Staar, and I. Tavernelli, J. Phys. A: Math. Theor. **49** (2016), 10.1088/1751-8113/49/29/295301, arXiv:1510.04048 .

[40] S. Bravyi, J. M. Gambetta, A. Mezzacapo, and K. Temme, , 1 (2017), arXiv:1701.08213 .

[41] K. Setia, R. Chen, J. E. Rice, A. Mezzacapo, M. Pistoia, and J. Whitfield, , 1 (2019), arXiv:1910.14644 .

[42] S. McArdle, X. Yuan, and S. Benjamin, Phys. Rev. Lett. **122**, 180501 (2019), arXiv:1807.02467 .

[43] X. Bonet-Monroig, R. Sagastizabal, M. Singh, and T. E. O'Brien, Phys. Rev. A **98**, 062339 (2018).

[44] R. Sagastizabal, X. Bonet-Monroig, M. Singh, M. A. Rol, C. C. Bultink, X. Fu, C. H. Price, V. P. Ostroukh, N. Muthusubramanian, A. Bruno, M. Beekman, N. Haider, T. E. O'Brien, and L. DiCarlo, Phys. Rev. A **100**, 010302 (2019), arXiv:1902.11258 .

[45] A. F. Izmaylov, T.-C. Yen, and I. G. Ryabinkin, Chem. Sci. **10**, 3746 (2019), arXiv:1810.11602 .

[46] A. F. Izmaylov, T.-C. Yen, R. A. Lang, and V. Verteletskyi, J. Chem. Theory Comput. **16**, 190 (2020), arXiv:1907.09040 .

[47] P. Gokhale, O. Angiuli, Y. Ding, K. Gui, T. Tomesh, M. Suchara, M. Martonosi, and F. T. Chong, (2019), arXiv:1907.13623 .

[48] P. Jordan and E. Wigner, Z. Angew. Phys. **47**, 631 (1928).

[49] A. Tranter, S. Sofia, J. Seeley, M. Kaicher, J. McClean, R. Babbush, P. V. Coveney, F. Mintert, F. Wilhelm, and P. J. Love, Int. J. Quantum Chem. **115**, 1431 (2015).

[50] A. Tranter, P. J. Love, F. Mintert, and P. V. Coveney, J. Chem. Theory Comput. **14**, 5617 (2018), arXiv:1812.02233 .

[51] S. B. Bravyi and A. Y. Kitaev, Ann. Phys. **298**, 210 (2002), arXiv:0003137 [quant-ph] .

[52] J. R. McClean, M. E. Schwartz, J. Carter, and W. A. de Jong, Phys. Rev. A **95**, 042308 (2016), arXiv:1603.05681 .

[53] P. Gokhale and F. T. Chong, (2019), arXiv:1908.11857 .

[54] V. Verteletskyi, T.-C. Yen, and A. F. Izmaylov, , 1 (2019), arXiv:1907.03358 .

[55] T. P. Peixoto, figshare (2014), 10.6084/m9.figshare.1164194.

[56] H. Abraham, AduOffei, R. Agarwal, I. Y. Akhalwaya, G. Aleksandrowicz, T. Alexander, M. Amy, E. Arbel, Arijit02, A. Asfaw, A. Avkhadiev, C. Azaustre, AzizNgoueya, A. Banerjee, A. Bansal, P. Barkoutsos, G. Barron, G. S. Barron, L. Bello, and Y. B.-H. et al., "Qiskit: An open-source framework for quantum computing," (2019).

[57] J. Koch, T. M. Yu, J. Gambetta, A. A. Houck, D. I. Schuster, J. Majer, A. Blais, M. H. Devoret, S. M. Girvin, and R. J. Schoelkopf, Phys. Rev. A **76**, 042319 (2007).

[58] J. M. Chow, A. D. Córcoles, J. M. Gambetta, C. Rigetti, B. R. Johnson, J. A. Smolin, J. R. Rozen, G. A. Keefe, M. B. Rothwell, M. B. Ketchen, and M. Steffen, Phys. Rev. Lett. **107**, 080502 (2011).

[59] C. J. Wood, J. D. Biamonte, and D. G. Cory, Quantum Information and Computation **15**, 759 (2015), arXiv:1111.6950 .

[60] Cjwood, "How good is basic_device_noise_model() simulating the noise in the quantum computer?" (2019), https://quantumcomputing.stackexchange.com/questions/8958/how-good-is-basic-device-noise-model-simulating-the-noise-in-the-quantum-compu, accessed November 4th, 2020.

[61] M. A. Nielsen and I. L. Chuang, *Cambridge University Press* (Cambridge University Press, Cambridge, 2010).

CHAPTER 8

RELAXATION OF STATIONARY STATES ON A QUANTUM COMPUTER FOR UNIQUE CHARACTERIZATION OF NOISE ON A QUANTUM COMPUTER

Material from: Smart, S. E., Hu, Z., Kais, S., & Mazziotti, D. A., Relaxation of stationary states on a quantum computer yields a unique spectroscopic fingerprint of the computer's noise., Communications Physics, published 2022, 5(28).

8.1 Introduction

Quantum computing, as conceived by Feynman [1], has the potential to revolutionize computing for certain classes of problems with exponential scaling in the physical and social sciences and engineering [2–10]. Central to the quantum computing paradigm is the quantum process of entanglement by which a pure-state quantum system develops a probability distribution over multiple classical outcomes. Entanglement allows us to process and store exponentially more information than a classical computer. This potential capability and its advantages, however, come with a significant sensitivity to noise [6, 11–13] that introduces errors that degrade performance, especially on current-to-near-term quantum computers. Significant advances have been made in the past decade in error correction and mitigation [14–19], but further advances are needed to not only understand noise but also control noise for its mitigation or exploitation.

In quantum mechanics, a closed system which is in a stationary state will remain in that state for all time. If, however, the closed quantum system is opened to an environment, also referred to as a bath, then the system becomes an open quantum system, and a stationary state of that system will potentially become time-dependent and non-stationary [11]. The precise time dependence of the open quantum system depends upon the nature of the bath.

If the relaxation of the bath is fast relative to the dynamics of the system, then the quantum dynamics is purely dissipative and described as Markovian, but if the dynamics of the bath and system are on the same timescale, then the dynamics causes energy to be exchanged both to and from the bath and is described as non-Markovian [11, 13, 20]. In non-Markovian dynamics the more complex interaction between the system and bath causes the system to develop a memory of its state as a function of time.

We can broadly characterize noise or the effects of noise through spectroscopic or tomographic techniques. In the context of quantum computing, characterization of the bath, which is commonly assumed to be Markovian, gives a basic assessment of the qubit and gate performance. While quantum process tomographic techniques can be used[21–24], they are costly and potentially unreliable for realistic measurement, and other alternatives such as randomized benchmarking or quantum gate set tomography have emerged as more robust tools[25–27]. Non-Markovian behavior is present in a variety of systems, but is generally more challenging to characterize[28, 29]. Efficient characterization of an underlying interaction is also possible for one or two-qubit systems[30, 31]. In the frame of a simulated quantum system however, we are not usually concerned with the characterization of the device, but more so the bath in relation to the simulated system. The effects of this bath can also be utilized in the simulation of other noisy quantum systems or potentially in algorithmic approaches for improving quantum simulations[32, 33].

In this paper, we simulate stationary states on a quantum computer to obtain a unique spectroscopic fingerprint of the computer's noise. If a quantum system in a stationary state is simulated on an ideal quantum computer, the quantum system will remain in that stationary state for all time. However, if the same system is simulated on a noisy intermediate-scale quantum (NISC) computer, the noise causes the simulated state to become non-stationary. The resulting time dependence in the frame of the simulation provides us with a frequency profile of the noise as it is experienced by the simulated stationary quantum state. Com-

putations are performed on multiple superconducting-qubit IBM quantum computers. We find that each quantum computer has a unique spectroscopic signature for a given simulation of stationary states. The noise generates an effective bath that exhibits both colored noise and non-Markovian behavior [11, 13, 20]. Characterization of the bath provides an application-oriented assessment of the fidelity of the quantum device. Our results provide a direction for noise mitigation but also suggest how to use noise for quantum simulations of open systems [8, 34–41].

8.2 Results

8.2.1 Stationary-State Evolution with Noise

Time evolution of a stationary state prepared on a noisy quantum computer can be described by the equation of motion of the density matrix according to the Nakajima−Zwanzig integro-differential equation D [11, 13, 42]

$$\frac{dD}{dt} = -\frac{i}{\hbar}[\hat{H}, D] + \int_0^t \mathcal{K}(t,\tau)D(t,\tau)d\tau, \tag{8.1}$$

where $\hat{H}$ is the Hamiltonian operator of the stationary state and $\mathcal{K}(t,\tau)$ is the memory kernel representing the quantum computer's noise. The memory kernel as represented here also includes the contribution of memoryless (i.e. Markovian) noise effects, which can be represented by a Dirac delta function at t in the kernel. In the limit that the noise on the quantum computer vanishes, the memory kernel vanishes and the equation simplifies to the quantum Liouville (von Neumann) equation. If the initial state is a stationary state of $\hat{H}$, all of the non-trivial time dependence results from the noise. Normal noise spectroscopy or characterization of a system could be performed by using a number of techniques, such as with Rabi spectroscopy, swap spectroscopy, or with a tunable system [43–51]. Here, to probe the frequency dependence of the noise, we consider the family of scaled Hamiltonians

$\hat{H} = \hbar\omega\hat{O}$ where $\hat{O}$ is a dimensionless operator. By changing ω, we can control the energy difference between the ground and first excited state of the Hamiltonian. The time-dependent response of the system to different values of ω provides us with spectral information about the noise on the quantum computer. From one perspective we are attempting to simulate the solution of the quantum Liouville equation on the quantum computer—dynamics with the memory kernel set to zero. Consequently, all deviations from the closed-system evolution are originating from the noise of the given quantum computer which creates without our direction an effective memory kernel for the time evolution (including memoryless effects).

8.2.2 Single-qubit Hamiltonians

We begin with a single qubit system with the Hamiltonian matrix $H(\omega) = \omega\sigma_z$ where we use atomic units with $\hbar = 1$, and σ_z is the Pauli-Z matrix. We prepare the system in the excited state $|\psi\rangle = |1\rangle$ and evolve the system according to $\exp[-iH\tau] = R_z(-\omega\tau)$, using repeated single qubit gates with the results shown in Fig. 8.1. The time step is arbitrary to the extent that it can be rescaled with the strength of V and ω, and hence, we set $\tau = \frac{1}{3}$, which serves to highlight system-bath interactions when the frequency $\omega \in [0, 1]$. If we allowed the system to relax without applying any gates, this would essentially be a T_1 experiment (where we could use the physical gate times), measuring the relaxation time for an excited state. However, the noise sources here, represented by the non-vanishing memory kernel, generate non-Markovian behavior. In Fig. 8.1 the non-Markovian behavior can be seen from the oscillations in the population of the ground state, which reveal a memory dependence beyond the pure decay of Markovian dynamics. Furthermore, the oscillations are more pronounced at lower frequencies, indicating a bath with colored noise. Note that for these time-independent simulations there is a equivalence between the forward and reverse time evolutions—evolutions of $\hat{H}_0$ and $-\hat{H}_0$, which leads to symmetrical patterns emerging.

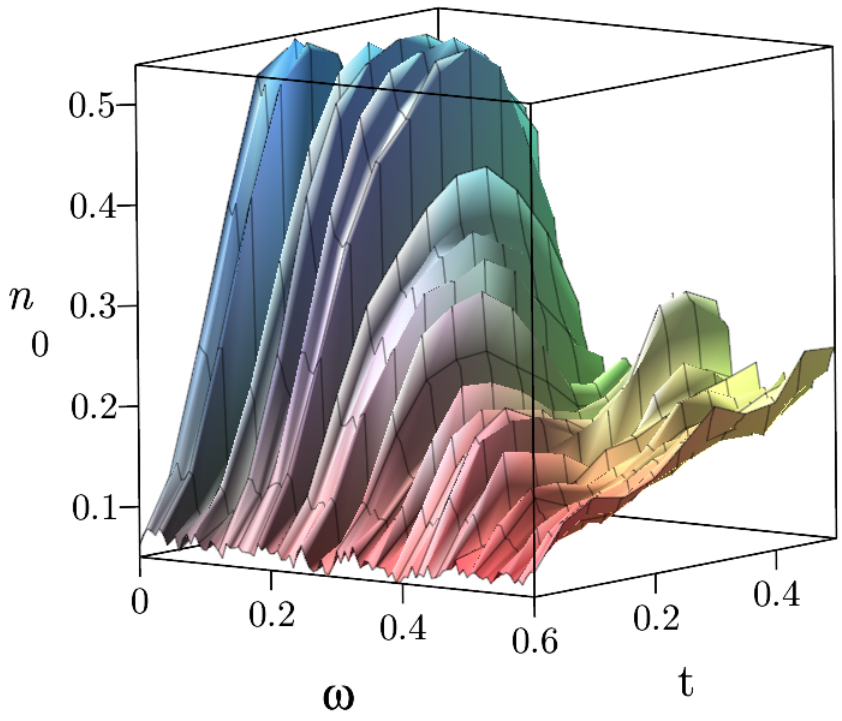

Figure 8.1: Frequency scan of simulated time evolution for a single qubit. Scan of population of the $|0\rangle$ state (n_0) as a function of simulated time t and frequency ω on the ibmq_armonk device. We initially prepare the state in the 1 state and then apply 100 total gate sequences of $\exp[-i\tau H]$, where the time step is $\tau = \frac{1}{3}$, the system Hamiltonian is $H = \omega\sigma_z$, and $\omega \in (0, 0.6)$. The time t is equal to the number of gates times τ multiplied by the scaling factor 0.015. The oscillatory behavior reveals non-Markovian effects with the oscillations becoming less pronounced at higher frequencies.

The spectral density with respect to a quantum noise source A can be characterized as:

$$\begin{aligned} S_A(\omega) &= \int_{-\infty}^{\infty} d\tau \exp[i\omega\tau] \sum_{\alpha\beta} \rho_{\alpha\alpha} \langle\alpha|A(\tau)|\beta\rangle\langle\beta|A(0)|\alpha\rangle \\ &= 2\pi \sum_{\alpha,\beta} \rho_{\alpha\alpha} |V_{\alpha\beta}|^2 \delta(\epsilon_\beta - \epsilon_\alpha - \omega), \end{aligned} \tag{8.2}$$

where α and β are energy eigenstates of H and ρ represents elements of the density matrix. The spectral density can be related to the rate of population change through first-order perturbation theory with the well-known Fermi's golden rule [12, 49, 52]. Figure 8.2 is constructed from Fig. 8.1, showing the rate of change in the initial part of the time evolution as a function of frequency, which provides a rough spectrum of the noise on the quantum computer from the perspective of the simulated system. Note that for frequencies above 0.6 (relative to a value of $\tau = 1/3$), the noise profile shows low intensity signals, likely from thermal noise. The appropriate resolution is difficult to determine, and the wells are not stochastic, as a purely stochastic phenomena would not be continuous along the time series since each time series is sampled independently.

The significant portion of the noise can be ascribed to a transverse noise source (σ_x, σ_y) which allows for transitions between the ground and excited states. The quantum devices we studied utilize a sequence of elementary gates denoted as U_1, U_2, and U_3 gates. In particular, these gates consist of alternating frame changes (R_z gates) and rotations (X90 rotation, R_x gates), where U_k contains k frame changes and $k-1$ transverse rotations (in the current iteration of IBM systems, these gates are represented with a series of intertwined R_z and $\sqrt{X}$ gates, which can also be used in a similar manner to represent generic single-qubit unitaries). If only the U_1 gate is used to model $\exp[-i\omega\sigma_z\tau]$, then a pulse is not applied, and the gate applications correspond to a standard T_1 experiment, measuring the relaxation of the excited state. However, here we specifically use U_3 gates, which are generic single qubit rotations, and which alternate between transverse and longitudinal rotations. In fact, one

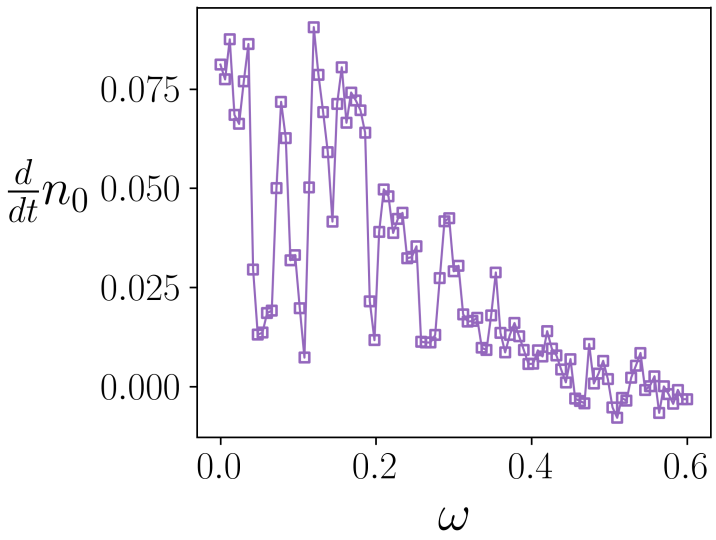

Figure 8.2: Rate of population change with respect to simulated time for a single qubit. Approximate rate of ground-state populations changes $\frac{d}{dt}n_0$ as a function of frequency ω evaluated after the first time step, which is proportional to the spectral density. The data is taken from the scan in Fig. 8.1 from ibmq_armonk.

way to model the observed behavior in the qubit system is to apply a constant $\exp[i\theta\sigma_x]$, where θ is taken to be a small angle, following every gate application. However, this does not account for the troughs seen within the range from 0.03 to 0.3 radians, which are not stochastic effects. Whether or not the noise channels are a result of an improper calibration of the $X90$ gate resulting in a systematic over rotation, or are part of a completely different noise source, becomes irrelevant for the noisy system in that the quantum system could be equivalently described from either perspective [45, 53]. For a user or algorithm that does not control the qubit and gate level of the simulation, we posit that the effects of the two are the same, and the quantum system could be viewed as experiencing the same.

In addition to using different devices, we also can highlight system-specific responses on a single device by choosing different qubits to simulate our system. We demonstrate this in Figure 8.3. For some systems, such as (B2) or (b2), it appears that only one or two frequencies in the simulated evolution show a frequency dependent response. However, for others, like

(a0), (B0), or (c0), we see strong non-Markovian behavior at lower frequencies. The higher frequencies in each case appear to exhibit simple exponential decay, and so can be taken as an indicator of the simulated relaxation time. Despite this, it is difficult to compare the expected performance of the device (predicted through error rates and decoherence times) to the simulated relaxation. For low error single qubit sequences we might expect the T_1 time to potentially mirror the simulated relaxation rate (see Section 8.4 for a comparison). The simulated relaxation rates, however, also have contributions from the gates and their errors, which obfuscates the comparison. Also, the evolution by gate applications introduces energy into the system, which causes the system to relax into a mixed ensemble state rather than the computational ground state.

We can also observe how the quantum state vector moves in the Bloch sphere. For frequencies in the high region of the spectral density and not allowing for coupling between the bath and system, a slow precession around the axis corresponding to H is observed. However, for frequencies which couple to the bath, the system can be strongly pulled around the Bloch sphere resulting in various trajectories through the state space. We model some of the trajectories in Fig. 8.4, and instances with other starting trajectories are included in Section 8.4.

8.2.3 Two-qubit Hamiltonians

By identifying frequencies of interest on the qubits themselves, we can construct systems which respond uniquely to the bath, allowing for selective transitions between different eigenstates of the system. With this in mind we first simulated a two-qubit system with a local Hamiltonian defined by:

$$H(\omega_1, \omega_2) = \omega_1 \sigma_z^1 + \omega_2 \sigma_z^2. \tag{8.3}$$

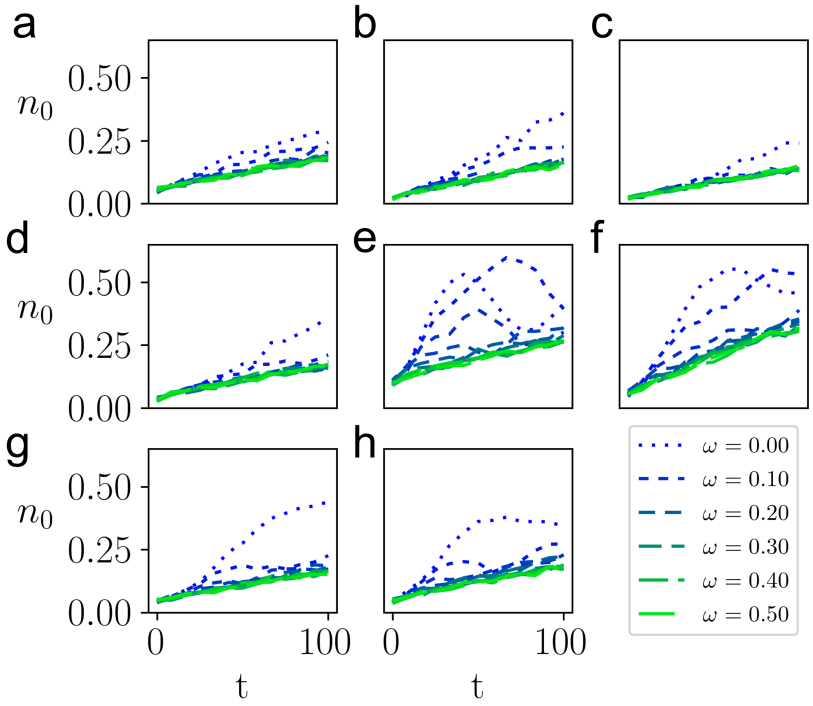

Figure 8.3: Demonstration of simulated time evolution for different devices and qubits. Different device and qubit (indicated by the i^{th} qubit Qi)) simulations over simulated time t for frequencies ω with a system Hamiltonian $H = \omega\sigma_z$, with a time step $\tau = \frac{1}{3}$. **a** Q0, ibmq_armonk. **b** Q2, ibmq_belem. **c**−**e** Q0, Q2, Q4, ibmq_bogota. **f**−**h** Q0, Q2, Q4, ibmq_casablanca. Legend shows frequencies ranging from $\omega \approx 0$ (blue, shortest dashes) to $\omega = 0.5$ (green, longest dashes).

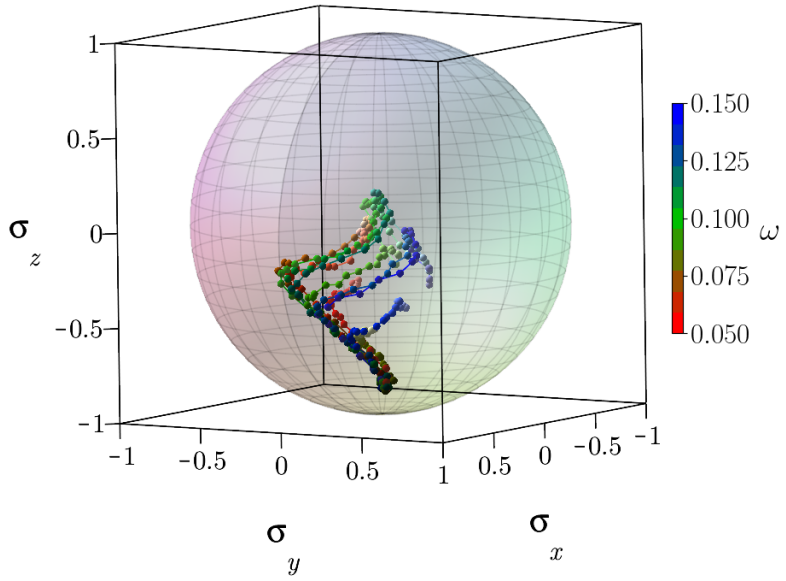

Figure 8.4: Single qubit state trajectories with respect to simulated time for a range of transition frequencies. Scan of several trajectories represented in the Bloch sphere for a single qubit device for a range of transition frequencies $\omega \in [0.05, 0.15]$ in increments of 0.01, from ibmq_armonk. σ_i represents the expectation with respect to that Pauli operator as a function of time. Each simulation has an equal number of gate applications and changes only the frequency ω in the propagation with time step τ, $\exp[-i\tau H] = \exp[-i\frac{\omega\sigma_z}{3}]$. ω decreases from red ($\omega = 0.05$) to green ($\omega = 0.10$) to blue ($\omega = 0.15$).

		$\frac{d}{dt}n_i$ ($\times 10^{-3}$)			
ω_1	ω_2	n_{00}	n_{01}	n_{10}	n_{11}
$\frac{1}{20}$	$\frac{1}{20}$	-16.4	12.4	2.5	1.5
$\frac{1}{20}$	$\frac{1}{2}$	-4.7	0.5	4.1	0.2
$\frac{1}{2}$	$\frac{1}{20}$	-13.7	13.5	0.0	0.2
$\frac{1}{2}$	$\frac{1}{2}$	-1.1	0.7	0.4	0.0

Table 8.1: Rate of population change for different frequencies for the local two-qubit Hamiltonian. Rate of population change for eigenstates n_{ij}, where ij are indices (corresponding to the computational basis), immediately after initialization for the two qubit system depicted in Fig. 8.5, where $H = \sigma_z^1\omega_1 + \sigma_z^2\omega_2$, and time step $\tau = \frac{1}{3}$. The rate was averaged over 15 time steps. The strongest bath interaction is related to a small frequency ω_1, which when isolated or in conjunction with ω_2 has strong enough coupling to induce state transitions. The only significant increase in the n_{11} state occurs when a low transition frequency is available for both qubits. Additionally, these rates are substantially lower than what is observed in the single qubit system, which corresponds with the better gate fidelities for this system (see Section 8.4).

where σ_z^j refers to the Pauli-Z matrix acting on the j^{th} site. This Hamiltonian has the computational basis as its energy eigenbasis, and it can be shown that changing a frequency ω_i can lead to a small energy transition between states differing locally on qubit i. By scanning over single qubit frequencies, we can obtain a simple noise profile, and then choose appropriate ω_i to influence the system. Using these frequencies we highlight four different cases in Fig. 8.5, showing interacting and non-interacting frequencies for each qubit. Additionally, we presented the calculated transition rates for each population in Table 8.1.

The system here demonstrates asymmetry between the two qubits, with stronger coupling present on the second qubit. For large ω_1 and ω_2, which do not strongly couple the bath and qubit system, we witness a region of linear decay towards a uniformly depolarized state. For smaller ω_1 and ω_2, we clearly have a very dynamic system, allowing for transitions amongst all four states.

We can expand this idea naturally to look at a potentially non-local Hamiltonian, namely:

$$H(\omega_1, \omega_2, \omega_3) = \omega_1\sigma_z^1 + \omega_2\sigma_z^2 + \omega_3\sigma_z^1\sigma_z^2. \tag{8.4}$$

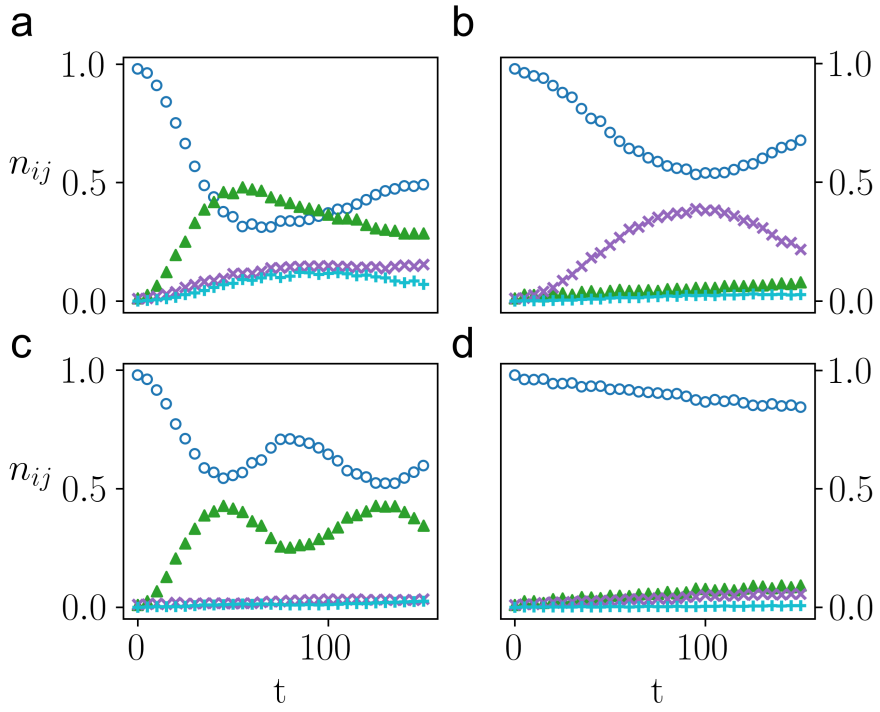

Figure 8.5: Simulated time evolution of a two-qubit local system which demonstrates controlled local state transitions. Populations n_{ij} where ij refers to the eigenstate (which is the computational basis) of the two-qubit system undergoing simulated evolution for time t with time step $\tau = 1/3$ prepared on ibmq_rome. The system Hamiltonian can be described with two frequencies: $H(\omega_1, \omega_2) = \omega_1 \sigma_z^1 + \omega_2 \sigma_z^2$. The different plots describe permutations of two different values of ω_1 and ω_2. **a** $(\frac{1}{20}, \frac{1}{20})$; **b** $(\frac{1}{20}, \frac{1}{2})$; **c** $(\frac{1}{2}, \frac{1}{20})$, and; **d** $(\frac{1}{2}, \frac{1}{2})$. Note that the bath is not symmetric with respect to the swapping of the qubits, as there is a stronger interaction of the bath with the second qubit relative to the first qubit. The populations are represented as $n_{00} : \circ$ (blue), $n_{01} : \triangle$ (green), $n_{10} : \times$ (purple), and $n_{11} : +$ (cyan).

The time propagator for this step is still relatively simple, as all elements commute and there are no trotterization errors. Additionally, the eigenstates correspond to elements of the computational basis. Practically, the propagator requires only 2 CNOT gates with a sequence of exponential Z rotations. If we consider the eigenstate state with density matrix $\rho_0 = |11\rangle\langle 11|$, we can easily elucidate information on the eigenstates and relative differences. Given the Hamiltonian above, we can describe state to state transitions with energy gaps given by:

$$\epsilon_{00} - \epsilon_{11} = 2(\omega_1 + \omega_2) \tag{8.5}$$

$$\epsilon_{01} - \epsilon_{11} = 2(\omega_1 - \omega_3) \tag{8.6}$$

$$\epsilon_{10} - \epsilon_{11} = 2(\omega_2 - \omega_3). \tag{8.7}$$

For local Hamiltonians, transitions from the 00 state are predominantly induced by local transitions ($\epsilon_{00} - \epsilon_{11}$ for Eq. (3) is $\omega_1 + \omega_2$, and so for small frequencies we will generally induce other transitions first). For this correlated Hamiltonian we can independently control each energy level, and thus have more control over the available transitions. However, we also expect that noise from multi-qubit gates will be more predominant. By using a diagonal Hamiltonian, we can perform propagation without any trotterization errors, and so we can isolate the effects of noise. Figure 8.6 shows simulated evolution for two sets of frequencies demonstrating different potential behaviors which the system exhibits in response to the bath. The evolution here involves 144 time steps, or 288 CNOT gates, which can be seen to eventually lead to a fully mixed ensemble state where each population is approximately 1/4. In (a) we choose frequencies that do not demonstrate a particular bath response, i.e. a large ω_3, ω_1, and ω_2. As a result the system displays exponential decay. In (b), we choose a large ω_3 with small values of ω_1 and ω_2, allowing for a correlated transition between the $|00\rangle$ and $|11\rangle$ states that is not mediated by other transitions. Thus, we demonstrate that we can

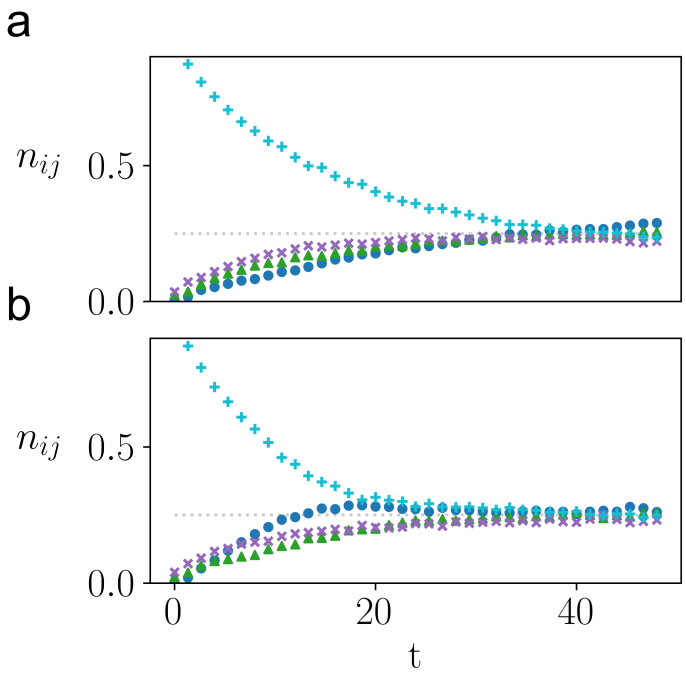

Figure 8.6: Demonstration of a $|00\rangle \leftrightarrow |11\rangle$ eigenstate transition in the simulated time evolution of a correlated two-qubit system. Simulated evolution for time t on ibmq_bogota where the timestep $\tau = 1/3$, and the Hamiltonian is composed of three variable frequencies ω_i, $\hat{H} = \omega_1\sigma_z^1 + \omega_2\sigma_z^2 + \omega_3\sigma_z^1\sigma_z^2$. **a** Using $\omega_3 = 1$, and $\omega_1,\ \omega_2 = \frac{1}{2}$, the system demonstrates expected exponential decay to the thermally mixed state. **b** With $\omega_3 = 1$ and frequencies, $\omega_1 = \frac{1}{10}$ and $\omega_2 = -\frac{1}{20}$, the difference in populations (relative to the decay seen in **a**) show a *correlated* two-qubit transition between the $|00\rangle$ and $|11\rangle$ eigenstates. The populations are represented as $n_{00} : \circ$ (blue), $n_{01} : \triangle$ (green), $n_{10} : \times$ (purple), and $n_{11} : +$ (cyan).

characterize the unique system-bath behavior of a correlated simulated quantum system.

8.3 Conclusions

By characterizing noise properties of the system, we may be able to design better error mitigation techniques or approaches to the simulation of open quantum systems where the quantum computer's noise is harnessed as an effective bath. For example, examining the spectral profile of the bath from the simulation of stationary quantum states may provide a unique spectroscopic fingerprint of the quantum computer. With such a fingerprint we

may be able to design simulation algorithms that account for this fingerprint, providing a potentially elegant approach to error mitigation for real-world applications. Furthermore, there may be certain scenarios such as open-quantum-system simulation where the presence of noise may be a beneficial quantum resource. To model an open quantum system, we may be able to use the quantum computer's noise to represent a significant part of the model's bath. Use of the quantum computer's inherent noise could potentially permit the simulation of an open quantum system at a significantly reduced computational cost in terms of both gate and qubit resources.

Additionally, although noise sources in driven evolution cannot typically be attributed to singular sources, the absence of such specificity is not necessarily an issue for practical quantum computing. As mentioned above, characterizing whether the transverse signal is a systematic over-rotation or an errant noise source is critical in calibration but not so important for system applications. For a complex quantum simulation, the effects of a single source of error (unless uniquely distinct) cannot be easily distinguished amidst the entire chorus of potential noise sources. From the complex set of instructions on a quantum computer emerges a complex noise profile, which is manifest in the difficulty of simulating multi-qubit noise phenomena. Through a simulated system specific approach, we can utilize the effective bath's spectroscopic information to design more device-specific techniques and algorithms that could improve future applications.

In this work we simulate the time evolution of arbitrary stationary quantum states on a noisy quantum computer through the application of the time evolution operator. Noise causes a system-specific response which exhibits Markovian and non-Markovian behaviors for certain frequency domains. Spectroscopic analysis of this time evolution provide a frequency spectrum—a spectroscopic fingerprint—of the noise on the effective bath induced by the quantum computer. Understanding the noise profile may allow us to create parameterized systems in which we influence state transitions with the quantum device serving as a non-

Markovian bath. The characterization of the bath is shown to be robust through simulations on multiple IBM superconducting-qubit quantum computers with different qubit numbers, connectivities, and fidelities. Although the present work employs superconducting-qubit quantum computers, in future work we plan to use this approach to characterize the noise on other types of quantum computers such as ion-trap quantum devices. These ideas provide a further step towards harnessing the unique quantum noise profile which emerges from the perspective from a simulated system on a quantum computer, that could be utilized in approaches for error mitigation and the simulation of open quantum systems.

Methods

In each simulation we used atomic units, and the time steps were relative to meaningful scales on the quantum device. While we could associate the results to a physical time through the known gate lengths, we focus on presenting the time evolution from the perspective of the simulated system, which could have arbitrary energies and time values, and which ultimately is beholden to the gate errors. As mentioned in the text, the system Hamiltonian have single qubit or in the two-qubit system, a sum of two-single qubit gates, both of which can be implemented as exact exponentials. These are implemented with U_3 gates on the quantum computer, which have the form:

$$U_3(\theta,\phi,\lambda) = R_z(\phi)R_x(-\frac{\pi}{2})R_z(\theta)R_x(\frac{\pi}{2})R_z(\lambda) \tag{8.8}$$

$$= \begin{pmatrix} \cos(\frac{\theta}{2}) & -\mathrm{e}^{i\lambda}\sin(\frac{\theta}{2}) \\ \mathrm{e}^{i\phi}\sin(\frac{\theta}{2}) & \mathrm{e}^{i(\phi+\lambda)}\cos(\frac{\theta}{2}) \end{pmatrix}. \tag{8.9}$$

In preparing the manuscript, the user-input basis gate sequence for the ibmq devices was updated, so that now the U_3 transformation is implemented as a series of 3 R_z gates interleaved with $\sqrt{X}$ gates (using the identity $R_x(\frac{\pi}{2}) = \mathrm{e}^{-\frac{i\pi}{4}}\sqrt{X}$). The correlated two-qubit

example required 2 CNOT gates in addition to the U_3 sequences.

Each circuit (representing a particular time point) was prepared by evolving in time according to the given time step, and then measuring the particular step 2^{13} times. Sampling errors throughout were smaller than the depicted markers, even in Fig. 8.6 where in **b.** we depict a difference of populations. The simulations used cloud-available quantum devices accessible through IBM Quantum Experience. The particular results reported here were performed on ibmq_armonk, ibmq_rome, ibmq_belek, ibmq_casablanca, and ibmq_bogota. The devices use fixed-frequency transmon qubits with co-planer waveguide resonators [54, 55]. We use the Python package Qiskit (v0.17.0) [56] to interface with the device. Specific device properties relevant to each run can be found in Section 8.4.

8.4 Supplemental Information

Alternative single-qubit Hamiltonians

As mentioned in the main text, we also looked at other single-qubit Hamiltonians, namely $H_0 = \omega\sigma_x$ and $H_0 = \omega\sigma_y$, with the results in Figure 8.8. For the σ_x and σ_y simulations, the higher frequency ($\omega = 0.5$) appears to be more noisy, which might be due to increased variances in measurement noise, or a systematic error in a frame rotation. Regardless, a somewhat stationary oscillating behavior is observed for the higher frequency, whereas the lower frequency ($\omega = 0.1$) is 'pushed' towards the center of the Bloch sphere. Scans of these trajectories also revealed similar trends, although we did not obtain as detailed data as in Figure 8.1 in the main text.

Comparison with T_1 relaxation times.

Looking at individual quantum devices, in some instances we see a linear relation between the simulated T_1 times, and the device T_1 times. While we expect this to be the case for

Figure 8.7: Different trajectories for two frequencies, $\omega = 0.5$ (blue) and $\omega = 0.1$ (green), with three varying Hamiltonians: (a) $H_0 = \omega\sigma_x$; (b) $H_0 = \omega\sigma_y$, and; (c) $H_0 = \omega\sigma_z$. Points were taken after 5 gate applications with each gate equal to $\tau = 1/3$.

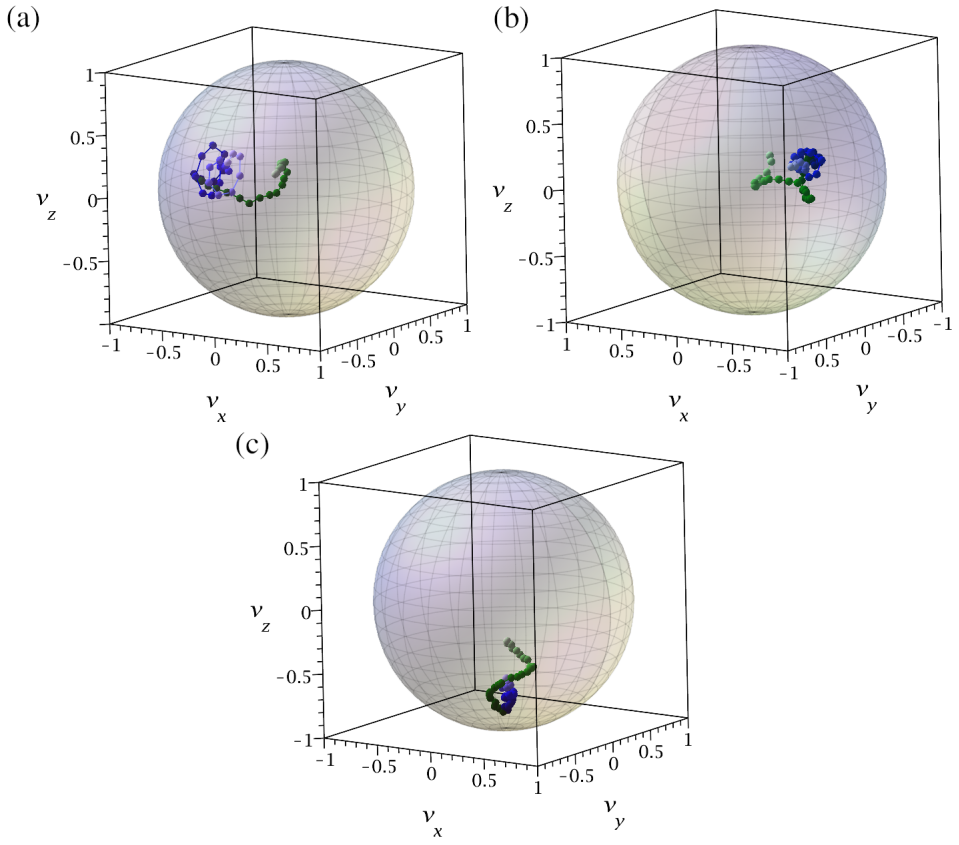

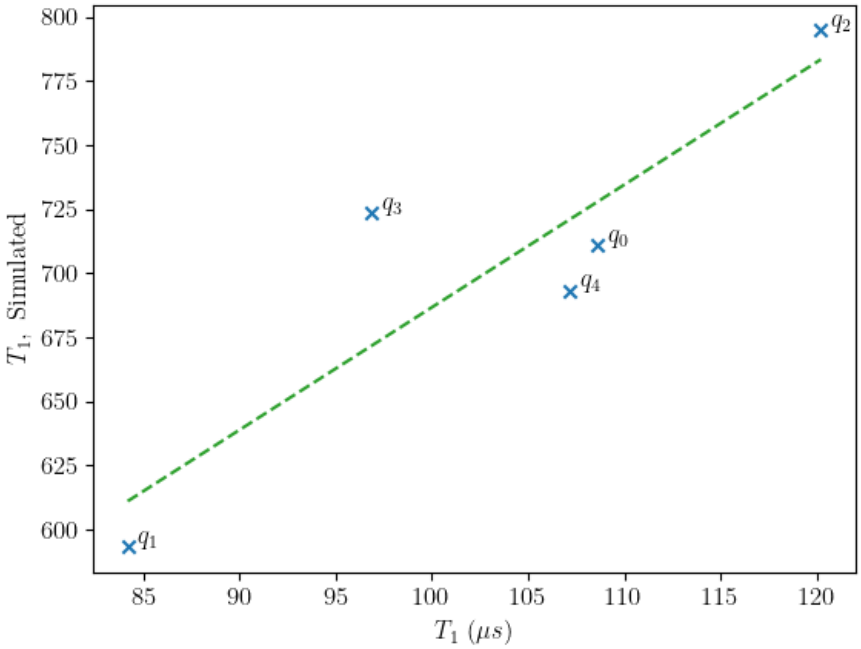

Figure 8.8: T_1 times for the simulated system (vertical axis, unitless), and the ibmqbogota device. For the simulated system, the $\exp[i\tau\hat{H}]$ operator was implemented 600 times, where $\hat{H} = \sigma_z$ ($\omega = 1$). 2^{11} measurements were taken for each experiment.

uniform systems, in some instances gate errors could be uniquely worse than corresponding qubit coherence times (which becomes more commonplace with multi-qubit gates). We give an example in Figure 8.8, where we compare the relaxation of the ibmqbogota qubit system, and the simulated quantum system. Note, while one can perform parallel measurements of the T_1 times, we found parallel simulation of the local qubit Hamiltonians introduced significant cross-qubit interactions, and so each relaxation time was measured separately.

Table 8.2: Calibration data for ibmq armonk taken over several days. Figure 8.1 and 8.2 were generated using data from 09-18-20, and Figure 8.3 and Figure 8.8 were measured between 11-12-20 and 11-13-20.

Date	**Frequency** GHz	$\mathbf{U_2}$ 10^{-4}	$\mathbf{U_3}$ 10^{-4}	$\mathbf{RO_{0\|1}}$ 10^{-2}	$\mathbf{RO_{1\|0}}$ 10^{-2}	$\mathbf{T_1}$ μs	$\mathbf{T_2}$ μs
09-18-20	4.974	7.1	14.3	4.9	6.1	193.4	202.0
11-12-20	4.974	6.4	12.7	5.5	4.4	157.5	222.6
11-13-20	4.974	5.0	10.0	4.8	3.9	157.9	190.0

Table 8.3: Calibration from IBMQ Rome on 11-17-2020, used to generate Figure 8.4 in the main text.

Qubit i	**Frequency** GHz	$\mathbf{U_2}$ 10^{-4}	$\mathbf{U_3}$ 10^{-4}	$\mathbf{RO_{0\|1}}$ 10^{-2}	$\mathbf{RO_{1\|0}}$ 10^{-2}	$\mathbf{T_1}$ μ s	$\mathbf{T_2}$ μ s	[j] $\mathbf{CNOT}_i^j$ (gate length) 10^{-2} (ns)
0	4.969	2.5	4.9	2.5	0.4	68.9	76.3	[1] 0.7 (320)
1	4.770	2.7	5.4	4.0	3.0	86.6	65.9	[0] 0.7 (356)

Quantum Device Specifications

For the quantum computations we use variety of devices provided through the IBM Quantum Experience. The particular results reported here were performed on ibmq armonk (single-qubit results) and ibmq rome. The devices use fixed-frequency transmon qubits with co-planer waveguide resonators [54, 55], and the Python package Qiskit (v 0.15.0, 0.17.1) [56] were used to interface with the device. Device properties can be found below.

In particular, we report the qubit frequency, errors in the U_2 and U_3 gates, as well as readout errors, and T_1 and T_2 qubit times. For connected devices we include data on the CNOT gates as well. While preparing this draft, the basis set of operations changed to $\sqrt{X}$ and R_z gates, and so where appropriate we report the given performance of these gates.

Table 8.4: Calibration data from ibmq-bogota, taken on 09-16-2021. See Figure 6 in the main text.

Qubit i	**Frequency** GHz	$\sqrt{X}$ 10^{-4}	X 10^{-4}	$\mathbf{RO}_{0\|1}$ 10^{-2}	$\mathbf{RO}_{1\|0}$ 10^{-2}	$\mathbf{T}_1$ μ s	$\mathbf{T}_2$ μ s	[j] $\mathbf{CNOT}_i^j$ (gate length) 10^{-2} (ns)
0	5.000	1.6	1.6	2.6	1.0	102.2	123.4	[1] 0.8 (690)
1	4.850	2.3	2.3	2.2	2.0	81.4	75.2	[0] 0.8 (654) [2] 0.9 (498)
2	4.783	2.1	2.1	2.6	0.7	78.1	115.5	[1] 0.9 (533) [3] 3.5 (341)
3	4.858	3.1	3.1	1.8	0.5	90.5	148.7	[2] 3.5 (306) [4] 0.8 (370)
4	4.978	1.5	1.5	4.2	0.9	98.4	171.2	[3] 0.8 (334)

Table 8.5: Single-qubit calibration data from ibm devices, taken on 09-18-2021. See Figure 3 in the main text.

Backend i	**Qubit** GHz	**Frequency** 10^{-4}	$\sqrt{X}$ 10^{-4}	X 10^{-2}	$\mathbf{RO}_{0\|1}$ 10^{-2}	$\mathbf{RO}_{1\|0}$ μ s	$\mathbf{T}_1$ μ s	$\mathbf{T}_2$ 10^{-2} (ns)
armonk	0	4.972	1.9	1.9	3.3	2.5	166.4	188.5
belem	0	5.090	1.6	1.6	8.0	6.4	104.2	115.4
	1	5.245	7.0	7.0	13.7	4.7	103.6	61.4
	2	5.361	2.5	2.5	2.9	1.0	98.6	33.4
	3	5.170	5.6	5.6	7.1	1.2	83.7	36.4
	4	5.258	3.6	3.6	3.7	0.9	90.3	135.3
bogota	0	5.000	1.7	1.7	1.8	1.4	104.9	136.2
	1	4.850	2.3	2.3	2.3	1.3	77.3	69.4
	2	4.783	1.9	1.9	2.3	0.6	118.5	186.3
	3	4.858	3.0	3.0	2.7	0.4	95.4	162.3
	4	4.978	1.4	1.4	2.7	1.5	104.0	190.7
casablanca	0	4.822	2.4	2.4	4.0	1.5	41.1	37.5
	1	4.760	2.3	2.3	3.5	0.8	34.7	79.2
	2	4.906	3.4	3.4	5.1	3.5	100.2	235.9
	3	4.879	3.0	3.0	2.2	0.9	73.7	143.6
	4	4.871	2.6	2.6	3.8	1.4	89.0	67.6
	5	4.964	1.8	1.8	1.7	0.7	88.8	172.1
	6	5.177	3.9	3.9	5.3	1.5	72.9	68.5

References

[1] R. P. Feynman, **21**, 467 (1982).

[2] D. S. Abrams and S. Lloyd, Physical Review Letters **83**, 5162 (1999), arXiv:9807070 [quant-ph] .

[3] S. Lloyd, Science **273**, 1073 (1996).

[4] A. Kandala, A. Mezzacapo, K. Temme, M. Takita, M. Brink, J. M. Chow, and J. M. Gambetta, Nature **549**, 242 (2017).

[5] S. McArdle, S. Endo, A. Aspuru-Guzik, S. C. Benjamin, and X. Yuan, Reviews of Modern Physics **92**, 015003 (2020).

[6] K. Head-Marsden, J. Flick, C. J. Ciccarino, and P. Narang, Chemical Reviews (2020), 10.1021/acs.chemrev.0c00620.

[7] E. Farhi, J. Goldstone, and S. Gutmann, , 1 (2014), arXiv:1411.4028 .

[8] Z. Hu, R. Xia, and S. Kais, Scientific Reports **10** (2020), 10.1038/s41598-020-60321-x.

[9] L. M. Sager, S. E. Smart, and D. A. Mazziotti, Physical Review Research **2** (2020), 10.1103/physrevresearch.2.043205.

[10] S. E. Smart and D. A. Mazziotti, Physical Review Letters **126** (2021), 10.1103/physrevlett.126.070504.

[11] H. P. Breuer and F. Petruccione, *The Theory of Open Quantum Systems*, Vol. 9780199213900 (Oxford University Press, 2007) pp. 1–656.

[12] A. A. Clerk, M. H. Devoret, S. M. Girvin, F. Marquardt, and R. J. Schoelkopf, Reviews of Modern Physics **82**, 1155 (2008), arXiv:0810.4729 .

[13] D. A. Lidar, (2019), arXiv:1902.00967 .

[14] P. Krantz, M. Kjaergaard, F. Yan, T. P. Orlando, S. Gustavsson, and W. D. Oliver, Applied Physics Reviews **6**, 1 (2019), arXiv:1904.06560 .

[15] A. Kandala, K. Temme, A. D. Córcoles, A. Mezzacapo, J. M. Chow, and J. M. Gambetta, Nature **567**, 491 (2019).

[16] S. McArdle, X. Yuan, and S. Benjamin, Physical Review Letters **122**, 180501 (2019), arXiv:1807.02467 .

[17] S. E. Smart and D. A. Mazziotti, Physical Review A **100**, 022517 (2019).

[18] S. E. Smart, J.-N. Boyn, and D. A. Mazziotti, http://arxiv.org/abs/2103.06876v1 .

[19] S. Endo, Z. Cai, S. C. Benjamin, and X. Yuan, , 1 (2020), arXiv:2011.01382 .

[20] K. Head-Marsden and D. A. Mazziotti, Physical Review A **99** (2019), 10.1103/physreva.99.022109.

[21] M. Mohseni and D. A. Lidar, Physical Review A - Atomic, Molecular, and Optical Physics **75**, 1 (2007), arXiv:0601034 [quant-ph] .

[22] M. Mohseni, A. T. Rezakhani, and D. A. Lidar, Physical Review A - Atomic, Molecular, and Optical Physics **77**, 1 (2008), arXiv:0702131 [quant-ph] .

[23] Z. Wu, S. Li, W. Zheng, X. Peng, and M. Feng, Journal of Chemical Physics **138** (2013), 10.1063/1.4774119.

[24] R. Rey-De-Castro, R. Cabrera, D. I. Bondar, and H. Rabitz, New Journal of Physics **15** (2013), 10.1088/1367-2630/15/2/025032.

[25] E. Knill, D. Leibfried, R. Reichle, J. Britton, R. B. Blakestad, J. D. Jost, C. Langer, R. Ozeri, S. Seidelin, and D. J. Wineland, Physical Review A - Atomic, Molecular, and Optical Physics **77**, 1 (2008), arXiv:0707.0963 .

[26] R. Blume-Kohout, J. K. Gamble, E. Nielsen, J. Mizrahi, J. D. Sterk, and P. Maunz, **87185** (2013), arXiv:1310.4492 .

[27] E. Nielsen, J. K. Gamble, K. Rudinger, T. Scholten, K. Young, and R. Blume-Kohout, Quantum **5**, 557 (2021), arXiv:2009.07301 .

[28] L. Xiang, Z. Zong, Z. Zhan, Y. Fei, C. Run, Y. Wu, W. Jin, Z. Jia, P. Duan, J. Wu, Y. Yin, and G. Guo, , 1 (2021), arXiv:2105.03333 .

[29] G. A. White, C. D. Hill, F. A. Pollock, L. C. Hollenberg, and K. Modi, Nature Communications **11** (2020), 10.1038/s41467-020-20113-3, arXiv:2004.14018 .

[30] M. Mohseni, A. T. Rezakhani, and A. Aspuru-Guzik, Physical Review A - Atomic, Molecular, and Optical Physics **77**, 1 (2008), arXiv:0708.0436 .

[31] S. J. Devitt, J. H. Cole, and L. C. Hollenberg, Physical Review A - Atomic, Molecular, and Optical Physics **73**, 1 (2006).

[32] K. Head-Marsden, S. Krastanov, D. A. Mazziotti, and P. Narang, Physical Review Research **3**, 013182 (2021), arXiv:2005.00029 .

[33] B. Rost, B. Jones, M. Vyushkova, A. Ali, C. Cullip, A. Vyushkov, and J. Nabrzyski, , 1 (2020), arXiv:2001.00794 .

[34] C. H. Tseng, S. Somaroo, Y. Sharf, E. Knill, R. Laflamme, T. F. Havel, and D. G. Cory, Physical Review A **62** (2000), 10.1103/physreva.62.032309.

[35] D. Bacon, A. M. Childs, I. L. Chuang, J. Kempe, D. W. Leung, and X. Zhou, Physical Review A **64** (2001), 10.1103/physreva.64.062302.

[36] H. Wang, S. Ashhab, and F. Nori, Physical Review A **83** (2011), 10.1103/physreva.83.062317.

[37] R. Sweke, I. Sinayskiy, D. Bernard, and F. Petruccione, Physical Review A **91** (2015), 10.1103/physreva.91.062308.

[38] S. Endo, J. Sun, Y. Li, S. C. Benjamin, and X. Yuan, Physical Review Letters **125** (2020), 10.1103/physrevlett.125.010501.

[39] Z. Hu, K. Head-Marsden, D. A. Mazziotti, P. Narang, and S. Kais, http://arxiv.org/abs/2101.05287v1 .

[40] K. Head-Marsden, S. Krastanov, D. A. Mazziotti, and P. Narang, Physical Review Research **3** (2021), 10.1103/physrevresearch.3.013182.

[41] H. Kamakari, S.-N. Sun, M. Motta, and A. J. Minnich, http://arxiv.org/abs/2104.07823v1 .

[42] K. Head-Marsden and D. A. Mazziotti, Journal of Chemical Physics **151** (2019), 10.1063/1.5100143.

[43] F. Yoshihara, Y. Nakamura, F. Yan, S. Gustavsson, J. Bylander, W. D. Oliver, and J. S. Tsai, Physical Review B - Condensed Matter and Materials Physics **89**, 1 (2014), arXiv:1402.1247 .

[44] L. M. Norris, G. A. Paz-Silva, and L. Viola, Physical Review Letters **116**, 1 (2016), arXiv:1512.01575 .

[45] F. Yan, S. Gustavsson, J. Bylander, X. Jin, F. Yoshihara, D. G. Cory, Y. Nakamura, T. P. Orlando, and W. D. Oliver, Nature Communications **4** (2013), 10.1038/ncomms3337, arXiv:1508.06436 .

[46] C. C. Yu, Journal of Low Temperature Physics **137**, 251 (2004).

[47] P. V. Klimov, J. Kelly, Z. Chen, M. Neeley, A. Megrant, B. Burkett, R. Barends, K. Arya, B. Chiaro, Y. Chen, A. Dunsworth, A. Fowler, B. Foxen, C. Gidney, M. Giustina, R. Graff, T. Huang, E. Jeffrey, E. Lucero, J. Y. Mutus, O. Naaman, C. Neill, C. Quintana, P. Roushan, D. Sank, A. Vainsencher, J. Wenner, T. C. White, S. Boixo, R. Babbush, V. N. Smelyanskiy, H. Neven, and J. M. Martinis, Physical Review Letters **121**, 90502 (2018).

[48] M. Y. Niu, V. Smelyanskyi, P. Klimov, S. Boixo, R. Barends, J. Kelly, Y. Chen, K. Arya, B. Burkett, D. Bacon, Z. Chen, B. Chiaro, R. Collins, A. Dunsworth, B. Foxen, A. Fowler, C. Gidney, M. Giustina, R. Graff, T. Huang, E. Jeffrey, D. Landhuis, E. Lucero, A. Megrant, J. Mutus, X. Mi, O. Naaman, M. Neeley, C. Neill, C. Quintana, P. Roushan, J. M. Martinis, and H. Neven, **0**, 1 (2019), arXiv:1912.04368 .

[49] R. J. Schoelkopf, A. A. Clerk, S. M. Girvin, K. W. Lehnert, and M. H. Devoret, Quantum Noise in Mesoscopic Physics , 175 (2003), arXiv:0210247 [cond-mat] .

[50] G. Ithier, E. Collin, P. Joyez, P. J. Meeson, D. Vion, D. Esteve, F. Chiarello, A. Shnirman, Y. Makhlin, J. Schriefl, and G. Schön, Physical Review B - Condensed Matter and Materials Physics **72**, 1 (2005).

[51] J. Bylander, S. Gustavsson, F. Yan, F. Yoshihara, K. Harrabi, G. Fitch, D. G. Cory, Y. Nakamura, J. S. Tsai, and W. D. Oliver, Nature Physics **7**, 565 (2011), arXiv:arXiv:1101.4707v1 .

[52] A. Tokmakoff, "Time-Dependent Quantum Mechanics and Spectroscopy," (2014).

[53] D. C. McKay, T. Alexander, L. Bello, M. J. Biercuk, L. Bishop, J. Chen, J. M. Chow, A. D. Córcoles, D. Egger, S. Filipp, J. Gomez, M. Hush, A. Javadi-Abhari, D. Moreda, P. Nation, B. Paulovicks, E. Winston, C. J. Wood, J. Wootton, and J. M. Gambetta, , 1 (2018), arXiv:1809.03452 .

[54] J. Koch, T. M. Yu, J. Gambetta, A. A. Houck, D. I. Schuster, J. Majer, A. Blais, M. H. Devoret, S. M. Girvin, and R. J. Schoelkopf, Phys. Rev. A **76**, 042319 (2007).

[55] J. M. Chow, A. D. Córcoles, J. M. Gambetta, C. Rigetti, B. R. Johnson, J. A. Smolin, J. R. Rozen, G. A. Keefe, M. B. Rothwell, M. B. Ketchen, and M. Steffen, Phys. Rev. Lett. **107**, 080502 (2011).

[56] H. Abraham, AduOffei, R. Agarwal, I. Y. Akhalwaya, G. Aleksandrowicz, T. Alexander, M. Amy, E. Arbel, Arijit02, A. Asfaw, A. Avkhadiev, C. Azaustre, AzizNgoueya, A. Banerjee, A. Bansal, P. Barkoutsos, G. Barron, G. S. Barron, L. Bello, Y. Ben-Haim, D. Bevenius, A. Bhobe, L. S. Bishop, *et al.*, "Qiskit: An open-source framework for quantum computing," (2019).

Part III

Contracted Quantum Eigensolvers

CHAPTER 9

QUANTUM SOLVER OF CONTRACTED EIGENVALUE EQUATIONS FOR SCALABLE MOLECULAR SIMULATIONS ON QUANTUM COMPUTING DEVICES

At the time of writing, the qACSE was introduced as a quantum solver of a contracted eigenvalue equation. Since then, we generalized the notion of the quantum solver, and so now refer to a contracted quantum eigensolver, or CQE, as a technique for solving any contracted eigenvalue equation on a quantum computer. The following chapter (Ch. 10) provides a more developed view of the CQE for solving the ACSE.

9.1 Introduction

Quantum computing has the potential to remove the exponential scaling of many-fermion quantum systems by the direct representation and manipulation of quantum states [1–36]. Algorithms for solving the energy eigenvalue equation of many-fermion systems include quantum phase estimation (QPE) [7, 17], adiabatic state preparation (ASP) [9], and the variational quantum eigensolver (VQE) [10, 12, 14, 15, 22]. QPE requires deep circuits with substantial error correction and ASP utilizes a slow and long time evolution with the computational costs of both methods quickly outpacing the capabilities of near-term quantum computers. While VQE has shown practical improvements over QPE and ASP, it suffers from high-dimensional classical optimization over a non-ideal surface, typically relying upon derivative-free optimization [37] whose computational cost increases rapidly with system size. Here we introduce a quantum eigenvalue solver that solves a contraction (or projection) of

the eigenvalue equation for efficient, scalable molecular simulations on quantum computers.

We develop a novel quantum eigensolver that optimizes the lowest energy eigenvalue by solving a contracted eigenvalue equation. The projection of the Schrödinger equation onto 2-particle transitions from the wave function is known as the 2-particle contracted Schrödinger equation (CSE) [38–47]. Here we consider the anti-Hermitian part of the CSE known as the 2-particle anti-Hermitian CSE (ACSE) [48–58], which has been used in many-electron quantum theory to solve for the ground- and excited-state energies and properties of strongly correlated atoms and molecules [59–66]. As shown previously, the solution of the ACSE has a close connection to the variational minimization of the energy with respect to a series of 2-body unitary transformations [48–50, 67]. The gradient of the energy with respect to the 2-body unitary transformations is the residual of the ACSE, and hence, the gradient with respect to these transformations vanishes if and only if the ACSE is satisfied [48, 49, 67]. In the classical algorithms the solution of the ACSE for the 2-particle reduced density matrix (2-RDM) is indeterminant without reconstruction or exact calculation of the 3-RDM [43, 45, 48–54, 68]. In the quantum algorithm, however, we show that through the preparation and measurement of the quantum state, the ACSE can be solved for the 2-RDM without any reconstruction or storage of the 3-RDM. The algorithm exhibits an exponential speedup relative to the exact classical algorithm.

A quantum contracted-eigenvalue-equation solver for solving the ACSE is applied to several problems on IBM quantum computers and a quantum simulator. On a quantum computer we solve for the ground-state dissociation of the hydrogen molecule. Both energies and 2-RDMs are computed. On a one-qubit IBM device we also solve a one-qubit Hamiltonian to demonstrate the trajectory of the solution of the ACSE in iteratively optimizing the ground-state energy. Lastly, we compute the ground-state dissociation of the linear H_3 molecule on a quantum simulator. While the solution of linear H_3 by the classical algorithm yields a ground-state energy that is limited by the accuracy of the approximate cumulant

reconstruction of the 3-RDM, the quantum-computing algorithm yields a ground-state potential energy curve that can be converged to the exact solution for all computed internuclear distances.

9.2 Theory

We begin with the Schrödinger equation for a many-electron quantum system

$$(\hat{H} - E)|\Psi\rangle = 0, \tag{9.1}$$

with the Hamiltonian operator

$$\hat{H} = \sum_{pqst} {}^2K_{st}^{pq} \hat{a}_p^\dagger \hat{a}_q^\dagger \hat{a}_t \hat{a}_s, \tag{9.2}$$

where ${}^2K$ is the two-electron reduced Hamiltonian matrix, containing the one- and two-electron integrals, and the second-quantized operators $\hat{a}_p^\dagger$ and $\hat{a}_p$ create and annihilate an electron in the spin orbital p, respectively. The projection (or contraction) of the Schrödinger equation onto the space of two-electron transitions generates the CSE [38–46], and the anti-Hermitian part of the CSE produces the ACSE [48–55, 68]

$$\langle\Psi|[\hat{a}_i^\dagger \hat{a}_j^\dagger \hat{a}_l \hat{a}_k, \hat{H}]|\Psi\rangle = 0. \tag{9.3}$$

The ACSE is important for many-electron quantum systems, especially—as we show below—in quantum computing, because its residual contains the gradient for the optimization of many-electron wave functions.

Consider the variational ansatz for the wave function in which the wave function is

iteratively constructed from unitary two-body exponential transformations [48, 49, 67]

$$|\Psi_{n+1}\rangle = e^{\epsilon \hat{A}_n}|\Psi_n\rangle, \tag{9.4}$$

where $\hat{A}_n$ is an anti-Hermitian two-electron operator

$$\hat{A}_n = \sum_{pqst} {}^2A_n^{pq;st}\hat{a}_p^\dagger\hat{a}_q^\dagger\hat{a}_t\hat{a}_s. \tag{9.5}$$

The energy at the $(n+1)^{\text{th}}$ iteration through order ϵ is given by

$$E_{n+1} = E_n + \epsilon\langle\Psi_n|[\hat{H}, \hat{A}_n]|\Psi_n\rangle. \tag{9.6}$$

Consequently, the gradient of the energy with respect to ${}^2A_n$ is

$$\frac{\partial E_{n+1}}{\partial({}^2A_n^{ij;kl})} = -\langle\Psi_n|[\hat{a}_i^\dagger\hat{a}_j^\dagger\hat{a}_l\hat{a}_k, \hat{H}]|\Psi_n\rangle. \tag{9.7}$$

From this equation we observe two important facts [48, 49, 67]: (1) the residual of the ACSE is the negative of the energy gradient with respect to all two-body unitary transformations parametrized by ${}^2\hat{A}_n$ and (2) the residual of the ACSE with respect to Ψ_n vanishes if and only if the sequence of wave functions has converged at n to an eigenstate of the Hamiltonian.

The ACSE can be solved to compute the 2-RDM directly without storage of the many-electron wave function. In the algorithm previously implemented on classical computers [48–55, 68], the wave function at the n^{th} iteration is substituted into the definition of the 2-RDM

$${}^2D_{st}^{pq} = \langle\Psi|\hat{a}_p^\dagger\hat{a}_q^\dagger\hat{a}_t\hat{a}_s|\Psi\rangle \tag{9.8}$$

to yield an expression for the 2-RDM at the $(n+1)^{\text{th}}$ iteration

$$ {}^2D^{pq;st}_{n+1} =^2 D^{pq;st}_{n} + \epsilon \langle \Psi_n | [\hat{a}^\dagger_p \hat{a}^\dagger_q \hat{a}_t \hat{a}_s, \hat{A}_n] | \Psi_n \rangle. \tag{9.9} $$

where the operator $\hat{A}_n$ can be selected to be the residual of the ACSE, which causes the 2-RDM to follow the energy's gradient towards its minimum

$$ {}^2A^{ij;kl}_{n} = \langle \Psi_n | [\hat{a}^\dagger_i \hat{a}^\dagger_j \hat{a}_l \hat{a}_k, \hat{H}] | \Psi_n \rangle. \tag{9.10} $$

By using the fact that $\hat{A}_n$ and $\hat{H}$ are two-body operators in Eqs. (9.5) and (9.2), the 2-RDM at the $(n+1)^{\text{th}}$ iteration can be expressed as a linear functional of the 1-, 2-, and 3-RDMs at the n^{th} iteration. The indeterminacy in these recursion relations for the 2-RDM can be removed by calculating the 3- through N-RDMs at an exponential cost, or by reconstructing the 3-RDM approximately from the 2-RDM [48–51]. For example, the cumulant part of the 3-RDM in its cumulant expansion can be neglected or approximated to provide a reconstruction of the 3-RDM in terms of the 2-RDM [44, 48, 56].

We propose an algorithm for solving the ACSE for the 2-RDM on the quantum computer, which is shown in Table I. While the classical computer uses matrices and vectors to represent quantum states, the quantum computer allows us to prepare a form of the quantum state itself in terms of qubits where the scaling of the preparation is non-exponential for states with polynomially scaling Hamiltonians [69]. Utilizing this capability, as well as methods of fermionic quantum computation (allowing us to transform fermionic operators to quantum operators through tools such as the Jordan-Wigner or Bravyi-Kitaev transformations [6, 70], and to express the exponential of anti-Hermitian operators), we prepare the wave function at the $(n+1)^{\text{th}}$ in Eq. (9.4) on the quantum computer (Step 3 of Table I) and perform measurements of its 2-RDM's matrix elements in Eq. (11.7) on the quantum computer (Step 4). In Step 5 we optimize the parameter ϵ by minimizing the energy by a model-trust

Newton's method [71]. Before we can perform the preparation in Step 3, however, we need to compute the ${}^2A$ matrix by evaluating the residual of the ACSE. While we could evaluate the ACSE on the classical computer using Eq. (11.3) with cumulant reconstruction of the 3-RDM, we can compute the residual of the ACSE on the quantum computer directly without a formal approximation. We prepare the auxiliary state $|\Lambda_n\rangle$ in Step 1 of the algorithm

$$|\Lambda_n\rangle = e^{i\delta\hat{H}}|\Psi_n\rangle \tag{9.11}$$

where δ is a small nonnegative parameter and measure the imaginary part of its 2-RDM on the quantum computer giving us the residual of the ACSE to second order in δ —the elements of the ${}^2A$ matrix

$${}^2A_n^{ij;kl} = \delta^{-1}\mathrm{Im}\langle\Lambda_n|\hat{a}_i^\dagger\hat{a}_j^\dagger\hat{a}_l\hat{a}_k|\Lambda_n\rangle + O(\delta^2). \tag{9.12}$$

Steps (1-4) can be repeated until convergence. Because we are following the gradient, for a suitably small choice of ϵ the algorithm is guaranteed to converge. The algorithm can be initiated with any initial wave function including the mean-field (Hartree-Fock) wave function. The only errors in the quantum solution of the ACSE for the 2-RDM arise from noise on the quantum computer, and hence, even with an initial Hartree-Fock wave function, the algorithm can treat strongly correlated molecular quantum systems. Importantly, Steps (1-4) yield exact expressions without reconstruction of higher RDMs, yielding an exponential advantage over classical algorithms in obtaining the ${}^2D$ and ${}^2A$ matrices.

9.3 Results

To illustrate the solution of the ACSE on the quantum computer, we apply the quantum ACSE algorithm to three applications: the solution of a generic one-qubit Hamiltonian and the dissociation of the H_2 and H_3 molecules. Solutions of the one-qubit and H_2 Hamiltonians

Table 9.1: Quantum ACSE algorithm for 2-RDM optimization. A classical solution of the ACSE with a reconstruction of the 3-RDM can be substituted in Steps (1-2) yielding a hybrid quantum-classical algorithm (denoted later as the Classical ACSE).

Algorithm: Quantum ACSE method for 2-RDM optimization

Given $n = 0$ *and* $0 < \delta \leq 1$.
Choose initial wave function $|\Psi_0\rangle$.
Repeat until $||^2 A_n||$ *is small.*

Step 1: *Prepare* $|\Lambda_n\rangle$ *from* $|\Lambda_n\rangle = e^{i\delta\hat{H}}|\Psi_n\rangle$,
Step 2: *Measure* ${}^2A_n$ *from* ${}^2A_n^{ij;kl} = \mathrm{Im}\langle\Lambda_n|\hat{a}_i^\dagger\hat{a}_j^\dagger\hat{a}_l\hat{a}_k|\Lambda_n\rangle$,
Step 3: *Prepare* $|\Psi_{n+1}\rangle$ *from* $|\Psi_{n+1}\rangle = e^{\epsilon\hat{A}_n}|\Psi_n\rangle$,
Step 4: *Measure* ${}^2D_{n+1}$ *from* ${}^2D_{n+1}^{pq;st} = \langle\Psi_{n+1}|\hat{a}_p^\dagger\hat{a}_q^\dagger\hat{a}_t\hat{a}_s|\Psi_{n+1}\rangle$,
Step 5: *Iterate Steps 3 and 4 to minimize the energy with respect to* ϵ,
Step 6: *Set* $n = n + 1$.

are performed on the one- and five-qubit IBM quantum computers Armonk and Ourense, respectively. Section 9.5 contains additional details of the computations and specifications of the quantum computers. The dissociation of H_3 is implemented on a quantum simulator to probe the method's accuracy in the absence of noise.

We first examine the solution of a one-qubit Hamiltonian $\hat{H} = \frac{1}{2}\left(\hat{\sigma}_x - \hat{\sigma}_y + \hat{\sigma}_z\right)$ where $\hat{\sigma}_x$, $\hat{\sigma}_y$, and $\hat{\sigma}_z$ are the Pauli matrices in the x, y, and z directions. In the basis of the Bloch sphere we can express the Hamiltonian and the initial density matrix as vectors $(1, -1, 1)$ and $(0, 0, 1)$, respectively. Beginning at the initial density-matrix vector, the solution from the ACSE reaches the ground-state vector, indicated by v_-, in approximately 8 iterations on the quantum computer, as shown in Fig. 1. The quantum solution of the ACSE provides an efficient mechanism for moving along the surface of the Bloch sphere, where the pure states exist, to reach the ground-state solution. In the special case of the Bloch sphere the $\hat{A}$ operator can be computed as a Bloch vector from the cross product of the Hamiltonian vector with the density-matrix vector; geometrically, from the definition of the cross product the $\hat{A}$ vector, indicated in Fig. 1 at each iteration by an arrow, is orthogonal to the plane formed by the Hamiltonian and density-matrix vectors.

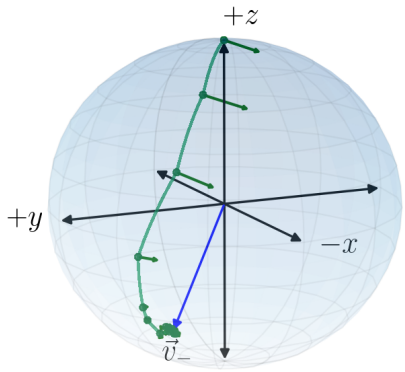

Figure 9.1: For a 1-qubit Hamiltonian the solution of the quantum ACSE converges to the ground state, indicated by v_-, in about 8 iterations on a 1-qubit IBM quantum computer.

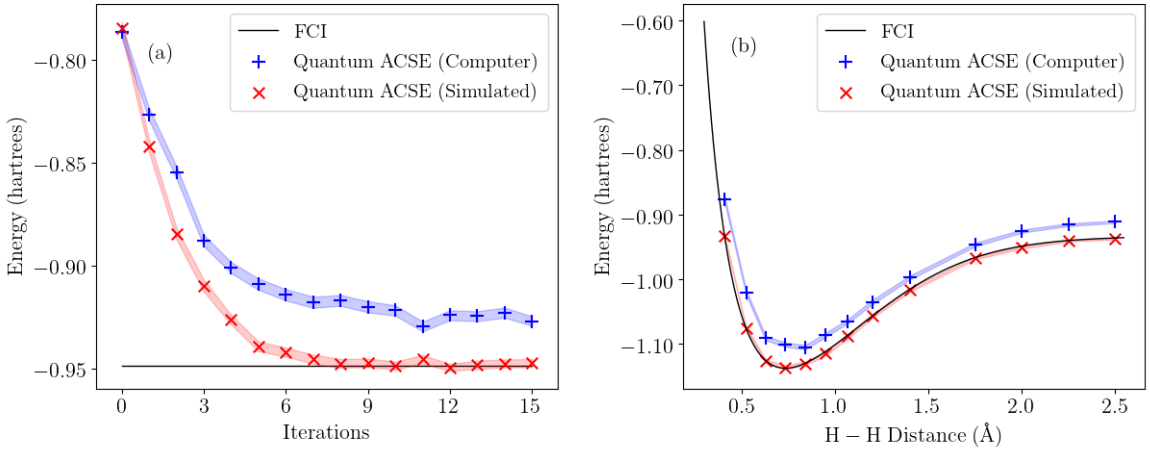

Figure 9.2: For the H_2 molecule the figure shows (a) the energy at each iteration in the solution of the ACSE at an internuclear distance R of 2 Å and (b) the energy dissociation curve of the molecule. The error in the ACSE on the quantum computer, due to noise, is fairly uniform throughout the dissociation, indicating that the ACSE captures the spin entanglement.

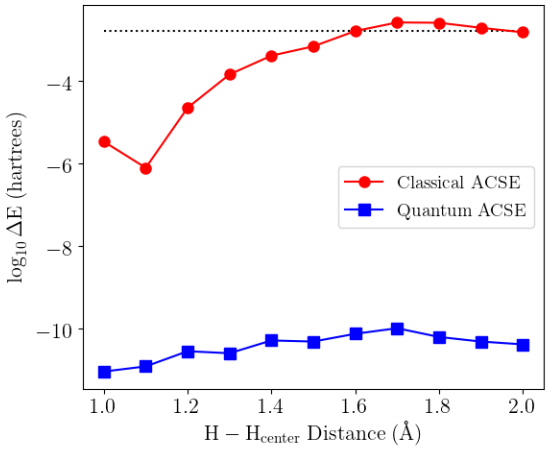

Figure 9.3: The error in the potential energy curves from the equal-bond dissociation of the H_3 molecule are shown for the classical and quantum solutions of the ACSE where the state is simulated on a quantum computer. The quantum solution to the ACSE is more accurate by 6 orders of magnitude. Errors are relative to the exact solution (from full configuration-interaction). Dotted line indicates "chemical accuracy" (1 kcal/mol).

Second, we compute the dissociation of the hydrogen molecule in a minimal Slater-type orbital (STO-3G) basis set. On the quantum computer the molecule is represented in the ACSE algorithm by a two-qubit compact mapping. The energy at each iteration in the solution of the ACSE for H_2 at 2 Å is shown in Fig. 2a. The ACSE energy from a quantum simulator converges to the energy from full configuration interaction (FCI) in about 9-to-10 iterations. The ACSE energy on the quantum computer converges in approximately the same number of iterations to an energy that is approximately 25 mhartrees higher than the FCI energy. This error is due to the noise present on the quantum computer; in fact, a nearly identical curve in the iterations is generated by a quantum simulator with the QISKIT noise model, a noise model based on the device T1, T2, and readout parameters. Figure 2b shows the energy dissociation curve of the hydrogen molecule. While the noise error is visible in the potential energy curve from the ACSE, the error is importantly uniform throughout the curve, indicating that the ACSE algorithm is capturing the significant electron correlation from spin entanglement in the dissociation region.

Finally, we calculate the dissociation of the H_3 molecule in the minimal Slater-type orbital (STO-3G) basis set on a quantum simulator without noise. The purpose of this calculation is to examine the accuracy of the quantum ACSE algorithm on an ideal, noise-free quantum computer. Stretching the two bonds of the molecule equally causes a Mott metal-to-insulator transition with the stretched geometry being highly correlated due to nontrivial spin entanglement [28]. The energy errors from the classical and quantum ACSE algorithms, relative to the FCI energy, are shown in Fig. 3. Most strikingly, the energies from the quantum ACSE are about six orders of magnitude more accurate than the energies from the classical ACSE. While the classical ACSE algorithm requires an approximate cumulant-based reconstruction [44] of the 3-RDM from the 2-RDM, the quantum ACSE algorithm does not require any reconstruction approximation because the updates of the ${}^2A$ and ${}^2D$ matrices are performed, in principle exactly, through a combination of state preparation and tomography. Figure 3 also shows that the quantum solution of the ACSE remains accurate at stretched bond distances where the electron correlation— the deviation from the Hartree-Fock solution—is significant.

9.4 Discussion and Conclusions

Key features of the quantum algorithm for solving the ACSE include: (1) computation of the energy and 2-RDM without any approximate reconstruction of higher RDMs as in the classical algorithm and (2) evaluation of the energy gradient— residual of the ACSE—on the quantum computer for accurate and efficient gradient-based optimization. The ACSE algorithm's computation of the gradient on the quantum computer offers a significant advantage over VQE algorithms [10, 12, 14, 15, 22] that approximate the gradient on the classical computer by derivative-free optimization methods [37] like the simplex method that are limited to hundreds of degrees of freedom. The quantum ACSE algorithm is also much faster to converge than adiabatic algorithms like ASP [9] due to its gradient-based optimization. Finally,

it has much lower tomography costs than other methods for accelerating ASP like Lanczos-based imaginary-time evolution methods which can require higher RDMs [20, 24]. Unlike unitary coupled cluster which uses a single unitary exponential transformation of commuting operators [16], the ACSE method represents the wave function as a product of unitary exponential transformations of two-body, non-commuting operators that represent the higher excitations as non-trivial products of two-body operators; furthermore, the ACSE's iterative approximation to the construction of the wave function decreases Trotterization errors, errors from the application of Trotter's formula for representing the exponential transformation on the quantum computer.

The quantum algorithm for solving the ACSE provides a direct computation of ground-state energies and 2-RDMs with an efficient generation of the search direction from the ACSE residual. In the context of quantum algorithms, it has the benefits of good ansatz depth, modest tomography requirements, and no derivative-free classical optimization. Importantly, while the focus here is on the solution of many-fermion systems, the ACSE algorithm is also applicable to solving many-boson systems as well as many-qubit systems governed by arbitrary p-body interactions. Future work will also explore the application of the ACSE algorithm to electronic excited states and active-space calculations for the treatment of strong electron correlation in larger molecules. Because the quantum ACSE algorithm is an iterative approach to computing the N-representable 2-RDM [72–74] of a given eigenstate, it offers a polynomial-scaling approach to computing energies and properties of strongly correlated many-fermion quantum systems on both near-to-intermediate-term and future quantum devices with applications across quantum chemistry and physics.

9.5 Methods

Details on Calculations

To calculate the electron integrals, (open and restricted) Hartree-Fock calculations, and full configuration interaction (FCI) calculations, we used the Quantum Chemistry Toolbox in Maple (Maple2020, Waterloo)[75] and PySCF [76–78]. Gate and measurement sequences for the quantum computers were controlled using the python package Qiskit [79].

Single-Qubit Calculation

The single qubit calculations were performed on a single qubit device from IBM using Euler's method (no optimization of the step size ϵ). Because the implementation of general single qubit unitaries is well known [69], there is ideally no trotterization error. Similarly, an exponential addition formula is known based on the law of cosines, so that in the propagator step we take the composition of the state $|\Psi_n\rangle$ and $e^{i\delta\hat{H}}$ to re-express $|\Lambda_n\rangle$ as a single unitary being implemented. Note that $\delta = 0.1$, a full state tomography was performed, and 2^{12} measurements were used for each state, with no error mitigation or measurement corrections used.

Two-Qubit Simulation of H_2

The molecular Hamiltonian for H_2 in a minimal basis set has been well studied and numerous examples using 1-, 2-, and 4-qubit simulations have been explored [1]. Some two-qubit cases involve using the Brayvi-Kitaev or pairty mapping which allows for the truncation of two-qubit in a four-qubit mapping due to symmetry. Because only number operators, coulomb operators, and some double excitation terms are captured in the H_2 Hamiltonian, we can simply map the Hamiltonian via a compact mapping to two-qubits. We can map from our

wavefunction (as Slater determinants) to the computational basis as:

$$\begin{aligned} |1010\rangle &\rightarrow |00\rangle \\ |1001\rangle &\rightarrow |01\rangle \\ |0110\rangle &\rightarrow |10\rangle \\ |0101\rangle &\rightarrow |11\rangle \end{aligned} \tag{9.13}$$

The phase of the fermionic pair is kept constant, and so the action of the second-quantized operators transforms naturally, and we find that the operator $\hat{H}$ can be expressed as:

$$\begin{aligned} \hat{H} &= h_1\sigma_i^1\sigma_i^2 + \frac{h_2}{2}(\sigma_z^1\sigma_i^2 + \sigma_i^1\sigma_z^2) + h_3\sigma_z^1\sigma_z^2 + h_4\sigma_x^1\sigma_x^2 \\ &= \begin{pmatrix} h_1 + h_2 + h_3 & 0 & 0 & h_4 \\ 0 & h_1 - h_3 & h_4 & 0 \\ 0 & h_4 & h_1 - h_3 & 0 \\ h_4 & 0 & 0 & h_1 - h_2 + h_3 \end{pmatrix} \end{aligned} \tag{9.14}$$

The exponential of this can implemented fairly easy using standard techniques. To simplify the computation, and because the Hamiltonian and state are ideally real, we perform a projection onto the real space of measurements, and so only perform measurements of $\sigma_z^1\sigma_z^2$, $\sigma_x^1\sigma_x^2$, and $\sigma_y^1\sigma_y^2$ to obtain the real components. Similarly, in obtaining the S values, we only perform tomography on $\sigma_x^1\sigma_y^2$ and $\sigma_y^1\sigma_x^2$, representing the imaginary contributions of the double excitations. We simplified the unitary gate sequences using standard compilation techniques. As such, we could implement iterations of $|\Psi_n\rangle$ and $|\Lambda_n\rangle$ utilizing only a single CNOT gate (the latter step include extra R_z rotations).

A simple noise model (available in Qiskit and which is detailed more extensively in recent work [79, 80]) was used to compare with the experimental results, and showed very similar results. In particular, the model involves applying a depolarizing channel, and then a thermal

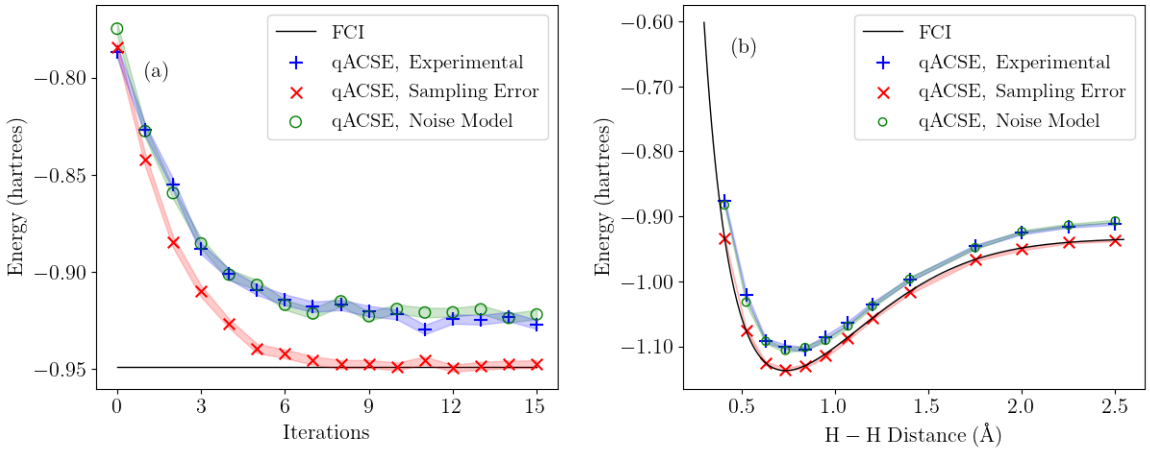

Figure 9.4: Expanded from Figure 2 in the main text, and includes the noise model as compared with the experimental results. For the H_2 molecule the figure shows (a) the energy at each iteration in the solution of the ACSE at an internuclear distance R of 2 Å and (b) the energy dissociation curve of the molecule. The error in the ACSE on the quantum computer, due to noise, is fairly uniform throughout the dissociation, indicating that the ACSE captures the spin entanglement.

relaxation step based on the T_1 and T_2 times, and finally including a single-qubit bit-flip error based on the device readout characteristics. We include these results in Figure 1. The large agreement in this case is likely due to the small circuit depth and and limitation of the system to only 2 qubit, limiting correlated qubit errors across the system.

Details Regarding H_3 *Simulation*

For our simulation of H_3 we used the Jordan-Wigner mapping to map the six spin-orbitals onto six qubits. The quantum simulation was carried out using the quantum simulator provided by Qiskit[79]. For both the classical ACSE and quantum ACSE methods we used a model-trust Newton's method to find the optimal step-size ϵ in $e^{\epsilon A}$. In general, if no suitable trust region could be found (i.e. where the second derivative was negative), set $\epsilon = 1$ and continue in an appropriate direction. Convergence criteria in the objective function and Taylor series approximation of the trust region were set to 10^{-10}.

Table 9.2: Calibration data for the ibm-5 and ibm-1 devices during benchmarking. U_2 and U_3 represent the errors for single qubit unitaries containing one and two $X_{\pi/2}$ pulses and two and three frame changes respectively, as well as the duration of the pulse. RO represents the readout error, and we have the T_1 depolarization and T_2 dephasing times. $[j]$ specifies the target qubit with control qubit i, and we report the error. For the ibm-5 device, U_2 gates were 35 ns, and U_3 gates were 71 ns. For ibm-1, U_2 gates were 142 ns, and U_3 gates were 284 ns.

Qubit i	$\mathbf{U}_2$ (10^{-4})	$\mathbf{U}_3$ (10^{-4})	**RO** (10^{-2})	$\mathbf{T}_1$ (μs)	$\mathbf{T}_2$ (μs)	$[j]$ $\mathbf{CX}_i^j$ (10^{-2})		
ibm-5 (ourense)								
0	3.2	6.3	1.5	117	95	[1] 7.2 (270)		
1	4.2	8.5	3.1	95	38	[0] 7.2 (235)	[2] 9.2 (391)	[3] 14 (612)
2	3.0	6.1	1.2	93	101	[1] 9.2 (427)		
3	3.2	6.4	3.2	92	110	[1] 14 (576)	[4] 9.4 (306)	
4	4.3	8.7	4.8	83	37	[2] 9.4 (270)		
ibm-5 (ourense)								
0	3.1	6.1	1.5	105	81	[1] 6.0 (270)		
1	3.8	7.6	3.1	113	38	[0] 6.0 (235)	[2] 6.3 (391)	[3] 14 (612)
2	2.2	4.5	1.2	144	101	[1] 6.3 (427)		
3	3.9	7.8	3.2	84	82	[1] 14 (576)	[4] 8.1 (306)	
4	5.6	11	4.8	118	33	[2] 8.1 (270)		
ibm-1 (armonk)								
0	4.8	9.6	3.3	111	160			

Quantum Computer Specifications

For the quantum computation we used the IBM Quantum Experience devices Oursense (5-qubits) and Armonk (1-qubit), available online. The former has triangular-type coupling between qubits. These cloud accessible quantum devices are fixed-frequency transmon qubits with co-planer waveguide resonators [81, 82]. The quantum information software development kit Qiskit [79] was used to interface with the device. The specifications and pulse lengths can be seen below.

References

[1] S. McArdle, S. Endo, A. Aspuru-Guzik, S. C. Benjamin, and X. Yuan, Reviews of Modern Physics **92**, 15003 (2020), arXiv:1808.10402 .

[2] R. P. Feynman, Int. J. Theor. Phys. **21**, 467 (1982).

[3] S. Lloyd, Science **273**, 1073 (1996).

[4] D. S. Abrams and S. Lloyd, Phys. Rev. Lett. **79**, 2586 (1997).

[5] D. S. Abrams and S. Lloyd, Phys. Rev. Lett. **83**, 5162 (1999).

[6] S. B. Bravyi and A. Y. Kitaev, Ann. Phys. **298**, 210 (2002).

[7] A. Aspuru-Guzik, A. D. Dutoi, P. J. Love, and M. Head-Gordon, Science **309**, 1704 (2005).

[8] B. P. Lanyon, J. D. Whitfield, G. G. Gillett, M. E. Goggin, M. P. Almeida, I. Kassal, J. D. Biamonte, M. Mohseni, B. J. Powell, M. Barbieri, A. Aspuru-Guzik, and A. G. White, Nat. Chem. **2**, 106 (2010).

[9] J. Du, N. Xu, X. Peng, P. Wang, S. Wu, and D. Lu, Phys. Rev. Lett. **104**, 030502 (2010).

[10] A. Peruzzo, J. McClean, P. Shadbolt, M.-H. Yung, X.-Q. Zhou, P. J. Love, A. Aspuru-Guzik, and J. L. O'Brien, Nat. Commun. **5**, 4213 (2014).

[11] Y. Wang, F. Dolde, J. Biamonte, R. Babbush, V. Bergholm, S. Yang, I. Jakobi, P. Neumann, A. Aspuru-Guzik, J. D. Whitfield, and J. Wrachtrup, ACS Nano **9**, 7769 (2015).

[12] D. Wecker, M. B. Hastings, and M. Troyer, Phys. Rev. A **92**, 042303 (2015).

[13] P. O'Malley, R. Babbush, I. Kivlichan, J. Romero, J. McClean, R. Barends, J. Kelly, P. Roushan, A. Tranter, N. Ding, B. Campbell, Y. Chen, Z. Chen, B. Chiaro, A. Dunsworth, A. Fowler, E. Jeffrey, E. Lucero, A. Megrant, J. Mutus, M. Neeley, C. Neill, C. Quintana, D. Sank, A. Vainsencher, J. Wenner, T. White, P. Coveney, P. Love, H. Neven, A. Aspuru-Guzik, and J. Martinis, Phys. Rev. X **6**, 031007 (2016).

[14] J. R. McClean, J. Romero, R. Babbush, and A. Aspuru-Guzik, New J. Phys. **18**, 023023 (2016).

[15] A. Kandala, A. Mezzacapo, K. Temme, M. Takita, M. Brink, J. M. Chow, and J. M. Gambetta, Nature **549**, 242 (2017).

[16] Y. Shen, X. Zhang, S. Zhang, J.-N. Zhang, M.-H. Yung, and K. Kim, Phys. Rev. A **95**, 020501 (2017).

[17] S. Paesani, A. Gentile, R. Santagati, J. Wang, N. Wiebe, D. Tew, J. O'Brien, and M. Thompson, Phys. Rev. Lett. **118**, 100503 (2017).

[18] J. Lee, W. J. Huggins, M. Head-Gordon, and K. B. Whaley, J. Chem. Theory Comput. **15**, 311 (2018).

[19] A. Kandala, K. Temme, A. D. Córcoles, A. Mezzacapo, J. M. Chow, and J. M. Gambetta, Nature **567**, 491 (2019).

[20] M. Motta, C. Sun, A. T. K. Tan, M. J. O'Rourke, E. Ye, A. J. Minnich, F. G. S. L. Brandão, and G. K.-L. Chan, Nat. Phys. **16**, 205 (2019).

[21] H. R. Grimsley, S. E. Economou, E. Barnes, and N. J. Mayhall, Nat. Commun. **10**, 3007 (2019).

[22] D. Wang, O. Higgott, and S. Brierley, Phys. Rev. Lett. **122**, 140504 (2019).

[23] M. Ganzhorn, D. Egger, P. Barkoutsos, P. Ollitrault, G. Salis, N. Moll, M. Roth, A. Fuhrer, P. Mueller, S. Woerner, I. Tavernelli, and S. Filipp, Phys. Rev. Appl **11**, 044092 (2019).

[24] S. McArdle, T. Jones, S. Endo, Y. Li, S. C. Benjamin, and X. Yuan, npj Quantum Inf. **5**, 75 (2019).

[25] G. Mazzola, P. J. Ollitrault, P. K. Barkoutsos, and I. Tavernelli, Phys. Rev. Lett. **123**, 130501 (2019).

[26] S. E. Smart, D. I. Schuster, and D. A. Mazziotti, Commun. Phys. **2**, 11 (2019).

[27] T. Bian, D. Murphy, R. Xia, A. Daskin, and S. Kais, Mol. Phys. **117**, 2069 (2019).

[28] S. E. Smart and D. A. Mazziotti, Phys. Rev. A **100**, 022517 (2019).

[29] Y. Matsuzawa and Y. Kurashige, J. Chem. Theory Comput. **16**, 944 (2020).

[30] S. Wei, H. Li, and G. Long, Research **2020**, 1 (2020).

[31] I. G. Ryabinkin, R. A. Lang, S. N. Genin, and A. F. Izmaylov, J. Chem. Theory Comput. **16**, 1055 (2020).

[32] B. T. Gard, L. Zhu, G. S. Barron, N. J. Mayhall, S. E. Economou, and E. Barnes, npj Quantum Inf. **6**, 10 (2020).

[33] N. H. Stair, R. Huang, and F. A. Evangelista, J. Chem. Theory Comput. **16**, 2236 (2020).

[34] L. Xu, J. T. Lee, and J. K. Freericks, http://arxiv.org/abs/2001.06957v1 .

[35] H.-Y. Huang, R. Kueng, and J. Preskill, http://arxiv.org/abs/2002.08953v1 .

[36] K. Mitarai, Y. O. Nakagawa, and W. Mizukami, Phys. Rev. Research **2**, 013129 (2020).

[37] J. Larson, M. Menickelly, and S. M. Wild, Acta Numer. **28**, 287 (2019).

[38] D. A. Mazziotti, ed., *Reduced-Density-Matrix Mechanics: With Application to Many-Electron Atoms and Molecules* (John Wiley & Sons, Inc., 2007).

[39] A. J. Coleman and V. I. Yukalov, *Reduced Density Matrices: Coulson's Challenge* (Springer Berlin Heidelberg, 2000).

[40] F. Colmenero and C. Valdemoro, Phys. Rev. A **47**, 979 (1993).

[41] H. Nakatsuji and K. Yasuda, Phys. Rev. Lett. **76**, 1039 (1996).

[42] K. Yasuda and H. Nakatsuji, Phys. Rev. A **56**, 2648 (1997).

[43] D. A. Mazziotti, Phys. Rev. A **57**, 4219 (1998).

[44] D. A. Mazziotti, Chem. Phys. Lett. **289**, 419 (1998).

[45] D. A. Mazziotti, Phys. Rev. A **60**, 4396 (1999).

[46] D. A. Mazziotti, J. Chem. Phys. **116**, 1239 (2002).

[47] R. M. Erdahl, in *Reduced-Density-Matrix Mechanics: With Application to Many-Electron Atoms and Molecules* (John Wiley & Sons, Inc., 2007) pp. 61–91.

[48] D. A. Mazziotti, Phys. Rev. Lett. **97**, 143002 (2006).

[49] D. A. Mazziotti, Phys. Rev. A **76**, 052502 (2007).

[50] D. A. Mazziotti, J. Chem. Phys. **126**, 184101 (2007).

[51] D. A. Mazziotti, Phys. Rev. A **75**, 022505 (2007).

[52] A. E. Rothman, J. J. Foley, and D. A. Mazziotti, Phys. Rev. A **80**, 052508 (2009).

[53] G. Gidofalvi and D. A. Mazziotti, Phys. Rev. A **80**, 022507 (2009).

[54] A. M. Sand and D. A. Mazziotti, J. Chem. Phys. **143**, 134110 (2015).

[55] D. R. Alcoba, C. Valdemoro, L. M. Tel, E. Perez-Romero, and O. B. Ona, J. Phys. Chem. A **115**, 2599 (2011).

[56] D. Mukherjee and W. Kutzelnigg, J. Chem. Phys. **114**, 2047 (2001).

[57] T. Yanai and G. K.-L. Chan, J. Chem. Phys. **124**, 194106 (2006).

[58] C. Li and F. A. Evangelista, J. Chem. Phys. **144**, 164114 (2016).

[59] S. E. Smart, P. G. Scrape, L. J. Butler, and D. A. Mazziotti, J. Chem. Phys. **149**, 024302 (2018).

[60] A. W. Schlimgen and D. A. Mazziotti, J. Phys. Chem. A **121**, 9377 (2017).

[61] E. J. Sturm and D. A. Mazziotti, Mol. Phys. **114**, 335 (2016).

[62] J. W. Snyder and D. A. Mazziotti, Phys. Chem. Chem. Phys. (2011).

[63] J. W. Snyder and D. A. Mazziotti, J. Chem. Phys. **135**, 024107 (2011).

[64] L. Greenman and D. A. Mazziotti, J. Chem. Phys. **134**, 174110 (2011).

[65] J. W. Snyder, A. E. Rothman, J. J. Foley, and D. A. Mazziotti, J. Chem. Phys. **132**, 154109 (2010).

[66] D. A. Mazziotti, J. Phys. Chem. A **112**, 13684 (2008).

[67] D. A. Mazziotti, Phys. Rev. A **69**, 012507 (2004).

[68] D. A. Mazziotti, Reduced-density-matrix Mechanics - with Application to Many-electron Atoms and Molecules **134**, 331 (2007).

[69] M. A. Nielsen and I. L. Chuang, *Cambridge University Press* (Cambridge University Press, Cambridge, 2010).

[70] P. Jordan and E. Wigner, Zeitschrift für Physik **47**, 631 (1928).

[71] J. Nocedal and S. Wright, *Numerical Optimization* (Springer-Verlag GmbH, 2006).

[72] D. A. Mazziotti, Phys. Rev. Lett. **108**, 263002 (2012).

[73] C. Schilling, D. Gross, and M. Christandl, Phys. Rev. Lett. **110**, 040404 (2013).

[74] M. Piris, Phys. Rev. Lett. **119**, 063002 (2017).

[75] J. M. Montgomery and D. A. Mazziotti, Journal of Chemical Education **97**, 3658 (2020).

[76] Q. Sun, T. C. Berkelbach, N. S. Blunt, G. H. Booth, S. Guo, Z. Li, J. Liu, J. D. McClain, E. R. Sayfutyarova, S. Sharma, S. Wouters, and G. K.-L. Chan, Wiley Interdisciplinary Reviews: Computational Molecular Science **8**, e1340 (2018).

[77] Q. Sun, Journal of Computational Chemistry **36**, 1664 (2015).

[78] Q. Sun, J. Yang, and G. K.-L. Chan, Chemical Physics Letters **683**, 291 (2017).

[79] G. Aleksandrowicz, T. Alexander, P. Barkoutsos, L. Bello, Y. Ben-Haim, D. Bucher, F. J. Cabrera-Hernádez, J. Carballo-Franquis, A. Chen, C.-F. Chen, J. M. Chow, A. D. Córcoles-Gonzales, A. J. Cross, A. Cross, J. Cruz-Benito, *et al.*, "Qiskit: An open-source framework for quantum computing," (2019).

[80] S. E. Smart and D. A. Mazziotti, , 1 (2020), arXiv:2008.06027 .

[81] J. Koch, T. M. Yu, J. Gambetta, A. A. Houck, D. I. Schuster, J. Majer, A. Blais, M. H. Devoret, S. M. Girvin, and R. J. Schoelkopf, Phys. Rev. A **76**, 042319 (2007).

[82] J. M. Chow, A. D. Córcoles, J. M. Gambetta, C. Rigetti, B. R. Johnson, J. A. Smolin, J. R. Rozen, G. A. Keefe, M. B. Rothwell, M. B. Ketchen, and M. Steffen, Phys. Rev. Lett. **107**, 080502 (2011).

CHAPTER 10

RESOLVING CORRELATED STATES OF BENZYNE ON A QUANTUM COMPUTER WITH AN ERROR-MITIGATED QUANTUM CONTRACTED EIGENVALUE SOLVER

Material from: Smart, S. E., Boyn, J.-N., & Mazziotti, D. A. (2022). Resolving correlated states of benzyne with an error-mitigated contracted quantum eigensolver. Physical Review A, 105 (2) 022405

10.1 Introduction

The simulation of many-body quantum systems is a key application for near-term quantum computing [1–4]. The complexity of these simulations is such that algorithms on even moderately sized quantum devices—tens of qubits—with sufficient error mitigation will likely be competitive with existing classical methods [5–8]. A particular instance is the simulation of strongly correlated molecular systems, such as occur in many chemical reactions, transition-metal complexes, energetically degenerate processes, and solid-state materials [9–11]. These systems, which often cannot be treated consistently with perturbative or polynomially scaling approaches relying on a single determinant, are ideal candidates for realizing an advantage from the use of quantum computers in lieu of classical computers, known as quantum advantage. Realizing such as advantage, however, requires algorithms that are optimal for quantum computers in terms of state preparation, measurement, and error mitigation for the noise present in near-to-intermediate-term devices [12, 13].

Various variational quantum eigensolvers (VQE) for molecular simulation exist [14–21], most of which attempt to minimize the energy of a parameterizable ansatz against the Schrödinger equation. An alternative family of algorithms known as contracted quantum eigensolvers (CQE) [22], involves minimizing the residual of a projection (or contraction) of

the N-electron Schrödinger equation onto the space of two electrons, known as the contracted Schrödinger equation (CSE) [23–30]. Closely connected to classical reduced density matrix theory, the CQE has several key features that are favorable to efficient quantum molecular simulations. First, the solution of the CSE, it has been shown, produces an exact, rapidly convergent parametrization of the wave function from a product of only two-body exponential transformations [31, 32]. Furthermore, solution of the anti-Hermitian part of the CSE, known as the anti-Hermitian CSE (ACSE) [33–36], can yield a parameterization of the wave function in terms of two-body unitary transformations [33, 35], which is theoretically exact [37] and readily implementable through unitary gates for state preparation on a quantum computer. Second, the residual of the ACSE yields the gradient of the energy with respect to two-body unitary transformations, which allows for more efficient optimization on quantum computers than derivative-free schemes [14, 38–41] that could be limited to hundreds of parameters. Indeed, recent work by our group introduced a CQE algorithm which can solve the ACSE efficiently on a quantum computer [22].

Solution of the ACSE for the 2-RDM on classical computers has been applied to treating both ground and excited states of strongly correlated molecules including non-trivial conical intersections [35, 42–48]. The solution of the ACSE on quantum computers—a CQE algorithm or quantum ACSE—can potentially avoid the approximate reconstruction of the three-particle RDM (3-RDM) from the 2-RDM through preparation of the wave function on the quantum computer in polynomial time [49]. The quantum ACSE also shares certain similarities with the methods that attempt to decoupled and expand the single exponential unitary coupled cluster (UCC) ansatz [50, 51], such as the adaptive derivative-assembled pseudo-trotterization VQE (ADAPT-VQE) method [52]. The quantum ACSE circumvents issues of the trotterization of the ansatz (necessary for an exact exponential expression) and high variational cost involved in an update step, and contains a natural selection of a pool of unitary transformations through the elements of the ACSE. Moreover, because the ACSE

generates the 2-RDM, it is readily combined with error mitigation strategies that correct the N-representability of the 2-RDM. With its theoretical advantages and promising computational results, the ACSE method provides a potentially flexible framework for molecular simulation on quantum computers.

In the present work we apply the quantum ACSE solver to resolve the relative ground-state energies of the correlated isomers of benzyne on a superconducting quantum computer. The *ortho*-, *meta*-, and *para*-benzyne (C_6H_4) isomers contain non-trivial electron correlation, especially *para*-benzyne which is a biradical [53–58]. The computed relative energies are accurate to less than 0.005 hartrees, and the natural-orbital occupations reflect the differences in electron correlation among the isomers. The accuracy of the results demonstrates the benefits of both the solver and the error mitigation strategies. Because these strategies are general, they can be applied to larger, more correlated molecules and represent a step towards performing strongly-correlated calculations on a quantum computer

10.2 Theory

In this section we review the theoretical framework for the quantum ACSE algorithm [22], and explore the error mitigation schemes necessary for the calculation, including the use of N-representability conditions for the purification of the measured 2-RDM[59, 60].

10.2.1 Quantum Solver of the Anti-Hermitian Contracted Schrödinger Equation

For a many-electron system the two-electron contracted Schrödinger equation [23–30] is

$$\langle \Psi | \hat{a}_i^\dagger \hat{a}_j^\dagger \hat{a}_l \hat{a}_k \hat{H} | \Psi \rangle = E \; {}^2D_{kl}^{ij}, \tag{10.1}$$

where ${}^2D$ is the 2-RDM, $\hat{a}_i^\dagger$ and $\hat{a}_i$ are creation and annihilation operators for a spin orbital i, and $\hat{H}$ is the Hamiltonian operator that is given by

$$\hat{H} = \sum_{pqrs} {}^2K_{st}^{pq} \hat{a}_p^\dagger \hat{a}_q^\dagger \hat{a}_t \hat{a}_s, \tag{10.2}$$

in which ${}^2K$ is the reduced Hamiltonian matrix containing the one- and two-electron integrals. Taking the anti-Hermitian part of Eq. (10.1) produces the ACSE [33–35, 46, 47]:

$$\langle \Psi | [\hat{a}_i^\dagger \hat{a}_j^\dagger \hat{a}_l \hat{a}_k, \hat{H}] | \Psi \rangle = 0, \tag{10.3}$$

which depends upon not only the 2-RDM but also the 3-electron RDM (3-RDM) (see Refs. [34, 61, 62] and Appendix 10.6.2). The residual of the ACSE is equal to the gradient of the energy with respect to two-body unitary transformations, and hence, the residual of the ACSE vanishes if and only if the gradient vanishes. Consequently, the ACSE provides a framework for the iterative optimization of a product of two-body unitary transformations on a reference wave function, which leads to the quantum ACSE algorithm presented in Figure 10.1.

Let $|\Psi_n\rangle$ be the n-th iteration of the wave function, where ${}^2D_0$ is the 2-RDM of the initial Hartree-Fock state $|\Psi_0\rangle$. The 2-RDM of the $(n+1)$-th iteration is

$${}^2D_{n+1}^{pq;st} = \langle \Psi_n | e^{-\epsilon_n \hat{A}_n} \hat{a}_p^\dagger \hat{a}_q^\dagger \hat{a}_t \hat{a}_s e^{\epsilon_n \hat{A}_n} | \Psi_n \rangle, \tag{10.4}$$

where ϵ_n is theoretically an infinitesimal step and ${}^2\hat{A}_n$ is an anti-Hermitian operator

$${}^2\hat{A}_n = \sum_{ijkl} {}^2A_n^{ij:kl} \hat{a}_i^\dagger \hat{a}_j^\dagger \hat{a}_l \hat{a}_k. \tag{10.5}$$

The energy at each iteration is computable from the 2-RDM

$$E_{n+1} = \sum_{pqst} {}^2K_{st}^{pq}\ {}^2D_{n+1}^{pq;st}. \tag{10.6}$$

Elements of the ${}^2A_n$ matrix can be selected [34] as the residual of the ACSE

$${}^2A_n^{ij;kl} = \langle \Psi_n | [\hat{a}_i^\dagger \hat{a}_j^\dagger \hat{a}_l \hat{a}_k, \hat{H}] | \Psi_n \rangle, \tag{10.7}$$

which is effective because the ACSE's residual is related to the gradient of the energy with respect to the elements of ${}^2A_n$

$$\langle \Psi_n | [\hat{a}_i^\dagger \hat{a}_j^\dagger \hat{a}_l \hat{a}_k, \hat{H}] | \Psi_n \rangle = -\frac{1}{\epsilon_n} \frac{\partial E_{n+1}}{\partial\ {}^2A_n^{ij;kl}} + O(\epsilon_n). \tag{10.8}$$

Hence, by using the residual, we are choosing a search direction that maximizes the change in the energy for small ϵ_n. The ACSE can be expressed in terms of the 2- and 3-RDMs and can be evaluated classically with an $O(r^6)$ cost using a reconstructed 3-RDM in which r is the rank of the one-electron basis set. On a quantum computer, we can obtain elements of ${}^2A_n$ in a potentially more efficient manner without the reconstructed 3-RDM. Define an auxiliary 2-RDM:

$${}^2_{\pm}\Lambda_n^{ij;kl} = \langle \Psi_n | e^{\mp i\delta \hat{H}} \hat{a}_i^\dagger \hat{a}_j^\dagger \hat{a}_l \hat{a}_k e^{\pm i\delta \hat{H}} | \Psi_n \rangle, \tag{10.9}$$

in which the n-th wave function is propagated through a time-like step δ in the forward or reverse direction. Then, we can obtain elements of the residual from tomography of these auxiliary RDMs with $O(r^4)$ scaling:

$${}^2A_n^{ij;kl} = \frac{1}{2i\delta}({}^2_{+}\Lambda_n^{ij;kl} - {}^2_{-}\Lambda_n^{ij;kl}) + O(\delta^2). \tag{10.10}$$

These equations suggest an iterative approach to finding a solution of the ACSE, which is

depicted in Fig. 10.1. After initializing the wave function and 2-RDM, for a given iteration we construct the operator ${}^2A$ through classical or quantum approaches, prepare and measure ${}^2D_{n+1}$ (possibly optimizing ϵ_n and carefully selecting elements of ${}^2A_n$ to include in the wave function), and iterate between ${}^2D_n$ and ${}^2A_n$ until $||{}^2A_n||$ is less than a certain threshold.

In the classical-computing algorithm the solution of the ACSE requires an approximate reconstruction of the 3-RDM from the 2-RDM through a cumulant expansion [61, 63, 64] to compute the 2-RDM without the wave function. In the quantum-computing algorithm, in contrast, the wave function is prepared with polynomial scaling, and hence, approximate reconstruction of the 3-RDM is not necessary. A hybrid quantum-classical approach exists as well, where we prepare the wave function and measure the RDMs on the quantum computer but evaluate the ACSE for the residual (gradient) on the classical computer. In the noiseless limit the ACSE can be solved by the quantum-computing algorithm to an arbitrary level of accuracy. The errors arising from the expansion in Eq. (6) are controllable with respect to δ. Computationally, we find in the noiseless limit that the solution of the ACSE yields a wave function, parameterized by two-body unitary transformations, that solves not only the ACSE but also the N-electron Schrödinger equation.

Finally, several variations of the algorithm are possible for practical implementations on quantum computers. For example, a limited portion of ${}^2A_n$, such as its largest terms, can be used; a stochastic gradient or reduced gradient sampling technique can be implemented, lowering the measurement cost of ${}^2\Lambda_n$ at each step. The quantum and classical methods can be combined where direct quantum tomography is only employed for the parts of the 2-RDM that are strongly correlated.

10.2.2 Quantum Computation

In this work we utilize the QACSE method and generate ${}^2D_n$ on the quantum computer, and obtain elements of ${}^2A_n$ on the quantum computer for the smaller qubit calculations

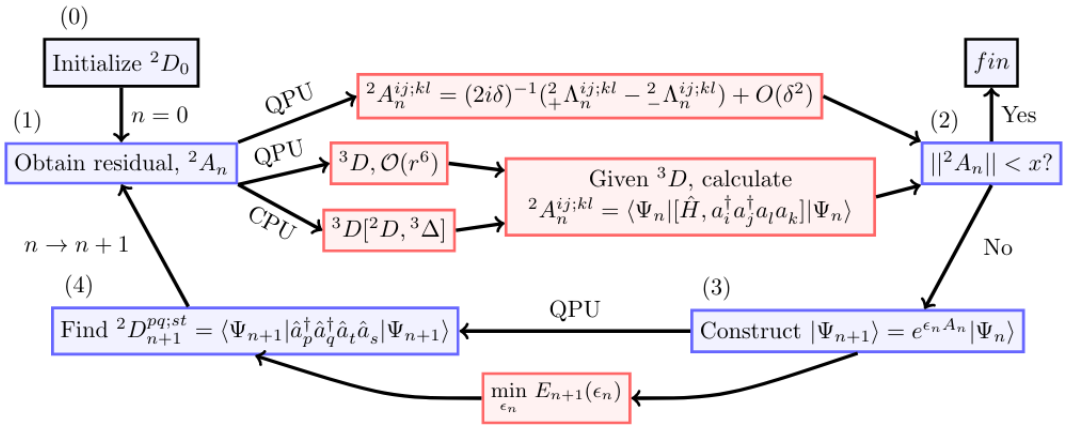

Figure 10.1: The quantum-ACSE algorithm. After initializing the state (0), we begin an iterative process of obtaining the ${}^2A$ elements (1) using a quantum (QPU) or classical (CPU) processor, which will have errors in the series expansion ($O(\delta^2)$), a higher measurement cost ($O(r^6)$), or errors from the 3-electron reduced cumulant matrix (${}^3\Delta$). After checking for convergence against a threshold x (2), we construct the next ansatz (3), and optionally perform a classical minimization against the step size. Finally, we measure the new 2-RDM (4), and proceed to (1) until we converge or $n = n_{\text{max}}$.

(Eq. 10.10), and classically with a reconstructed 3-RDM for the larger qubit calculations (Eq. 10.8). Figure 10.2 provides an overview of the process to obtain a fully error mitigated ${}^2D_n$. We also include details related to the specific techniques and other aspects of the calculation in Appendix 10.6.2.

To obtain ${}^2D_n$, at a given step, we first transform the ${}^2A_n$ operator into a suitable form for the quantum computer (including our qubit reduction scheme). Explicitly, this is done through a first order trotterization of the exponential of Eq. (5), where each element of the ${}^2A_n$ matrix is implemented separately. However, because we would like to avoid implementing all the operators at once, we use an element threshold to determine inclusion in the ansatz. To implement the gate sequence, we prepare and manually simplify the set of 2-RDM operators corresponding with possible elements of ${}^2A_n$. These are assembled according to our inclusion criteria, and then the circuits are run. After measurement, we apply a filter (via construction and inversion of a state transition matrix, referred to as SPAM) and then apply a projection into the proper number and projected spin space ($N \in \{2, 4\}$, $S_z = 0$)

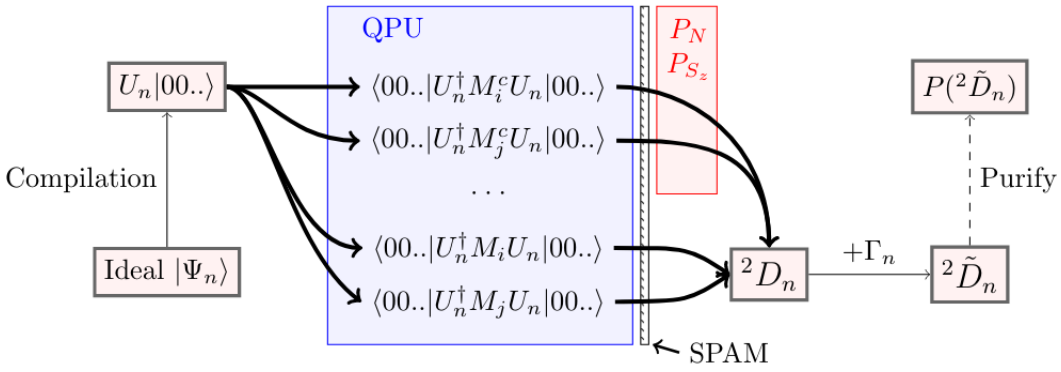

Figure 10.2: Error mitigation scheme to obtain corrected 2-RDMs. We first take a set of instructions, and construct the appropriate circuit design. We run these on the quantum computer to obtain a set of measurement results which are then corrected through the inversion of a state preparation matrix (SPAM, small hatched rectangle). Measurements corresponding to diagonal elements of the 2-RDM (M_i^c) will commute with the $\hat{N}$ and $\hat{S}_z$ symmetries, and so are projected onto the proper operator space. We then apply our shift correction, Γ_n, which also preserves trace but can introduce negative eigenvalues, and optionally, a purification of the 2-RDM.

for measurements which commuted with these operators (which are Z_i type measurements). In some cases we then apply our limit-preserving correction Γ_n to the ansatz (see below), followed by an optional purification of the 2-RDM.

To our knowledge, the penultimate error mitigation technique has not been used elsewhere, and the final technique was recently introduced for quantum simulations [60] but not yet demonstrated experimentally, and so we briefly detail them here. The first is a correction targeting errors in an iterative ansatz that arise simply from adding extra gates, whereas the second is an expansion of techniques related to ensuring the physicality of the measured RDM through $N-$representability constraints.

10.2.3 Limit-Preserving Correction for an Iterative Ansatz

To compensate for errors which occur at each step due to the increasing the number of gates in an iterative scheme, we present an error mitigation strategy which we call a limit-preserving

correction or a ${}^2\Gamma$-correction. Consider the n-th iteration of the QACSE algorithm. Given the elements of ${}^2A_n$, we can consider the $(n+1)$-th 2-RDM as a function of ϵ_n as it approaches 0 from the positive direction:

$$
\begin{aligned}
{}^2D^{pq;st}_{n+1}(0^+) &= \lim_{\epsilon_n \to 0^+} {}^2D^{pq;st}_{n+1}(\epsilon_n) && (10.11)\\
&= {}^2D^{pq;st}_{n}(\epsilon_{n-1}) + \lim_{\epsilon_n \to 0^+} \epsilon_n \langle \Psi_n | [a_p^\dagger a_q^\dagger a_t a_s, {}^2\hat{A}_n] | \Psi_n \rangle. && (10.12)
\end{aligned}
$$

While this quantity theoretically approaches ${}^2D_n(\epsilon_{n-1})$ as $\epsilon_n \to 0^+$, in practice the discrete unitary gates are subject to substantial noise on current-to-intermediate-term quantum computers and hence, do not collapse to the identity operator for any actual gate sequence. The noise channels in general will contract the set of possible 2-RDMs (e.g., for systems with strong depolarizing errors this is to a fully depolarized 2-RDM). For our system, this can lead to a result that any energy obtained will be higher than the energy of the previous step (see Appendix 10.6.3 for an example). In these instances, the change in energy due to noise is greater than any change from the optimization.

Let ${}^2\Gamma_n$ be a matrix of the same rank as the 2-RDM, and ${}^2\tilde{D}_n(\epsilon_n)$ be the corrected 2-RDM. Then we define a correction by the following system of equations:

$$
\begin{aligned}
{}^2\tilde{D}_{n+1}(\epsilon_n) &= {}^2D_{n+1}(\epsilon_n) + \sum_{i=0}^{n} {}^2\Gamma_i && (10.13)\\
{}^2\Gamma_n &= {}^2D_n(\epsilon_{n-1}) - {}^2D_{n+1}(0^+), && (10.14)\\
{}^2D_0 &= {}^2D_{\mathrm{HF}}. && (10.15)
\end{aligned}
$$

Eq. (10.13) defines the error mitigated 2-RDM at each step. The ${}^2\Gamma_n$ in Eq. (10.14) is the difference between the new state with $\epsilon_n = 0^+$ and the previous state. Eq. (10.15) gives the initial condition of the system. The correction helps to avoid noise-related barriers in the optimization surface (as ${}^2\tilde{D}_{n+1}(0^+) = {}^2D_n(\epsilon_{n-1})$), allowing us to reach 2-RDMs that are

normally inaccessible due to the noise. For a noise-free simulation, we also have that ${}^2\Gamma_n = 0$ for all n, ensuring that we would maintain the exact result on a perfect quantum computer. We use the corrected 2-RDM ${}^2\tilde{D}_{n+1}$ throughout the optimization in evaluating the energy as well as choosing the elements of ${}^2A_{n+1}$. While the gradient information reflected in ${}^2A$ around ${}^2D$ and ${}^2\tilde{D}$ will not be the same when ${}^2\Gamma$ is large, because we are optimizing $E[{}^2\tilde{D}_n]$, and because we generate ${}^2A_n$ with Eq. (10.8), this is the appropriate choice. If we were to use Eq. (10.10) instead, then we would obtain information around ${}^2D_n$, and would have to correct ${}^2A$ as well.

There are a number of practical considerations in the implementation of the ${}^2\Gamma$-correction such as the potential variability of the noise. Because we are adding RDMs with separate uncertainties, the uncertainty in the result increases (if we assumed independent ${}^2\Gamma_i$ with equal standard deviations σ, this would be $\sqrt{n}\sigma$ after n iterations), which may require us to increase the sampling of ${}^2\Gamma_i$. The errors affecting the quantum computer may exhibit a time dependence on the order of the run time. To avoid this possibility, we run the results as contiguously as possible with the total number of iterations n being kept relatively low (for all instances $n \leq 5$). Additionally, the 2-RDM is purified in some cases to ensure that the negative eigenvalues of the 2-RDM and the related 2-hole and particle-hole RDMs (see next section) are eliminated. Regardless, we find this error mitigation strategy to be necessary to obtain meaningful results within the context of an iterative ansatz.

10.2.4 Purification of the 2-RDM

As mentioned above, the effect of noise in a quantum simulation is that measured quantum state might no longer represent a physical system. While we cannot directly assess the purity or fidelity of an RDM, we can "purify" the 2-RDM to ensure that the eigenvalues of the various permutations of the particle and hole reduced density matrices are positive semidefinite, which are necessary criteria for a pure-state or ensemble N-representable 2-

RDM [65]. A matrix is positive semidefinite if and only if its eigenvalues are nonnegative. For instance, for the 2-RDM, the 2-particle (${}^2D$), 2-hole (${}^2Q$), and particle-hole (${}^2G$) matrices must have nonnegative probabilities, and hence, must be positive semidefinite in a set of conditions known as the 2-positivity (or DQG) conditions [59, 66–68]

$$ {}^2D \succcurlyeq 0, \tag{10.16} $$

$$ {}^2Q \succcurlyeq 0, \tag{10.17} $$

$$ {}^2G \succcurlyeq 0, \tag{10.18} $$

where the elements of these metric matrices are given by

$$ {}^2D^{ij}_{kl} = \langle \Psi | \hat{a}^\dagger_i \hat{a}^\dagger_j \hat{a}_l \hat{a}_k | \Psi \rangle, \tag{10.19} $$

$$ {}^2Q^{kl}_{ij} = \langle \Psi | \hat{a}_k \hat{a}_l \hat{a}^\dagger_j \hat{a}^\dagger_i | \Psi \rangle, \tag{10.20} $$

$$ {}^2G^{il}_{kj} = \langle \Psi | \hat{a}^\dagger_i \hat{a}_l \hat{a}^\dagger_j \hat{a}_k | \Psi \rangle. \tag{10.21} $$

We accomplish the purification by semidefinite programming, which allows us to minimize an function of a matrix subject to linear constraints while ensuring that the matrix remains positive semidefinite [69–71]. The general method was developed by one of the authors for reconstructing noisy processes for quantum tomography [59], and was more recently applied in the context of quantum simulation by Rubin et al. [60].

The objective in this work is to create a purified 2-RDM, ${}^2D_{\mathrm{SDP}}$, which minimizes the norm of the error matrix $E = {}^2D - {}^2D_{\mathrm{SDP}}$, subject to the constraints (DQQ) ensuring that ${}^2D_{\mathrm{SDP}}$ represents a physical system. To express this as a semidefinite program, we take F to be a matrix of free variables, and then minimize the trace of the following block matrix:

$$ \begin{pmatrix} I & E \\ E^\dagger & F \end{pmatrix} \succcurlyeq 0. \tag{10.22} $$

Taking the determinant of the 2×2 block matrix allows us to relate the trace of F to the Frobenius norm, providing a semidefinite relaxation for the minimization problem. The DQG constraints can be expressed in a block-diagonal form:

$$\begin{pmatrix} {}^2D & 0 & 0 \\ 0 & {}^2Q & 0 \\ 0 & 0 & {}^2G \end{pmatrix} \succcurlyeq 0. \tag{10.23}$$

These semidefinite conditions, the linear mappings between the metric matrices, and the trace of the 2-RDM define the constraints in the SDP. To solve the SDP, we use a boundary-point algorithm for the direct variational calculation of the 2-RDM [71–74]. The algorithm for purification of the 2-RDM with the DQG conditions has a scaling of $O(r^6)$.

10.3 Benzyne Calculations

In this work we use the QACSE method to investigate the ortho-, meta-, and para- isomers of benzyne, which may be obtained via the elimination of two substituents in the relevant positions of the benzene ring. Owing to their versatility as reactive intermediates in biological processes, derivatives of the isomeric benzynes have been the subject of a growing interest in the synthetic research community in the development of biomimetic reactions [75], such as the Diels-Alder reaction [76] and in so-called "click chemistry" [77], with a wide range of applications to the synthesis of heterocycles [78] and natural products [76]. Even though biradicals such as benzyne play key roles across synthetic and materials chemistry, making their accurate theoretical description quintessential to the understanding of chemical processes, their exact treatment continues to pose a challenge to electronic structure theory [53, 54]. Details regarding the electronic structure treatment of these systems are included in Appendix 10.6.1.

Figure 10.3 shows the structures for each of the three isomers, as well as the occupa-

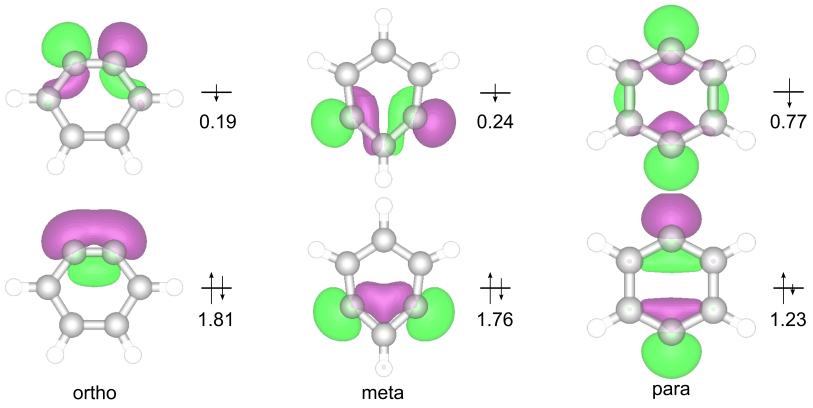

Figure 10.3: Molecular orbital diagram and natural-orbital occupations of the highest and occupied lowest natural orbitals for ortho-, meta-, and para-benzyne. Geometries for the ortho- and meta- isomers were obtained from reference [80] and optimized with spin-flip time dependent density functional theory (SF-TDDFT), and the para- isomer was obtained from reference [81] and optimized with spin-flip coupled cluster with singles and doubles (SF-CCSD).

tions of the highest and lowest occupied natural orbitals. The energetic ordering of the three isomers follows their degree of diradical character, with experimental gas phase heats of formation showing ortho as the energetically lowest isomer, followed by the meta and then para isomers, at energies of 10 ± 3 kcal/mol and 22 ± 3 kcal/mol relative to the ortho reference, respectively [79]. The variations in ground-state energy and diradical character are driven by the degree to which the geometric constraints of the given isomer allow for overlap between the singly occupied carbon-p orbitals, which is demonstrated by the electron densities of the highest occupied natural orbital (HONO) and the lowest unoccupied natural orbital (LUNO), shown in Fig. 10.3. In the ortho isomer, adjacency of the singly occupied orbitals allows for good overlap and energetically favorable formation of a bond with significant π character, giving this isomer C-C triple bond character. While somewhat compensated by geometric distortion, driven by the greater C-C radical distance the magnitude of this bonding interaction is reduced in the meta isomer, and essentially diminished in the para geometry, where no overlap between the lobes of the carbon-based radical orbitals is geometrically feasible.

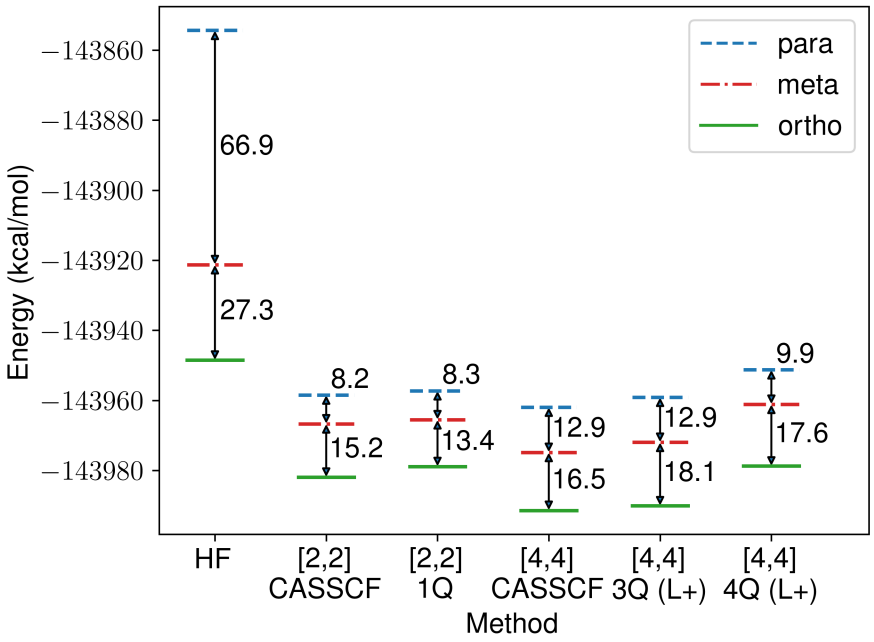

Figure 10.4: Overview of results shows active space calculations for the different configurations of benzyne across several methods, including Hartree-Fock, CASSCF, and QACSE for [2,2] and [4,4] active spaces. The 3- and 4-qubit results utilize the limit-preserving correction (L) and purification (+) schemes of error mitigation. The data corresponds with results taken in Table 10.1.

Besides the relative ground-state energies, the singlet-triplet gaps of these isomers are well documented experimentally and are used for benchmarking multi-reference electronic structure methods [53, 54, 57]. In this work we focus on resolving the differing degrees of correlation present solely in the ground-state 2-RDMs. As the radical electrons are localized in orbitals perpendicular to the π-system, a minimal [2,2] active space is sufficient to describe the multi-reference correlation in these systems and the inclusion of additional orbitals solely results in the recovery of additional dynamic correlation. A recently published companion work utilizes these results as the kernel for a classical calculation that includes dynamic correlation effects from orbitals beyond the active space [82]. The inclusion of these orbitals as well as larger basis sets is necessary for more rigorous experimental comparisons. An exploration of the singlet-triplet gaps is the goal of future work.

The relative energies from the complete active space self-consistent field method (CASSCF) and from the quantum calculations are listed in Table 10.1 and Figure 10.3 for the [2,2] and [4,4] active spaces where the notation [X,Y] denotes X electrons in Y orbitals. The CASSCF calculations optimize the active electrons and orbitals in the mean-field of the remaining electrons and orbitals. The target CASSCF results yield the correct ordering, although each gap is slightly higher than experimental values. For the [2,2] case, the meta and para energies relative to ortho are 15 and 23 kcal/mol, respectively. For the [4,4] active space, the meta and para energies relative to the ortho configuration are 13 and 29 kcal/mol respectively. The [2,2] active space corresponds with a 1-qubit quantum calculation, whereas the [4,4] calculation was performed with 4 and 3 qubits, representing exact and near-exact symmetries respectively (see Appendix 10.6.2, 10.6.2, and 10.6.2). The error mitigation ranges from a simple measurement correction to our full scheme of corrections (denoted L+, or MPL+). M refers to a state preparation and measurement, P to the application of the number projection, L to the use of the $^2\Gamma$-correction, and + to the SDP corrected state. The error in the obtained relative energies on the quantum computer in the [4,4] case is 1.6 kcal/mol (2.6 mhartree) for both the 3-qubit (3Q) and 4-qubit (4Q) cases, whereas for the [2,2] space, we obtain a result within 2 kcal/mol (3 mhartree). The number of unique iterations is between $3-6$, depending on the ansatz developed. The operators in the qubit basis (see Appendix 10.6.2) for the 3-qubit calculations have $0-8$ CNOT gates, while the pool of operators for the 4-qubit operators each have 8-12 CNOT gates.

Finally, the natural-orbital occupation numbers, which are the eigenvalues of the 1-RDM, can help infer the nature and degree of electron correlation in the system. The Hartree-Fock state, corresponding with a single determinant, has eigenvalues of 2 or 0 across all (spatial) orbitals, while a biradical system would exhibit equal occupations of 1 in the highest occupied and lowest unoccupied natural orbitals. We report the natural orbital occupations for the CASSCF and purified results in Table 10.3 for the 1-,3-, and 4-qubit QACSE calcu-

Table 10.1: Relative energies between the configurations of benzyne with classical CASSCF and QACSE methods for differing active spaces and levels of error mitigation, in kcal/mol. [0,0] active space refers to the initial Hartree-Fock calculation. M refers to a state preparation and measurement error, P to the application of the number projection, L to the use of the ${}^2\Gamma_n$-correction, and + to the SDP corrected state.

		Number	Error	$E_{\text{isomer}} - E_{\text{ortho}}$ (kcal/mol)	
Method	[X,Y]	Qubits	Mitigation	meta	para
CASSCF	[0,0]			27.3	94.2
	[2,2]			15.2	23.4
	[4,4]			16.5	29.5
QACSE	[2,2]	1	M	13.4	21.7
	[4,4]	3	MP	19.6	15.4
	[4,4]	3	MPL	32.5	55.7
	[4,4]	3	MPL+	18.1	31.0
	[4,4]	4	MPL	27.1	23.6
	[4,4]	4	MPL+	17.6	27.5
Expt. [79]				10 ± 3	22 ± 3

Table 10.2: Difference in energy between the QACSE methods including various error mitigation schemes and the CASSCF result in millihartrees (mhartree).

	Number	Error	Error Relative to CASSCF (mhartree)		
[X,Y]	Qubits	Mitigation	ortho	meta	para
[2,2]	1	M	4.8	1.9	1.9
[4,4]	3	MP	51.9	43.2	29.5
[4,4]	3	MPL	-53.6	-28.1	-11.8
[4,4]	3	MPL+	2.1	4.6	4.5
[4,4]	4	MPL	-25.9	-9.0	-35.3
[4,4]	4	MPL+	20.2	21.9	17.0

lations. In each case, we see significant differences between the para isomer and the other two isomers (ortho and meta) on the quantum computer. The para-benzene, which does not have any overlapping density between the carbon p orbitals (see Fig. 10.3), exhibits biradical character, whereas the other two configurations exhibit more single-reference character. This is also reflected in the amount of correlation energy recovered ($E_{\text{CASSCF}} - E_{\text{HF}}$) for each configuration (see Fig. 10.3). When compared to the CASSCF occupations, the results for the 3-qubit case were all with 0.09 of the target occupations. In the 4-qubit case the ortho (0.14) and meta (0.19) HONO and LUNO occupations have more significant errors,

which could be expected from the increased absolute energies seen for each of these isomers. By looking at the HONO-1 and LUNO+1 orbitals in the [4,4] space, we also see that the fractional occupations of the HONO and LUNO are not an artifact of error on the quantum computer, as the closeness of the HONO-1 and LUNO+1 occupations to 2 and 0 is maintained.

Table 10.3: Largest natural-orbital occupation numbers for the CASSCF results and the purified, $^2\Gamma$-corrected results for the [2,2] and [4,4] active spaces on the quantum computer. In each case, the para-benzyne solution exhibits biradical character in the highest occupied and lowest unoccupied natural orbitals, though to differing degrees based on the method.

		Number		Orbital Occupations		
Method	[X,Y]	Qubits	Orbital	ortho	meta	para
CASSCF	[2,2]		HONO	1.811	1.712	1.232
	[2,2]		LUNO	0.189	0.288	0.768
QACSE	[2,2]	1	HONO	1.695	1.604	1.127
	[2,2]	1	LUNO	0.305	0.396	0.873
CASSCF	[4,4]		HONO−1	1.947	1.977	1.981
	[4,4]		HONO	1.813	1.756	1.235
	[4,4]		LUNO	0.187	0.244	0.765
	[4,4]		LUNO+1	0.053	0.023	0.019
QACSE	[4,4]	3	HONO−1	1.956	1.976	1.992
	[4,4]	3	HONO	1.851	1.761	1.148
	[4,4]	3	LUNO	0.149	0.239	0.852
	[4,4]	3	LUNO+1	0.045	0.012	0.008
QACSE	[4,4]	4	HONO−1	1.973	1.985	1.956
	[4,4]	4	HONO	1.938	1.570	1.200
	[4,4]	4	LUNO	0.054	0.433	0.790
	[4,4]	4	LUNO+1	0.036	0.012	0.055

10.4 Discussion

The results of these benzyne calculations highlight the potential for quantum simulation on near-term devices, particularly with quantum RDM methods and error mitigation tools designed for RDMs. Though work in our group and elsewhere has investigated and obtained highly accurate results for small systems or particular configurations of electrons (namely in taking advantage of pure N-representability constraints) [4, 20, 83], this work represents a

step towards more general quantum computing algorithms based on RDM theory. Indeed, the [4,4] active space represents an important step from model systems and minimal cases towards the end goal of robustly treating strongly correlated many-body systems. These results also demonstrate a useful classical-quantum hybrid approach, incorporating elements from both classical and quantum techniques.

With regards to the number of iterations and the variational cost, for many systems, including the benzyne isomers, the QACSE method is consistently able to recover a large part of the correlation energy within a few iterations. While we also evaluated derivative-free 1-dimensional optimizers that might be able to help in a noisy landscape [14, 20, 39], practically, the trust-region optimization combined with a rejection criteria provides a reliable way of choosing a step size for Eq. (4), and making sure that convergence progresses as a whole. The rejection criteria in particular eliminate iterations which do not contribute to the ansatz properly with an optional reevaluation of the last ${}^2A_n$ step. This helps in particular with overcoming instances where the errors in the gradient are too large to take a meaningful step. It is also worth mentioning that the experiment requirements for convergence and termination of the method are different from ideal conditions. While lowering the residuals of the ACSE is ideal, and ensures a properly converged state, noise will combat the ability of actually reaching a meaningful RDM. Because of the limitations of noise, in the present multi-qubit examples the ${}^2A$ matrix is updated by a classical algorithm with reconstruction of the 3-RDM rather than the quantum algorithm shown in Eq.(10.10). In these instances, error from reconstruction of the 3-RDM is lower than the error from the noise on the quantum devices. Importantly, the classical and quantum algorithms can be interchanged depending upon the complexity of the circuit and the level of noise on a given device.

These results highlight the necessity of different error mitigation schemes. The qubit reduction technique allows for significant simplification of the problem (although not to a trivial degree for the [4,4] case), as well as different thresholds of accuracy. It is somewhat

known that with the Jordan-Wigner transformation and r spatial orbitals, for molecular systems one can always find two Z symmetries of length r, corresponding to the constant parity of the α and β sets of orbitals in a N and S_z preserving simulation, which reduces the number of qubits to $2r - 2$ (similar to ideas covered elsewhere[3, 84]). Applying additional symmetries from the Hamiltonian is exact, with the limitation that the final and initial states share the same symmetries. For systems with near-symmetries (symmetries existing in a modified Hamiltonian), elimination of small nonzero elements can help to find these symmetries (see Appendix 10.6.2). In general, further tapering of a state to a symmetry that does not exactly commute with the Hamiltonian will constrain the state space, yielding an approximation to the eigenstate.

To further motivate this, we can consider the symmetry constrained state as an approximation to the full state. Within quantum chemistry numerous approximations are commonly made based on available computational resources, such as the use of finite basis sets, the separation of nuclear and electronic motion, and the truncation of the manifold of excitations.[9] On a quantum computer a significant consideration is the level of noise generated in a preparation and measurement from the complexity of the circuits. In the context of NISQ systems, a theoretically lower quality ansatz can produce a better result than a higher quality, or even exact, ansatz if the added noise offsets the improvement in accuracy from the theoretically superior ansatz. Additionally, the combination of noise and error mitigation techniques can result in 2-RDMs whose energies are below those from noiseless simulations but above those from an exact calculation in the given basis set. For these reasons, it is not surprising that the 3-qubit case can produce results that are superior to the 4-qubit case with approximate symmetries.

We did not explicitly identify the effect of the measurement errors involving the inversion of the state transition matrix, although these have been documented elsewhere to help improve results on the order of the measurement error. Because incorrectly measured states

can easily lead to different particle states, this can lead to large differences in the obtained energies. However, regardless of the measurement error, the projection of the RDM onto the correct particle number space in the diagonal entries is a critical step. The energetic effect of this correction is system dependent, but can easily be on the order of hartrees. Quite simply put, the results are often not meaningful without this correction, which can also be seen in its success in other work[4, 83]. While it is preferable in theory to correct the diagonal and off-diagonal elements of the 2-RDM, for the latter instances, a measurement sequence which commutes with the particle number operator must be developed. Additionally, this greatly changes the tomography requirements of the 2-RDM, rendering useless the advantages of local measurement commutation. The incremental improvements in the quantum devices over the last year are also critically important, as other devices were tested that did not achieve the same level of results (not reported).

The ${}^2\Gamma$-correction serves indirectly to expand the set of accessible 2-RDMs while preserving the integrity of the iterative optimization. While the application here to an iterative ansatz is unique, the idea at each iteration could be seen as a zeroth-order extrapolative procedure, like the Richardson extrapolation, repeated at each iteration [17, 85]. Instead of attempting a linear or higher order fit to a variable noise strength, we simply add a correction RDM. As a result, we do not have to deal with adjusting how noise is applied in the underlying pulse, and the cost of the mitigation procedure is kept low. Even if at each step we recalculated ${}^2\Gamma$, the number of evaluations would be linear with respect to n. While the implementation here is straightforward, it is likely that this method or variations on it could be applied to other iterative methods in a straightforward manner. In terms of the set of possible RDMs that can be measured, this approach slowly shifts our corrected RDM by ${}^2\Gamma$ through the set of all possible RDMs. Qualitatively, the effect of this strategy on the obtained benzyne energies is to improve the result usually by tens of mhartrees, and in some instances up to 0.1 Hartree. However, as it is possible to move beyond the boundary of the

set of physical RDMs, purification of the RDM is a necessary step, albeit with approximate N-representability conditions. The distance between the ${}^2\Gamma-$corrected 2-RDM and the purified 2-RDM, which is also not consistent, can be used as an exclusionary criteria in the optimization.

Both QACSE and ADAPT-VQE use the ACSE wave function ansatz [31–34] that was developed in the ACSE literature [33–36] . The structure of this wave function—product of unitary two-body exponential operators on a reference wave function—has the ACSE as its stationary equation [31, 34]. The ACSE ansatz is related to the single-term two-body exponential ansatzes [86–93] and the two-body exponential product ansatzes [31, 32], which were investigated in the context of the contracted Schrödinger equation (CSE) [23–30]. Notably, while this wave function has been stated heuristically and called an adaptive generalized unitary coupled-cluster singles and doubles wave function in the ADAPT-VQE literature, its stationary equation is not a coupled cluster equation, and its definition in the ACSE literature significantly predates its recent discussion. In fact, Grimsley *et al.* [52] describe ADAPT-VQE as "not so much an approximation to UCC [unitary coupled cluster] as it is a wholly unique ansatz." From this perspective, by minimizing the ACSE wave function, both QACSE and ADAPT-VQE are seeking solutions of the ACSE–rather than a direct solution of the Schrödinger equation as in VQE, and hence, both can be understood as types of contracted quantum eigensolvers. The distinction between the VQE and CQE is important because the CQE framework informs both the structure of the wave function and its stationary condition.

Although both QACSE and ADAPT-VQE can be viewed as quantum solutions of the ACSE, their motivations and initial implementations have significant differences. Unlike the ADAPT-VQE which optimizes all parameters in the wave function simultaneously in the spirit of the variational principle of the wave function governing VQE, the ACSE takes a greedy, iterative approach in which the wave function is optimized only with respect to

the two-body exponential transformation of the current iteration. This more targeted optimization leads to a contracted stationary condition—the solution of the ACSE, which is a hallmark of the ACSE theory [31–34].

Specifically, the ADAPT-VQE [52] defines a predefined pool of parameterized unitary two-body exponential operators from which the ACSE wave function can potentially be constructed from the reference (Hartree-Fock) wave function. The algorithm improves the trial ACSE wave function at the n^{th} iteration by (*i*) multiplying the $(n-1)^{\text{th}}$ ACSE wave function by the operator from the pool with the largest energy gradient and (*ii*) reoptimizing the energy with respect to all parameters in the pool operators. In contrast, the QACSE does not use a predefined pool of operators but rather computes the residual of the ACSE either from a an efficient quantum measurement of an effective 2-RDM as shown in Eq. (10) or a classical evaluation where the 3-RDM is approximately reconstructed. This generality gives the QACSE additional flexibility, which may become increasingly important in the treatment of larger, more correlated atoms and molecules where a limited operator pool may miss significant correlation effects. Perhaps most importantly, because the QACSE is aiming to satisfy the ACSE rather than the standard variational principle for the wave function, the QACSE does not reoptimize its parameters in previous steps as in part (*ii*) of the ADAPT-VQE algorithm. While a reoptimization phase decreases circuit depth, especially for small molecules, it is not necessary for converging to a solution of the ACSE, and it may require a significantly larger number of energy function and gradient evaluations for larger molecules.

10.5 Conclusions

Molecular simulations on quantum computers have the potential to treat strongly correlated problems that are currently intractable on conventional computers. The practical realization of such simulations, however, requires quantum molecular algorithms that are mappable to transformations, such as products of unitary transformations, that are natural for quan-

tum computers. Here we implement a novel contracted quantum eigensolver (CQE) from a contraction of the Schrödinger equation onto the space of only two electrons, known as the anti-Hermitian contracted Schrödinger equation (ACSE). To make the solution of the ACSE more practical for more realistic chemical problems on quantum computers, we utilize robust error mitigation techniques, including techniques based on N-representability constraints. The solution of the anti-Hermitian CSE (ACSE) through iterative minimization of its residual generates a rapidly convergent product of two-body unitary transformations that is natural for implementation on quantum computers. Furthermore, unlike the solution of the ACSE on the classical computer, the contracted Schrödinger solver on quantum computers can fully or partially remove approximate reconstructions of higher RDMs, and hence, can potentially achieve exact results without the exponential complexity of the many-electron wave function.

The combination of the ACSE solver with robust error mitigation provides a scalable approach to molecular simulations on quantum computers with low circuit depth and few variational parameters. We apply the algorithm to the resolution of the *ortho*-, *meta*-, and *para*-isomers of benzyne C_6H_4. The relative energies exhibit single-digit millihartree errors, and the computed natural-orbital occupations capture the biradical nature of the *para*-isomer. The molecular simulation of the benzyne isomers represents an important step in eigensolver and error-mitigation technologies towards the practical simulation of larger, even more complex molecules on quantum computers.

10.6 Appendix

10.6.1 Electronic Structure Calculation

Complete active state self consistent field (CASSCF) calculations were performed as implemented in the Maple Quantum Chemistry Package [94–96] using [2,2] and [4,4] active spaces

with the correlation-consistent valence double-zeta (cc-pVDZ) basis set [97]. Following convergence of the CASSCF procedure, effective active space electron integrals for the quantum ACSE calculation were obtained via the folding of the core-active cross terms into the active space, such that effective active space energy is given by:

$$\tilde{E}_{\text{act}} = \frac{1}{2} \sum_{pqst} {}^2\tilde{K}^{pq}_{st} \, {}^2D^{pq}_{st} \tag{10.24}$$

where ${}^2\tilde{K}^{pq}_{st}$ are the active space electron integrals containing the core-active cross terms. The elements of the effective active space integral matrix ${}^2\tilde{K}^{pq}_{st}$ are constructed from the one- and two-electron integrals as follows:

$${}^2\tilde{K}^{pq}_{st} = \frac{1}{N-1}({}^1\tilde{K}^{p}_{s}\delta^{q}_{t} + {}^1\tilde{K}^{q}_{t}\delta^{p}_{s}) + {}^2K^{pq}_{st} \, , \tag{10.25}$$

where

$${}^1\tilde{K}^{p}_{s} = {}^1K^{p}_{s} + \sum_{i} (2 \, {}^2K^{pi}_{si} - {}^2K^{pi}_{is}) \, , \tag{10.26}$$

and p, q, s, t runs over all active orbitals and i runs over all core orbitals.

While we could also include number excitation terms, because we start with a multi-reference guess solution, the number-excitation terms are small, even after a few iterations, and can be mostly ignored. Using solely double excitations allows for sufficient quality results convergence. Part of the difficulty in describing the meta-benzyne configuration is that the solution could be described as more single reference, and requires more than a few excitation terms with small coefficients to be described properly.

10.6.2 Quantum Calculations

Using the electron integrals for the active space from above, we perform a quantum calculation on different IBMQ devices. In particular, we perform [2,2] and [4,4] calculation under

the Jordan-Wigner transformation. Different IBMQ devices were utilized through the IBM Quantum Experience. These devices utilize fixed-frequency transmon qubits with co-planer waveguide resonators [98, 99]. We use the PYTHON 3 package QISKIT (v 0.15.0) [100] to interface with the device. The calculations themselves are multifaceted, with nonstandard approaches taken in a number of different areas. We document these in subsequent sections. Each measurement was performed with 2^{13} shots. Stochastic effects were on the order of mhartree, though are affected in a substantial way through the purification scheme. For the collection of all 2-RDMs we utilized a symmetry projected operator basis using the $\hat{N}$ and $\hat{S}_z$ symmetries [101].

For the 1-qubit calculations, we utilized ibmq-armonk, while for the 3- and 4-qubit calculations, we utilized ibmq-bogota and ibmq-santiago. QISKIT was used to interface with the IBMQ devices.

Quantum $[2, 2]$ Active Space Calculations

Using the Jordan-Wigner transformation, the [2,2] case with 4 spin orbitals maps to 4 qubits. The [2,2] calculations contain two Pauli symmetries related to the parities of the total number of electrons and the number of electrons in a subset of spin orbitals (either α or β), and a further symmetry is found for most molecular systems, allowing the [2,2] system to be represented with a single-qubit. These can be expressed as:

$$S_1 = \{Z_1Z_2, Z_1Z_3, Z_1Z_4\}. \tag{10.27}$$

The elements of ${}^2A$ were determined through the quantum ACSE method, with Euler's method being used to propagate the ansatz. An l_2 norm of ${}^2A$ below 0.01 was used as the stopping criterion, which was usually reached in 10-12 iterations. The exact exponential of any combination of Pauli operators is well known for the single-qubit case, and so we are

able to exactly express $U = \prod_i e^{A_i}$ as well as $U' = e^{iH\delta} \prod_i e^{A_i}$. For these runs, we chose $\delta = 0.25$.

Quantum $[4, 4]$ Active Space Calculations

The Jordan-Wigner representation maps the [4,4] case with 8 spin orbitals to 8 qubits. Again, two symmetries related to fermionic parity can be utilized, and then depending on the Hamiltonian we can find additional symmetries. For these particular integrals, we find 2 additional symmetries across all configurations, and then an additional symmetry for the para- configurations, which can be applied to the ortho- and meta- configurations as approximate symmetries. A more detailed discussion on the process of finding these symmetries is included in the next section. While we can also find approximate symmetries through truncation of the Hamiltonian, the application of this additional symmetry from the para−isomer yielded sufficient results for the ortho-isomer case, with a difference from the target (CASSCF) energy of 9.2×10^{-4} H. For the meta case, we found an additional symmetry with approximately 0.6×10^{-3} H error from the CASSCF. The solutions are exact for the 3-qubit para, and all of the 4-qubit cases. We show the effects of some approximate tapering schemes in the next section.

The symmetries are listed in the follow set for the 4- and 5-symmetry cases respectively:

$$S_4 = \{Z_1Z_2Z_3Z_4, Z_1Z_2Z_5Z_6, Z_1Z_3Z_5Z_6, Z_2Z_3Z_5Z_8\}, \tag{10.28}$$

$$S_3^{p/q} = \{Z_1Z_2Z_3Z_4, Z_1Z_5, Z_2Z_6, Z_3Z_7, Z_1Z_2Z_3Z_8\}, \tag{10.29}$$

$$S_3^{m} = \{Z_1Z_4, Z_2Z_3, Z_1Z_2Z_5Z_6, Z_1Z_2Z_5Z_7, Z_5Z_8\}. \tag{10.30}$$

As a result, we are able to perform 3- and 4- qubit simulations of these systems on the 5-qubit linearly connected ibmq-bogota device, and ibmq-santiago. When tapering off qubits, we use eigenvalues which match the eigenvalues of the initial Hartree-Fock determinant. While the initial determinant in this paper is consistently a closed-shell configuration, it can also represent an open-shell configuration for an extension of the procedure to open-shell systems.

The calculations themselves utilized a 1-dimensional model-trust region Newton's method, where the initial trust region was taken to be 2, and the quadratic fit was taken from $\epsilon_n = \pm 1$. Additionally, we used a threshold of $0.75 \times a_{max}$ where a_{max} indicated the largest magnitude term in the ${}^2A$ for a given iteration. The convergence criteria was taken to be 0.02-0.03 in the trust region criteria (or in the norm of ${}^2A$), and we used 5-8 iterations. Instances of the runs themselves are included in the open-source HQCA software package [102].

Qubit Reduction by Tapering and Hamiltonian Truncation

The qubit reduction scheme follows previous work by Bravyi et al. and expanded by Setia et al. for applications to point group symmetries [84, 103]. In particular, we express the Hamiltonian in the Pauli basis and then put these terms in a check sum representation to construct the generator and parity check matrices from the field of quantum error correction [104]. By performing Gaussian elimination on the parity check matrix, we can find generators of the Hamiltonian, which in turn allow us to select a basis for the corresponding null space. Elements of the null space will commute with every term in the Hamiltonian, and thus are symmetries of H. Thus, the nullity of this matrix is the number of symmetry elements, and thus the number of qubits which we can taper. By using a particular unitary transformation:

$$U_i = \frac{1}{\sqrt{2}}(X_j + s_i) \tag{10.31}$$

where X_j is selected so that X_j anticommutes with s_i, and commutes with all other s_i, $i \neq j$, we transform the Hamiltonian so that qubits j have only X or I in each term. By selecting an appropriate eigenvalue of X, we can taper off these terms, resulting in a modified fermionic transformation. We use eigenvalues which agree with the eigenvalues of the initial closed-shell singlet Hartree-Fock determinant.

For a general $\hat{N}$ and $\hat{S}_z$ preserving state, there exist two symmetries related to the parities of the α or β electrons. One can see this simply by noting that there exist two Pauli strings of length r, over the α and β electrons respectively, which can be selected. These symmetries preserve the commuting and anti-commuting relations described in Bravyi et al.[84], and hence, can be tapered as symmetries of the Hamiltonian (or more generally, the set of all 2-RDM operators). While mappings such as the parity or Bravyi-Kitaev mapping explicitly assign these symmetries to qubits, we still can identify and utilize these symmetries with the Jordan-Wigner transformation.

As mentioned in the discussion, we can exploit approximate symmetries for a decrease in circuit complexity by either projecting the state onto a nearby symmetry or truncating the Hamiltonian. To show the effect of using approximate symmetries through tapering Hamiltonian elements, Figure 10.6.2 shows the accuracy and potential symmetries that can be found for a given truncation of elements of the Hamiltonian. In particular, we are interested in finding the highest symmetry state—the state whose generator matrix has the largest nullspace—with the lowest energy error. For these instances, the ortho-, meta- and para-isomers all have exact representations with 4 symmetries (and 5 for the para-isomer). The meta-isomer has the highest error 3-qubit representation, which we safely assume to be less than contributions of noise in the present work.

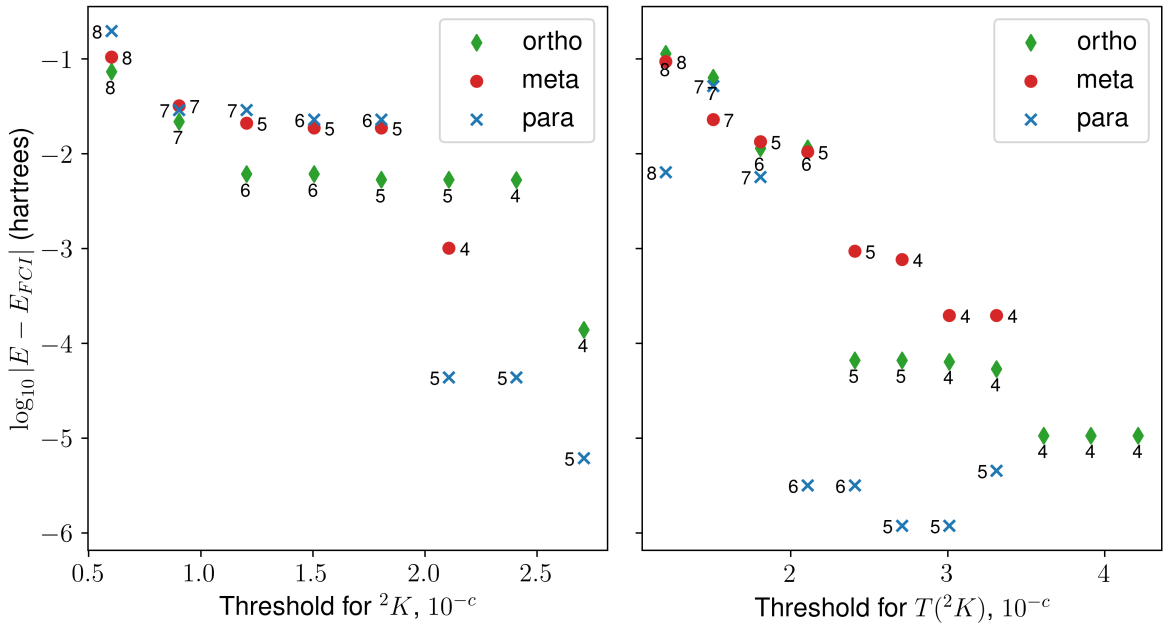

Figure 10.5: Comparison of the truncation used in the ${}^2K$ matrix for ortho-, meta- and para-benzyne, with respect to the resulting accuracy given in the representation against the CASSCF result. Additionally, the number of symmetries found (i.e., the nullity of the generator) is reported next to the appropriate marker.

Classical Solution to the ACSE

In the fully quantum algorithm, the quantum computer is used in both the calculation of the ${}^2A$ and ${}^2D$ matrices. For the [4,4] cases we used a classical approach in solving for elements of ${}^2A$, which reduces the computational demands on the quantum computer and yields sufficient accuracy in this case. This can be found by calculating elements of ${}^2A$ from:

$$ {}^2A^{i,k}_{j,l} = \langle \Psi | [\hat{a}^\dagger_i \hat{a}^\dagger_k \hat{a}_l \hat{a}_j, \hat{H}] | \Psi \rangle. \tag{10.32} $$

More specifically, for a molecular system, the reduced Hamiltonian ${}^2K$ can be written as:

$$ {}^2K^{p,r}_{q,s} = \frac{1}{2(N-1)} \left(\delta^{p1}_q K^r_s + \delta^{r1}_s K^p_q + {}^2V^{p,r}_{q,s}(N-1) \right) \tag{10.33} $$

we define an operator $W^{p,r}_{q,s} = {}^2K^{p,r}_{q,s} - {}^2K^{p,r}_{s,q}$, which then leads to an expression for the total ACSE equation as [33, 34]:

$$ \begin{aligned} {}^2A^{i,k}_{j,l} = &\sum_{p,q} \left({}^2D^{p,q}_{i,k} W^{p,q}_{j,l} - {}^2D^{p,q}_{j,l} W^{p,q}_{i,k} \right) \\ &+ \sum_{pqr} \left({}^3D^{p,r,k}_{j,l,q} W^{p,r}_{i,q} - {}^3D^{p,r,i}_{j,l,q} W^{p,r}_{k,q} - {}^3D^{i,k,p}_{r,q,j} W^{p,l}_{r,q} + {}^3D^{i,k,p}_{r,q,l} W^{p,j}_{r,q} \right). \end{aligned} \tag{10.34} $$

Notably, this expression involves the 3-RDM, which can be reconstructed from its cumulant expansion [61]:

$$ {}^3D^{i,j,k}_{p,q,s} = 6\, {}^1D^i_p \wedge {}^1D^j_q \wedge {}^1D^k_s + 9\, {}^2\Delta^{i,j}_{p,q} \wedge {}^1D^k_s + {}^3\Delta^{i,j,k}_{p,q,s} \tag{10.35} $$

Here, the wedge product denotes the Grassmannian operator, combining antisymmetric permutations of upper and lower indices and dividing by the total number of permutations, ${}^n\Delta$ represents the n-th order reduced cumulant matrix, and we assume that ${}^3\Delta = 0$.

Simulated Quantum Results

Using the above schemes, we can provide simulated results without noise of the different benzyne isomers. Table 10.4 shows simulated results with the quantum solution of the ACSE at different convergence criteria and number of qubits. Table 10.5 shows similar results where the evaluation of the ACSE residual on the quantum computer is replaced by a classical evaluation including classical reconstruction of the 3-RDM from the 2-RDM by a cumulant expansion.

Table 10.4: Energetic error results (millihartrees) for different convergence thresholds and qubit representations for the QACSE with a quantum solution of the ACSE (or measured 3-RDM) for the ortho-, meta-, and para-benzyne configurations. The number of qubits refers to the qubit-representation and related symmetries utilized, which for ortho and meta have non-zero errors. Values of $|^2|A||$ refers to the convergence criteria, which is the norm of the ^2A matrix.

	Energy Error Relative to CASSCF (mhartree)								
	ortho			meta			para		
Qubits/$||^2A||$	0.05	0.01	0.001	0.05	0.01	0.001	0.05	0.01	0.001
3	1.393	1.393	0.916	11.197	1.108	0.869	0.284	0.284	0.003
4	2.957	0.033	0.006	10.563	0.363	0.115	0.284	0.284	0.003
8	13.634	0.200	0.008	14.042	0.240	0.101	5.711	0.042	0.005

In Table 10.4, we can see that with more strict convergence criteria, we are able to obtain highly accurate results for our given representation. Because there is error in the 3 and 4 qubit simulations, given a low norm in ^2A (which is taken relative to the truncated Hamiltonian operator and not the reduced Hamiltonian matrix ^2K), these results return essentially the approximation in the ortho and meta cases (0.92 and 0.8 mH, respectively). Additionally, these results show the most ideal case for the QACSE algorithm with the current choice of tapering, highlighting its potential on beyond-NISQ devices.

If we consider the systems with a reconstructed 3-RDM, as seen in Table 10.5, we note several differences. Because the ^2A matrix from the reconstructed 3-RDM does not represent the true gradient, we use one-dimensional trust region convergence criteria for our convergence threshold as in previous work. The criteria are (1) the quadratic model of the

Table 10.5: Error in energy results (millihartree) for different convergence thresholds and qubit representations for the QACSE algorithm with a reconstructed 3-RDM. The number of qubits refers to the qubit-representation and related symmetries utilized. Instead of the norm of the ${}^2A$ matrix, we use a trust region and energetic increase stopping criteria. We also indicate where or not all of the elements of the ${}^2A$ matrix are implemented.

		Energy Error Relative to CASSCF (mhartree)					
		ortho		meta		para	
Trust Criterion	Entire ${}^2A$	3Q	4Q	3Q	4Q	3Q	4Q
5×10^{-2}	No	1.113	1.112	4.913	4.174	5.675	5.675
1×10^{-3}	No	1.113	1.112	2.975	2.077	1.231	1.234
1×10^{-6}	No	1.113	1.112	2.976	2.077	0.267	0.269
1×10^{-6}	Yes	1.126	0.181	3.687	3.002	0.182	0.182

trust region, and (2) the error in the energy. In some cases we also trim the ${}^2A$ matrix in generating the ansatz—discard elements in our current iteration that are below a given threshold (in his case, 0.5). If we do not trim the operator, then all of the terms are utilized.

These results are not unexpected, as errors from cumulant reconstruction in the literature are often in the single mhartree region. It also is possible that on a quantum computer, the disconnect between an exact 2-RDM and inexact ${}^2A$ leads to an increase in errors. Unlike the quantum ACSE, here the 4-qubit results match the full-qubit result for each instance, and so the latter are not reported. The ortho and para calculations achieve good accuracy, while the meta appears to have slightly more error. Despite this, the results recover the majority of the correlation energy, demonstrating that the reconstructed approach is not unsuitable for noisy simulations where errors are generally much larger than 1 mhartree.

Circuit Implementations

Once the ${}^2A$ operator is obtained for each step, we use a threshold to truncate the operator, and at each step add only one or two additional fermionic terms. As mentioned in the main text, the circuits are constructed by expressing $e^{\epsilon_n A_n}$ as a first order trotterization, resulting in products of exponentials Pauli strings which can be realized generally with CNOT gates

and single-qubit rotations. In some instances we see a reduction in the number of two-qubit gates by using the following single-qubit identity:

$$e^{i\pi}U^{\dagger}\sigma_j U = \begin{cases} \sigma_x & \text{if } j{=}x \\ \sigma_y & \text{if } j{=}z \\ \sigma_z & \text{if } j{=}y \end{cases} \tag{10.36}$$

where $U = S^{\dagger}HS$. This can just as easily applied to exponential transformations as well, and with this, we can transform an operator such as $e^{\alpha(X_1X_2+Y_1Y_2)}$, which is expressed in 3 or 4 CNOT gates, to $U^{\dagger}e^{-\alpha(X_1X_2+Z_1Z_2)}U$ which can be expressed with only 2 CNOT gates. In general, we utilize straightforward concatenation techniques which possibly reduced the CNOT gates while preserving the connectivity of the device (which is linear).

While performing simulations under noiseless, stochastic, and simulated device-like noise, we examined the pool of required operators, and then performed simplifications to reduce the number of CNOT gates that were involved. While in general this is not required, for optimal performance on near-term devices circuit simplifications are critical. Different compilation methods were attempted, but ultimately (likely due to the connectivity constraints of the devices), manual simplifications yielded lower CNOT counts. The symmetries have the effect of reducing the number of nonzero excitation operators, as certain excitation sequences act outside the symmetry state. Acting on the imaginary elements of the 2-RDM, we can find the nonzero elements and then prepare circuits accordingly. For the 3-qubit case this resulted in 6 unique Pauli strings. A similar procedure was carried out with the 4-qubit case, although we found that we did not have to prepare the entire pool of operators.

Quantum Device Specifications

For the quantum computation we used three different quantum devices. For the single qubit simulation, we used IBMQ Rome (5-qubit device), whereas for the 3- and 4-qubit calculations we used IBMQ Bogota as well as IBMQ Santiago, which are same generation linearly connected 5-qubit devices. These were accessed through the IBM Quantum Experience. The quantum devices use fixed-frequency transmon qubits with co-planer waveguide resonators [98, 99]. The Python package Qiskit (v 0.15.0, 0.17.1) [100] was used to interface with the device. Device properties can be found in Tables 10.6, 10.7, and 10.8.

U_2 and U_3 represent single qubit gate errors containing one and two $X_{\pi/2}$ pulses and two and three frame changes respectively. Newer devices (see Table 10.8) directly express these as rotations using the $\sqrt{X}$ and X gates with intermediate frame changes representing rotations along the $z-$axis. $\mathrm{RO}_{i|j}$ represents the probability of measuring the state i given a prepared state j. T_1 and T_2 are the given thermal relaxation times for each qubit. Frequency refers to the qubits operational frequency, and influences the excited state population based on the device temperature. $[j]$ specifies the target qubit with control qubit i, and the number in parenthesis after each entry in the CNOT column indicates the gate length. The gate lengths for the U_2 and U_3 gates were 35 ns and 71 ns respectively.

Table 10.6: Calibration data for the IBMQ Rome device taken on November 11^{th}, 2020, from randomized benchmarking of the qubit gates. The gate lengths for the U_2 and U_3 gates were 35 ns and 71 ns respectively.

Qubit	**Frequency**	$\mathbf{U}_2$	$\mathbf{U}_3$	$\mathbf{RO}_{0\|1}$	$\mathbf{RO}_{1\|0}$	$\mathbf{T}_1$	$\mathbf{T}_2$	$[j]$ $\mathbf{CNOT}_i^j$ (gate length)
i	GHz	10^{-4}	10^{-4}	10^{-2}	10^{-2}	μ s	μ s	10^{-2} (ns)
0	4.969	2.4	4.7	2.0	0.6	92.0	66.3	[1] 0.7 (320)
1	4.770	2.9	5.7	4.9	3.4	104.1	68.3	[0] 0.7 (356) [2] 2.0 (1109)
2	5.015	3.5	7.1	7.0	2.2	74.3	155.0	[1] 2.0 (1145) [3] 1.0 (377)
3	5.259	5.8	11.7	3.2	1.0	67.7	101.1	[2] 1.0 (341) [4] 1.6 (476)
4	4.997	2.7	5.3	1.6	0.7	50.1	103.0	[3] 1.6 (512)

Table 10.7: Calibration data taken for IBMQ Bogota from December 4^{th} to 7^{th}, 2020. from benchmarking. See Table 10.6 for descriptions. The gate lengths for the U_2 and U_3 gates were 35 ns and 71 ns respectively.

Qubit	**Frequency**	$\mathbf{U}_2$	$\mathbf{U}_3$	$\mathbf{RO}_{0\|1}$	$\mathbf{RO}_{1\|0}$	$\mathbf{T}_1$	$\mathbf{T}_2$	$[j]$ $\mathbf{CNOT}_i^j$ (gate length)
i	GHz	10^{-4}	10^{-4}	10^{-2}	10^{-2}	μ s	μ s	10^{-2} (ns)
				$12-04-20$				
0	5.000	4.8	9.6	4.0	1.4	93.5	141.4	[1] 1.7 (690)
1	4.845	2.2	4.4	4.4	2.9	134.4	76.1	[0] 1.7 (654) [2] 0.7 (498)
2	4.783	1.7	3.4	4.9	1.5	128.2	206.2	[1] 0.7 (533) [3] 3.3 (626)
3	4.858	15.7	31.3	4.6	1.2	84.6	36.8	[2] 3.3 (590) [4] 2.5 (370)
4	4.978	4.2	8.3	4.9	1.6	50.9	87.1	[3] 2.5 (334)
				$12-05-20$				
0	5.000	3.0	6.1	3.7	1.3	91.5	119.8	[1] 1.7 (690)
1	4.845	2.6	5.2	4.3	3.3	137.4	75.4	[0] 1.7 (654) [2] 0.8 (498)
2	4.783	1.5	3.0	3.3	1.3	133.0	226.5	[1] 0.8 (533) [3] 0.6 (626)
3	4.858	1.6	3.3	3.4	0.6	159.7	244.4	[2] 0.6 (590) [4] 0.8 (370)
4	4.978	1.9	3.9	2.8	1.0	107.3	146.1	[3] 0.8 (334)
				$12-06-20$				
0	5.000	3.5	7.0	5.3	1.6	88.2	107.7	[1] 1.8 (690)
1	4.845	2.4	4.9	3.8	2.2	145.0	95.8	[0] 1.8 (654) [2] 0.7 (498)
2	4.783	1.8	3.6	4.7	1.4	165.0	211.2	[1] 0.7 (533) [3] 0.6 (626)
3	4.858	2.6	5.2	1.9	0.7	160.2	311.7	[2] 0.6 (590) [4] 0.7 (370)
4	4.978	1.9	3.8	3.6	1.2	126.0	149.4	[3] 0.7 (334)
				$12-07-20$				
0	5.000	3.5	7.0	8.2	1.6	44.8	55.7	[1] 1.8 (690)
1	4.845	2.4	4.9	4.7	2.6	178.2	98.8	[0] 1.8 (654) [2] 0.8 (498)
2	4.783	1.8	3.6	3.9	0.9	126.0	231.0	[1] 0.8 (533) [3] 0.8 (626)
3	4.858	2.6	5.2	2.8	0.4	124.0	168.6	[2] 0.8 (590) [4] 0.9 (370)
4	4.978	1.9	3.8	3.9	1.3	93.5	188.0	[3] 0.9 (334)

Table 10.8: Calibration data taken for IBMQ Santiago from August 24^{th}. The gate lengths for the $\sqrt{X}$ and X gates are both 35 ns. Santiago was used to calculate the 3-qubit meta-isomer calculation.

Qubit	**Frequency**	$\sqrt{X}$	X	$\mathbf{RO}_{0\|1}$	$\mathbf{RO}_{1\|0}$	$\mathbf{T}_1$	$\mathbf{T}_2$	$[j]$ $\mathbf{CNOT}_i^j$ (gate length)
i	GHz	10^{-4}	10^{-4}	10^{-2}	10^{-2}	μ s	μ s	10^{-2} (ns)
2	4.821	2.0	2.0	1.5	0.5	99.0	89.8	[3] 0.7 (377)
3	4.742	3.0	3.0	1.4	0.5	75.7	67.4	[2] 0.7 (412) [4] 0.7 (377)
4	4.816	1.6	1.6	2.2	1.0	99.5	155.1	[3] 0.7 (341)

10.6.3 Error Mitigation Methods

To directly mitigate the effects of noise on the quantum computer, we use a variety of techniques in addition to the ones listed in the main text (limit-preserving correction and the purification of the 2-RDM).

Number Preserving Projection to Diagonal Elements of the 2-RDM

The most effective error correction comes by filtering diagonal elements of the 2-RDM, of the form ${}^2D^{p,q}_{p,q}$, so that the number operator is preserved. Because these elements commute with single-qubit measurements that are performed, they can be filtered according to the measurement result. Counts that have differing values of N or S_z are rejected, and so we are filtered to a set of RDMs with the proper trace and projected spin properties (i.e., Tr ${}^2D = N(N-1)$). While heavily erroneous off-diagonal elements can also lead to non-physical eigenvalues[4], correcting for these in the 2-RDM case is not straightforward and likely would not reduce the overall errors.

Measurement Correction of Prepared States (SPAM)

Finally, the state preparation and measurement, which involves preparing all possible quantum states for some qubit space, and constructing a transition matrix with the associated inverse, was utilized to mitigate measurement errors. We applied this to local qubits, and so did not correct for correlated measurement errors. This procedure has been documented in many places [105, 106] and can be implemented through QISKIT.

Limit-Preserving Correction for an Iterative Ansatz

In the main text we described our error mitigation strategy which we denoted as a limit-preserving correction for an iterative ansatz, and described the framework or context in which

it could be useful. To illustrate these points, Figure 10.6.3 highlights the effect of performing a traditional (3-qubit) calculation with an iterative design, versus a ${}^2\Gamma-$corrected result. The increasing energy can be seen in each iteration with the standard result. For the ortho, meta, and para results, only 1, 2/3, and 1 step(s), respectively, are able to be taken in each case before the ansatz has been too corrupted and can no longer provide a reasonable ground state. However, though the optimization with the ${}^2\Gamma$ correction is still noisy, and not always smooth, we are able to keep or improve upon the energy gains in each case, and achieve results closer to the true ground state.

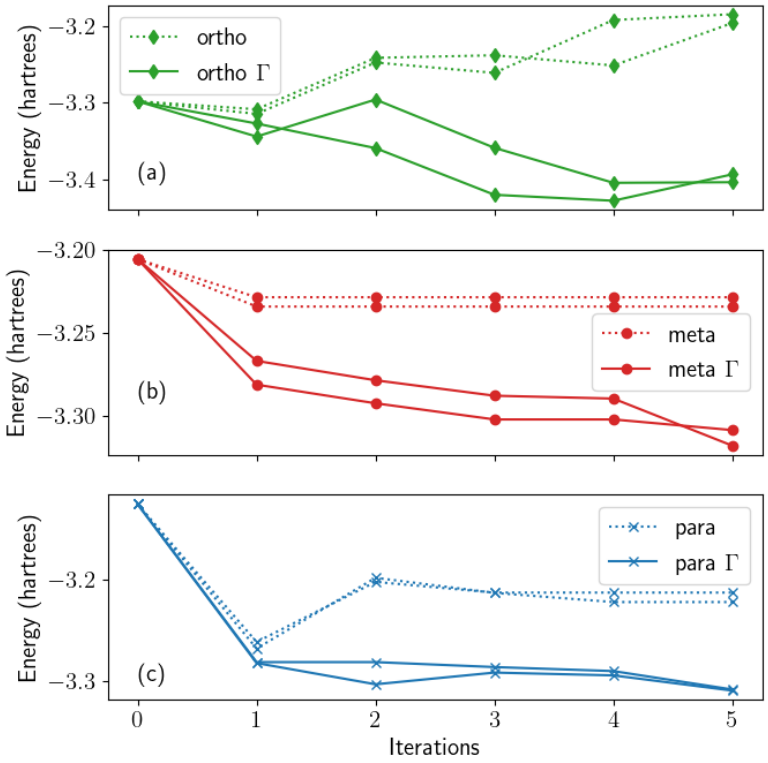

Figure 10.6: Two optimization attempts for (a) ortho-, (b) meta-, and (c) para-benzyne configurations with and without the ${}^2\Gamma$ preserving correction showing the first 5 iterations. In the meta-isomer case without the ${}^2\Gamma$ correction, unfavorable steps in choosing ϵ_n are rejected and so the run plateaus after the first step.

10.6.4 Symmetry and the ACSE

Given a symmetry operator $\hat{S}$ (where $[\hat{S}, \hat{H}] = 0$) utilizing the qACSE method leads to natural advantages in terms of the generated ansatz and preserving the symmetry subspace. In particular, we can readily see that any symmetry of the system is not violated throughout the qACSE iterations.

Let $\hat{P}_s$ be the projection operator into a particular eigenstate s of $\hat{S}$. Take a particular iteration of the ACSE algorithm for a generic system, where we have that $|\psi\rangle$ is an eigenstate s_0 of $\hat{S}$. Then we can write our Hamiltonian and wavefunction as:

$$\hat{H} = \sum_s \hat{P}_s \hat{H} \hat{P}_s \tag{10.37}$$

$$|\psi\rangle = \hat{P}_{s_0} |\psi\rangle. \tag{10.38}$$

Here, the resulting structure of H is block-diagonal with respect to each symmetry space of $\hat{S}$. Elements of $\hat{A}$ can be found as:

$$\hat{A}^i_j = \langle\psi|[\hat{M}^i_j, \hat{H}]|\psi\rangle \tag{10.39}$$

$$= \sum_s \langle\psi|\hat{P}_{s_0}[\hat{M}^i_j, \hat{P}_s \hat{H} \hat{P}_s]\hat{P}_{s_0}|\psi\rangle \tag{10.40}$$

$$= \langle\psi|[\hat{P}_{s_0} \hat{M}^i_j \hat{P}_{s_0}, \hat{H}]|\psi\rangle \tag{10.41}$$

where $\hat{M}^i_j$ represents a measurement operator between two basis elements, which is effectively projected into the symmetry subspace s_0. This expression shows that the residual is essentially projected into the same initial subspace as the wavefunction. Exponentiation of the residual will necessarily preserve any symmetry as powers of the projected operators will still be in the same symmetry subspace. If ψ is not a true eigenstate, then we can easily have mixing between different eigenspaces of $\hat{S}$.

Note that this only applies if we are in the symmetry basis of $\hat{S}$. Practically, this is not

always the case. For instance, the standard second quantized representation for a fermionic simulation uses Slater determinants, which commute with the number and projected spin operators (Slater determinants). While using the entire ${}^2A$ operator will preserve all symmetries, using a truncated ${}^2A$ operator can lead to symmetry violations in the total spin, requiring the use of a symmetry-adapted basis.

References

[1] I. Kassal, J. D. Whitfield, A. Perdomo-Ortiz, M.-h. Yung, and A. Aspuru-Guzik, Annual Review of Physical Chemistry **62**, 185 (2011), arXiv:1007.2648 .

[2] P. J. J. O'Malley, R. Babbush, I. D. Kivlichan, J. Romero, J. R. McClean, R. Barends, J. Kelly, P. Roushan, A. Tranter, and N. e. a. Ding, Physical Review X **6**, 031007 (2016), arXiv:1512.06860 .

[3] S. McArdle, S. Endo, A. Aspuru-Guzik, S. C. Benjamin, and X. Yuan, Reviews of Modern Physics **92**, 15003 (2020), arXiv:1808.10402 .

[4] F. Arute, K. Arya, R. Babbush, D. Bacon, J. C. Bardin, R. Barends, S. Boixo, M. Broughton, B. B. Buckley, and D. A. e. a. Buell, Science **369**, 1084 (2020), arXiv:2004.04174 .

[5] A. Aspuru-Guzik, A. D. Dutoi, P. J. Love, and M. Head-Gordon, Science **309**, 1704 (2005), arXiv:0905.0887 .

[6] S. Lloyd, Science **273**, 1073 (1996).

[7] D. Lu, B. Xu, N. Xu, Z. Li, H. Chen, X. Peng, R. Xu, and J. Du, Physical Chemistry Chemical Physics **14**, 9411 (2012).

[8] V. E. Elfving, B. W. Broer, M. Webber, J. Gavartin, M. D. Halls, K. P. Lorton, and A. Bochevarov, , 1 (2020), arXiv:2009.12472 .

[9] T. Helgaker, P. Jørgensen, and J. Olsen, *Molecular Electronic-Structure Theory* (John Wiley & Sons, Ltd, Chichester, UK, 2000) p. 908.

[10] H. Lischka, D. Nachtigallová, A. J. Aquino, P. G. Szalay, F. Plasser, F. B. MacHado, and M. Barbatti, Chemical Reviews **118**, 7293 (2018).

[11] F. A. Evangelista, Journal of Chemical Physics **149** (2018), 10.1063/1.5039496.

[12] J. Preskill, Quantum **2**, 79 (2018), arXiv:arXiv:1801.00862v3 .

[13] K. Head-Marsden, J. Flick, C. J. Ciccarino, and P. Narang, Chemical Reviews (2020), 10.1021/acs.chemrev.0c00620.

[14] A. Peruzzo, J. McClean, P. Shadbolt, M.-H. Yung, X.-Q. Zhou, P. J. Love, A. Aspuru-Guzik, and J. L. O'Brien, Nature Communications **5**, 4213 (2014), arXiv:1304.3061 .

[15] J. R. McClean, J. Romero, R. Babbush, and A. Aspuru-Guzik, New Journal of Physics **18**, 023023 (2016), arXiv:1509.04279 .

[16] A. Kandala, A. Mezzacapo, K. Temme, M. Takita, M. Brink, J. M. Chow, and J. M. Gambetta, Nature **549**, 242 (2017), arXiv:1704.05018 .

[17] A. Kandala, K. Temme, A. D. Córcoles, A. Mezzacapo, J. M. Chow, and J. M. Gambetta, Nature **567**, 491 (2019), arXiv:1805.04492 .

[18] E. Fontana, N. Fitzpatrick, D. M. Ramo, R. Duncan, and I. Rungger, , 1 (2020), arXiv:2011.01125 .

[19] S. McArdle, X. Yuan, and S. Benjamin, Physical Review Letters **122**, 180501 (2019), arXiv:1807.02467 .

[20] S. E. Smart and D. A. Mazziotti, Physical Review A **100**, 022517 (2019).

[21] X. Bonet-Monroig, R. Sagastizabal, M. Singh, and T. E. O'Brien, Physical Review A **98**, 062339 (2018).

[22] S. E. Smart and D. A. Mazziotti, Physical Review Letters **126**, 070504 (2021), arXiv:2004.11416 .

[23] D. A. Mazziotti, Phys. Rev. A **57**, 4219 (1998).

[24] H. Nakatsuji and K. Yasuda, Phys. Rev. Lett. **76**, 1039 (1996).

[25] K. Yasuda and H. Nakatsuji, Phys. Rev. A **56**, 2648 (1997).

[26] F. Colmenero and C. Valdemoro, Phys. Rev. A **47**, 979 (1993).

[27] C. Valdemoro, L. M. Tel, E. Pérez-Romero, and D. R. Alcoba, International Journal of Quantum Chemistry **108**, 1090 (2008).

[28] D. A. Mazziotti, J. Chem. Phys. **116**, 1239 (2002).

[29] D. A. Mazziotti, Phys. Rev. A **60**, 4396 (1999).

[30] A. J. Coleman and V. I. Yukalov, *Reduced Density Matrices: Coulson's Challenge* (Springer Berlin Heidelberg, 2000).

[31] D. A. Mazziotti, Physical Review A **69**, 012507 (2004).

[32] D. A. Mazziotti, Physical Review A **102**, 30802 (2020), arXiv:2010.02191 .

[33] D. A. Mazziotti, Physical Review Letters **97**, 143002 (2006).

[34] D. A. Mazziotti, Physical Review A - Atomic, Molecular, and Optical Physics **75**, 1 (2007).

[35] G. Gidofalvi and D. A. Mazziotti, Physical Review A - Atomic, Molecular, and Optical Physics **80**, 1 (2009).

[36] D. Mukherjee and W. Kutzelnigg, The Journal of Chemical Physics **114**, 2047 (2001).

[37] F. A. Evangelista, G. K. L. Chan, and G. E. Scuseria, Journal of Chemical Physics **151** (2019), 10.1063/1.5133059, arXiv:1910.10130 .

[38] R. Santagati, J. Wang, A. A. Gentile, S. Paesani, N. Wiebe, J. R. McClean, S. Morley-Short, P. J. Shadbolt, D. Bonneau, J. W. Silverstone, D. P. Tew, X. Zhou, J. L. O'Brien, and M. G. Thompson, Science Advances **4**, eaap9646 (2018), arXiv:1611.03511 .

[39] S. M. Robinson, *Numerical Optimization* (2006).

[40] P. Rakshit and A. Konar, *Principles in Noisy Optimization*, Cognitive Intelligence and Robotics (Springer Singapore, Singapore, 2018).

[41] A. Daskin and S. Kais, Molecular Physics **109**, 761 (2011), arXiv:arXiv:1004.2242v4 .

[42] J. W. Snyder, A. E. Rothman, J. J. Foley, and D. A. Mazziotti, J. Chem. Phys. **132**, 154109 (2010).

[43] J. W. Snyder and D. A. Mazziotti, Phys. Chem. Chem. Phys. (2011).

[44] J. W. Snyder and D. A. Mazziotti, J. Chem. Phys. **135**, 024107 (2011).

[45] L. Greenman and D. A. Mazziotti, J. Chem. Phys. **134**, 174110 (2011).

[46] A. M. Sand and D. A. Mazziotti, Journal of Chemical Physics **143** (2015), 10.1063/1.4931471.

[47] D. R. Alcoba, C. Valdemoro, L. M. Tel, E. Pérez-Romero, and O. B. Oña, Journal of Physical Chemistry A **115**, 2599 (2011).

[48] S. E. Smart, P. G. Scrape, L. J. Butler, and D. A. Mazziotti, J. Chem. Phys. **149**, 024302 (2018).

[49] M. A. Nielsen and I. L. Chuang, *Cambridge University Press* (Cambridge University Press, Cambridge, 2010) p. 702, arXiv:arXiv:1011.1669v3 .

[50] J. Romero, R. Babbush, J. R. McClean, C. Hempel, P. Love, and A. Aspuru-Guzik, ASA Refresher Courses in Anesthesiology , 1 (2017), arXiv:1701.02691 .

[51] J. Lee, W. J. Huggins, M. Head-Gordon, and K. B. Whaley, Journal of Chemical Theory and Computation **15**, 311 (2018), arXiv:1810.02327 .

[52] H. R. Grimsley, S. E. Economou, E. Barnes, and N. J. Mayhall, Nature Communications **10**, 3007 (2019), arXiv:1812.11173 .

[53] Y. Yang, D. Peng, E. R. Davidson, and W. Yang, Journal of Physical Chemistry A **119**, 4923 (2015).

[54] J. Shee, E. J. Arthur, S. Zhang, D. R. Reichman, and R. A. Friesner, Journal of Chemical Theory and Computation **15**, 4924 (2019), arXiv:1905.13316 .

[55] A. L. McManus, E. P. Hoy, and D. A. Mazziotti, Phys. Chem. Chem. Phys. **17**, 12521 (2015).

[56] S. G. Wierschke, J. J. Nash, and R. R. Squires, Journal of the American Chemical Society **115**, 11958 (1993).

[57] S. L. Debbert and C. J. Cramer, International Journal of Mass Spectrometry **201**, 1 (2000).

[58] J. J. Nash and R. R. Squires, Journal of the American Chemical Society **118**, 11872 (1996).

[59] J. J. Foley and D. A. Mazziotti, Physical Review A **86**, 012512 (2012).

[60] N. C. Rubin, R. Babbush, and J. McClean, New Journal of Physics **20**, 053020 (2018), arXiv:1801.03524 .

[61] D. a. Mazziotti, Chemical Physics Letters **289**, 419 (1998).

[62] A. E. Deprince and D. A. Mazziotti, Journal of Chemical Physics **127**, 1 (2007).

[63] W. Kutzelnigg and D. Mukherjee, The Journal of Chemical Physics **110**, 2800 (1999).

[64] J. P. Misiewicz, J. M. Turney, and H. F. Schaefer, Journal of Chemical Theory and Computation **16**, 6150 (2020).

[65] D. A. Mazziotti, Physical Review E - Statistical Physics, Plasmas, Fluids, and Related Interdisciplinary Topics **65**, 1 (2002).

[66] C. Garrod and J. K. Percus, Journal of Mathematical Physics **5**, 1756 (1964).

[67] A. J. Coleman, Reviews of Modern Physics **35**, 668 (1963), arXiv:0310359v1 [arXiv:cond-mat] .

[68] R. M. Erdahl, International Journal of Quantum Chemistry **XIII**, 697 (1978).

[69] L. Vanderberghet and S. Boyd, SIAM Review **38**, 49 (1996).

[70] D. A. Mazziotti, Physical Review Letters **106**, 7 (2011).

[71] D. A. Mazziotti, Physical Review Letters **93**, 19 (2004).

[72] D. A. Mazziotti, ed., *Advances in Chemical Physics*, Advances in Chemical Physics, Vol. 134 (John Wiley & Sons, Inc., Hoboken, NJ, USA, 2007) p. 574.

[73] J. M. Montgomery and D. A. Mazziotti, Journal of Physical Chemistry A **122**, 4988 (2018), arXiv:1805.08746 .

[74] J. N. Boyn, J. N. Boyn, J. Xie, J. S. Anderson, D. A. Mazziotti, and D. A. Mazziotti, Journal of Physical Chemistry Letters **11**, 4584 (2020), arXiv:2005.03637 .

[75] W. Sander, Accounts of Chemical Research **32**, 669 (1999), https://doi.org/10.1021/ar960153k .

[76] S. P. Ross and T. R. Hoye, Nature Chemistry **9**, 523 (2017).

[77] F. Shi, J. P. Waldo, Y. Chen, and R. C. Larock, Organic Letters **10**, 2409 (2008), pMID: 18476707, https://doi.org/10.1021/ol800675u .

[78] A. V. Dubrovskiy, N. A. Markina, and R. C. Larock, Org. Biomol. Chem. **11**, 191 (2013).

[79] P. G. Wenthold, R. R. Squires, and W. C. Lineberger, J. Am. Chem. Soc. **120**, 5279 (1998).

[80] Y. A. Bernard, Y. Shao, and A. I. Krylov, The Journal of Chemical Physics **136**, 204103 (2012), https://doi.org/10.1063/1.4714499 .

[81] L. V. Slipchenko and A. I. Krylov, The Journal of Chemical Physics **117**, 4694 (2002), https://doi.org/10.1063/1.1498819 .

[82] J.-N. Boyn, A. O. Lykhin, S. E. Smart, L. Gagliardi, and D. A. Mazziotti, The Journal of Chemical Physics **155**, 244106 (2021), arXiv:2106.11972 .

[83] S. E. Smart and D. A. Mazziotti, Physical Review Research **023048**, 1 (2020).

[84] S. Bravyi, J. M. Gambetta, A. Mezzacapo, and K. Temme, , 1 (2017), arXiv:1701.08213 .

[85] K. Temme, S. Bravyi, and J. M. Gambetta, Physical Review Letters **119**, 1 (2017), arXiv:1612.02058 .

[86] H. Nakatsuji, J. Chem. Phys. **113**, 2949 (2000).

[87] M. Nooijen, Phys. Rev. Lett. **84**, 2108 (2000).

[88] T. V. Voorhis and M. Head-Gordon, J. Chem. Phys. **115**, 5033 (2001).

[89] H. Nakatsuji, J. Chem. Phys. **115**, 2465 (2001).

[90] E. R. Davidson, Phys. Rev. Lett. **91**, 123001 (2003).

[91] S. Ronen, Phys. Rev. Lett. **91**, 123002 (2003).

[92] P. Piecuch, K. Kowalski, P.-D. Fan, and K. Jedziniak, Phys. Rev. Lett. **90**, 113001 (2003).

[93] W. Kutzelnigg and D. Mukherjee, Phys. Rev. A **71**, 022502 (2005).

[94] Maplesoft, a division of Waterloo Maple Inc., Waterloo, Ontario., (2019).

[95] RDMChem, Chicago, Illinois., (2019).

[96] Q. Sun, T. C. Berkelbach, N. S. Blunt, G. H. Booth, S. Guo, Z. Li, J. Liu, J. D. McClain, E. R. Sayfutyarova, S. Sharma, S. Wouters, and G. K.-L. Chan, WIREs Computational Molecular Science **8**, e1340 (2018), https://onlinelibrary.wiley.com/doi/pdf/10.1002/wcms.1340 .

[97] T. H. Dunning, J. Chem. Phys. **90**, 1007 (1989).

[98] J. Koch, T. M. Yu, J. Gambetta, A. A. Houck, D. I. Schuster, J. Majer, A. Blais, M. H. Devoret, S. M. Girvin, and R. J. Schoelkopf, Phys. Rev. A **76**, 042319 (2007).

[99] J. M. Chow, A. D. Córcoles, J. M. Gambetta, C. Rigetti, B. R. Johnson, J. A. Smolin, J. R. Rozen, G. A. Keefe, M. B. Rothwell, M. B. Ketchen, and M. Steffen, Phys. Rev. Lett. **107**, 080502 (2011).

[100] H. Abraham, AduOffei, R. Agarwal, I. Y. Akhalwaya, G. Aleksandrowicz, T. Alexander, M. Amy, E. Arbel, Arijit02, A. Asfaw, A. Avkhadiev, C. Azaustre, AzizNgoueya,

A. Banerjee, A. Bansal, P. Barkoutsos, G. Barron, G. S. Barron, L. Bello, Y. Ben-Haim, D. Bevenius, A. Bhobe, L. S. Bishop, *et al.*, "Qiskit: An open-source framework for quantum computing," (2019).

[101] S. E. Smart and D. A. Mazziotti, Physical Review A **103**, 012420 (2021), arXiv:2008.06027 .

[102] S. E. Smart and D. A. Mazziotti, "hqca - hybrid quantum computing algorithms for quantum chemistry," .

[103] K. Setia, R. Chen, J. E. Rice, A. Mezzacapo, M. Pistoia, and J. D. Whitfield, Journal of Chemical Theory and Computation **16**, 6091 (2020), arXiv:1910.14644 .

[104] D. Gottesman, **2008** (1997), arXiv:9705052 [quant-ph] .

[105] H. P. Breuer and F. Petruccione, *The Theory of Open Quantum Systems*, Vol. 9780199213 (Oxford University Press, 2007) pp. 1–656.

[106] L. C. Govia, G. J. Ribeill, D. Ristè, M. Ware, and H. Krovi, Nature Communications **11**, 1 (2020), arXiv:1902.10821 .

CHAPTER 11

MANY-FERMION SIMULATION FROM THE CONTRACTED QUANTUM EIGENSOLVER WITHOUT FERMIONIC ENCODING OF THE WAVE FUNCTION

The current chapter has been submitted for publication, authored by Scott E. Smart and David A. Mazziotti.

11.1 Introduction

Simulations on quantum computers have a potentially exponential advantage for the computation of many-fermion quantum systems such as molecules and materials [1, 2]. However, if each qubit represents the particle filling of an orbital, as in the formalism of second quantization, the natural particles for simulation on a quantum computer—qubit particles—are hard-core bosons rather than fermions [3, 4]. Consequently, as originally recognized by Feynman [5], the simulation of a many-fermion quantum system is potentially more complicated than the simulation of an equivalent many-boson quantum system. The particle statistics of fermions are typically encoded in the qubit wave function in a process known as fermionic encoding, which increases computational complexity in terms of the quantum state preparation and tomography [1, 6–10].

To avoid this additional complexity, hardware-efficient wave functions have been developed for fermionic systems in which a wave function is prepared on the quantum computer such that its simulated particles are neither bosons nor fermions [11–13]. Encoding the Hamiltonian with fermion statistics in these instances still recovers the many-fermion energy from the arbitrary statistics of the prepared wave function. While the absence of particle statistics can produce optimization difficulties such as barren plateaus, more accurate results have recently been obtained by using qubit-particle wave functions whose particles

have the statistics of hard-core bosons [14–19]. We have shown that, in contrast to the hardware-efficient wave functions, the qubit-particle wave functions are isomorphic to the fermion wave functions, and hence, they uniquely parameterize the set of ground-state two-fermion reduced density matrices (2-RDMs) [3]. Consequently, the energy and 2-RDM of a many-fermion quantum system can be computed from a qubit-particle wave function with the accuracy associated with a fermion wave function but at a potentially reduced computational cost.

Recently, we presented a hybrid quantum-classical algorithm for the many-fermion problem known as the contracted quantum eigensolver (CQE) [20–22]. The CQE minimizes the residual of a contraction (projection) of the Schrödinger equation onto the space of two particles. The algorithm updates the fermion wave function iteratively with two-body exponential transformations to minimize the residual. To keep the transformations unitary, we use the anti-Hermitian part of the contraction of the Schrödinger equation, known as the anti-Hermitian contracted Schrödinger equation (ACSE) [23–30]. In contrast to the variational quantum eigensolver (VQE) [31–33] in which the variational form of the wave function is not specified, the CQE produces a compact wave function Ansatz consisting of a series of two-body exponential transformations applied to the reference wave function. This CQE Ansatz [24], which is significantly more flexible than a truncated coupled cluster Ansatz, can be converged to the exact solution of the Schrödinger equation. The CQE algorithm, which stores just the 2-RDM on the classical computer, has a potentially exponential advantage over classical methods for solving the N-fermion problem like full configuration interaction.

Here we develop a generalization of the CQE algorithm for the many-fermion problem that solves an unencoded ACSE in which the anti-Hermitian part of the Schrödinger equation is contracted onto two qubit particles rather than two fermions. The generalized algorithm solves for the fermionic ground-state energy and 2-RDM by updating a qubit-particle wave function at each iteration with a two-qubit-particle unitary transformation that minimizes

the residual of the unencoded ACSE. We explore the accuracy and efficiency of the proposed algorithm through quantum simulations of the hydrogen fluoride molecule, the dissociation of diatomic oxygen O_2, and a series of hydrogen chains. Both the encoded (fermion) and the unencoded (qubit-particle) CQE algorithms show similar convergence to the exact ground-state energies and 2-RDMs, but the unencoded CQE has potentially important computational savings in terms of the number of two-qubit gates required in the state preparation and the locality of the 2-RDM tomography.

11.2 Theory

We review the ACSE and its CQE algorithm for quantum simulation in section 11.2.1, present the unencoded ACSE and its CQE algorithm that avoid fermionic encoding of the wave function in section 11.2.2, explore the connection between the encoded and unencoded ACSEs in section 11.2.4, and discuss practical considerations for both encoded and unencoded CQE algorithm in section 11.2.5.

11.2.1 Encoded ACSE and its CQE algorithm

Consider a fermionic quantum system of N fermions in r orbitals described by the Schrödinger equation

$$\hat{H}|\Psi\rangle = E|\Psi\rangle. \tag{11.1}$$

Here E and $|\Psi_n\rangle$ are the many-fermion ground-state energy and wave function, and $\hat{H}$ is the Hamiltonian operator

$$\hat{H} = \sum_{pqst} {}^2K_{st}^{pq} \hat{a}_p^\dagger \hat{a}_q^\dagger \hat{a}_t \hat{a}_s \tag{11.2}$$

in which ${}^2K$ is the reduced Hamiltonian matrix, the indices ranging from one to r denote the orbitals, and $\hat{a}_i^\dagger$ and $\hat{a}_i$ are the creation and annihilation operators of the fermion in the i^{th} orbital. The ACSE is the anti-Hermitian contraction of the many-fermion Schrödinger

equation onto two fermions [23–30]:

$$\langle\Psi|[\hat{a}_i^\dagger \hat{a}_k^\dagger \hat{a}_l \hat{a}_j, \hat{H}]|\Psi\rangle = 0. \tag{11.3}$$

As shown in previous work, iterative solution of the ACSE generates a unitary two-body exponential Ansatz for the wave function [20, 24]

$$\mathrm{e}^{\hat{A}_m^{\mathrm{F}}} \cdots \mathrm{e}^{\hat{A}_2^{\mathrm{F}}} \mathrm{e}^{\hat{A}_1^{\mathrm{F}}} |\Psi_0\rangle \tag{11.4}$$

in which $|\Psi_n^0\rangle$ is the reference wave function and the unitary transformation at the m^{th} iteration is determined by a two-body anti-Hermitian operator

$$\hat{A}_m^{\mathrm{F}} = \epsilon_m \sum_{ijkl} {}_{\mathrm{F}}^{2} A_m^{ij;kl} \hat{a}_i^\dagger \hat{a}_j^\dagger \hat{a}_l \hat{a}_k \tag{11.5}$$

that corresponds to the residual of the ACSE

$${}_{\mathrm{F}}^{2} A_m^{ij;kl} = \langle\Psi_{m-1}|[\hat{H}, \hat{a}_i^\dagger \hat{a}_j^\dagger \hat{a}_l \hat{a}_k]|\Psi_{m-1}\rangle. \tag{11.6}$$

The residual the ACSE at the m^{th} iteration equals the gradient of the energy with respect to the two-body anti-Hermitian operator $\hat{A}_m^{\mathrm{F}}$. Hence, the residual the ACSE is zero not only when the ACSE is satisfied but also when the gradient of the energy vanishes. The ϵ_m is a step-like parameter that can be optimized at the m^{th} iteration to minimize the energy. From the wave function the elements of the 2-RDM at the m^{th} iteration can be computed

$${}^2 D_m^{pq;st} = \langle\Psi|\hat{a}_p^\dagger \hat{a}_q^\dagger \hat{a}_t \hat{a}_s|\Psi\rangle. \tag{11.7}$$

While calculation of the residual the ACSE and the 2-RDM on the classical computer typically requires a cumulant approximation for the three-particle reduced density matrix (3-

RDM) [34, 35] to avoid storage of the wave function, both the ACSE residual and the 2-RDM in the CQE algorithm can be directly calculated by quantum tomography. Implementation of the state preparation and tomography in the CQE requires fermionic encoding in which the fermionic creation and annihilation operators are expressed in terms of qubit operators through a transformation such as the Jordan-Wigner mapping.

11.2.2 Unencoded ACSE and its CQE algorithm

In this paper we generalize the CQE algorithm to solve the many-fermion problem using a qubit-particle wave function that does not require fermionic encoding. Consider the anti-Hermitian contraction of the Schrödinger equation onto two qubit particles to generate the unencoded ACSE

$$\langle\Psi|[\hat{\sigma}_i^\dagger\hat{\sigma}_k^\dagger\hat{\sigma}_l\hat{\sigma}_j,\hat{H}]|\Psi\rangle = 0. \tag{11.8}$$

where the Hamiltonian is defined with fermionic operators as in Eq. (11.1) but the $\hat{\sigma}_i^\dagger$ and $\hat{\sigma}_i$ are the creation and annihilation operators of a qubit particle in the i^{th} orbital. As in the previous case of the contraction onto two fermions to generate the ACSE (or encoded ACSE), iterative solution of the unencoded ACSE generates a unitary two-qubit-particle exponential Ansatz for the wave function

$$\mathrm{e}^{\hat{A}_m^{\mathrm{Q}}}\cdots\mathrm{e}^{\hat{A}_2^{\mathrm{Q}}}\mathrm{e}^{\hat{A}_1^{\mathrm{Q}}}|\Psi_0\rangle \tag{11.9}$$

in which the unitary transformation at the m^{th} iteration is determined by a two-qubit-particle anti-Hermitian operator

$$\hat{A}_m^{\mathrm{Q}} = \epsilon_m\sum_{ijkl}{}_{\mathrm{Q}}^{2}A_m^{ij;kl}\hat{\sigma}_i^\dagger\hat{\sigma}_j^\dagger\hat{\sigma}_l\hat{\sigma}_k \tag{11.10}$$

that corresponds to the residual of the unencoded ACSE

$${}_{\mathrm{Q}}^{2}A_m^{ij;kl} = \langle\Psi_{m-1}|[\hat{H},\hat{\sigma}_i^\dagger\hat{\sigma}_j^\dagger\hat{\sigma}_l\hat{\sigma}_k]|\Psi_{m-1}\rangle. \tag{11.11}$$

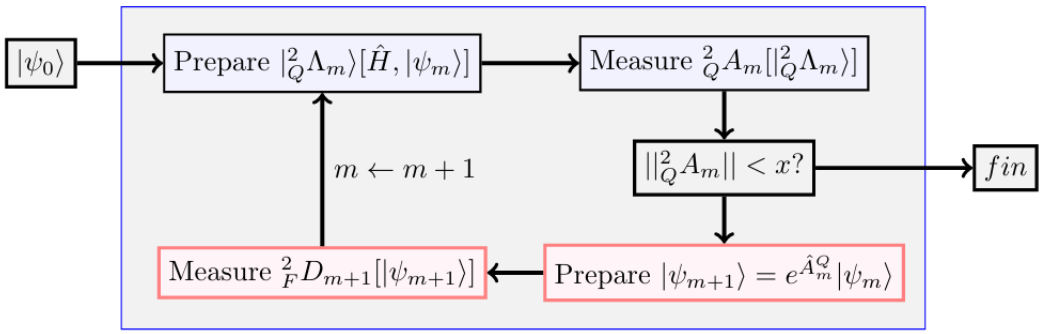

Figure 11.1: Unencoded CQE algorithm. Given some initial state that we can prepare on the quantum computer, we alternate between solving the unencoded ACSE on the quantum computer, and updating the new wave function given information from the unencoded ACSE.

The residual of the unencoded ACSE at the m^{th} iteration equals the gradient of the energy with respect to the two-qubit-particle anti-Hermitian operator. Computation of the 2-RDM uses the definition in Eq. (11.7). Importantly, the CQE algorithm for solving the unencoded ACSE does not require fermionic encoding in the preparation of the wave function since the exponential Ansatz in Eq. (11.9) is expressed entirely in terms of qubit-particle creation and annihilation operators. Only the definitions of the 2-RDM and the Hamiltonian use fermionic second-quantized operators that require fermionic encoding into qubits for evaluation on quantum computers. A schematic of the CQE algorithm is shown in Fig. 11.1.

Following previous work [20], we can compute the residual of the ACSE through an auxiliary state

$$|{}^2_Q\Lambda_{m-1}\rangle = e^{-i\delta\hat{H}}|\Psi_{m-1}\rangle \tag{11.12}$$

such that

$${}^2_QA^{ij;kl}_m + \mathcal{O}(\delta^2) = \delta^{-1}\Im\left(\langle\Lambda_{m-1}|\hat{\sigma}^\dagger_i\hat{\sigma}^\dagger_j\hat{\sigma}_l\hat{\sigma}_k|\Lambda_{m-1}\rangle\right), \tag{11.13}$$

where $\Im(x)$ is the imaginary component of x and δ is a short time-like step, which for stochastic simulations should be larger than the sampling error. If the RDM solutions are complex, we can evaluate the residual by a centered finite difference using two auxiliary states at $\pm\delta$ [20]. The approximation from a finite δ can potentially be minimized by using

extrapolative techniques as in the unitary decomposition of operators [36]. As discussed in the Appendix, the evaluation of the residual via the auxiliary state can be implemented efficiently in terms of the two-qubit gate count through first-order or Cholesky factorizations of the Hamiltonian. For completeness we also note that it is possible to compute the residual without defining an auxiliary state but that the required tomography involves the measurement of a 4-particle RDM.

11.2.3 Second-order Corrections to the Wave Functions and 2-RDMs

Solution of either the encoded or unencoded ACSE can be accelerated through a second-order correction at each iteration. We have the following generalized exponential expansions

$$\mathrm{e}^{\hat{B}^{\mathrm{F}}_m} \cdots \mathrm{e}^{\hat{B}^{\mathrm{F}}_2} \mathrm{e}^{\hat{B}^{\mathrm{F}}_1} |\Psi_0\rangle \tag{11.14}$$

and

$$\mathrm{e}^{\hat{B}^{\mathrm{Q}}_m} \cdots \mathrm{e}^{\hat{B}^{\mathrm{Q}}_2} \mathrm{e}^{\hat{B}^{\mathrm{Q}}_1} |\Psi_0\rangle \tag{11.15}$$

in which

$$\hat{B}^{\mathrm{F}}_m = \hat{A}^{\mathrm{F}}_m + \hat{C}^{\mathrm{F}}_m \tag{11.16}$$

and

$$\hat{B}^{\mathrm{Q}}_m = \hat{A}^{\mathrm{Q}}_m + \hat{C}^{\mathrm{Q}}_m \tag{11.17}$$

where either $\hat{C}^{\mathrm{F}}_m$ or $\hat{C}^{\mathrm{Q}}_m$ are modifications to the gradient direction and can be equal to (i) zero to recover the first-order Ansatz or (ii) a second-order correction such as that from a quasi-Newton method [37]. In general, a quasi-second-order correction accelerates convergence of the CQE, the implementation and further development of which is explored in concurrent work [38].

11.2.4 Connection between the Encoded and Unencoded ACSEs

Before we consider the relationship of the solutions to the encoded ACSE, or just ACSE, and the unencoded ACSE, we examine the relationship between the solution of the ACSE and the solution of the many-fermion Schrödinger equation. Consider the contracted Schrödinger equation (CSE) [34, 39, 40]

$$\langle\Psi|\hat{a}_i^\dagger\hat{a}_j^\dagger\hat{a}_l\hat{a}_k\left(\hat{H}-E\right)|\Psi\rangle = 0. \tag{11.18}$$

If we expand the wave function in terms the eigenfunctions of the Hamiltonian

$$|\Psi\rangle = \sum_n c_n|\Psi_n\rangle, \tag{11.19}$$

we can formally write the CSE as

$$\sum_{mn} c_m^* c_n E_n \langle\Psi_m|\hat{a}_i^\dagger\hat{a}_j^\dagger\hat{a}_l\hat{a}_k|\Psi_n\rangle - E = 0. \tag{11.20}$$

Because the CSE is equivalent to the energy variance which implies the Schrödinger equation, the CSE is satisfied by an N-fermion wave function if and only if the Schrödinger equation is satisfied [34, 39, 40]. Hence, the CSE is zero for the ground state if and only if the expansion coefficients c_n of excited states ($n > 1$) vanish. Substitution of the wave function expansion into the ACSE in Eq. (11.3) yields the expression

$$\sum_{mn} c_m^* c_n \left(E_n - E_m\right) \langle\Psi_m|\hat{a}_i^\dagger\hat{a}_j^\dagger\hat{a}_l\hat{a}_k|\Psi_n\rangle. \tag{11.21}$$

As with the CSE, the ACSE is zero if the expansion coefficients c_n of excited states ($n > 1$) vanish. This condition also implies the CSE as well as the Schrödinger equation. In contrast to the CSE, however, the ACSE does not strictly imply the Schrödinger equation [24]. It

is theoretically possible for the ACSE to vanish due to a cancellation of the anti-Hermitian terms, which in the expansion are represented by the energy differences $(E_n - E_m)$. Practical calculations, however, indicate that such cancellations do not occur easily and that the ACSE can in principle be converged to exact ground-state energies and 2-RDMs, especially with quasi-second-order corrections.

To understand the relationship between the solutions of the ACSE and unencoded ACSE, we express the residuals of both equations in terms of two parts

$$\underset{\mathrm{F}}{{}^{2}}A_{kl}^{ij} = \langle\Psi|[\hat{H}, \hat{a}_i^\dagger \hat{a}_j^\dagger \hat{a}_l \hat{a}_k]|\Psi\rangle_+ + \langle\Psi|[\hat{H}, \hat{a}_i^\dagger \hat{a}_j^\dagger \hat{a}_l \hat{a}_k]|\Psi\rangle_- \tag{11.22}$$

and

$$\underset{\mathrm{Q}}{{}^{2}}A_{kl}^{ij} = \langle\Psi|[\hat{H}, \hat{\sigma}_i^\dagger \hat{\sigma}_j^\dagger \hat{\sigma}_l \hat{\sigma}_k]|\Psi\rangle_+ + \langle\Psi|[\hat{H}, \hat{\sigma}_i^\dagger \hat{\sigma}_j^\dagger \hat{\sigma}_l \hat{\sigma}_k]|\Psi\rangle_- \tag{11.23}$$

where the plus (minus) indicates the contributions from the wave function to the expectation value with net even (odd) permutations of particles. Because the fermion and qubit-particle expectation values differ only from the sign of the odd permutations, we have the following two important relations

$$\langle\Psi|[\hat{H}, \hat{\sigma}_i^\dagger \hat{\sigma}_j^\dagger \hat{\sigma}_l \hat{\sigma}_k]|\Psi\rangle_+ = +\langle\Psi|[\hat{H}, \hat{a}_i^\dagger \hat{a}_j^\dagger \hat{a}_l \hat{a}_k]|\Psi\rangle_+ \tag{11.24}$$

$$\langle\Psi|[\hat{H}, \hat{\sigma}_i^\dagger \hat{\sigma}_j^\dagger \hat{\sigma}_l \hat{\sigma}_k]|\Psi\rangle_- = -\langle\Psi|[\hat{H}, \hat{a}_i^\dagger \hat{a}_j^\dagger \hat{a}_l \hat{a}_k]|\Psi\rangle_-. \tag{11.25}$$

Substituting these relations into the residual of the unencoded ACSE yields the following equation

$$\underset{\mathrm{Q}}{{}^{2}}A_{kl}^{ij} = \langle\Psi|[\hat{H}, \hat{a}_i^\dagger \hat{a}_j^\dagger \hat{a}_l \hat{a}_k]|\Psi\rangle_+ - \langle\Psi|[\hat{H}, \hat{a}_i^\dagger \hat{a}_j^\dagger \hat{a}_l \hat{a}_k]|\Psi\rangle_- \tag{11.26}$$

Comparing this equation for the qubit-particle residual with the fermion residual in Eq. (11.22), we observe that the only difference in the two residuals is the sign change of the second term. If both the plus and minus terms converge to zero, then both the ACSE and unencoded ACSE

produce identical solutions. While it is in principle possible for the plus and minus terms to produce a spurious solution through an exact cancellation, because the Schrödinger equation implies both the ACSE and the unencoded ACSE, both the positive and negative terms will tend to zero as the energy is minimized towards a stationary state by either encoded or unencoded unitary transformations. The relative magnitudes of the residuals $||^2_{\mathrm{F}}A||$ and $||^2_{\mathrm{Q}}A||$ are related to the relative rates of convergence of the ACSE and the unencoded ACSE. A larger residual norm indicates less cancellation of the plus and minus terms which is likely to result in a faster rate of convergence towards the solution of the Schrödinger equation.

11.2.5 Practical Considerations of the CQE Algorithm

Finally, we introduce two practical aspects of the CQE , applicable to both encoded and unencoded variants, that are important for its implementation on a quantum computer. We discuss: (i) a sparsification of the $\hat{A}_m$ operators in which at each iteration matrix elements below a given threshold are set to zero, and (ii) an approximate combination of $\hat{A}_{m-n}$ operators for $n \in [0, p]$ in which parts of the set of $p+1$ operators are combined to decrease the circuit length. Given the matrix elements of the residual of the encoded or unencoded ACSE in Eqs. (11.6) or (11.11), respectively, we define a sparsification operation that zeros matrix elements below a given threshold

$$ {}^2\tilde{A}^{ij;kl}_m = \textsc{sparse}[c]({}^2A^{ij;kl}_m) = \begin{cases} 0 & \text{if } |{}^2A^{ij;kl}_m| < c||{}^2A_m||_\infty \\ {}^2A^{ij;kl}_m & \text{if } |{}^2A^{ij;kl}_m| \geq c||{}^2A_m||_\infty \end{cases}, \tag{11.27} $$

where the scalar factor $c \in [0, 1]$ and the infinity norm $||A||_\infty$ of A is the element with the largest absolute value. When $c = 0$, $\textsc{sparse}[0]$ is equivalent to the identity mapping, and when $c = 1$, $\textsc{sparse}[1]$ is equivalent to selecting only the highest amplitude element. Given a choice of the parameter c, we use this mapping at each iteration of the CQE to prune the residual matrix ${}^2A_m$. Formally, at each iteration ${}^2A_m$ is replaced by ${}^2\tilde{A}_m$.

After defining a sparser matrix ${}^2\tilde{A}_m$ in $\hat{A}_m$, we still need to express the operator $\hat{A}_m$ as a product of unitary transformations, which is traditionally performed by trotterization. We choose a first-order trotterization which is valid in the case that $||{}^2\tilde{A}_m||$ is not too large. Moreover, because the algorithm is greedy by design with the gradient being used at each iteration, the algorithm has the ability to adjust itself in part to errors in previous iterations including those from trotterization.

To address the growth of the circuit length with iterations, we define an approximate combination of $\hat{A}_{m-n}$ operators for $n \in [0, p]$, which we call the p-depth. When updating the wave function at the m^{th} iteration, we examine the elements of ${}^2A_m^{ij;kl}$ that were not pruned in one of the p previous steps. If ${}^2\tilde{A}_{m-n}^{ij;kl}$ for an n in $[0, p]$ is non-zero, we update that term as follows:

$$ {}^2\tilde{A}_{m-n}^{ij;kl} \leftarrow {}^2\tilde{A}_{m-n}^{ij;kl} + {}^2A_m^{ijkl}. \tag{11.28}$$

In this manner we collect terms to decrease circuit length even if the collection is approximate. Importantly, the computed residual of the ACSE at the next iteration adjusts for errors introduced in previous terms in the product expansion of the wave function. Other works exploit a classification of the commutating operators in the Hamiltonian or the unitary transformation of the wave function to minimize the circuit length, and these schemes can also be applied to the CQE algorithm.

The p-depth and SPARSE[c] techniques are closely related, and in their extreme limits they produce specific Ansätze. For $c = 1$, a large p is reasonable, because each iteration will contain only one or a few terms, and hence, setting $p = 1$ or $p = 2$ will not simplify the product of terms. On the other hand, when $c = 0$, setting $p = 1$ or $p = 2$ may be necessary because a larger p may generate a single exponential Ansatz, which negates a critical benefit of the CQE—the ACSE Ansatz for the wave function.

11.3 Applications

11.3.1 Molecular Simulations

We compare the encoded and unencoded CQE for several molecular systems, H_4, H_5, H_6, as well as hydrogen fluoride, at equilibrium geometries in the minimal Slater-type orbital basis (STO-3G) set [41]. The convergence of the two CQE algorithms is shown in Fig. 11.2. For H_6 we select $c = 1$ in the truncation, whereas for the other cases $c = 0.1$. In all cases the encoded and unencoded algorithms show convergence towards the solution of the Schrödinger equation in the given basis set even without any second-order acceleration of the transformations at each iteration. In some instances, the two algorithms can exhibit nearly identical convergence, especially in systems with significant pairing of the orbitals, as in an antisymmetrized geminal power wave function [42–45], where the particle statistics become less important [46]. One such example is hydrogen fluoride whose hole wave function in the minimal basis set is a single two-hole function or a geminal. The molecule H_5 exhibits greater differences between the fermionic and qubit-particle Ansätze, which is expected for open-shell or strongly correlated molecules.

To examine performance for non-equilibrium geometries, we apply the encoded and unencoded CQE to computing the potential energy curves of H_4 and O_2. We use approximate second-order transformations, based on a qusi-Newton method, as each iteration to accelerate convergence. Figure 11.3 shows the obtained energies across the dissociation curve. For a convergence criteria of 0.001 in the ACSE's residual norm, we consistently obtain high accuracy results at both equilibrium and non-equilibrium geometries regardless of the encoding.

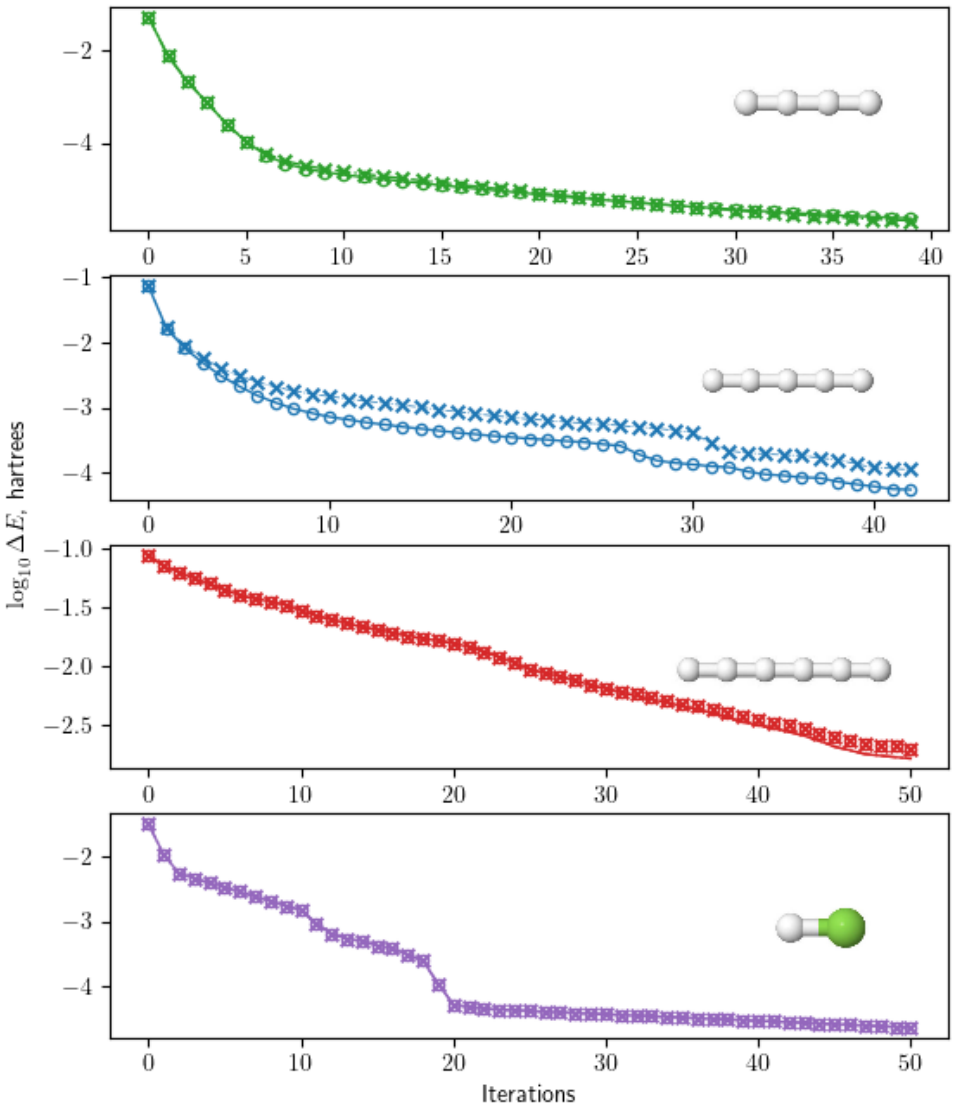

Figure 11.2: Depictions of the quantum ACSE with an unencoded ${}^{2}_{Q}A_n$ ($\times$) and an encoded ${}^{2}A_n$ ($\circ$) for linear H_4, H_5, H_6 and hydrogen fluoride at equilibrium bond distance (in the STO-3G basis). For most systems, nearly identical rates of convergence are obtained with similar accuracy.

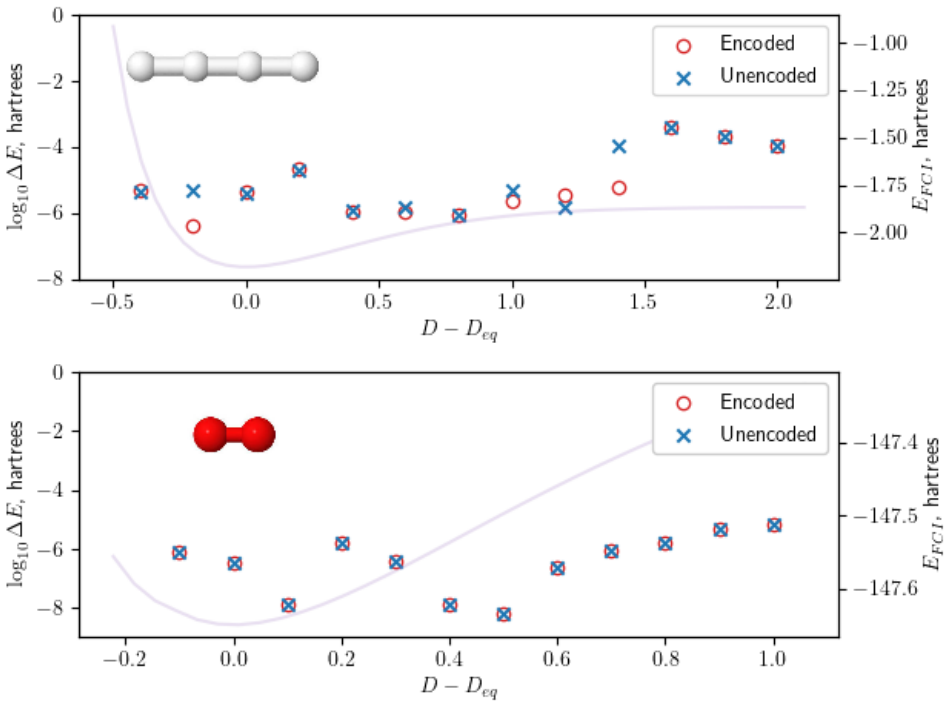

Figure 11.3: Dissociation plots for 8 qubit simulations of H_4 and a 6-electron and 4-orbital active space of O_2 with the encoded and unencoded CQE. Convergence criteria is 0.001 for the norm of the ${}^2B$ matrix which contains a correction to the ${}^2A$ matrix from a second-order approach. A quasi-Newton quantum CQE approach which adjusts the step direction based on a limited-memory Broyden-Fletcher-Goldarb-Shanno (BFGS) approach, where 2 or 3 vectors are stored. More details regarding this method will be presented in a subsequent work. Both the encoded and unencoded CQE exhibit similar accuracy at both equilibrium and non-equilibrium geometries.

11.3.2 Investigation of Resource Requirements

We examine the resource requirements for the encoded and unencoded methods. Two cases, equilibrium and stretched geometries of linear H_4, are considered. We examine the necessary resources to converge the residual of the ACSE within 0.01 as a function of the p-depth and the SPARSE c parameter with results in Table 11.1.

First, in the equilibrium case (top half), for $c = 1$, neither the fermionic nor the qubit-particle Ansatz changes with depth but each requires more iterations than when $c = 0$ or $c = 0.1$. In all of the instances, the qubit-particle wave function matches the fermionic wave function's trends but has 70±3% of the fermionic CNOT cost. Additionally, the p-depth leads to a significant reduction in the number of terms. Including the previous iteration ($p = 1$) results in 55% of the $p = 0$ count for $c = 0$, and 66% of the $p = 0$ count for $c = 0.1$ (equivalent circuits for $c = 1$). The $p = 3$ case shows even further reductions, requiring about 13% and 34% of the $p = 0$ cost for the $c = 0$ and $c = 0.1$ cases, respectively. We can reasonably infer that the p-depth and SPARSE of the ${}^2A$ operator can greatly impact the CQE's resource requirements as well as its rate of convergence.

For the stretched geometries the savings are more difficult to analyze. For $c = 1$ again we have a similar picture across p-depths, with notably more iterations required than for the equilibrium case. Again, the qubit case appears to have a similar advantage in the the CNOT gate reduction versus the fermionic case. For other truncations, we lose the correspondence between the qubit-particle and fermionic wave functions. For multiple cases (i.e., when $(c, p) = (0, 0), (0.1, 3), (0.1, 0)$), the qubit case requires either more iterations or yields a higher CNOT gate count. However, the shortest apparent Ansatz is still the qubit $c = 0,\ p = 3$ case. The difference in the p-depth plays a more significant role, which leads to almost a 100-fold decrease in CNOT requirements between $p = 3$ and $p = 0$ for $c = 0$, as well as a similar trend for $c = 0.1$.

While it is clear that low CNOT cases overall can be found with the $c = 1$ instance,

Table 11.1: Comparing the p-depth and differing values of SPARSE$[c]$ (for ${}^{2}_{F}A$ and ${}^{2}_{Q}A$ in terms of their elements relative to the largest element) for two different lengths of H_4, in terms of the maximal CNOT gate count and number of iterations (in brackets, $[\cdot]$). A stopping criteria of 0.01 is selected for the gradient, and a quadratic trust-region step is used for choosing the step length at each step. For each instance, a similar accuracy is achieved in the fermionic and qubit cases, and for the most part, the qubit results displays a constant reduction in the number of necessary CNOT gates.

$D = D_{eq}$

	SPARSE$[c]$	$p-$depth			Average ΔE
		$p=3$	$p=1$	$p=0$	
${}^{2}_{F}\hat{A}_n$	$c=0$	1568 [9]	6782 [9]	12494 [9]	$2*10^{-5}$
	$c=\frac{1}{10}$	2020 [8]	3858 [8]	6068 [8]	$3*10^{-5}$
	$c=1$	1263 [16]	1408 [16]	1408 [16]	$3*10^{-5}$
${}^{2}_{Q}\hat{A}_n$	$c=0$	1162 [9]	4974 [9]	9014 [9]	$2*10^{-5}$
	$c=\frac{1}{10}$	1414 [8]	2756 [8]	4098 [8]	$3*10^{-5}$
	$c=1$	840 [16]	928 [16]	928 [16]	$4*10^{-5}$
$D = D_{eq} + 1\text{Å}$					
${}^{2}_{F}\hat{A}_n$	$c=0$	1558 [37]	46146 [60]	56058 [38]	$6*10^{-4}$
	$c=\frac{1}{10}$	1574 [26]	34190 [45]	38706 [30]	$7*10^{-4}$
	$c=1$	10468 [146]	12190 [161]	12322 [161]	$2*10^{-4}$
${}^{2}_{Q}\hat{A}_n$	$c=0$	1162 [19]	41992 [80]	102540 [95]	$5*10^{-4}$
	$c=\frac{1}{10}$	10938 [42]	26840 [52]	85324 [86]	$7*10^{-4}$
	$c=1$	6814 [155]	7376 [141]	7464 [141]	$3*10^{-4}$

there is potentially a trade off with the number of iterations. Figure 11.4 explores the total resource count for the two H_4 geometries that accounts for the number of iterations, circuit measurements, and function and gradient evaluations. In the equilibrium case the lowest resource count for both the encoded and unencoded CQE is not $c = 0$ but $c = 0.1$ with $p = 3$. The highest, on the other hand, is $c = 0$ and $p = 0$, which highlights the importance of simplifying the Ansatz. Additionally, in all cases the unencoded Ansatz outperforms the encoded Ansatz. The non-equilibrium geometry yields a similar picture to the equilibrium geometry, albeit at higher costs overall. The key difference arises for $c = 0$ and $p = 3$ where significant improvements visible. Results indicate that the qubit-particle Ansatz can require more resources than the fermionic one, and that care should be taken in choosing both c and p.

11.3.3 Generation of the ${}^{2}_{Q}A$ Matrix

In the ACSE scheme, a clear advantage of the unencoded ACSE Ansatz is in the tomography of the ${}^{2}_{Q}A$ matrix, which as seen in prior work [47] results in a potentially logarithmic scaling entity. We show a basic comparison between the Jordan-Wigner transformation and the qubit-particle transformation in Fig. 11.5. The left side shows the effective scaling with respect to the number of qubits, i.e. r in $O(q^r)$. The right side shows the ratio of vertices to cliques in the corresponding graph problem, which is the ratio of the number of measured 2-RDM element contributions which can be recovered per grouping.

It is known that the grouping fermionic tomography is challenging due to the antisymmetry requirement that results in non-local groupings [15, 47]. Despite this challenge, the $O(r^4)$ cost of 2-RDM tomography in molecular systems can be reduced by grouping to an $O(r^3)$ scheme [48] while even lower scaling schemes can be accomplished with additional swap circuits [47], as well as with random unitary sampling techniques [49]. We obtain our circuits through a graph theoretic approach with symmetry projection [50]. In the qubit

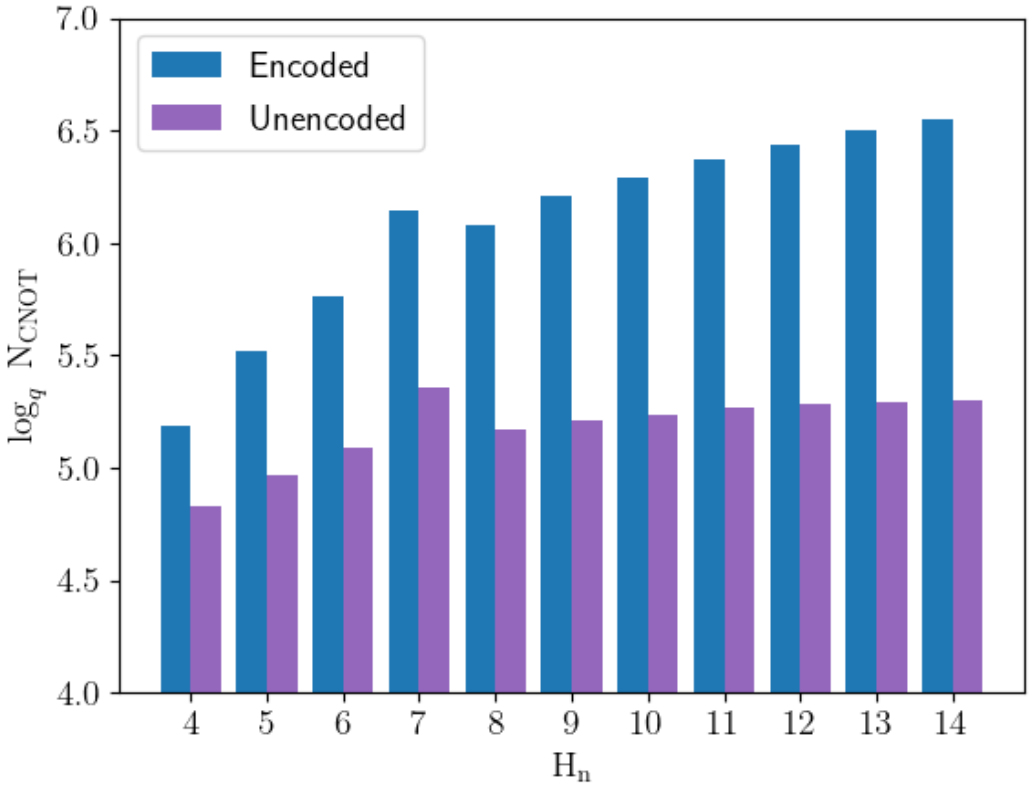

Figure 11.4: Comparison of total resource count (given in $\log_{10}$ number of CNOT gates required) for equilibrium (left) and non-equilibrium (right) H_4 geometries, mirroring data seen in Table 11.2. The vertical axis contains information on whether encoded or unencoded operators are used, as well as the sparsification of ${}^2A$. The horizontal axis indicates the p-depth, or the number of previous iterations in the Ansatz to which terms are added. The resource count also accounts for the number of fermionic energy and gradient evaluations.

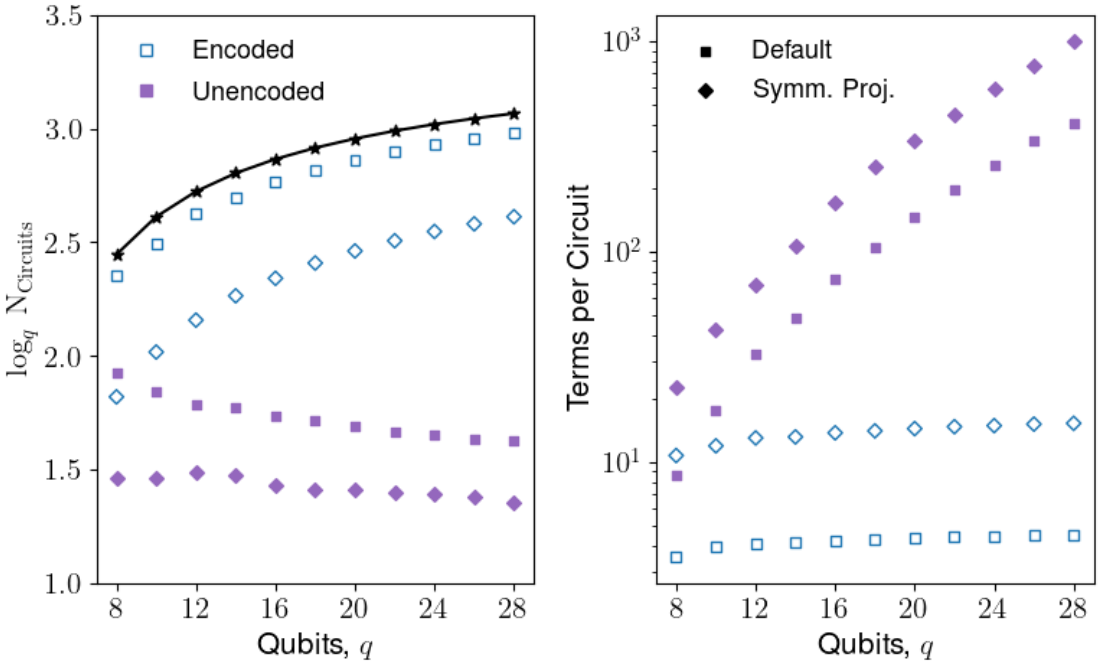

Figure 11.5: (Left) Effective scaling of the tomographic complexity of the qubit-particle and fermionic ${}^2A$ matrices (under the Jordan-Wigner transformation) with symmetry projection of $\hat{N}$ and $\hat{S}_z$. The top and bottom black bars represent estimates of the complexity from the number of terms ((Right) the number of vertices per measurement group under a coloring scheme. In particular, while this number is constant for fermionic tomography, for the qubit operators this number increases at a nearly exponential rate.

case for a $k-$local operator, however, one can achieve a logarithmic scaling through known combinatorical schemes [47]. In our unencoded, qubit-particle case, a $k-$body excitation embodies only k- to $\frac{k}{2}$-body operators, and so does not span the full k-body operator space. Consequently, the measurement scheme provides a super-linear scaling in required circuit preparation. As an example, for 28 qubits with over 200 million possible quantum states, the 2-RDM has 92092 elements, and in the scheme represented in Fig. 11.5 requires 6036 measurements in the encoded case, but only 92 measurements in the unencoded case.

Because the unencoded ACSE cannot be formulated in terms of qubit-RDMs alone, we implement $e^{i\delta H}$ through the tomography of an auxiliary state, which still requires the use of fermionic operators. While it might make sense to simply measure the partially encoded

operators on a quantum computer, similar to measuring the 3-RDM in the encoded case, the scaling of the resulting 4-RDM like object is currently prohibitive for more than small systems. although utilizing measurement schemes, such as shadow tomography, might yield more efficient approximations in the future.

Table 11.2 presents the cost of evaluating the ACSE residual via Eq. 11.13 in both the encoded and unencoded CQE for a first-order Trotterization and a Cholesky decomposition of the Hamiltonian. The total number of CNOT counts is a product of the number of circuits and the scaling of the operator, in terms of the number of qubits. In the case of the Cholesky decomposition, we take the product of the number of distinct Cholesky terms and the number of unencoded or encoded 2-RDM terms. The unencoded ACSE with the Cholesky decomposition approach generally yields the most favorable scaling. Additionally, the average number of CNOT gates required for each auxillary state using the Cholesky decomposition is orders of magnitude smaller than the number from the corresponding first-order trotterized approach, and hence, Cholesky decomposition is likely much more suitable for near-term approaches.

11.4 Discussion

While the wave function from many electronic structure methods such as coupled cluster theory require significant alterations for implementation on quantum computers, the iterative solution of the ACSE naturally generates a wave function that is assembled from products of two-body unitary transformations that are amenable to implementation on a quantum computer. Solution of the ACSE on a quantum computer—a CQE algorithm—does not require approximate reconstruction of the 3-RDM like its classical counterpart [20, 23], and hence, at least in the absence of device noise, can yield energies and 2-RDMs that are in agreement with those from full configuration interaction. In this paper we further develop the theory and results from Mazziotti *et al.* [3] for solving the CQE with an unencoded wave

Table 11.2: Upper bounds on the number of CNOT gates for evaluation of the residuals of the unencoded and encoded ACSE on the quantum computer for numerous systems. The hydrogen chains ($H_2 - H_{12}$ are in a minimal basis, with the exception of H_2 (DZ), which has a double zeta basis set. *Trotter* (or Trot.) refers to a first-order trotterization, *CD* $\langle$CNOT$\rangle$ to the average number of CNOT gates per decomposed term in the Cholesky decomposition, and *Order* refers to the number of terms in the Cholesky decomposition. We use a threshold of 10^{-6} in the Cholesky decomposition, but more (or less) strict truncations can be taken. The bottom portion of the graph refers to the effective scaling in terms of total number of applied CNOT gates.

	H_2	H_4	H_6	H_8	H_{10}	H_{12}	N_2	H_2 (DZ)	C_2H_2
Trotter CNOT	36	1088	12020	63760	191868	416168	38868	38868	102016
CD $\langle$CNOT$\rangle$	15	81	188	257	521	700	196	184	263
Order	4	8	12	16	20	24	49	55	70
Total of CNOTs for Auxiliary Simulation, $\log_q$									
Encoded, Trot.	3.6	5.2	5.9	6.3	6.5	6.6	6.0	6.0	6.2
Encoded, CD	3.9	4.9	5.3	5.3	5.6	5.6	5.5	5.5	5.6
Unencoded, Trot.	3.6	4.7	5.1	5.3	5.4	5.3	4.8	4.8	4.9
Unencoded, CD	3.9	4.4	4.4	4.3	4.4	4.3	4.4	4.4	4.3

function, a wave function expressed in terms of qubit particles rather than fermions.

Results show that the encoded and unencoded CQE yield similar accuracy across a variety of molecules at both equilibrium and non-equilibrium geometries. As we discussed in Ref. [3] and the theory section here, the flexibility provided by the product of unencoded two-body operators is similar to the encoded operators. Unlike the hardware-efficient wave functions that do not specify the particle statistics and hence, have a many-to-one mapping to the fermion wave functions, the qubit-particle wave functions have an isomorphic mapping to the fermionic wave functions that can help to prevent optimization difficulties such as barren plateaus [51]. Moreover, the highly commutative structure of the qubit-particle operators can be more easily leveraged than their equivalent fermionic operators to generate more compact state preparations and more efficient tomographies.

Qubit-particle wave functions have recently been applied in the coupled cluster singles-doubles (CCSD) Ansatz [14, 16] as well as in hybrid VQE schemes like the ADAPT-VQE [19, 52]. In UCCSD the use of qubit particles has been shown to produce a linear scaling reduction

in the number of CNOT gates. While the qubit-particle UCCSD can be less accurate than fermionic UCCSD due to the highly nonlinear nature of the Ansatz, in the calculations shown here the unencoded CQE can use its iterative formulation to continue its convergence towards the solution of the contracted equation. The present theory and results provide a first step in exploring CQE algorithms for solving the unencoded ACSE. Future work will consider further improvements from exploiting more compact wave functions as well as additional applications to larger molecules and materials.

11.5 Conclusion

Quantum simulation has the potential to reduce the cost of solving many-fermion problems. Because quantum computers are based on qubits, however, their natural particles are not fermions but rather hard-core bosons known as qubit particles. We have recently shown that there exists an isomorphism between fermion wave functions and qubit-particle wave functions, which suggests a natural parameterization of the *two-fermion* RDM in terms of the qubit-particle wave function that avoids fermionic encoding of the wave function. Here we demonstrate that the recently proposed CQE algorithm for computing 2-RDMs by quantum simulation can be adapted to use unencoded qubit-particle wave functions rather than fermionic wave functions. The unencoded CQE has similar theoretical accuracy as the encoded CQE, which can be converged to the exact, finite-basis solution of the Schrödinger equation at least in the absence of quantum-device noise. We illustrate the unencoded CQE's convergence, cost, and accuracy relative to that of the encoded CQE by quantum simulations of molecules at both equilibrium and non-equilibrium geometries. Results show that the unencoded CQE has the potential in many cases to reduce the cost of quantum simulations of many-fermion problems without sacrificing accuracy even for strongly correlated systems.

11.6 Appendix

ACSE Residuals from Hamiltonian Factorizations

On near-term devices Hamiltonian simulation is challenging due to the generally high number of multi-qubit gates required, though numerous optimal approaches exist with varying resource requirements [53–55]. Because we are interested in only a very small time step, we can exploit first-order approximations such as decomposing $\exp(i\delta\hat{H})$ as a sum of smaller, easier to implement operators, $\exp(i\delta H_p)$. If we take $|\Lambda^p_{m-1}\rangle$ to be auxiliary states of these operators, we can express the residuals as:

$$ {}^2_Q A^{ij;kl}_m + \mathcal{O}(\delta^2) = \sum_p \delta^{-1} \Im \langle \Lambda^p_{m-1} | \hat{\sigma}^\dagger_i \hat{\sigma}^\dagger_j \hat{\sigma}_l \hat{\sigma}_k | \Lambda^p_{m-1} \rangle. \tag{11.29} $$

The extreme of this strategy would be to simulate separately every term ${}^2K^{pr}_{qs}$ of the Hamiltonian. This approach would not only lead to a substantial increase in the required sampling from the addition of $O(r^4)$ terms but also be most likely less efficient than exponentiating the 2-RDM operators and then taking the expectation of $\hat{H}$. Utilizing the commutative structure of the 2-RDM allows for more effective grouping, and a native $O(r^3)$ grouping pattern of Hamiltonian terms should be viable, similar to tomography-based grouping schemes.

Another approach involves decomposing the Hamiltonian, such as with the Cholesky decomposition of the two-electron integrals [56–59]. While this offers benefits in both the encoded and unencoded 2-RDMs, this approach is potentially more practical in the latter case because of the substantial difference in the number of measurements required to measure the encoded and unencoded 2-RDMs, which we show in the Applications.

Computational Details

A pivoted Cholesky decomposition [60] is utilized to obtain properly ordered terms in the Cholesky decomposition. The PYTHON module HQCA as well as QISKIT [61] are used, with electron integrals obtained through PySCF [62, 63].

References

[1] D. S. Abrams and S. Lloyd, Physical Review Letters **79**, 2586 (1997), arXiv:9703054 [quant-ph] .

[2] J. D. Whitfield, J. Biamonte, and A. Aspuru-Guzik, Molecular Physics **109**, 735 (2011), arXiv:1001.3855 .

[3] D. A. Mazziotti, S. E. Smart, and A. R. Mazziotti, New Journal of Physics **23**, 113037 (2021), arXiv:2101.11607 .

[4] L.-A. Wu and D. A. Lidar, Journal of Mathematical Physics **43**, 4506 (2002), arXiv:0109078 [quant-ph] .

[5] R. P. Feynman, International Journal of Theoretical Physics **21**, 467 (1982).

[6] P. Jordan and E. Wigner, Zeitschrift für Physik **47**, 631 (1928).

[7] S. B. Bravyi and A. Y. Kitaev, Annals of Physics **298**, 210 (2002), arXiv:0003137 [quant-ph] .

[8] J. T. Seeley, M. J. Richard, and P. J. Love, The Journal of Chemical Physics **137**, 224109 (2012), arXiv:1208.5986 .

[9] M. B. Hastings, D. Wecker, B. Bauer, and M. Troyer, arXiv (2014), arXiv:1403.1539 .

[10] D. Wecker, B. Bauer, B. K. Clark, M. B. Hastings, and M. Troyer, Physical Review A - Atomic, Molecular, and Optical Physics **90**, 1 (2014), arXiv:1312.1695 .

[11] A. Kandala, A. Mezzacapo, K. Temme, M. Takita, M. Brink, J. M. Chow, and J. M. Gambetta, Nature **549**, 242 (2017), arXiv:1704.05018 .

[12] A. Choquette, A. Di Paolo, P. K. Barkoutsos, D. Sénéchal, I. Tavernelli, and A. Blais, arXiv , 1 (2020), arXiv:2008.01098 .

[13] G. S. Barron, B. T. Gard, O. J. Altman, N. J. Mayhall, E. Barnes, S. E. Economou, and V. Tech, arXiv , 1 (2020), arXiv:arXiv:2003.00171v1 .

[14] R. Xia and S. Kais, Quantum Science and Technology **6**, 15001 (2020), arXiv:2005.08451 .

[15] A. F. Izmaylov, T.-C. Yen, R. A. Lang, and V. Verteletskyi, Journal of Chemical Theory and Computation **16**, 190 (2020), arXiv:1907.09040 .

[16] I. G. Ryabinkin, T. C. Yen, S. N. Genin, and A. F. Izmaylov, Journal of Chemical Theory and Computation **14**, 6317 (2018), arXiv:1809.03827 .

[17] I. G. Ryabinkin, R. A. Lang, S. N. Genin, and A. F. Izmaylov, Journal of Chemical Theory and Computation **16**, 1055 (2020), arXiv:1906.11192 .

[18] I. G. Ryabinkin, A. F. Izmaylov, and S. N. Genin, Quantum Science and Technology **6** (2021), 10.1088/2058-9565/abda8e, arXiv:2009.13622 .

[19] H. L. Tang, V. Shkolnikov, G. S. Barron, H. R. Grimsley, N. J. Mayhall, E. Barnes, and S. E. Economou, PRX Quantum **2**, 020310 (2021), arXiv:1911.10205 .

[20] S. E. Smart and D. A. Mazziotti, Physical Review Letters **126**, 070504 (2021), arXiv:2004.11416 .

[21] J.-N. Boyn, A. O. Lykhin, S. E. Smart, L. Gagliardi, and D. A. Mazziotti, The Journal of Chemical Physics **155**, 244106 (2021), arXiv:2106.11972 .

[22] S. E. Smart, J.-N. Boyn, and D. A. Mazziotti, Physical Review A **105**, 022405 (2022), arXiv:2103.06876 .

[23] D. A. Mazziotti, Physical Review Letters **97**, 143002 (2006).

[24] D. A. Mazziotti, Physical Review A - Atomic, Molecular, and Optical Physics **75**, 1 (2007).

[25] D. A. Mazziotti, Physical Review A - Atomic, Molecular, and Optical Physics **76**, 1 (2007).

[26] G. Gidofalvi and D. A. Mazziotti, Journal of Chemical Physics **127** (2007), 10.1063/1.2817602.

[27] A. E. Rothman, J. J. Foley, and D. A. Mazziotti, Physical Review A **80**, 1 (2009).

[28] J. W. Snyder and D. A. Mazziotti, Phys. Chem. Chem. Phys. **14**, 1660 (2012).

[29] A. M. Sand and D. A. Mazziotti, The Journal of Chemical Physics **143**, 134110 (2015).

[30] J. N. Boyn and D. A. Mazziotti, Journal of Chemical Physics **154** (2021), 10.1063/5.0045007, arXiv:2104.00626 .

[31] A. Peruzzo, J. McClean, P. Shadbolt, M.-H. Yung, X.-Q. Zhou, P. J. Love, A. Aspuru-Guzik, and J. L. O'Brien, Nature Communications **5**, 4213 (2014), arXiv:1304.3061 .

[32] J. R. McClean, J. Romero, R. Babbush, and A. Aspuru-Guzik, New Journal of Physics **18**, 023023 (2016), arXiv:1509.04279 .

[33] J. Romero, R. Babbush, J. R. McClean, C. Hempel, P. J. Love, and A. Aspuru-Guzik, Quantum Science and Technology **4**, 1168 (2019), arXiv:1701.02691 .

[34] D. A. Mazziotti, Physical Review A **57**, 4219 (1998).

[35] D. a. Mazziotti, Chemical Physics Letters **289**, 419 (1998).

[36] A. W. Schlimgen, K. Head-Marsden, L. M. Sager, P. Narang, and D. A. Mazziotti, Physical Review Letters **127**, 270503 (2021), arXiv:2106.12588 .

[37] J. Nocedal and S. J. Wright, *Numerical Optimization*, Springer Series in Operations Research and Financial Engineering (Springer New York, 2006).

[38] S. E. Smart and D. A. Mazziotti, Unpublished work (2022).

[39] D. A. Mazziotti, ed., *Advances in Chemical Physics*, Advances in Chemical Physics, Vol. 134 (John Wiley & Sons, Inc., Hoboken, NJ, USA, 2007) p. 574.

[40] H. Nakatsuji, Physical Review A **14**, 41 (1976).

[41] J. A. Hehre, W. J.; Ditchfield, R.; Pople, J. Chem. Phys. **56**, 2257 (1972).

[42] A. J. Coleman, International Journal of Quantum Chemistry **63**, 23 (1997).

[43] A. Coleman and V. Yukalov, *Reduced Density Matrices: Coulson's Challenge* (Springer, Berlin Heidelberg New York, 2000).

[44] P. A. Johnson, P. W. Ayers, P. A. Limacher, S. D. Baerdemacker, D. V. Neck, and P. Bultinck, Computational and Theoretical Chemistry **1003**, 101 (2013).

[45] T. Stein, T. M. Henderson, and G. E. Scuseria, Journal of Chemical Physics **140** (2014), 10.1063/1.4880819.

[46] L. A. M. Sager and D. A. Mazziotti, Physical Review Research **4**, 1 (2022).

[47] X. Bonet-Monroig, R. Babbush, and T. E. O'Brien, Physical Review X **10**, 031064 (2020), arXiv:1908.05628 .

[48] P. Gokhale and F. T. Chong, arXiv (2019), arXiv:1908.11857 .

[49] A. Zhao, N. C. Rubin, and A. Miyake, Physical Review Letters **127**, 110504 (2020), arXiv:2010.16094 .

[50] S. E. Smart and D. A. Mazziotti, Physical Review A **103**, 012420 (2021), arXiv:2008.06027 .

[51] J. R. McClean, S. Boixo, V. N. Smelyanskiy, R. Babbush, and H. Neven, Nature Communications **9**, 1 (2018), arXiv:1803.11173 .

[52] Y. S. Yordanov, V. Armaos, C. H. Barnes, and D. R. Arvidsson-Shukur, Communications Physics **4**, 1 (2021), arXiv:2011.10540 .

[53] D. W. Berry, A. M. Childs, and R. Kothari, Proceedings - Annual IEEE Symposium on Foundations of Computer Science, FOCS **2015-Decem**, 792 (2015), arXiv:1501.01715 .

[54] G. H. Low and I. L. Chuang, Quantum **3**, 163 (2019), arXiv:1610.06546 .

[55] J. Lemieux, B. Heim, D. Poulin, K. Svore, and M. Troyer, Quantum **4** (2020), 10.22331/Q-2020-06-29-287, arXiv:1910.01659 .

[56] N. H. F. Beebe and J. Linderberg, Int. J. Quant. Chem. **12**, 683 (1977).

[57] M. Motta, E. Ye, J. R. McClean, Z. Li, A. J. Minnich, R. Babbush, and G. K.-L. Chan, npj Quantum Information **7**, 83 (2021), arXiv:1808.02625 .

[58] E. G. Hohenstein and C. D. Sherrill, Journal of Chemical Physics **132** (2010), 10.1063/1.3426316.

[59] I. D. Kivlichan, J. McClean, N. Wiebe, C. Gidney, A. Aspuru-Guzik, G. K. L. Chan, and R. Babbush, Physical Review Letters **120**, 110501 (2018), arXiv:1711.04789 .

[60] H. Harbrecht, M. Peters, and R. Schneider, Applied Numerical Mathematics **62**, 428 (2012), third Chilean Workshop on Numerical Analysis of Partial Differential Equations (WONAPDE 2010).

[61] S. E. Smart and D. A. Mazziotti, "hqca - hybrid quantum computing algorithms for quantum chemistry," (2022).

[62] H. Abraham, AduOffei, R. Agarwal, I. Y. Akhalwaya, G. Aleksandrowicz, T. Alexander, M. Amy, E. Arbel, Arijit02, A. Asfaw, A. Avkhadiev, C. Azaustre, AzizNgoueya, A. Banerjee, A. Bansal, P. Barkoutsos, G. Barron, G. S. Barron, L. Bello, Y. Ben-Haim, D. Bevenius, A. Bhobe, L. S. Bishop, *et al.*, "Qiskit: An open-source framework for quantum computing," (2019).

[63] Q. Sun, T. C. Berkelbach, N. S. Blunt, G. H. Booth, S. Guo, Z. Li, J. Liu, J. D. McClain, E. R. Sayfutyarova, S. Sharma, S. Wouters, and G. K.-L. Chan, WIREs Computational Molecular Science **8**, e1340 (2018), https://onlinelibrary.wiley.com/doi/pdf/10.1002/wcms.1340 .

CHAPTER 12

ACCELERATED CONVERGENCE OF CONTRACTED QUANTUM EIGENSOLVERS THROUGH A QUASI-SECOND-ORDER, LOCALLY PARAMETERIZED OPTIMIZATION

The current chapter has been submitted for publication, authored by Scott E. Smart and David A. Mazziotti.

12.1 Introduction

The contracted Schrödinger equation (CSE),[1–3] describes the projection of the molecular Schrödinger equation for a N-electron system onto a two-electron space, which generates the stationary-state condition of the two-electron reduced density matrix (2-RDM) instead of the wavefunction. Satisfaction of the anti-Hermitian part of the contacted Schrödigner equation (ACSE) by a quantum state is equivalent to its invariance with respect to all infinitesimal two-body unitary transformations,[4–6] Solution of the ACSE for the 2-RDM was initially challenging because the equation depends on both the 2-RDM and three-electron RDM (3-RDM), making it indeterminate without additional information. However, the ACSE has been practically solved by reconstructing the 3-RDM by its cumulant expansion as an functional of the 2-RDM[4, 5, 7, 8] and applied to computing strongly correlated ground and excited states in both chemical reactions and conical intersections.[9–12]

Recently, the ACSE has been solved on quantum devices with applications to hydrogen chains as well as the benzyne isomers.[13–15] On a quantum computer the ACSE algorithm, known as a contracted quantum eigensolver (CQE), iteratively minimizes the residual of the ACSE in contrast to the variational quantum eigensolvers (VQE) that minimize the energy with respect to parameters according to the Rayleigh-Ritz variational principle. Instead of

propagating only the 2-RDM as in the classical algorithm, we propagate a wave function through state preparation on a quantum computer. Thus, we avoid reconstructed RDMs, as the 2-RDM can be directly measured from the quantum state while the ACSE residual can be directly measured from an auxiliary quantum state. The resulting ACSE algorithm is a potentially exact RDM approach that scales polynomially in the size of the molecular system.

In this paper we accelerate the convergence of the CQE for the ACSE by developing quasi-second-order algorithms with superlinear convergence. Convergence acceleration is important for avoiding the accumulation of noise on near-term intermediate-scale quantum (NISQ) computers as well as achieving highly accurate solutions on future fault-tolerant quantum devices. We draw upon research on optimization algorithms on manifolds,[16–18] which have applications across science and engineering from vision to robotics as well as related algorithms in electronic structure for orbital optimization.[19, 20] We specifically develop and implement a quasi-Newton scheme with the Broyden-Fletcher-Goldfarb-Shanno update and non-linear conjugate gradient algorithms. The quasi-second-order algorithms avoid storage of the Hessian matrix while providing superlinear convergence. We also demonstrate convergence properties as well as some approximate implementations of the search direction and finally compare the resulting CQE algorithms with classes of common quantum algorithms, including the variational quantum eigensolver.

12.2 Theory

We discuss the solution of the ACSE via CQE in section 12.2.1, the local parameterization of the wavefunction in section 12.2.2, the quasi-second-order accelerations in section 12.2.3, and resource optimization in section 12.2.4.

12.2.1 Solution of the ACSE

Given a molecular system with Hamiltonian $\hat{H}$, we can write a contraction of the Schrödinger equation onto the two-particle space, known as the contracted Schrödinger equation (CSE):

$$\langle\Psi|\hat{H}\hat{a}_i^\dagger\hat{a}_k^\dagger\hat{a}_l\hat{a}_j|\Psi\rangle = E\ {}^2D_{jl}^{ik} \tag{12.1}$$

The CSE can be split into a Hermitian and an anti-Hermitian part, the latter of which is called the anti-Hermitian CSE, or ACSE:

$$\langle\Psi|[\hat{H},\hat{a}_i^\dagger\hat{a}_k^\dagger\hat{a}_l\hat{a}_j]|\Psi\rangle = {}^2A_{jl}^{ik}. \tag{12.2}$$

Here, ${}^2A_{jl}^{ik}$ is the residual of the ACSE, which is necessarily zero when $|\Psi\rangle$ is an eigenstate of the wave function. We can also obtain the ACSE in Eq (12.2) by considering unitary transformations $\exp(\epsilon\hat{P})$ generated by a parameter ϵ and a two-body anti-Hermitian operator $\hat{P}$

$$\hat{P} = \sum_{ij;kl} {}^2P_{kl}^{ij}\hat{a}_i^\dagger\hat{a}_k^\dagger\hat{a}_j\hat{a}_l. \tag{12.3}$$

The derivative of the energy with respect to the elements of the operator ${}^2P$ yields

$$\frac{\partial E(\hat{P})}{\partial({}^2P_{jl}^{ik})} + O(\epsilon^2) = \epsilon\langle\Psi|[\hat{H},\hat{a}_i^\dagger\hat{a}_k^\dagger\hat{a}_l\hat{a}_j]|\Psi\rangle = \epsilon\,{}^2A_{jl}^{ik}, \tag{12.4}$$

which we observe is equal to the residual of the ACSE. In the solution of the ACSE,[5] the energy and 2-RDM can be expressed as a system of differential equations in terms of a discretized, time-like parameter λ that controls the transformation of the implicit wave function to minimize the energy. As λ increases, we approach a solution of the ACSE. On a quantum computer,[13] we have a potentially exponential advantage in terms of simulating the exact 2-RDM (or 3-RDM) and ${}^2A$ matrices.

12.2.2 Local Parameterization of the Contracted Quantum Eigensolver

We can describe the generic problem in the variational quantum eigensolver[21–24] for finding the ground-state wave function of a quantum system as:

$$\min_{\vec{\theta}\in\mathbb{R}^{\nu}} \langle\Psi_0|U^{\dagger}(\vec{\theta})\hat{H}U(\vec{\theta})|\Psi_0\rangle. \tag{12.5}$$

where $\vec{\theta}$ represents a vector of ν real parameters and we assume the wave function is properly normalized. Upon convergence the following equation is satisfied for all k,

$$\frac{\partial}{\partial\theta_k}\langle\Psi_0|U^{\dagger}(\vec{\theta})\hat{H}U(\vec{\theta})|\Psi_0\rangle = 0, \tag{12.6}$$

indicating that the gradient with respect to all parameters vanishes. However, there can be significant problems associated with describing the appropriate parameterization of Ψ. The exact solution of the wavefunction scales exponentially, which might imply that an exponential number of parameters is necessary in a variational scheme. Using an operator like unitary coupled cluster provides an exponential ansatz, but because the mapping from the Euclidean space to the unitary space is nonlinear, there can be singularities or unphysical minima in the optimization surface.[25, 26] Additionally, it has been shown that high-dimensional parameterizations in a random variational ansatz generate barren plateaus where the variance in the energy gradients vanishes as the system size increases.[27, 28] Because an exponential scaling parameterization is not feasible for larger systems, and limited excitation ansatz such as UCC singles and doubles are not sufficiently accurate, a slew of iterative schemes based on the VQE and UCC schemes which deviate from the traditional CC formalism have been proposed, providing scalable approaches that generally repeat or extend upon certain ansatz fragments.[29–31] One such approach is the adaptive derivative assembled pseudo-trotterized VQE method, or ADAPT-VQE, which takes elements of the ACSE (or generalized UCCSD) to generate an increasingly more complex variational problem.[32]

In the CQE approach, we instead forgo the global parametrization of the state and use an atlas of local parametrizations,[16] describing the trajectory of the state, with the parameter space being dependent on the contracted eigenvalue equation (which here is the ACSE). Each local parameterization in the atlas is concretely generated by the exponential transformation of a two-body anti-Hermitian operator, providing a map between the Euclidean parameter space and the space of unitary transformations. Thus, the optimization is no longer defined by a fixed reference set of parameters but rather by a local parameterization at each iteration n:

$$\min_{\hat{P}_n \in \mathbb{R}^\mu} \langle \Psi_n | e^{-\hat{P}_n} \hat{H} e^{\hat{P}_n} | \Psi_n \rangle, \quad ||P_n|| < \delta, \tag{12.7}$$

where μ denotes the dimension of the two-body operator space, and the norm on P_n indicates that we are staying within a neighborhood around the wave function (replacing the ϵ in previous formulations). Our optimization is then satisfied if we have a Ψ_n such that for all two-body operators;

$$\begin{aligned} 0 &= \frac{\partial}{\partial P_n^{ij;kl}{}_q} \langle \Psi_n | e^{-\hat{P}_n} \hat{H} e^{\hat{P}_n} | \Psi_n \rangle \\ &= \langle \Psi_n | [\hat{H}, \hat{a}_i^\dagger \hat{a}_j^\dagger \hat{a}_k \hat{a}_l] | \Psi_n \rangle, \end{aligned} \tag{12.8}$$

which implies that we have fulfilled the ACSE. At each iteration n, our current state is mapped to a new state through the exponential mapping. While it might be thought that the restriction of $\hat{P}$ to a set of two-body operators is too restrictive, as clearly the two-body operator space does not parameterize the unitary group, the current approach iteratively constructs higher order excitations from the reference wave function [5, 33, 34] (see Section II.E. of Ref. [5] for a discussion of the ACSE Ansatz). As we discuss in the next section, because the ACSE is solved iteratively, we can construct quasi-second-order algorithms if we choose each $\hat{P}_n$ in the ansatz by considering not only the gradient of the current iteration

but also the gradients of previous iterations, which contain information about the curvature.

12.2.3 Quasi-Second-Order CQE Algorithms

Previous algorithms for solving the ACSE use path-following[5] or descent[8] algorithms based on the gradient. While these algorithms are robust to reconstruction errors, gradient-descent algorithms are first-order algorithms with generally linear convergence. To accelerate convergence, we can consider choosing the search direction ${}^2P_k$ by a second-order approach such as the Newton-Raphson method:

$$ {}^2P_k = -\mathrm{H}_k^{-1}\ {}^2A_k, \tag{12.9}$$

where $\mathrm{H_k}$ is the Hessian matrix. Within a certain region of the state space we are guaranteed quadratic convergence[35]. However, the elements of the Hessian are evaluated according to:

$$\begin{aligned} \mathrm{H}_{npq;rs}^{ij;kl} = \frac{\epsilon^2}{2}\big(&\langle\Psi_k|[\hat{a}_i^\dagger\hat{a}_j^\dagger\hat{a}_k\hat{a}_l,[\hat{a}_p^\dagger\hat{a}_q^\dagger\hat{a}_r\hat{a}_s,\hat{H}]]|\Psi_k\rangle \\ &+\langle\Psi_k|[\hat{a}_p^\dagger\hat{a}_q^\dagger\hat{a}_r\hat{a}_s,[\hat{a}_i^\dagger\hat{a}_j^\dagger\hat{a}_k\hat{a}_l,\hat{H}]]|\Psi_k\rangle\big), \end{aligned} \tag{12.10}$$

which requires the 4-RDM or its approximation.

To address this issue, we consider the BFGS quasi-Newton method, which uses the Broyden-Fletcher-Goldfarb-Shanno (BFGS) update within Davidon's method, [36, 37] and is summarized in Table 12.1. At each step of the BFGS method we update an approximate Hessian matrix through a secant equation where the update is designed to keep the Hessian positive definite. By including a direction based on the approximate Hessian, the BFGS method achieves a superlinear rate of convergence near the solution.

At any particular iteration, given a wave function $|\Psi_n\rangle$, the ACSE residual $\hat{A}_n$, and the

Table 12.1: Quasi-Newton CQE algorithm.

Quasi-Newton CQE

Set $0 \rightarrow n$
Initialize $|\Psi_0\rangle$, ${}^2A_0$, and B_0.
Continue until $||{}^2A_n|| < \delta$:
Step 1: Update ${}^2P_n = B_n^{-1}\ {}^2A_n$
Step 2: $\min_{\alpha_n} E_n(\alpha_n \hat{P})$
- $|\Psi_{n+1}\rangle = e^{\alpha_n \hat{P}_n}|\Psi_n\rangle$
- $s_n = \alpha_n {}^2P_n$

Step 3: Evaluate ${}^2A_{n+1}$
- $y_n = {}^2A_{n+1} - {}^2A_n$

Step 4: Calculate B_{n+1}^{-1}
Step 5: $n+1 \rightarrow n$

inverse of the approximate Hessian B_n, we define the step direction as:

$$ {}^2P_n^{ij;kl} = -\sum_{pqrs} (B_n^{-1})_{pq;rs}^{ij;kl}\ {}^2A_n^{pq;rs}. \tag{12.11}$$

We next minimize the energy by a line search to obtain a direction α_n which satisfies conditions of sufficient descent and curvature (Wolfe conditions). In our local frame, we have the following auxiliary BFGS functions $s_n = \alpha_n \hat{P}_n$ and $y_n = \hat{A}_{n+1} - \hat{A}_n$. Using these, we calculate B_{n+1}^{-1} according to the BFGS formula:

$$ B_{n+1}^{-1} = (I - \frac{s_n y_n^T}{y_n^T s_n}) B_n^{-1} (I - \frac{y_n s_n^T}{y_n^T s_n}) + \frac{s_n s_n^T}{y_n^T s_n}. \tag{12.12}$$

We then increase n and continue until the gradient norm $||{}^2A||$ satisfies a convergence threshold. Step 4 in Table 1 can be replaced with a suitable update replacement, and in the results we demonstrate the use of a limited-memory BFGS implementation, denoted l-BFGS. [37]

In practice, because of the redundancy of the certain elements of the 2-RDM, we can store the ${}^2A$ matrix as a vector in a compact representation, and then store the B^{-1} matrix exactly. For larger systems, it is likely that even this would be prohibitive, and instead the

limited-memory approach would be necessary, where we store only k previous steps, which is equivalent to k 2-RDMs. On a classical device, the algorithm would be very similar, although instead of updating the wave function, we would have a 2-RDM update step. Both the 2-RDM and ${}^2A$ updates would require the classical evaluation of the ACSE and hence, a reconstructed 3-RDM.

On a quantum computer we have significant advantages in that we are not reconstructing the 3-RDM. This means that we generate (up to statistical and noise-related errors) pure 2-RDMs at each step, and do not have to consider the N-representability of the 2-RDM, or the step size in the solution of the differential equations. An important note is that if we want to evaluate the ACSE's residual in the classical part of the algorithm rather than in the quantum part by tomography of an auxiliary state, we must be sure that the residual is sufficiently accurate to estimate the curvature. While an approximated 3-RDM can give good enough information to obtain chemical accuracy in a number of instances, for rigorous convergence the cumulant portion of the 3-RDM should be measured by tomography. Practically, this would entail alternating evaluations of the 3-RDM (for the ACSE) and the 2-RDM (for energy evaluations).

As an alternative to the quasi-Newton approaches, we can instead use the nonlinear conjugate gradient (CG) approaches.[37] The nonlinear CG method does not require the storage of a Hessian or approximate Hessian, and instead involves only a simple update step governing the contribution of the previous search direction $\hat{P}_k$. A description of the generic CQE algorithm with a CG solver is described in Table 12.2. There are numerous modifications to the conjugate gradient method, which we do not explore here.[38] Some such modifications include preconditioning schemes, modified update coefficients, as well as additional criteria on resets and step lengths.

Table 12.2: Conjugate Gradient CQE algorithm.

Conjugate Gradient CQE

Set $0 \leftarrow n$
Initialize $|\Psi_0\rangle, {}^2A_0$
While $||{}^2A_n|| > \delta$:
Step 2: $\min_{\alpha_n} E_n(\alpha_n \hat{P})$
Step 3: Evaluate ${}^2A_{n+1}$
Step 4: Calculate β_{n+1}
Step 5: ${}^2P_{n+1} = -{}^2A_{n+1} + \beta_{n+1}{}^2P_n$
Step 6: $n+1 \rightarrow n$

12.2.4 Resource-Optimized CQE Search Directions

In light of the current representation of the CQE algorithm, one can see that the resources demanded on the quantum computer will depend heavily on the selection and implementation on the search direction, as each term must be implemented individually. However, any modification to the search direction will be detrimental to the rate of convergence (and can potentially also negate the theoretical results). Thus, we would like to find a tradeoff between potentially reducing the number of terms and preserving a descent direction.[37]

We thus focus on two approximations which still preserve the essential nature of the ideal CQE approach: p-depth and operator sparsification. First, we introduce a more formal way of describing the ACSE ansatz at a given iteration n. Let $\{\hat{\mathcal{P}}_l^{(n)}\}$, be an ordered set of anti-Hermitian two-body operators:

$$\hat{\mathcal{P}}_l^{(n)} = \sum_{ijkl} \mathcal{P}_l^{(n)ij;kl} \hat{a}_i^\dagger \hat{a}_k^\dagger \hat{a}_l \hat{a}_j. \tag{12.13}$$

In the exact CQE approach, each iteration adds a new two-body operator to the set. In general, we can write the ACSE ansatz at the N-th iteration as:

$$|\Psi_n\rangle = \prod_l^m e^{\hat{\mathcal{P}}_l^{(n)}} |\Psi_0\rangle. \tag{12.14}$$

where m is the total number of two-body exponential operators we are implementing. We define the p-depth as follows. Given a search direction $\hat{P}_n$, we iterate over the elements $P_n^{ij;kl}$ and the set of operators $\{\hat{\mathcal{P}}_l^{(n)}\}$ from $l = m - p$ to $l = m$. If an element $P_n^{ij;kl}$ was included in a previous operator, we update that two-body operator as:

$$\mathcal{P}_{n-p}^{ijkl} \leftarrow \mathcal{P}_{n-p}^{ijkl} + P_n^{ijkl}. \tag{12.15}$$

From the definition, the element will only be in one of the p-previous operators. If elements cannot be assigned to a previous $\mathcal{P}_l^{(n)}$, a new operator is appended. The ACSE only provides information on the gradient around the exterior of the wavefunction, and because in general each iteration does not commute with previous iterations for $p > 0$, this can be considered an approximate scheme of implementing the CQE. As an example, if all terms are included in the initial $\hat{\mathcal{P}}$, then we have a single exponential form in the approximate linear region, and any p-depth greater than 1 will be equivalent. Note that such a case is similar to a generalized UCCSD ansatz with different ordering under the first-order trotterization; however, the method of updating does not reflect the true gradient terms, and as such provides an approximation of the operator in the linear region.

The second approach is an operator sparsification scheme, which effectively reduces the number of new terms appended at each step. The method of ordering is of particular importance, and we investigate two options. First, we can sort the elements according to their absolute value, which is important for implementation purposes (i.e., we can remove the smallest elements first). Alternatively, we can sort elements according to the energy contribution in the descent direction. This value is obtained element-wise as the product $A_n^{ij;kl} P_n^{ij;kl}$. For gradient-descent approaches, these two criteria are equivalent, and in previous work only the former approach was used.

We can also control the number of terms that are removed through a constant $c \in [0, 1]$. This is a constant scaling factor where $c = 1$ (strict truncation) indicates only the largest

term in $\hat{P}$ is included and $c = 0$ (no truncation) indicates that all terms in $\hat{P}$ are included. Another potentially useful control instead of a constant scaling factor (which we do not explore here) would be to limit explicitly the number of terms included in each term. Finally, we have an INCLUDE $= \{\text{True}, \text{False}\}$ option whereby elements of the search direction that would be assigned to the previous p-operators due to the p-depth specified, are included in the sparsification scheme.

12.3 Applications and Results

In this section we look at applications of the optimized CQE scheme. First, we investigate the role of different optimizers. Second, We present discuss schemes related to practical implementations and modifications to the search direction. Third. we show results with a CQE utilizing the unencoded ACSE, and finally, we compare our results to variational quantum eigensolvers, including the ADAPT-VQE algorithm.

12.3.1 Implementation of Optimized CQE

We begin by comparing the exact (up to a first-order trotterization) implementations of different methods for the H_4 system at different bond lengths, corresponding with differing degrees of electron correlation. In this work our convergence criteria is typically taken to be the Frobenius norm of the ${}^2A$ matrix. For the conjugate gradient approach, we do not utilize any preconditioning, and use the update strategies of Fletcher and Reeves.[37] The limited BFGS strategy utilizes 3 previously stored steps. Figure 12.1 displays our results. Further computational details are included in the Appendix.

While for the bond distance near equilibrium $D = 1$ Å , the different optimizers in the ACSE appear to have no apparent advantage, the more correlated distances show strong deviations between the different approaches. In particular, the 1.5 Å case, the convergence flattens when gradient-descent based approaches are used. For 2.0 Å this is accentuated, as

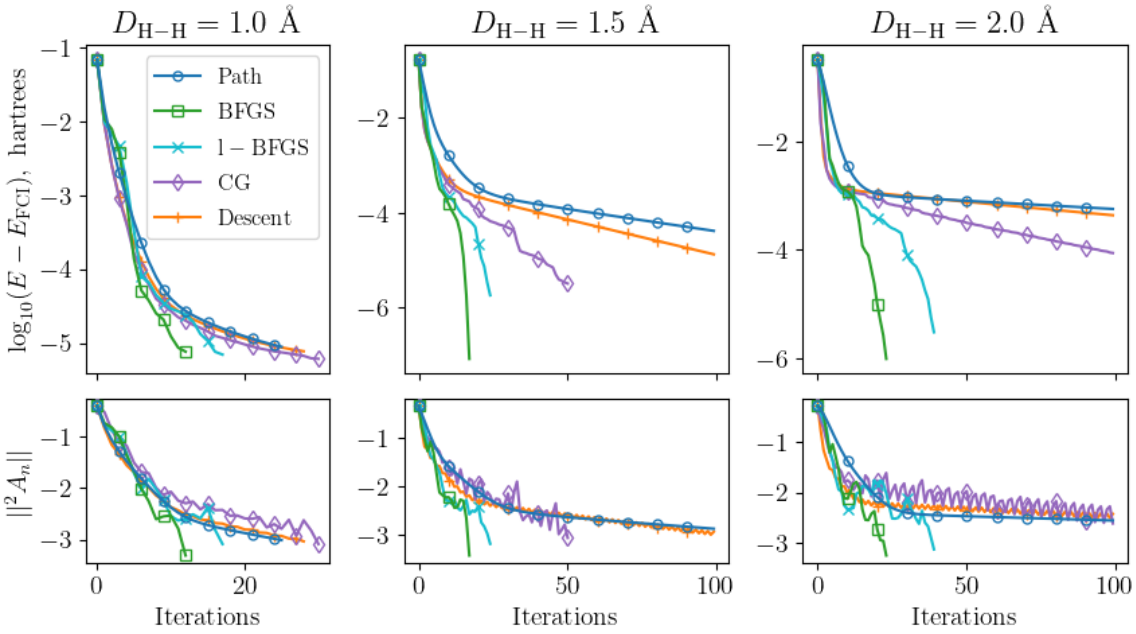

Figure 12.1: Comparison of methods for generating $\hat{P}$ at different H − H distances for H_4. Near equilibrium, similar patterns can be seen, but away from equilibrium, gradient-descent-based approaches slow down considerably. In particular, when optimizing the 1-d step size according to a quadratic fit, an oscillatory pattern can be seen in the norm of ${}^2A$, indicating a potential valley in a direction between the oscillating gradients. The conjugate gradient approach allows for slightly more flexibility but exhibits stronger oscillations in the gradient. The quasi-Newton approaches offer quick convergence across all regions of dissociation.

we appear to have entered a region where the gradient is quite shallow. The quadratic step appears to be even slightly worse in optimizing the norm of the ${}^2A$ matrix than a simple gradient descent. The conjugate gradient approach appears to be better but shows strong oscillations in the gradient norm (note if we loosen the update parameter, these oscillations decrease, but we do not observe a significant increase in convergence). The most successful approaches are the quasi-Newton methods, which are able to achieve high accuracy results in only a few iterations. The l-BFGS offers a reliable approach as well, with a quality between the conjugate gradient and full BFGS methods.

While this approach is the closest to the ideal implementation, and offers some advantages for a classical quantum simulation (i.e., similar to the classical ACSE, except instead of the 2-RDM we only need to store the statevector), for near-term applications there are several constraints. In a noiseless regime (note, the importance of noise is also relevant, but as this also changes the optimization strategy, is not addressed directly here), addressing the compactness or efficiency is an important problem. In particular, we would however like to know if we can reduce the amount of terms that are added at each iteration, using ideas mentioned above. These result in an appproximate search direction, which we constrain to represent a descent direction.

We use the 1.5 Å case, which contains nontrivial electron correlation and starts to differentiate between different optimizers, to look at ways we can modify the search direction. Table 12.3 explores the number of iterations and CNOT gate cost for a variety of options with the BFGS optimizer. In particular, we examine the absolute norm or energy contribution for the sparsity operator acting on the search direction (upper and lower quadrants), as well as the inclusion or exclusion of terms that appear in the p-depth addition scheme (specified by INCLUDE). For each of these criteria, we look at different p-depths and values of the SPARSE scheme.

A number of interesting trends emerge. First, there is a difference in application of the

Table 12.3: Reported number of iterations and CNOT gates (in brackets, $\times 10^3$) for approximate implementation schemes for the CQE with BFGS optimizer with linear H_4 at a distance of 1.5 Å. We varied the inclusion of terms in the selection of P (sorted by either $|P^{ij;kl}|$, or by the descent condition), the manner of truncation of P, as well as varying the sparsity and the $p-$depth for each condition. $*$ represents a run that did not converge, and $\times$ indicates runs that reached the maximum iterations (300).

	$\lvert P_n^{ij;kl}\rvert$										$(A_nP_n)_{kl}^{ij}$									
	INCLUDE = False					INCLUDE = True					INCLUDE = False					INCLUDE = True				
SPARSE[c]	$p-$depth					$p-$depth					$p-$depth					$p-$depth				
	9	7	5	3	1	9	7	5	3	1	9	7	5	3	1	9	7	5	3	1
0.9	*	*	*	*	*	76 [1.8]	73 [2.5]	*	65 [4.0]	117 [8.9]	×	×	283 [18]	×	×	47 [1.6]	48 [2.2]	60 [4.0]	80 [4.0]	107 [8.1]
0.5	*	*	*	*	*	25 [0.90]	25 [0.90]	42 [2.6]	*	*	71 [0.90]	139 [5.4]	123 [6.6]	119 [7.6]	75 [13]	26 [0.91]	35 [1.9]	35 [2.5]	39 [3.3]	63 [7.6]
0.25	26 [1.6]	28 [3.4]	28 [4.6]	27 [5.8]	31 [11]	24 [1.3]	24 [1.3]	24 [2.2]	28 [6.5]	29 [11]	63 [0.93]	67 [0.93]	70 [3.7]	81 [6.1]	76 [15]	26 [1.2]	26 [1.2]	30 [3.3]	36 [5.1]	46 [8.8]
0.125	22 [1.5]	22 [1.5]	22 [1.5]	23 [7.0]	24 [13]	21 [1.5]	21 [1.5]	22 [5.6]	21 [6.5]	24 [13]	47 [1.4]	56 [3.9]	74 [6.3]	44 [7.8]	54 [16]	24 [1.5]	26 [3.2]	26 [3.7]	29 [5.5]	38 [8.8]

sparsification operator acting on elements according to their energy contribution or absolute value. Namely, when using large c for the absolute value, problems in the optimization can occur. Namely, these are instances where the search direction has little overlap with the gradient, and the largest term selected is ordered in such a way that it is not strictly increasing. The descent condition however, is able to converge across every configuration, albeit at different rates of convergence. This also leads to a stratification in the rates of convergence for the DESCENT condition, which can be seen in Figure 12.2. While the absolute value condition leads to accelerated convergence in almost all instances, it does seem more sensitive to using restricted operators. Of course, the inclusion of previous terms does seem to alleviate this problem, and because it seems to occur when the search direction is nearly orthogonal to the gradient, resetting the optimization might allow the optimization to continue. It is also possible that the order of magnitude for the descent condition should be lower than the absolute value condition, although this could vary significantly based on the system.

Second, the INCLUDE option has a strong impact on the rate of convergence. For both selection criteria, inclusion of previous terms clearly helps in assisting the overall convergence. As this can be considered as a way of increasing the pool of operators at each step, depending on both c and the p-depth, the advantage here makes sense. Third, the p-depth appears to

have a two-fold role. First, and more generally, it serves to reduce the total number of terms needed in the ansatz. That is, as the p-depth increases, the number of total terms in the ansatz decreases. Additionally, for a given c, we do see numerous instances where the total number of iterations decreases as the p-depth increases when INCLUDE = True. When INCLUDE = False, the trends are a bit unclear, and the optimization tends to be more sensitive. Interestingly, for $c = 0.5, 0.25$,and 0.125, with INCLUDE = False the total iterations appear to increase with increasing p-depth, and then decrease. More sparse (see c =0.9, 0.5) truncations result in slower convergence, which can be aided with the INCLUDE option, but not completely mitigated.

While these results are obviously not generalizable to every system, it is likely that some of these trends can be seen elsewhere. We expect that the p-depth can lead to lower circuit depths. Additionally, while sparser operators are desirable from a NISQ perspective, optimization with respect to a single parameter is clearly detrimental to the rate of convergence. This can be mitigated through expanding the pool directly with more terms and the sparsification operator, or indirectly through the p-depth.

12.3.2 Encoding-Free CQE

The encoding-free (or unencoded CQE) approaches for preparing states as an alternative to fermionic state preparation have recently been explored[31, 39–41], within the VQE framework as well as in attempting to understand the success of heuristic and non-fermionic ansatz preparation. Recent works by the present authors showed that the fermionic 2-RDM can be functionalized from a qubit-particle wavefunction.[42] As long as fermionic tomography is performed on a N-qubit particle state, the 2-RDM represents a valid fermionic 2-RDM. Additionally, in recent work we introduce an encoding-free CQE algorithm which evaluates the anti-Hermitian component of the two-qubit-particle contraction onto the Schrödinger equation. Table 12.4 displays calculations for a number of bond distances of H_5 for both the

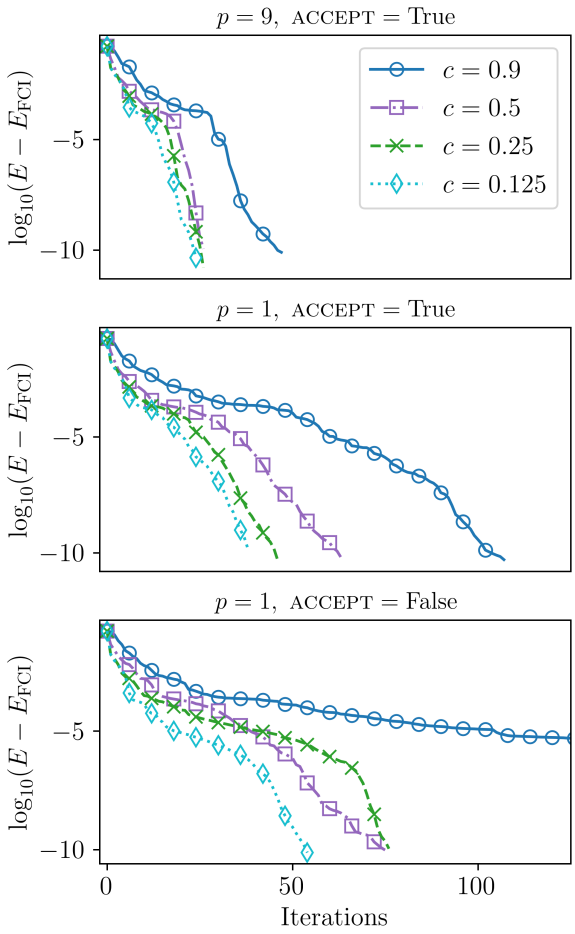

Figure 12.2: Low threshold ($||^2 A|| = 10^{-5}$) results for varying values of sparsity with different $p-$depths and acceptance criteria, utilizing the BFGS optimizer for molecular H_4 at the intermediate distance ($D = 1.5$ Å), with the DESCENT condition. In the top two plots, we use ACCEPT = True, where elements below the sparsity threshold are automatically included if they are in included in one of the previous $p-$terms. The bottom plot has ACCEPT = False. Only the first 125 iterations are shown.

Table 12.4: Comparisons of total iterations, total CNOT gate count, and average CNOT gates per iteration for unencoded and encoded CQE using the BFGS optimizer for H_5 at various bond distances from equilibrium in the minimal STO basis. The accuracy of both approaches is largely similar across the dissociation curve, though for +1.00 and +1.25 distance separation, the unencoded CQE requires more iterations.

$D - D_{\text{eq}}$ Å	Iterations (CQE,UCQE)	Total CNOT $\times 10^4$ (CQE,UCQE)	$\langle \text{CNOT}_\text{k} \rangle \times 10^2$ (CQE,UCQE)
−0.25	26, 33	1.7, 1.5	6.4, 4.5
+0.00	29, 36	2.1, 1.8	7.4, 5.0
+0.25	47, 49	3.8, 2.7	8.2, 5.5
+0.50	40, 34	4.3, 2.6	11., 7.8
+0.75	39, 28	5.7, 2.8	15., 9.9
+1.00	42, 43	6.9, 4.4	16., 10.
+1.25	47, 80	8.0, 7.4	17., 9.3

encoded and unencoded CQE cases with the BFGS algorithm as an example system.

The unencoded CQE under optimization matches the fermionic case in most instances, and consistently has a smaller average number of CNOT gates per iteration. For the two longest separation lengths, the number of iterations required does increase, leading to similar CNOT counts for the total ansatz. A future goal would be to incorporate compilation schemes or adjust the set of ACSE or unencoded ACSE excitations to favor a largely commuting pool.

12.3.3 Comparison with VQE

Finally, we compare the CQE approach utilizing a BFGS optimization with other known quantum algorithms. While in previous work[14] similarities between iterative nature of the ACSE and ADAPT-VQE were discussed, here, we provide example calculations of VQE, ADAPT-VQE, and the ACSE that demonstrate fundamental differences in these algorithms. These are included in Figure 12.3, as well as in Table 12.5.

While the VQE results in Figure 12.3 are not that surprising based on the use of the unitary coupled cluster ansatz, we still can see some interesting comparisons. For equilibrium

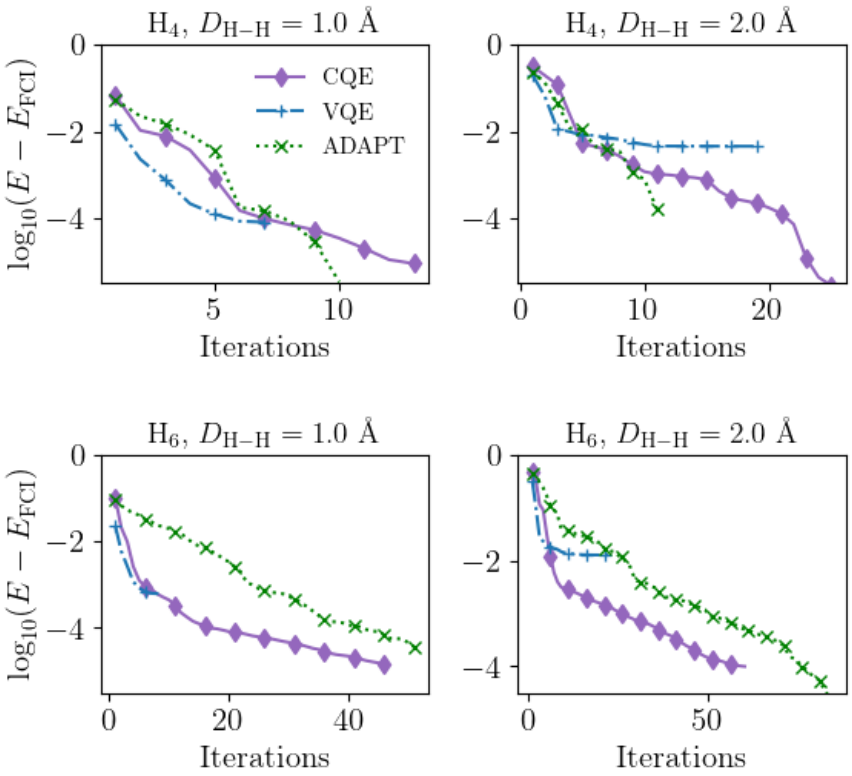

Figure 12.3: Simulations of molecular H_4 and H_6 for separations of 1 Å, and 2 Å utilizing the CQE, VQE, and ADAPT-VQE with a BFGS optimizer. For H_4 a minimal ansatz is reached in the ADAPT through the VQE subroutine, and for H_6 the CQE algorithm slightly outperforms the ADAPT. VQE, here using the UCCSD anastz, provides rapid convergence for near equilibrium states, but has significant errors at larger separations, which are overcome by the iterative ADAPT-VQE and CQE algorithms.

Table 12.5: Comparison of gradient element (VQE) and residual element (ACSE) evaluations for the CQE, VQE, and ADAPT-VQE methods, corresponding to simulations for molecular H_4 and H_6 at separations of 1 Å, and 2 Å. Note the ADAPT-VQE here has a symmetry adapted pool of operators, which are not implemented here in the CQE or VQE approaches. The VQE tolerance is also taken to be quite low, i.e. 10^{-3} in the norm of the parameter vector (whereas the VQE subroutine in the ADAPT procedure is generally lower).

Method	Quantity	H_4, 1 Å	H_4, 2 Å	H_6, 1 Å	H_6, 2 Å
CQE	Iterations	13	25	46	60
	Residuals	1950	3750	38640	50400
VQE	Iterations	7	19	9	22
	Gradients	182	494	1053	2574
ADAPT-VQE	Macro	10	12	51	84
	Micro	71	167	1221	5854
	Gradients	362	1226	43112	354988
	Residuals	660	792	16830	27720

distances, UCCSD provides a good ansatz, and there are numerous methods exploring the UCC ansatz [29, 43]. By comparison, with ADAPT we are able to obtain seemingly arbitrary convergence, matching previous work. However, it is worth noting that the iterative cost of the ADAPT is much higher than either VQE or the CQE. The CQE on the other hand performs quite well in a variety of instances, with the most challenging case being dissociated H_6, where higher order excitations dominate and the system is strongly correlated. While the number of macro iterations for the ADAPT procedure might look only slightly worse than the CQE or VQE approaches, when taken into account with the VQE cost, (i.e. micro + macro iterations), the length of the ADAPT procedure is somewhat unwieldy, namely due to the VQE subroutine. The total number of gradient and residual evaluations for each of these instances is seen in Table 12.5.

We can also look at qubit implementation of the ADAPT scheme, which here follows the qubit-particle excitation based scheme of Yordanov et al. [41], and not the quasi-particle approach taken by the original authors. We find a similar result to previous work, namely that for stretched LiH conserving the particle number and projected spin leads to essentially the same qubit-based excitations. The main difference seen (as a result of the relative scale

mostly) in these results is for the CNOT cost of the unencoded CQE approach, although a similar decrease in the CNOT cost of the IQEB approach exists as well. While the approaches appear to be inversely related in the rate of convergence (through total iterations), and the CNOT count (where the CQE schemes are more costly), the number of parameter evaluations differs substantially. While here we do not distinguish between the residuals of the ACSE as parameters and the VQE parameters, as these can be obtained a number of different ways (for instance, the ACSE residuals can be taken from either the 2-RDM with a quantum solver or the 3-RDM on the quantum computer, and numerous methods of measuring VQE gradients exist as well), for larger system limits on the number of parameters should be considered.

Despite achieving quicker convergence, from all of these examples we see that the main drawback to the CQE algorithm is the iteratively increasing CNOT cost, which is due to the use of additional gates at each step. While this should be reasonable for high performing quantum devices, for near-term devices further reduction of the CNOT count is important. However, the gain in performance we see by performing a quasi-second order optimization in the local parameter space is quite significant. Additionally, when compared to CNOT gates of the gradient-descent-based methods (as in Fig. 12.1), the optimized-ACSE allows for more flexibility in constructing compact ansatz.

12.4 Discussion

While generic algorithms have been known for approaching the problem of quantum simulation for a while, calculations involving increasingly complex systems have only recently begun to emerge. These require the advancement and development of new quantum algorithms, similar to the past century of classical quantum chemistry algorithms. The CQE offers an approach which is potentially beneficial in the near-term, and could potentially solve some of the shortcomings of VQE.

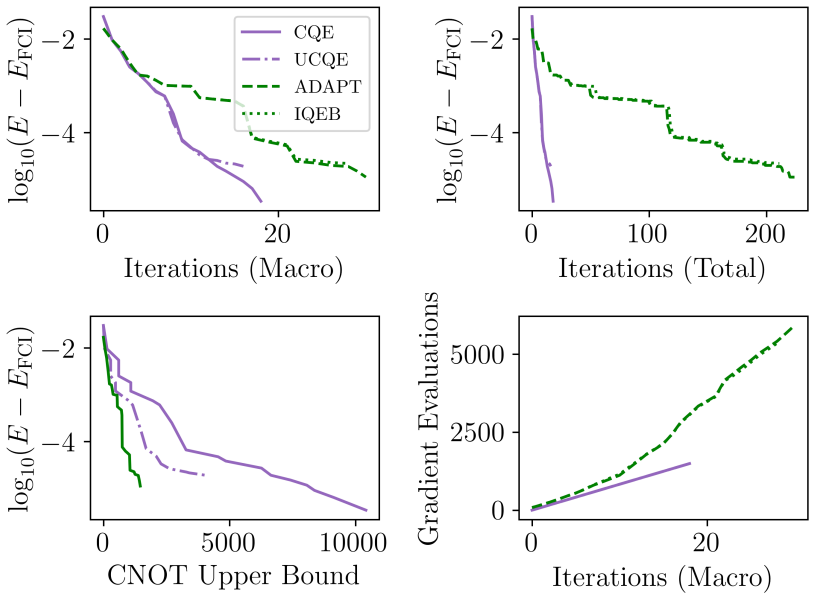

Figure 12.4: Simulations of molecular lithium hydride at a separation of 2 Å utilizing CQE, VQE, fermionic ADAPT-VQE and the iterative qubit-excitation based ADAPT-VQE (IQEB), essentially a unencoded APAPT-VQE algorithm. The upper-left shows the macro iterations of each scheme, which are nearly identical for the encoded and unencoded forms, and are only slightly slower for the ADAPT. The upper-right shows the total iterations, including micro iterations in the VQE procedure with a threshold of 10^{-3} in the parameter vector. The lower-left compares the energy convergence with the ansatz cost, showing that the ADAPT does produce a more compact representation of the ansatz. The lower-right shows the number of parameter evaluations (a lower bound on the number of gradients evaluated at each optimizer step), which is linear scaling with the ACSE procedure but for ADAPT becomes quadratic with respect to the number of iterations.

From the discussion in section 12.2.2, we can see that the variational principle used in the VQE and in the current CQE algorithm are similar in that they solve an optimization problem, but differ in the goal of the minimization. In the VQE we are often trying to minimize the energy of a state through a global parameterization, and thus finding a suitable unitary transformation is one issue. Barren plateaus or regions where the optimization fail become likely with an increasingly large parameter space. Additionally, the suitability (i.e. over or under paramterization) of our state is often in question. In the ACSE algorithm, the local parameterization which is more suitable for RDM representations leads to a locally updated optimization. Importantly, in a VQE the optimization converges *towards a solution of the VQE problem*, which is not the ACSE. As the VQE subproblem becomes larger and larger (i.e. in adaptive schemes), eventually the VQE solution can (but by design will not necessarily) satisfy the ACSE. In the CQE approach presented here, we have convergence *towards our contracted eigenvalue problem*, and not a variational subproblem.

From our calculations we can also understand some elements of the ADAPT-VQE algorithm as is related to the CQE algorithm. The ADAPT-VQE method chooses the largest ACSE residual at each macro iteration. This leads to a flexible and efficient ansatz, that when not restarted, will by construction improve the energy in the VQE. However, the re-optimized state is often not close to the previous state, highlighting the strong variational nature of the ADAPT algorithm. Restarting the VQE optimization, which has been done in some ADAPT work, can lead to a suboptimal solution of the ACSE, or for the VQE subroutine to fail. Recent work by Liu et al.[44] used a reconstructed 3-RDM in the ACSE to obtain approximate residuals to seed the ADAPT algorithm. Because these approximate gradients can differ in a substantial way from the exact gradients, more terms are needed, which significantly increases the variational flexibility of the ansatz. As a result, these calculations exhibited faster convergence and required fewer iterations than traditional ADAPT-VQE.

In this work, the effective number of parameters is kept to the size of the 2-RDM. However,

unlike Liu et. al,[44], it is important *not* to use the classical ACSE with reconstructed residuals from a reconstructed 3-RDM, as these will likely lead to convergence issues. However, the classical 3-RDM can still be obtained relatively easily on a quantum computer through a variety of techniques. Work involving qubit-particle approaches also shows promise, with another advantage being the increased number of commuting terms which exists between qubit-particle excitations as opposed to fermionic-particle excitations.

Another element which can be overlooked is that the ACSE is not necessarily equivalent to the CSE except when higher order excitations are incldued. Despite this limitation, in the exponential form of the ACSE, higher order excitations can be seen to emerge naturally through products of exponential two-body operations. Additionally, by considering information on the curvature of the space beyond the gradient, we also should include contributions from triple and higher excitations in our selection of operators to propagate the wavefunction. In practice, use of the CQE for solving the ACSE leads to a highly accurate solution.

Despite these benefits, there still are drawbacks with the CQE algorithm. The primary drawback when compared to an algorithm such as the ADAPT-VQE is the large number of CNOT gates. Even with low error CNOT gates, efficient and noise-robust means of obtaining accurate gradients and 2-RDMs will be necessary. All of these also affect the success or failure of the underlying optimization algorithm, and so exploring noise-tolerant approaches will also be critical for near-term applications.

12.5 Conclusion

In this work we address the convergence of the contracted quantum eigensolver using tools from optimization theory. By using methods beyond traditional gradient descent, we achieve superlinear convergence, allowing us to propagate the wavefunction rapidly towards a solution of the ACSE. Practical implementations where the search direction is modified to

conserve quantum resources show promising reductions in the cost of the algorithm, and we expect further simplification schemes to be attempted aimed at improving the efficiency of the CQE approach. Additionally, the present work provides a basis for understanding approaches which use the ACSE in pool selection, and could lead to further hybrid optimization schemes for use in NISQ applications.

12.6 Computational Details

All calculations were performed using the HQCA (v22.4)[45] set of tools, which utilizes QISKIT (v0.29.0)[46] and PYSCF (v1.7.6)[47] for interfacing with quantum simulators and obtaining electron integrals for circuit based simulations. Each simulation utilizes a minimal-basis Slater-type orbital representation (i.e. STO-3G). The Jordan-Wigner (or qubit-particle) mapping was utilized, with parity $\mathbb{Z}_2$ symmetries removed for the majority of examples. Statevector or unitary simulations with no noise were used for each run. The ADAPT-VQE results in Fig 12.3 were obtained using code from the respective publication[32], where analytical recursive solutions of the VQE gradients are used. The threshold for the VQE subroutine in those instances was 10^{-6}. In the lithium hydride case, code from HQCA was used. Parameters for the VQE optimization in the ADAPT-VQE optimizations were not reset in between runs - a single parameter is essentially appended to the parameter vector.

The line-search implementation used in the BFGS, nonlinear CG, and $l-$BFGS optimizations follows from the Nocedal algorithms[37], which is present in the scipy implementation. For some steps (notably the first few steps), often $\alpha_0 = 1$ is too large, and $\alpha_0 = 0.5$ is preferred. While a dynamic step-size is not necessary for BFGS, after the first step we interpolate the α_0 with a quadratic based on the current energy, previous energy, and previous gradient information, and then constrain $\alpha_0 \in [0.5, 1]$, which we expect in some instances leads to a more appropriate step size.

References

[1] D. A. Mazziotti, Physical Review A **57**, 4219 (1998).

[2] D. R. Alcoba and C. Valdemoro, Physical Review A - Atomic, Molecular, and Optical Physics **64**, 7 (2001).

[3] H. Nakatsuji, Physical Review A **14**, 41 (1976).

[4] D. A. Mazziotti, Phys. Rev. Lett. **97**, 143002 (2006).

[5] D. A. Mazziotti, Physical Review A - Atomic, Molecular, and Optical Physics **75**, 1 (2007).

[6] D. Mukherjee and W. Kutzelnigg, The Journal of Chemical Physics **114**, 2047 (2001).

[7] D. a. Mazziotti, Chemical Physics Letters **289**, 419 (1998).

[8] A. M. Sand and D. A. Mazziotti, The Journal of Chemical Physics **143**, 134110 (2015).

[9] G. Gidofalvi and D. A. Mazziotti, Physical Review A - Atomic, Molecular, and Optical Physics **80**, 1 (2009).

[10] J. J. Foley IV, A. E. Rothman, and D. A. Mazziotti, Journal of Chemical Physics **134** (2011), 10.1063/1.3526298.

[11] C. Valdemoro, D. R. Alcoba, L. M. Tel, and E. Pérez-Romero, International Journal of Quantum Chemistry **109**, 2622 (2009).

[12] D. R. Alcoba, C. Valdemoro, L. M. Tel, and E. Pérez-Romero, International Journal of Quantum Chemistry **109**, 3178 (2009).

[13] S. E. Smart and D. A. Mazziotti, Phys. Rev. Lett. **126**, 070504 (2021), arXiv:2004.11416 .

[14] S. E. Smart, J.-N. Boyn, and D. A. Mazziotti, (2021), arXiv:2103.06876 .

[15] J.-N. Boyn, A. O. Lykhin, S. E. Smart, L. Gagliardi, and D. A. Mazziotti, J. Chem. Phys. **155**, 244106 (2021).

[16] C. J. Taylor and D. J. Kriegman, Technical Report No. 9405 , 10 (1994).

[17] P. A. Absil, R. Mahony, and R. Sepulchre, *Optimization Algorithms on Matrix Manifolds* (Princeton University Press, 2007).

[18] W. Huang, K. A. Gallivan, and P.-A. Absil, SIAM Journal on Optimization **25**, 1660 (2015).

[19] F. Arute, K. Arya, R. Babbush, D. Bacon, J. C. Bardin, R. Barends, S. Boixo, M. Broughton, B. B. Buckley, and D. A. e. a. Buell, Science **369**, 1084 (2020), arXiv:2004.04174 .

[20] R. Shepard, S. R. Brozell, and G. Gidofalvi, J. Phys. Chem. A **119**, 7924 (2015).

[21] J. R. McClean, J. Romero, R. Babbush, and A. Aspuru-Guzik, New Journal of Physics **18**, 023023 (2016), arXiv:1509.04279 .

[22] A. Peruzzo, J. McClean, P. Shadbolt, M.-H. Yung, X.-Q. Zhou, P. J. Love, A. Aspuru-Guzik, and J. L. O'Brien, Nature Communications **5**, 4213 (2014), arXiv:1304.3061 .

[23] A. Kandala, A. Mezzacapo, K. Temme, M. Takita, M. Brink, J. M. Chow, and J. M. Gambetta, Nature **549**, 242 (2017), arXiv:1704.05018 .

[24] S. Endo, Z. Cai, S. C. Benjamin, and X. Yuan, , 1 (2020), arXiv:2011.01382 .

[25] J. Stuelpnagel, SIAM Rev. **6**, 422 (1964).

[26] F. A. Evangelista, G. K.-L. Chan, and G. E. Scuseria, The Journal of Chemical Physics **151**, 244112 (2019), arXiv:1910.10130 .

[27] J. R. McClean, S. Boixo, V. N. Smelyanskiy, R. Babbush, and H. Neven, Nature Communications **9**, 1 (2018), arXiv:1803.11173 .

[28] S. Wang, E. Fontana, M. Cerezo, K. Sharma, A. Sone, L. Cincio, and P. J. Coles, arXiv , 1 (2020), arXiv:2007.14384 .

[29] J. Lee, W. J. Huggins, M. Head-Gordon, and K. B. Whaley, Journal of Chemical Theory and Computation **15**, 311 (2019), arXiv:1810.02327 .

[30] J. Chen, H.-P. Cheng, and J. K. Freericks, , 1 (2021), arXiv:2109.14134 .

[31] I. G. Ryabinkin, T. C. Yen, S. N. Genin, and A. F. Izmaylov, Journal of Chemical Theory and Computation **14**, 6317 (2018), arXiv:1809.03827 .

[32] H. R. Grimsley, S. E. Economou, E. Barnes, and N. J. Mayhall, Nature Communications **10**, 3007 (2018), arXiv:1812.11173 .

[33] D. A. Mazziotti, Phys. Rev. A **69**, 012507 (2004).

[34] D. A. Mazziotti, Phys. Rev. A **102**, 030802 (2020).

[35] S. T. Smith, (1993), arXiv:1305.1886 .

[36] W. C. Davidon, SIAM Journal on Optimization **1**, 1 (1991), https://doi.org/10.1137/0801001 .

[37] J. Nocedal and S. J. Wright, *Numerical Optimization*, Springer Series in Operations Research and Financial Engineering (Springer New York, 2006).

[38] W. W. W. Hager and H. Zhang, Pacific journal of Optimization **2**, 35 (2006).

[39] R. Xia and S. Kais, Quantum Science and Technology **6**, 15001 (2020), arXiv:2005.08451 .

[40] H. L. Tang, V. Shkolnikov, G. S. Barron, H. R. Grimsley, N. J. Mayhall, E. Barnes, and S. E. Economou, PRX Quantum **2**, 020310 (2021), arXiv:1911.10205 .

[41] Y. S. Yordanov, V. Armaos, C. H. W. Barnes, and D. R. M. Arvidsson-Shukur, Communications Physics **4**, 228 (2021), arXiv:2011.10540 .

[42] D. A. Mazziotti, S. E. Smart, and A. R. Mazziotti, **60637**, 38 (2021), arXiv:2101.11607 .

[43] J. Romero, R. Babbush, J. R. McClean, C. Hempel, P. Love, and A. Aspuru-Guzik, ASA Refresher Courses in Anesthesiology , 1 (2017), arXiv:1701.02691 .

[44] J. Liu, Z. Li, and J. Yang, J. Chem. Phys. **154**, 244112 (2021), arXiv:2012.07047 .

[45] S. E. Smart and D. A. Mazziotti, "hqca - hybrid quantum computing algorithms for quantum chemistry," .

[46] M. S. ANIS, Abby-Mitchell, H. Abraham, AduOffei, R. Agarwal, and G. A. et al., "Qiskit: An open-source framework for quantum computing," (2021).

[47] Q. Sun, T. C. Berkelbach, N. S. Blunt, G. H. Booth, S. Guo, Z. Li, J. Liu, J. McClain, E. R. Sayfutyarova, S. Sharma, S. Wouters, and G. K.-L. Chan, , 1 (2017), arXiv:1701.08223 .

CHAPTER 13

QUANTUM CONTRACTED EIGENSOLVER FOR SOLVING THE CONTRACTED SCHRÖDIGNER EQUATION

The following chapter is an encapsulation of the theory and *preliminary* results, and has been developed with Prof. David Mazziotti. The interested reader should be look for future work by the authors.

13.1 Introduction

Reduced density matrix theory is based on the idea that a system with a $k-$body interaction can theoretically be solved with only information on the $k-$body interactions. This information is included in the $k-$body reduced density matrix[1]. The contracted Schrödigner equation (CSE) provides the contraction (or projection) of the Schrödigner equation onto the two-particle space [2, 3]. Importantly, the CSE is satisfied if and only if the complete Schrödigner equation is satisfied. However, the CSE leads to an expression containing the 4-electron RDM (4-RDM), and so realizing a scalable solution of the CSE is particularly challenging. If we take only the anti-hermitian part of the CSE, denoted as the ACSE, we are left with only the 3-electron reduced density matrix, which has $O(r^6)$ scaling and corresponds to a minimization in the space of two-body unitary transformations.

Despite classical progress towards solving these equations, the advent of quantum computers and their hope for the simulation of quantum mechanical systems has led to several new approaches, which are well documented in previous chapters. In particular, the contracted quantum eigensolvers, or CQE, attempt to find a solution to a contracted equation using a quantum computer [4, 5]. The quantum computer allows us to directly obtain the reduced density matrix of a wavefunction through measurement, removing the exponentially scaling hierarchy of RDMs needed to exactly solve the corresponding classical problem, and

by necessity automatically satisfying the $N-$representability problem. Additionally, quantum computers can efficiently implement unitary operations on the quantum state, allowing for theoretically efficient state preparation.

To address the hermitian component of the CSE requires expansions of generic two-body terms,[6] which are common in classical ab initio methods (for example coupled cluster, quantum Monte Carlo, imaginary time evolution, etc. [7]), but post substantial problems for quantum computing in that they correspond to potentially non-unitary operations[8]. For quantum simulation, both the method used to apply non-unitary evolution, as well as the method of implementing the non-unitary operators, are important questions.

In this chapter we develop a contracted quantum eigensolver for solving the hermitian contracted Schrödigner equation, or HCSE. Unlike the ACSE, the HCSE implies a solution of the Schrödigner equation, providing an exact condition on eigenstates of the simulated quantum system. We provide some example methods for implementing the anti-Hermitian operators, which can be solved through tomography of a 4-RDM, and the solution of a least squares problem, or an infinitesimal based methods involving operations on an extended state space and limited ancilla qubits, which scale relative to the number of iterative steps. The presented method implies a solution with iterations requiring only $O(r^4)$ scaling RDMs, with the potential for accelerated convergence. Some examples and applications on a superconducting qubit framework are presented.

13.2 Theory

13.2.1 Contracted Schrödinger Equation

For molecular systems, we can define the electronic Hamiltonian for a $N-$electron system in a basis set of m one-electron orbitals as:

$$\hat{H} = \frac{1}{2}\sum_{prsq} {}^2K^{pr}_{sq}\hat{a}^\dagger_p\hat{a}^\dagger_s\hat{a}_q\hat{a}_r \tag{13.1}$$

where ${}^2K^{pr}_{sq}$ is an element of the reduced Hamiltonian given by:

$${}^2K^{pr}_{sq} = \frac{1}{N-1}(\delta^{p1}_q K^r_s + \delta^{r1}_s K^p_q) + {}^2V^{pr}_{qs} + \delta^p_q\delta^r_s\frac{E_c}{N(N-1)} \tag{13.2}$$

where ${}^1K$ is the one-electron integral, ${}^2V$ is the two-electron repulsion integral, and E_c is the constant nuclear energy. Given a wavefunction ψ, we can contract (or project) the Schrödigner equation onto the space of two particles, yielding the contracted Schrödigner equation:

$$2\langle\psi|(\hat{H}-E)\hat{a}^\dagger_i\hat{a}^\dagger_k\hat{a}_l\hat{a}_j|\psi\rangle = 0 \tag{13.3}$$

where E is the energy of the system, and the right hand side is strictly zero if and only if ψ is a solution to the Schrödinger equation. Note, the factor of two is an arbitrary scaling factor which allows the anti-Hermitian and Hermitian parts to be normalized to their gradients (note, this also happens naturally when using the binomial normalization of the 2-RDM). When not zero, we refer to the remainder as the residual of the CSE. The necessity can be seen simply by plugging in a eigenstate of the Hamiltonian, and the sufficiency results from the dispersion relation when we multiply each residual by ${}^2K^{ps}_{qr}$. Formally, the CSE depends

on the 4-electron reduced density matrix, where the $k-$RDM is defined as:

$$ {}^{k}D^{i_1 i_2 \ldots i_k}_{j_1 j_2 \ldots j_k} = \langle \psi | \hat{a}^\dagger_{i_1} \hat{a}^\dagger_{i_2} \cdots \hat{a}^\dagger_{i_k} \hat{a}_{j_k} \cdots \hat{a}_{j_2} \hat{a}_{j_1} | \psi \rangle \tag{13.4} $$

and scales approximately as $O(m^{2k})$. When we take the anti-Hermitian component, we obtain the anti-Hermitian contracted Schrödinger equation:

$$ {}^{2}A^{ik}_{jl} = \langle \psi | [\hat{H}, \hat{a}^\dagger_i \hat{a}^\dagger_k \hat{a}_j \hat{a}_l] | \psi \rangle \tag{13.5} $$

which requires only the 3-RDM and describes the invariance of the wavefunction with respect to unitary two-particle excitations. If we instead consider the hermitian component, we obtain the Hermitian contracted Schrödigner equation, or HCSE, with residuals denoted by ${}^{2}R^{ij}_{jl}$:

$$ {}^{2}R^{ik}_{jl} = \langle \psi | \{ \hat{H}, \hat{a}^\dagger_i \hat{a}^\dagger_k \hat{a}_l \hat{a}_j \} | \psi \rangle - 2E^2 D^{ik}_{jl}. \tag{13.6} $$

As a final note, if we consider the residual vector, $\vec{r}_n$, and the reduced Hamiltonian vector, $\vec{k}$, then we have that:

$$ \mathrm{Var}[\hat{H}] = \langle \psi | \hat{H}^2 | \psi \rangle - \langle \psi | \hat{H} | \psi \rangle^2 = \frac{1}{2} \vec{r}_n \cdot \vec{k} \tag{13.7} $$

From the Cauchy-Schwarz inequality, we can show that:

$$ \mathrm{Var}[\hat{H}] = \frac{1}{2} \vec{r}_n \cdot \vec{k} \leq \frac{1}{2} || {}^{2}R_n || \; || {}^{2}K ||. \tag{13.8} $$

Showing that the variance is bounded by the norm of the residual times a constant factor. However, if we compare the variance to first order, we find a similar relation to the square of the residual norm, implying that the residual norm roughly relates to the standard deviation of the energy.

13.2.2 Quantum Eigensolver for Solving the CSE

Consider the energy of a normalized, iterative wavefunction at iteration n, ψ_n, expanded around a two-body Hermitian operator $\hat{P}_n = \sum_{ijkl} P_n^{ik;jl} \hat{a}_i^\dagger \hat{a}_k^\dagger \hat{a}_j \hat{a}_l$ with infinitesimal ϵ:

$$E_n(\epsilon, \hat{P}_n) = \frac{\langle \psi_n | e^{\epsilon \hat{P}_n} \hat{H} e^{\epsilon \hat{P}_n} | \psi_n \rangle}{N_\epsilon} \tag{13.9}$$

where we normalize the wavefunction with respect to $N_\epsilon = \langle \psi_n | e^{2\hat{P}_n} | \psi_n \rangle$. The derivative with respect to elements of $\hat{P}_n$ gives the following relation to the residuals of the HCSE:

$$\lim_{\epsilon \to 0} \frac{1}{\epsilon} \frac{dE}{dP_{n+1}^{ik;jl}} = {}^2R_{n+1}^{ij:kl}. \tag{13.10}$$

This implies a very straightforward way in which we can obtain a solution to the HCSE, and thus the CSE. Let $|\psi_n\rangle$, $\hat{R}_n$, and $\hat{P}_n$ denote the wavefunction, residuals of the HCSE, and the exponential operator at a given iteration n. The CQE for solving the HCSE is then given in Table 13.1, and consists of preparing a wavefunction where we have minimized the energy with respect to the operator $\hat{P}_n$ (which is constructed based on the gradient information $\hat{R}_n$), and then obtaining the new residuals. If we select $\hat{P}_n = \hat{R}_n$, we essentially perform a gradient descent routine, and so we can accelerate the convergence by choosing different operators.

The principal barrier to the algorithm in 13.1 is that $\exp \hat{P}_n$ is non-unitary. The residuals themselves also are not easily obtained. Due to the iterative nature of the ansatz, on a quantum computer we require the implementation of consecutive non-unitary operators, which is more challenging than a generic non-unitary operation.

Table 13.1: CQE algorithm for solving the CSE (HCSE).

CQE Algorithm

Set $0 \leftarrow n$

Initialize $|\Psi_0\rangle, \hat{R}_0$

While $||^2 R_n|| > \delta$:

Step 1: $\min E_n(\hat{P}_n)$

Step 2: Evaluate $^2\hat{R}_{n+1},\ \hat{P}_{n+1}[^2\hat{R}_{n+1}]$

Step 3: Construct $|\psi_{n+1}\rangle = e^{\hat{P}_n}|\psi\rangle$

Step 3: $n+1 \leftarrow n$

13.2.3 Obtaining the Residuals of the HCSE

To actually implement the proposed algorithm, we first explore two methods of obtaining the residuals. Both of these approaches provide the residuals with controllable approximations and a set resource cost.

The first method is as follow. Given sufficiently efficient measurement and storage capabilities, we can directly measure the $4-$RDM on the quantum computer, and then solve the classical RDM-based equation. We can also approximate the 4-RDM using cumulants of either the 3-RDM or the 2-RDM, though if approximated, one needs to incorporate optimization techniques suitable for inexact gradients. Approximate measurement schemes exist as well, which have been applied to four-body expectations, and reasonable could be applied here.

The second way to obtain the residuals requires two copies of the state, accessible through a single ancilla. That is, given a unitary U which acts in the ancilla space as:

$$U = \begin{bmatrix} 1 - \frac{\delta^2}{2}\hat{H}^2 & -\hat{H} \\ \hat{H} & 1 - \frac{\delta^2}{2}\hat{H}^2 \end{bmatrix}, \tag{13.11}$$

which acts on two copies of our state ψ:

$$|\Upsilon\rangle = \frac{1}{\sqrt{2}} U \begin{bmatrix} |\psi\rangle & |\psi\rangle \end{bmatrix}^T. \tag{13.12}$$

Performing the following 2-RDM related measurement:

$$\hat{M}_z{}^{ik}_{jl} = \begin{bmatrix} \hat{a}_i^\dagger \hat{a}_k^\dagger \hat{a}_l \hat{a}_j & 0 \\ 0 & -\hat{a}_i^\dagger \hat{a}_k^\dagger \hat{a}_l \hat{a}_j \end{bmatrix}, \tag{13.13}$$

yields the following residuals:

$$\frac{1}{\delta} \langle \Upsilon_n | \hat{M} | \Upsilon_n \rangle = {}^2R_n^{ij;kl} + O(\delta^2) \tag{13.14}$$

On a quantum computer, we can perform this operation quite easily. U here corresponds to a Pauli-conditioned time evolution operator:

$$U = \exp i\delta Y_a \otimes \hat{H}. \tag{13.15}$$

where Y_a is the Pauli-Y gate acting on the ancilla a which we have prepared with the Hadamard transform on the ancilla. The measurement is identical to standard measurement of the 2-RDM, except that for every string we apply a Z to the ancilla. Because this Z is present in every term, in a local tomography scheme this has the same scaling as the 2-RDM. For real Hamiltonians, the second order terms in the measurement cancel out, which when divided by ϵ yields the residuals to accuracy $O(\epsilon^2)$. Despite the enlargement of the state space through the ancilla, the success probability is still 1 due to both ancilla states contributing correct signs.

13.2.4 Implementing the Exponential Hermitian Operator

The first approach to implementing $\exp \epsilon \hat{P}_n$ follows work by Motta et al., and involves finding the least squares approximation of the two-body hermitian operators onto an anti-hermitian one [9]. The least-squares fit was shown to be exact in the limit that the set of anti-hermitian operators spans the $N-$body space[10] which is known to be exact as the unitary operator increases in size. In particular, using the 4-RDM we can construct the metric matrix, defined as:

$$G_{npq;rs}^{ij;kl} = \langle \psi_n | \hat{a}_i^\dagger \hat{a}_k^\dagger \hat{a}_j \hat{a}_l \hat{a}_p^\dagger \hat{a}_r^\dagger \hat{a}_s \hat{a}_q | \psi_n \rangle. \tag{13.16}$$

We can then find the least squares fit of the $\hat{P}$ operator onto a two-body anti-Hermitian operator, $\hat{A}$, through the linear problem:

$$(G - G^\dagger)\hat{A} = (G + G^\dagger)\hat{P}. \tag{13.17}$$

This matrix is quite costly to implement, naively requiring the 4-RDM. Given a 4-RDM, we can obtain ${}^2A$ and then (similar to work for CQEs involving the ACSE), implement the operator on a quantum computer.

The second approach, inspired by recent work for propagating non-unitary operators[11], and similar to recent work for propagating imaginary time[12] is to simulate the following operator:

$$\hat{V}_P = \begin{bmatrix} 1 & \epsilon\hat{P} \\ -\epsilon\hat{P} & 1 \end{bmatrix}, \tag{13.18}$$

with small ϵ. acts to produce a state:

$$\hat{V}_P \begin{bmatrix} |\psi\rangle & |\psi\rangle \end{bmatrix}^T = \begin{bmatrix} e^{\epsilon\hat{P}}|\psi\rangle & e^{-\epsilon\hat{P}}|\psi\rangle \end{bmatrix} + O(\epsilon). \tag{13.19}$$

Similar to the above scheme, the operator required here can be approximated to first order

as:

$$\hat{V}_P^n = \exp i\delta Y_a \otimes \hat{P}_n. \tag{13.20}$$

The remaining problem relates to subsequent steps. Because the resulting state is now not duplicated, we can either append another ancilla or perform a projective measurement. Both of these decrease the success probability by a factor of 2, which would lead to exponentially decreasing success rates. Instead, we somewhat naively simply implement the next operator, which can be shown to first order still yields the target operator:

$$\hat{V}_S^2 \hat{V}_S^1 \begin{bmatrix} |\psi\rangle & |\psi\rangle \end{bmatrix}^T = \begin{bmatrix} e^{\epsilon(\hat{P}_1+\hat{P}_2)}|\psi\rangle & e^{-\epsilon(\hat{P}_1+\hat{P}_2)}|\psi\rangle \end{bmatrix}^T + O(\epsilon^2). \tag{13.21}$$

After several steps (on the order of $\frac{1}{\epsilon}$) this will course becomes a less accurate depiction of the ansatz we are trying to propagate, and so we use a loose Wolfe condition to determine when to perform a reset or dilation onto another ancilla. The proposed method stills lead to an exponentially decreasing success probability, albeit prolonged with respect to the number of iterations. In theory, performing amplitude amplification before each reset would eliminate this, although for near-term results this can be challenging[13]. While the subspace selection for the amplitude amplification is quite simple (notably, our 'good' subspace corresponds only with the $|0\rangle$ ancilla state), a reflection around the wavefunction is more difficult to implement. The main advantage to this technique however is that only $O(m^4)$ steps are used, preventing the use of the 4-RDM or higher RDMs. Thus, the HCSE could function as a $O(r^4)$ scaling approach for quantum computing.

13.3 Results and Discussion

We first highlight one of the main advantages of the HCSE approach, notably that in minimizing the residual we are guaranteed to minimize the variance. While we see above that the variance is bounded by the norm of the residual matrix R, in practice, the error is dominated

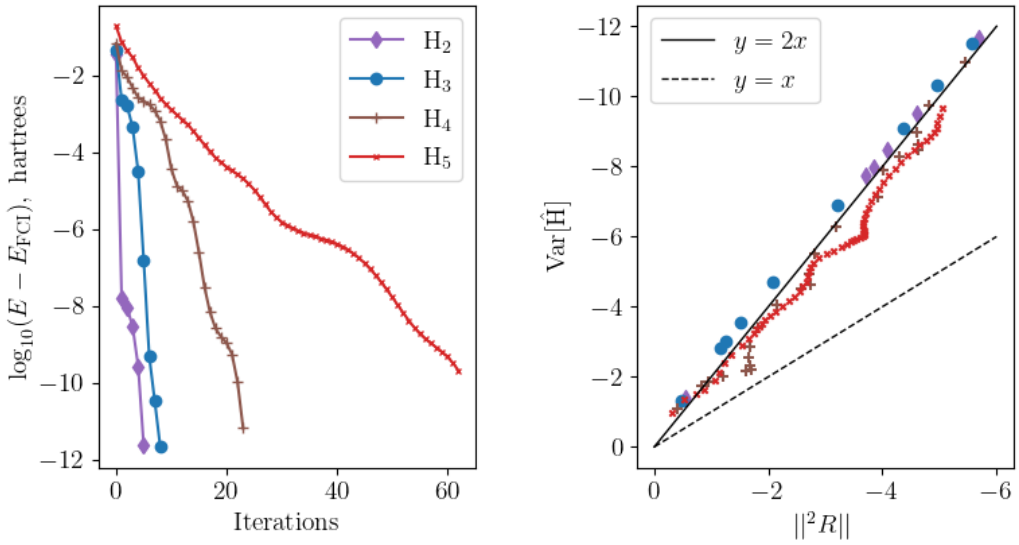

Figure 13.1: (Left) Energy convergence of hydrogen chains compared with Full Configuration Interaction results. (Right) Obtained values of the HCSE residual and calculated variances (from a simulation of the full density matrix) obtained during the iterations.

by the square of the norm. This can be seen in Figure 13.1, where we compare H_2, H_3, H_4, and H_5 in minimal basis sets (STO-3G). Here, each hydrogen chain except H_5 is run at 1 Å separation, which was run at 1.5 Å. Note that the scale is logarithmic. The dotted line ($y = x$) indicates the scaling (without the norm of the Hamiltonian, which for these systems is on the order of magnitude of 1), which is a boundary according to the Cauchy-Schwarz relation. While the ACSE is known to provide very accurate results, here we see that convergence to an eigenstate of the Hamiltonian is guaranteed as the residuals of the CSE go to zero.

We next wanted to investigate the properties of our implementations of the HCSE. Using the least-squares method, and the single-ancilla based approach, with variable resets as well as resets at each step, we looked at the dissociation of H_4 at different residual thresholds. These results are seen in 13.2. The results show consistently accurate results across the dissociation curve. Interestingly, the shortest bond lengths seem to be the most difficult to capture accurate energies with, although we still can achieve well below chemical accuracy.

Additionally, each method present is able to converge in each instance, albeit with different resource counts. While for other methods, the dissociated region generally is harder to obtain good results for, here, the HCSE method is successfully able to capture stretched and dissociated systems.

Finally, we provide a similar comparison, now focusing on the rate of convergence with a more challenging system. Figure 13.3 shows square H_4 at stretched bond distances, with each method as well as the ACSE. Even in these instances, we see that the HCSE performs quite well. One of the challenges with the infinitesimal method is highlight as well here - when the ancilla no longer represents the target application, it appears to be more easily pushed into a local minima, or an excited state. While this certainly could be useful in some instances, for ground state minimizations we are looking to first capture the lowest-energy state. Using step-wise resets (which again would likely require amplitude amplification), seems to overcome this, as in most cases we avoid getting stuck in a well and converge to the ground state. Additionally, here we see that the ACSE does quite well, but again, without the variance of the state, it is hard to infer in these instances (where there are degenerate states present) how close we are to a true ground state, without a calculation involving the CSE.

Importantly, these results show that an exact two-body method is possible on the quantum computer. Unlike with variational quantum eigensolvers or unitary coupled cluster, where the question of the parameter space is a considerable question, and it is quite possible to become isolated in barren plateaus[14], the work here represents an exact condition on the wavefunction. As such, the ideal implementation is robust in its very nature.

Future work involving the CSE would focus on actual implementations. In general, non-unitary evolution is challenging, and efforts to carry out realistic calculations have been minimal. While non-unitary methods such as imaginary time evolution are promising, the CSE provides potentially more flexibility, and we expect could outperform QITE methods

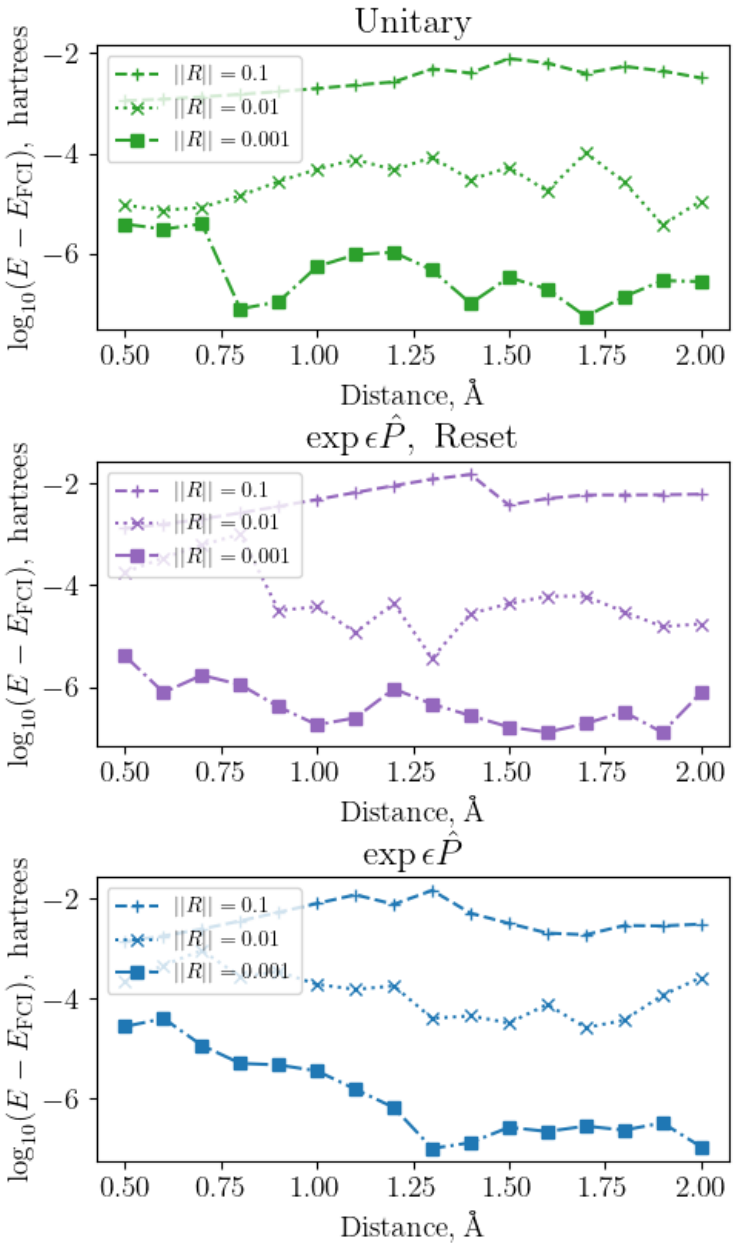

Figure 13.2: Comparison of accuracy of linear H_4 (in a minimal basis set) dissociation to the full configuration interaction energy. Comparison is at different residual cutoffs for different methods of preparing the non-unitary evolution. (Top) Exponential prepared through least-square fit to find anti-hermitian two-body operator. (Center) Method of single-ancilla infinitesimal evolution with resets occurring at each measurement. (Bottom) Method of single-ancilla infinitesimal evolution, but compacts $\hat{P}_n$ operators at each iteration until the energy no longer decreases. Resets occur less frequently. While there exist differences in the implementation, the level of accuracy is the same throughout each.

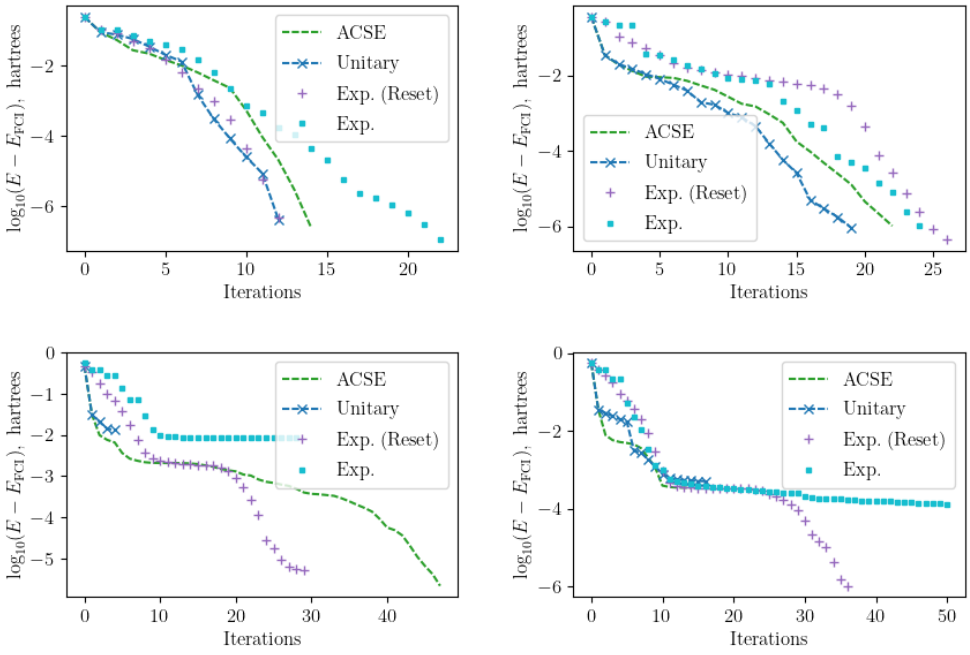

Figure 13.3: Simulations of square H_4 (in a minimal basis set) at different bond lengths for different CSE methods as well as the ACSE. Distances were taken at 1.5 Å, 2.0 Å, 2.5 Å, and 3 Å(ordered top to bottom, left to right). A minimal basis set was used. Notably, when not using reset options, some operators converged to excited states in several of the cases.

in some instances (especially for systems with near-degeneracies). Additionally, similar to the ACSE, the CQE for solving the CSE has self-correcting elements, and does not require a completely faithful implementation of the exponential operator.

The nature of the ansatz as well is quite simple, requiring only a single CNOT connection relative to the original two-body operator. Because the ancilla operator independently of one another, a all-to-all configuration would be highly ideal. Further work on reducing the measurement cost, which currently decreases exponentially with the number of 'resets' (or equivalently, the number of ancilla being utilized), is critical for any meaningful application. While the focus in this work is on the algorithm and is accompanied by noiseless simulation, numerous considerations for noisy devices exist.

13.4 Conclusion

In this chapter we present a contracted quantum eigensolver for solving the hermitian component of the contracted Schrödinger equation, opening up a solution for solving the generic CSE. The CQE provides a solution to the total Schrödinger equation, which has steps requiring between $O(r^4)$ and $O(r^8)$ measurements. Additionally, building on previous work, once we are within a region relatively close to the wavefunction, we have accelerated convergence toward a solutions.

While the HCSE approach is more challenging to simulate than the ACSE-based CQE approach in earlier chapters, the work here highlights the strength of the contracted quantum eigensolver. Building on this work, other techniques could be developed, such as combining the ACSE and HCSE as a CSE approach, emphasizing the HCSE as a check on the variance of the energy, developing encoding-free variations, exploring operator-free pools, or applying the CQEs to excited states. The contracted quantum eigensolver offers a robust means to look at electronic structure problem, with the HCSE providing a critical element in terms of the theoretical reliability of the algorithm. The method possess numerous qualities ideal

for near-term quantum applications, and exists as a scalable alternative to other quantum algorithms that are broadly applicable to numerous chemical systems. The previous chapters and current work have resulted in numerous research questions, and we hope will continue to provoke and guide many interesting avenues of research within quantum chemistry and quantum simulation.

References

[1] A. Coleman and V. Yukalov, *Reduced Density Matrices: Coulson's Challenge* (Springer, Berlin Heidelberg New York, 2000).

[2] H. Nakatsuji, Physical Review A **14**, 41 (1976).

[3] D. A. Mazziotti, Physical Review A **57**, 4219 (1998).

[4] S. E. Smart and D. A. Mazziotti, **60637**, 1 (2020), arXiv:2004.11416 .

[5] S. E. Smart, J.-N. Boyn, and D. A. Mazziotti, Physical Review A **105**, 022405 (2022), arXiv:2103.06876 .

[6] D. A. Mazziotti, Physical Review A **69**, 012507 (2004).

[7] H. Nakatsuji and E. R. Davidson, Journal of Chemical Physics **115**, 2000 (2001).

[8] A. Daskin and S. Kais, Quantum Information Processing **16**, 1 (2017), arXiv:1606.04315 .

[9] M. Motta, C. Sun, A. T. Tan, M. J. O'Rourke, E. Ye, A. J. Minnich, F. G. Brandão, and G. K. L. Chan, Nature Physics **16**, 205 (2020), arXiv:1901.07653 .

[10] H. Nishi, T. Kosugi, and Y. ichiro Matsushita, npj Quantum Information **7** (2021), 10.1038/s41534-021-00409-y.

[11] A. W. Schlimgen, K. Head-Marsden, L. M. Sager, P. Narang, and D. A. Mazziotti, , 2 (2021), arXiv:2106.12588 .

[12] T. Kosugi, Y. Nishiya, and Y.-i. Matsushita, (2021), arXiv:2111.12471 .

[13] G. Brassard, P. Høyer, M. Mosca, and A. Tapp, , 53 (2002), arXiv:0005055 [quant-ph] .

[14] J. R. McClean, S. Boixo, V. N. Smelyanskiy, R. Babbush, and H. Neven, Nature Communications **9**, 1 (2018), arXiv:1803.11173 .